

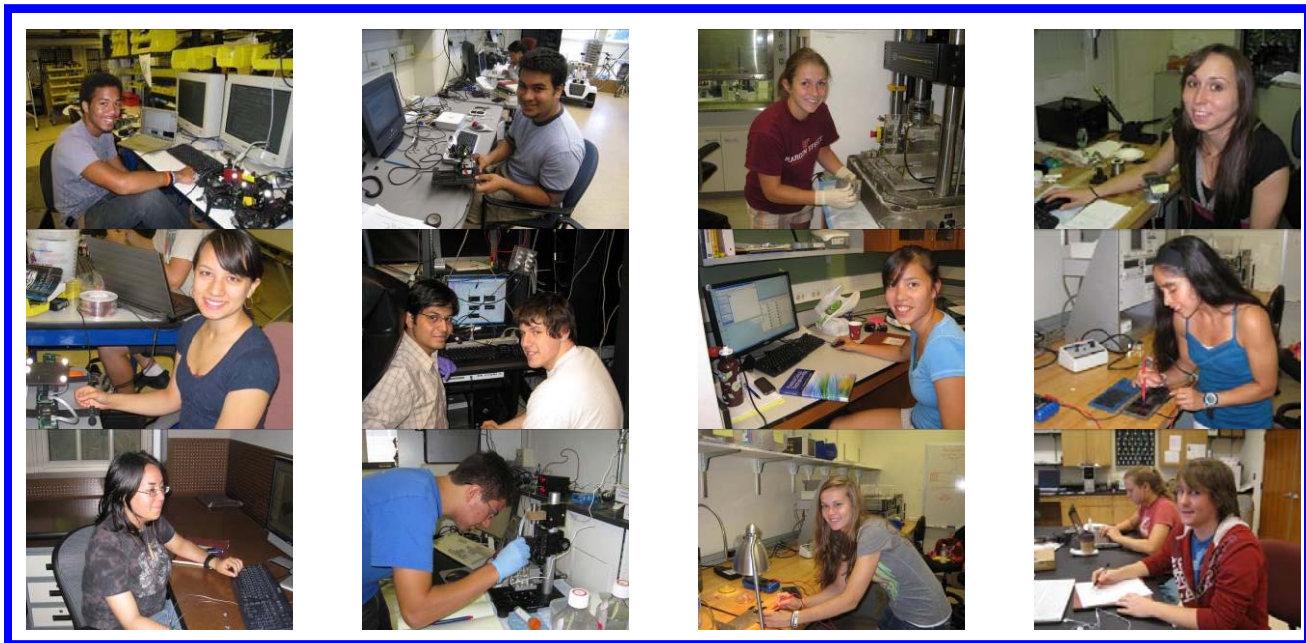
# SUNFEST

[www.seas.upenn.edu/~sunfest](http://www.seas.upenn.edu/~sunfest)



## 2009

### SUMMER UNDERGRADUATE FELLOWSHIPS IN SENSOR TECHNOLOGIES



*TECHNICAL REPORT*

*TR-CST25AUG09*

*Center for Sensor Technologies*

*University of Pennsylvania*

*Philadelphia, PA 19104*

## *Acknowledgement*

This material is based upon work supported by the National Science Foundation under Grant No. 0754741.

## *Disclaimer*

Any opinions, findings, and conclusions or recommendations expressed in this material are those of the author(s) and do not necessarily reflect the views of the National Science Foundation.

SUNFEST 2009



# SUNFEST 2009

## SUMMER UNDERGRADUATE FELLOWSHIP IN SENSOR TECHNOLOGIES

Sponsored by the National Science Foundation (Award no. EEC-0754741)

### PREFACE

*This report is the result of twelve undergraduate students' research efforts during the summer of 2009; from June 1 through August 8, 2009. Twelve students from Penn and other colleges participated in the SUNFEST program, which is organized by the Center for Sensor Technologies of the School of Engineering and Applied Science at the University of Pennsylvania. This unique "Summer Experience for Undergraduates in Sensor Technologies" program was initiated in 1986 and has grown considerably in size. It is now recognized as one of the most successful summer programs for undergraduates in the country. I would like to express my sincere gratitude to the National Science Foundation for their continued support for this REU Site.*

*The purpose of the SUNFEST program is to provide bright, motivated undergraduate students with the opportunity to become involved in active research projects under the supervision of a faculty member and his graduate student(s). The general area of research concentrates on sensor technologies and includes projects such as materials and technology for sensors, microstructures, smart imagers, bio-sensors and robotics. By providing the students with hands-on experience and integrating them with a larger research group where they can work together with other students, the program intends to guide them in their career choices. By exposing the students to the world of research, we hope they will be more inclined to go on for advanced degrees in science and engineering.*

*The students participated in a variety of hands-on workshops in order to give them the tools to do first-rate research or enhance their communication skills. These included "Ethics in Science and Engineering", "Information Retrieval and Evaluation", "Applying to Graduate School" and "Writing Technical Reports". Students also had plenty of opportunity for social interactions among themselves or with faculty and graduate student advisors.*

*This booklet contains reports from this year's projects, the quality of which testifies to the high level of research and commitment by these students and their supervisors. I would like to express my sincere thanks to the students for their enthusiastic participation; the help of the faculty members, graduate students and support staff is very much appreciated. I would also like to thank Sherri Butler, Delores Magobet, Valerie Lundy-Wagner, Sid Deliwala, and the rest of the ESE staff for their invaluable help in making this program run smoothly.*

Jan Van der Spiegel, Director

Center for Sensor Technologies

**FINAL REPORT**  
**2009 SUMMER UNDERGRADUATE FELLOWSHIP IN SENSOR TECHNOLOGIES**  
**Sponsored by the National Science Foundation**

<http://www.eese.upenn.edu/~sunfest/pastProjects/Projects09.html>

**TABLE OF CONTENTS**

<b>PREFACE and LIST OF STUDENT PARTICIPANTS</b>	iv - x
<b>DESIGN OF A SYSTEM TO STUDY HUMAN INTERNAL DISC STRAINS IN TORSION AND COMPRESSION MEASURED NONINVASIVELY USING MAGNETIC RESONANCE IMAGING</b> <i>Valerie, Walters (ESM) – Virginia Polytechnic Institute and State University</i> <i>Advisor: Dawn M. Elliot, PhD</i>	1 - 21
<b>AMPLIFICATION CIRCUITS AND PATTERNING METHODS OF ORGANIC FIELD-EFFECT TRANSISTORS</b> <i>Hank Bink (Electrical and Computer Engineering) – Lafayette College</i> <i>Advisor: Cherie Kagan</i>	22 - 36
<b>A VIRTUAL HEART MODEL FOR FORMAL AND FUNCTIONAL MEDICAL DEVICE VERIFICATION</b> <i>Allison Connolly, Biomedical Engineering, Johns Hopkins University</i> <i>Advisor: Rahul Mangharam, Ph.D.</i>	37 - 54
<b>AUTONOMIZATION OF A MOBILE HEXAPEDAL ROBOT USING A GPS</b> <i>Phillip Dupree (Mechanical Engineering) - Columbia University</i> <i>Advisors: Daniel E. Koditschek, Galen Clark Haynes</i>	55 - 90
<b>PEDIATRIC PHYSICAL ACTIVITY DYNAMOMETER</b> <i>Katherine Gerasimowicz (Bioengineering) – University of Pennsylvania</i> <i>Advisors: Dr. Jay N. Zemel, Dr. Babette Zemel</i>	91 - 115
<b>STABILITY CONTROL SYSTEM FOR THE BIOLOID HUMANOID ROBOT</b> <i>Willie W Gonzalez (EE) – University of Puerto Rico Mayagüez campus</i> <i>Advisor: Dr. Daniel D. Lee</i>	116 - 135
<b>AUTOMATED GAIT OPTIMIZATION FOR A CENTIPEDEINSPIRED MODULAR ROBOT</b> <i>Sarah Koehler (Mechanical Engineering) - Cornell University</i> <i>Advisor: Dr. Mark Yim, Dr. Daniel E. Koditschek</i>	136 - 155
<b>MODULAR PHOTOVOLTAIC-MILLIFLUIDIC ALGAL BIOREACTOR SYSTEM</b> <i>Linda McLaughlin, Electrical Engineering, Community College of Philadelphia</i> <i>Advisors: Jay Zemel, Jorge Santiago, David Graves, Michael Mauk</i>	156 - 181

<b>ANALYSIS OF DARK AND LIGHT CYCLES ON CHLORELLA GROWTH</b>	182 - 192
<i>Ieva Narkeviciute, Chemical Engineering, University of Massachusetts Amherst</i>	
<i>Advisor: Jay Zemel, Jorge Santiago, David Graves, Michael Mauk</i>	
<b>MICROMECHANICAL IMAGING ANALYSIS OF BULK VS. LOCAL PROPERTIES CONCERNING MESENCHYMAL STEM CELL HETEROGENEITY</b>	193 - 216
<i>Jeffrey Perreira (Mechanical Engineering) – Lehigh University</i>	
<i>Advisor: Dr. Robert Mauck, Graduate Student: Megan Farrell</i>	
<b>VIBRATIONAL ENERGY HARVESTING USING MEMS PIEZOELECTRIC GENERATORS</b>	217 - 241
<i>Andrew Townley – Electrical Engineering, University of Pennsylvania</i>	
<i>Advisor: Gianluca Piazza</i>	
<b>MIMOSA: MINE INTERIOR MODEL OF SMOKE AND ACTION</b>	242 - 259
<i>Desirée E. Velázquez Rios (Mathematics) – University of Puerto Rico at Humacao</i>	
<i>Advisors: Norman I. Badler and Jinsheng Kang</i>	

**LIST OF STUDENT PARTICIPANTS  
IN THE SUNFEST PROGRAM SINCE 1986**

**Summer 2009**

Bink Hank	Lafayette College
Connolly Allison	Johns Hopkin
Dupree Phillip	Columbia University
Gerasimowicz Katherine	University of Pennsylvania
Gonzalez Willie	Univ. of Puerto Rico, Mayaguez
Koehler Sarah	Cornell University
Mclaughlin Linda	Community College of Philadelphia
Narkeviciute Ieva	Univ. of Massachusetts Amherst
Perreira Jeffrey	Lehigh University
Townley Andrew	University of Pennsylvania
Velazquez Desiree	Univ. of Puerto Rico at Humacao)
Walters Valerie	Virginia Polytechnic Institute and State University

**Summer, 2008**

Clarence Agbi	Yale University
Uchenna Anyanwu	San Jose State University
Christopher Baldassano	Princeton University
Alta Berger	George Washington University
Ramon Luis Figueroa	University of Puerto Rico
David Joffe	Carnegie Mellon University
Erika Martinez	University of Puerto Rico
Alexei Matyushov	Arizona State University
Kamruzzaman Rony	Stony Brook University
Anil Venkatesh	University of Pennsylvania
Emily Wible	University of Pennsylvania

**Summer, 2007**

Mulutsga Bereketab	Virginia Polytechnic Institute
Sonia A. Bhaskar	Princeton University
Patrick Duggan	Providence College
Nataliya Kilevskaya	University of Florida
Ryan Li	Case Western Reserve University
Viktor L. Orekhov	Tennessee Technological University
Andrew Potter	Brown University
Pamela Tsing	University of Pennsylvania
Victor Uriarte	Florida International University
Adriane Wotawa-Bergen	University at Buffalo
Arellys Rosado Gomez	University of Puerto Rico

**Summer, 2006**

Sam Burden  
Jose M. Castillo Colon

Shakera Guess  
Journey Isip  
Nathan Lazarus  
Armand O'Donnell  
William Peeples  
Raúl Pérez Martínez  
Helen Schwerdt  
Xiaoning Yuan

University of Washington  
University of Puerto Rico  
Alexsandra Fridshtand  
Lehigh University  
Lincoln University  
Columbia University  
University of Pennsylvania  
University of Pennsylvania  
Lincoln University  
University of Puerto Rico  
Johns Hopkins University  
Duke University

**Summer, 2005**

Robert Callan  
David Cohen  
Louie Huang  
Roman Geykhman  
An Nguyen  
Olga Paley  
Miguel Perez Tolentino  
Ebenge Usip  
Adam Wang  
Kejia Wu

University of Pennsylvania  
University of California at Berkeley  
University of Puerto Rico  
University of Southern California  
University of Texas, Austin  
University of Pennsylvania

**Summer, 2004**

Benjamin Bau  
H. Chang  
Seth Charlip-Blumlein  
Ling Dong  
David Jamison  
Dominique Low  
Emmanuel U. Onyegam  
J. Miguel Ortigosa  
William Rivera  
Matthew Saucedo  
Olivia Tsai

Massachusetts Institute of Technology  
Alexander  
University of Pennsylvania  
University of Pennsylvania  
University of Rochester  
Johns Hopkins University  
University of Pennsylvania  
University of Texas, Dallas  
Florida Atlantic University  
University of Puerto Rico, Mayaguez  
Texas A&M University, Kingsville  
Carnegie Mellon University

### **Summer, 2003**

Emily Blem	Swarthmore College
Brian Corwin	University of Pennsylvania
Vinayak Deshpande	University of Virginia
Nicole DiLello	Princeton University
Jennifer Geinzer	University of Pittsburgh
Jonathan Goulet	University of Pennsylvania
Mpitulo Kala-Lufulwabo	University of Pittsburgh
Emery Ku	Swarthmore College
Greg Kuperman	University of Pennsylvania
Linda Lamptey	University of Pennsylvania
Prasheel Lillaney	University of Pennsylvania
Enrique Rojas	University of Pennsylvania

### **Summer, 2002**

Christopher Bremer	Colorado School of Mines
Aslan Ettehadien	Morgan State University
April Harper	Hampton University
Catherine Lachance	University of Pennsylvania
Adrian Lau	University of Pennsylvania
Cynthia Moreno	University of Miami
Yao Hua Ooi	University of Pennsylvania
Amber Sallerson	University of Maryland/Baltimore
Jiong Shen	University of California-Berkeley
Kamela Watson	Cornell University
John Zelena	Wilkes University

### **Summer, 2001**

Gregory Barlow	North Carolina State University
Yale Chang	University of Pennsylvania
Luo Chen	University of Rochester
Karla Conn	University of Kentucky
Charisma Edwards	Clark Atlanta University
EunSik Kim	University of Pennsylvania
Mary Kutteruf	Bryn Mawr College
Vito Sabella	University of Pennsylvania
William Sacks	Williams College
Santiago Serrano	Drexel University
Kiran Thadani	University of Pennsylvania
Dorci Lee Torres	University of Puerto Rico

### **Summer, 2000**

Lauren Berryman	University of Pennsylvania
Salme DeAnna Burns	University of Pennsylvania
Frederick Diaz	University of Pennsylvania (AMPS)
Hector Dimas	University of Pennsylvania (AMPS)
Xiomara Feliciano	University of Turabo (Puerto Rico)
Jason Gillman	University of Pennsylvania
Tamara Knutsen	Harvard University
Heather Marandola	Swarthmore College
Charlotte Martinez	University of Pennsylvania
Julie Neiling	University of Evansville, Indiana
Shiva Portonova	University of Pennsylvania

### **Summer, 1999**

David Auerbach	Swarthmore
Darnel Degand	University of Pennsylvania
Hector E. Dimas	University of Pennsylvania
Ian Gelfand	University of Pennsylvania
Jason Gillman	University of Pennsylvania
Jolymar Gonzalez	University of Puerto Rico
Kapil Kedia	University of Pennsylvania
Patrick Lu	Princeton University
Catherine Reynoso	Hampton University
Philip Schwartz	University of Pennsylvania

### **Summer, 1998**

Tarem Ozair Ahmed	Middlebury University
Jeffrey Berman	University of Pennsylvania
Alexis Diaz	Turabo University, Puerto Rico
Clara E. Dimas	University of Pennsylvania
David Friedman	University of Pennsylvania
Christin Lundgren	Bucknell University
Heather Anne Lynch	Villanova University
Sancho Pinto	University of Pennsylvania
Andrew Utada	Emory University
Edain (Eddie) Velazquez	University of Pennsylvania

### **Summer, 1997**

Francis Chew	University of Pennsylvania
Gavin Haentjens	University of Pennsylvania
Ali Hussain	University of Pennsylvania
Timothy Moulton	University of Pennsylvania
Joseph Murray	Oklahoma University
O'Neil Palmer	University of Pennsylvania
Kelum Pinnaduwage	University of Pennsylvania
John Rieffel	Swarthmore College
Juan Carlos Saez	University of Puerto Rico, Cayey

**Summer, 1996**

Rachel Branson  
Corinne Bright  
Alison Davis  
Rachel Green  
George Koch  
Sandro Molina  
Brian Tyrrell  
Joshua Vatsky  
Eric Ward

Lincoln University  
Swarthmore College  
Harvard University  
Lincoln University  
University of Pennsylvania  
University of Puerto Rico-Cayey  
University of Pennsylvania  
University of Pennsylvania  
Lincoln University

**Summer, 1995**

Maya Lynne Avent  
Tyson S. Clark  
Ryan Peter Di Sabella  
Osvaldo L. Figueroa  
Colleen P. Halfpenny  
Brandeis Marquette  
Andreas Olofsson  
Benjamin A. Santos  
Kwame Ulmer

Lincoln University  
Utah State University  
University of Pittsburgh  
University of Puerto Rico-Humacao  
Georgetown University  
Johns Hopkins  
University of Pennsylvania  
University of Puerto Rico-Mayaguez  
Lincoln University

**Summer, 1994**

Alyssa Apsel  
Everton Gibson  
Jennifer Healy-McKinney  
Peter Jacobs  
Sang Yoon Lee  
Paul Longo  
Laura Sivitz  
Zachary Walton

Swarthmore College  
Temple University  
Widener University  
Swarthmore College  
University of Pennsylvania  
University of Pennsylvania  
Bryn Mawr College  
Harvard University

**Summer, 1993**

Adam Cole  
James Collins  
Brandon Collings  
Alex Garcia  
Todd Kerner  
Naomi Takahashi  
Christopher Rothey  
Michael Thompson  
Kara Ko  
David Williams  
Vassil Shtonov

Swarthmore College  
University of Pennsylvania  
Hamilton University  
University of Puerto Rico  
Haverford College  
University of Pennsylvania  
University of Pennsylvania  
University of Pennsylvania  
University of Pennsylvania  
Cornell University  
University of Pennsylvania

**Summer, 1992**

James Collins	University of Pennsylvania
Tabbatha Dobbins	Lincoln University
Robert G. Hathaway	University of Pennsylvania
Jason Kinner	University of Pennsylvania
Brenelly Lozada	University of Puerto Rico
P. Mark Montana	University of Pennsylvania
Dominic Napolitano	University of Pennsylvania
Marie Rocelie Santiago	Cayey University College

**Summer, 1991**

Gwendolyn Baretto	Swarthmore College
Jaimie Castro	University of Puerto Rico
James Collins	University of Pennsylvania
Philip Chen	University of Pennsylvania
Sanath Fernando	University of Pennsylvania
Zaven Kalayjian	University of Pennsylvania
Patrick Montana	University of Pennsylvania
Mahesh Prakriya	Temple University
Sean Slepner	University of Pennsylvania
Min Xiao	University of Pennsylvania

**Summer, 1990**

Angel Diaz	University of Puerto Rico
David Feenan	University of Pennsylvania
Jacques Ip Yam	University of Pennsylvania
Zaven Kalayjian	University of Pennsylvania
Jill Kawalec	University of Pennsylvania
Karl Kennedy	Geneva
Jinsoo Kim	University of Pennsylvania
Colleen McCloskey	Temple University
Faisal Mian	University of Pennsylvania
Elizabeth Penadés	University of Pennsylvania

**Summer, 1989**

Peter Kinget	Katholiek University of Leuven
Chris Gerdes	University of Pennsylvania
Zuhair Khan	University of Pennsylvania
Reuven Meth	Temple
Steven Powell	University of Pennsylvania
Aldo Salzberg	University of Puerto Rico
Ari M. Solow	University of Maryland
Arel Weisberg	University of Pennsylvania
Jane Xin	University of Pennsylvania

**Summer, 1988**

Lixin Cao  
Adnan Choudhury  
D. Alicea-Rosario  
Chris Donham  
Angela Lee  
Donald Smith  
Tracey Wolfsdorf  
Chai Wah Wu  
Lisa Jones

University of Pennsylvania  
University of Pennsylvania  
University of Puerto Rico  
University of Pennsylvania  
University of Pennsylvania  
Geneva  
Northwestern University  
Lehigh University  
University of Pennsylvania

**Summer, 1987**

Salman Ahsan  
Joseph Dao  
Frank DiMeo  
Brian Fletcher  
Marc Loinaz  
Rudy Rivera  
Wolfram Urbanek  
Philip Avelino  
Lisa Jones

University of Pennsylvania  
University of Puerto Rico  
University of Pennsylvania  
University of Pennsylvania  
University of Pennsylvania

**Summer, 1986**

Lisa Yost  
Greg Kreider  
Mark Helsel

University of Pennsylvania  
University of Pennsylvania  
University of Pennsylvania

# **DESIGN OF A SYSTEM TO STUDY HUMAN INTERNAL DISC STRAINS IN TORSION AND COMPRESSION MEASURED NONINVASIVELY USING MAGNETIC RESONANCE IMAGING**

NSF Summer Undergraduate Fellowship in Sensor Technologies

Valerie, Walters (ESM) – Virginia Polytechnic Institute and State University

Advisor: Dawn M. Elliot, PhD

## **ABSTRACT**

Many people suffer from lower back pain, which can be caused by disc degeneration. We are studying the properties of non-degenerated and degenerated human lumbar intervertebral discs. The overall objective of this study is to quantify strains in the disc when it is under torsional and compressive loading, simultaneously. This will be done by using magnetic resonance images of discs before and after loading and advanced normalization tools, which is an image normalization technology. For this summer, the objective is to design a device that will load the specimen as previously described and be compatible with the magnetic resonance imaging machine. The protocol will consist of incrementally torquing the specimen while in constant compression. The torque and the compressive force will be monitored via a load cell throughout the test. We expect displacement results to agree with previous studies that have been done in standard mechanical testing equipment. We also hypothesize that the outer annulus fibrous will be the stiffest part of the disc, and that the posterior region will be stiffer than the anterior region. The strain results that we expect to obtain do not have a previous test to compare to; this is the first study that will quantify internal disc strains while the disc is in torsion. We expect the results to provide useful information about the properties of the human intervertebral disc.

## 1. INTRODUCTION

Disc degeneration in the human lumbar spine has been studied over the last decades. It continues to receive attention from the biomechanics and biomedical fields because it is believed to be a main source of lower back pain [1] [2]. Approximately 65 million Americans experience lower back pain per year [3], and Americans alone spend around fifty billion dollars each year on back pain [4].

Compression and torsion are both looked at when studying disc degeneration because these are two types of forces that act on the intervertebral disc. The spinal column is usually under compression of one's body weight; the function of the disc is to behave like a shock absorber and to distribute the stress and strain [5]. The disc also functions like a pivot point [5], which allows us to turn; this movement creates torsion on the disc. Past experiments have shown that discs simultaneously in torsion and compression can injure the spine's facet joints [1]. In another study it was shown, in vivo, that degeneration of the intervertebral disc (IVD) led to a decrease in torsional motion [6]. These previous studies, along with others [7] [8] [9], help lead to the conclusion that torsional movement, also known as axial rotation, is greatly affected by disc degeneration [9].

Previous studies done on the human lumbar spine in torsion include measuring the rotation when a known torque is applied for normal discs [10], measuring the stiffness / rotation of the discs when a known torque is applied for both normal and degenerated discs [7] [8] [9], and measuring maximum torque and rotation for both normal and degenerated discs [6]. While these previous provide useful information, they have certain limitations. These limitations include the use of physical markers and not applying a compressive load. Using physical markers can disrupt the disc's structural integrity, alter the deformation of the disc, and move separately from the tissue [11]. In vivo, the spine is in compression; therefore, a non-weight bearing study, in vitro, does not represent the spine's natural loading. Isolation of the disc was done in some studies and can be seen as a limitation depending on the ultimate goal of the research. Isolating the disc consists of removing the joints, tendons, and ligaments; while this is done in many studies, for example [6] [10]. However, isolation can be seen as a limitation because the facet joints are one of the key elements in the stability of the intervertebral disc [9], and the facet joints resist most of the torque loading, which causes them to experience yielding before the disc does [12]. On the other hand, if the properties of interest are related to the disc alone, isolating the disc is not a limitation.

The objective of this entire study is to quantify strain due to torsion and compression, simultaneously, noninvasively by using a combination of MRI and advanced normalization tools (ANTS), an image normalization technology. Strain due to compression was first quantified by O'Connell *et al* in 2007 [11], but strain due to torsion has yet to be quantified. This study will apply a constant compressive load along with incremental torsional loads. Both normal and degenerated isolated discs will be looked at during this study. The goal of this study is to better understand the disc's properties; therefore, the disc will be isolated. The tests will be conducted on individual cadaveric spinal motion segments, bone-disc-bone.

We hypothesize that the outer annulus fibrosus will be stiffer than the inner annulus fibrosus, which will be stiffer than the nucleus pulposus. We also expect that the anterior portion and the posterior portion of the disc to have the same stiffness. Our final hypothesis is that non-degenerated discs will be stiffer than degenerated discs, which has been shown in previous tests [7].

The project is in the early design stages. The objective of this summer's project is to design a device that will be able to load the specimen in torsion and compression, simultaneously. This device will also be able to be placed into a magnetic resonance imaging (MRI) machine. The goal for the completion of the device design is early August of this year. Preliminary testing can be done in the lab, outside the MRI machine, during the design stage. Preliminary tests will give information on the stress-relaxation times at various angle displacements. Tests for materials strength and durability will also be done when needed for the design. This will be an ongoing study for the next few months in order to collect sufficient data and analyze the results.

Section 2 of this paper gives background on disc degeneration, disc anatomy for both normal and degenerated discs, magnetic resonance imaging, and texture correlation. Section 3 of this paper discusses the design of the device. Section 4 then discusses the materials and methods that will be used for the upcoming study. Section 5 will discuss the preliminary testing results, if applicable. Section 6 will then discuss the limitations to this study, and then Section 7 will give the conclusions of this paper.

## **2. BACKGROUND**

### **2.1 Disc Degeneration**

Disc degeneration does not have just one definition; in fact, it includes the following features: alterations in the structure, cell-mediated changes, pain, and advanced signs of aging [1] [2]. Disc degeneration becomes more common with age, but is not to be confused with signs of aging. A key difference between the two is that degeneration increases metabolite transfer to the discs structure, whereas age decreases it [2]. Approximately 85% of people will show signs of disc degeneration by the time they reach the age of 50 [3]. Disc degeneration can be caused by factors such as mechanical loading [1] [2] and processes that inhibit the healing process [2]. However, the leading cause of disc degeneration is genetics. Between 50-70% of those affected by disc degeneration genetically inherited the trait [2].

### **2.2 Disc Anatomy**

#### **2.2.1 Normal Disc**

A human intervertebral disc is the soft tissue between the spine's vertebrae. The IVDs function as shock absorbers and pivot points. The disc is also responsible for distributing the stress and strain evenly throughout the disc [5]. The discs are thickest in the lumbar region, which supports the majority of the strain from the rest of the spine [5]. A disc is made up of endplates, the nucleus pulposus, and the annulus fibrosus [11].

The endplates of the spinal column separate the discs. The annulus fibrosus is composed mostly of lamellae, which is made of collagen fibers [2]. The nucleus pulposus is located in the center of the disc and is surrounded by the annulus fibrosus. The nucleus pulposus is a white substance composed of loose, wavy, gelatinous fibers [5]. See Figure 1 for a cross-sectional view of a human intervertebral disc [13]. The nucleus pulposus is generally under compression, which creates a tensile hoop stress on the annulus fibrosus. The pressurization of nucleus pulposus is responsible for maintaining disc height, transmitting the compressive load, and preventing large deformations [14].

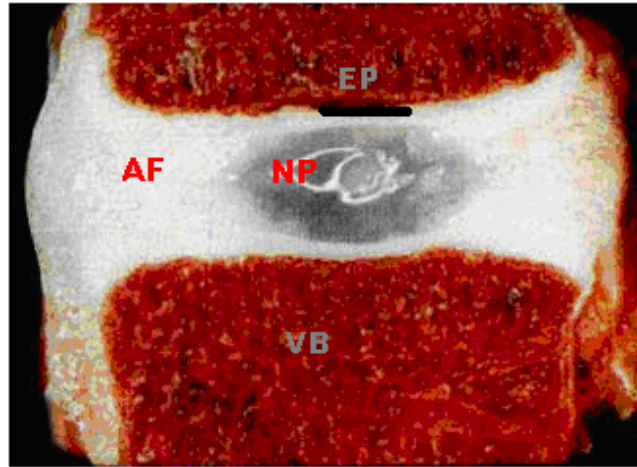


**Figure 1: Cross-sectional view of a human intervertebral disc [13], where NP represents the nucleus pulposus, AF represents the annulus fibrosus, EP represents an end plate, and VB represents the vertebral body.**

### **2.2.2 Degenerated Disc**

The anatomy of an intervertebral disc changes during degeneration. Early stages of degeneration are marked with a loss of proteoglycan content [14] [15] [16], which reduces the nucleus pulposus' ability to attract and bind water [15] [16]. The loss of hydration causes a decrease in the hydrostatic pressure of the nucleus pulposus [14] [15] [16]. The loss of hydration in the nucleus pulposus makes it a semi gelatinous structure instead of a pure gelatinous structure. This results in a less obvious distinction between the annulus fibrosus and the nucleus pulposus [5] and the disc behaves more like an elastic solid than a viscoelastic fluid [17]. Other physiological changes that occur in a degenerated disc include a decrease in disc height, radial tears and/or rim lesions [15]. See Figure 2 for a cross-sectional view of a degenerated human intervertebral disc [18].

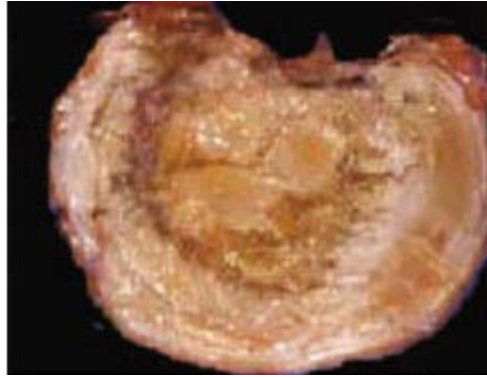


**Figure 2: Cross-section view of a degenerative human intervertebral disc [18].**

To determine the severity of disc degeneration, MR images of the discs are graded using a  $T_2$  or  $T_{1\rho}$  grading system.  $T_2$  is a quantitative method and is more widely known, used, and accepted system.  $T_2$  is the older system, whereas  $T_{1\rho}$  is a newer system that is more sensitive to early stages of degeneration because it measures the loss of proteoglycan content [14] [15] [16]. The  $T_2$  system is an integer-based system with grades from 1 to 5, where 1 is associated with a non-degenerated disc and 5 is associated with a severely degenerated disc [16]. Since the  $T_2$  system is integer-based, it makes it prone to observer bias [15]. The  $T_{1\rho}$  system uses a spin-lock technique and does not require any invasive biomarkers [14] [16].  $T_{1\rho}$  also uses a continuous scale, which reduces observer bias and makes its dynamic range larger than the  $T_2$  range [15]. See Figure 3 below for a comparison between the  $T_2$  and  $T_{1\rho}$  images [15].

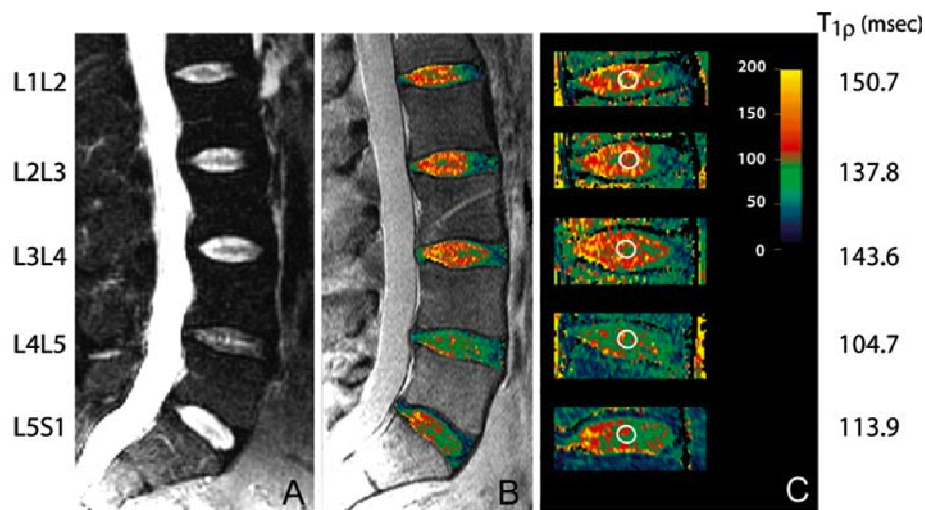


**Figure 3: A)  $T_2$ -weighted images B)  $T_{1\rho}$  images and C) enlarged maps from the  $T_{1\rho}$  images [15].**

### **2.2.3 Diurnal Effects**

Throughout the day disc height decreases. The total disc height decrease in the entire spine is on average 19 mm, which corresponds to approximately 1.5 mm height change in each lumbar disc [17]. The height change is associated with loss of fluid content, approximately 5-10% [19], due to compressive stresses throughout the day. At night, when there is minimal loading on the spine, the discs rehydrate and increase in height. Ludescher *et al* determined that there were no morphological changes in the disc when comparing images from the morning and the evening in the same individuals [19]. However, it has been shown that the spine is stiffer in the mornings, reducing the lumbar flexion range by approximately 5°, and it has been shown that the disc resists more of the stress in the morning [17]. Degenerated discs lose the ability to fully rehydrate during rest [19] [20]. Many in vivo studies have been done to look at the diurnal effects, such as [19] [20] [21] [22] [23].

### **2.3 Magnetic Resonance Imaging**

The advantage of using magnetic resonance imaging (MRI) for internal strain studies is that it does not require the use of physical markers. Chiu *et al* stated that since the intervertebral disc has a high water content it is a good area to use MRI; however, the location of the intervertebral disc makes it difficult to use MRI in vivo [24]. Nevertheless, MRI has been accepted as a valid and accurate method to use when imaging specimens. This method has been used in many previous studies, for example [7] [8] [9] [11] [24] [25]; however, to date MRI has not been used for internal strain measurements except by the McKay Orthopedic Research Laboratory.

## **3. MATERIALS AND METHODS**

The summer's objective was to design a device that will apply compression and torsion, simultaneously, to a spinal motion segment. The criteria of the device include: MRI compatible, measure the torque and compression throughout the test, and control the amount of torque and compression independently. Currently, there is no system that is capable of accomplishing the project's needs; therefore, a new design was needed.

This section includes details on the entire project, but mostly focuses on the design of the device.

### **3.1 Sample Preparation**

Human cadaveric spine sections will be obtained from an IRB approved tissue source. Before dissection,  $T_2$ -weighted and  $T_{1\pm\rho}$  images will be obtained for the whole spine. From these images, the degenerative grade of the discs will be determined based on the Pfirrmann scale [29]. From the spine, the lumbar motion segments, bone-disc-bone, will be used. The disc will be isolated, meaning the facet joints and other ligaments will be removed. Kirschner wires will be placed through the vertebral bodies, and then the motion segments will be potted in polymethyl methacrylate (PMMA) bone cement. The specimens will be stored at  $-20^\circ\text{C}$  until needed. In order to hydrate the specimen, the specimen will be placed in a phosphate buffered saline (PBS) bath in a refrigerator for 15 hours then at room temperature in a PBS bath 3 hours prior to testing.

### **3.2 Custom Built Device**

#### **3.2.1 Preliminary Design**

At the beginning of this project, the objective was to study the effects of just torsion on strain of the intervertebral disc. In order to measure the torque being applied to the specimen, it was decided that a load cell would be used. The load cell would have to be rotating with the specimen. An actuator would also be needed in order to apply a rotational movement. Ideally, the device would be small and lightweight since it would have to be moved from the lab to an MRI machine. Another obstacle that was present was to keep the metal approximately 8 inches away from the specimen to eliminate any imaging interference. This distance, 8 inches, was chosen because it was slightly greater than the minimum distance between a hydraulic cylinder and the specimen for a compression device that is currently used in the MRI.

With that in mind, it was decided to load the specimen in a device that would keep one side completely stationary. Four polyvinyl chloride (PVC) plastic rods with a diameter of 0.25 inches would be used to transfer the torque from the rotary actuator to the specimen. The interface between the rotary actuator and the specimen would be a thin rectangular block. Holes would be drilled through the PMMA that was connected to the specimen in order for the rods to slide

through. Another rod would be used to transfer the torque from the specimen back to the load cell, which would be mounted on the rotating rectangle. Figure 4 below gives an idea of what the device would look like; however, Figure 4 does not show the load cell or the load cell connection.

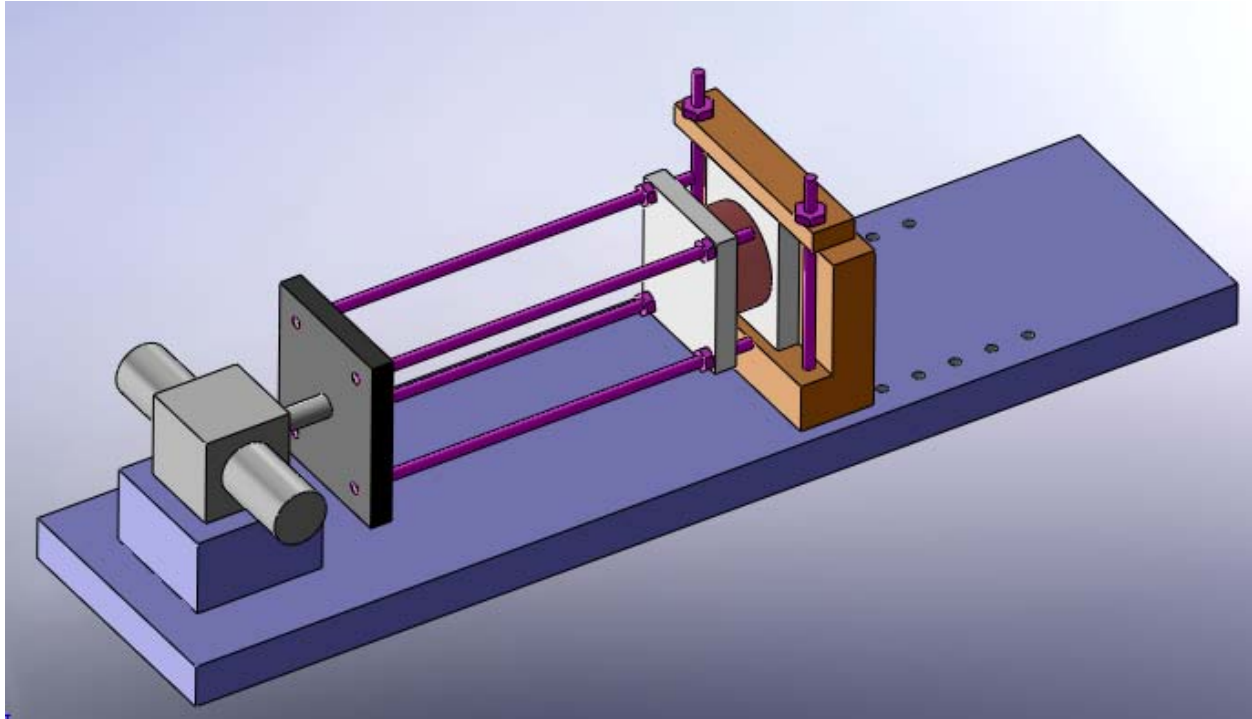


**Figure 4: A picture created in Solidworks 2008 shows the preliminary design. The blue shows the base; purple shows the rods; the orange shows the supports; the gray shows the PMMA; the red shows the motion segment; the black shows the rotating rectangle; the silver shows the rotary actuator.**

### **3.2.2 Design Issues**

While working on the preliminary design, some issues arose. The 0.25-inch diameter PVC rods were not stiff enough to resist the amount of torque; it was also noted that the torque would have to be applied in the opposite directions of the threads in order for the rods to transfer the rotation. The small diameter was chosen because, originally, it was thought that the tooling to transfer the torque needed to be as lightweight as possible in order for the rotary actuator to perform as expected. However, after talking with Doug Hamilton, a representative from Bimba, the manufacturer of the rotary actuator selected, it was determined that the weight of the tooling was not a large issue, but bending moment could affect the performance.

As this project progressed, it was decided that torsion and compression would be studied simultaneously, instead of just torsion. Therefore, a way to add compression to the device would have to be designed. It was also decided to incrementally increase the torque. This will increase the length of the test, which makes hydration of the specimen an issue. Another issue that arose was the distance the metal had to be from the specimen in order to get quality images. After meeting with Niels Oesingmann, a contractor from Siemens, which is the manufacturer of the both the 3T and the 7T MRI machine that might be used, it is thought that the load cell will have the greatest effect on the image quality, but the required minimum distances vary for each application. It was also noted that the orientation of each device could change the required minimum distance. A protocol was developed to determine the minimum distances for each device. The protocol is described below in Section 3.3.

### **3.2.3 Current Design**

A non-magnetic custom device is being designed that will apply torsion and axial compression, simultaneously, to a motion segment while in the MRI machine. The device will consist of a custom-built load cell to measure the torque and compression on the motion segment (LXT-920, Cooper Instruments), a custom-built rotary actuator (Bimba), and a stainless steel hydraulic cylinder (URR-17-1/2, Clippard Minimatic) that will apply compression. One pressurized nitrogen tank will control the rotary actuator, and another pressurized nitrogen tank will control the hydraulic cylinder. An accurate release of nitrogen will be required from these tanks; the valves to control the release of nitrogen have not been determined at this point. All other parts of the device will be made of PVC and Delrin plastics.

The load cell will be on one side of the specimen and the rotary actuator and the hydraulic cylinder will be placed on the other side. The wires from the load cell will be twisted and wrapped in order to help isolate them in order to reduce their interference. Since the weight of the tooling is no longer an issue, thicker rods, with a diameter of 1 inch, made of Delrin plastic will be used to transfer the torque and rotation from the rotary actuator to the specimen and then from the specimen to the load cell; only one rod will be used on each side. In order to reduce bending moment effects, each rod will have at least one support with a ball bearing. The number of supports depends on the length of the rods, which is currently unknown but will be decided from the results from the protocol described in Section 3.3. The ball bearings will be made of plastic and glass (ARG16-1B-G, KMS Bearings, Inc.). The specimen will be gripped using t-slots made from Delrin plastic. The motion segment will slide into one piece of the grips and

then be secured by Delrin screws. That piece will then slide into the other part of the t-slot, which will have a stopper to keep it from being off-centered. The t-slot will connect to the rods via Delrin screws. In order to keep the specimen hydrated, it will be submerged in a PBS bath; this should not affect the image quality.

Compression is being added to the device by the use of a hydraulic cylinder. Two design options were made to add compression to the device. For both options, the compressive hydraulic cylinder will be located behind the rotary actuator. One option, which is shown in Figure 5, has the hydraulic cylinder applying compression to the back of the rotary actuator support. The support would be allowed to slide and the compression would be transferred through the same rods that the torque and rotation would be transferred. The disadvantage to this option is the small surface area for the compression to be applied to the specimen. The second option, shown in Figure 6, has the hydraulic cylinder applying compression to a bar, which is connected to two 0.5-inch square rods made of Delrin plastic. These square rods extend on the outside of the rotary actuator to a PVC rectangular block, which will be adjacent to the grips of the specimen. The PVC block will have a circular cutout either larger than the diameter of the Delrin rod or a bearing will be placed in the cutout in order to transfer the rotation without adding friction. This design mimics the compression device that has previously been used. This design option increases the surface area for compression, but the issue is the Delrin rod would have to extend.

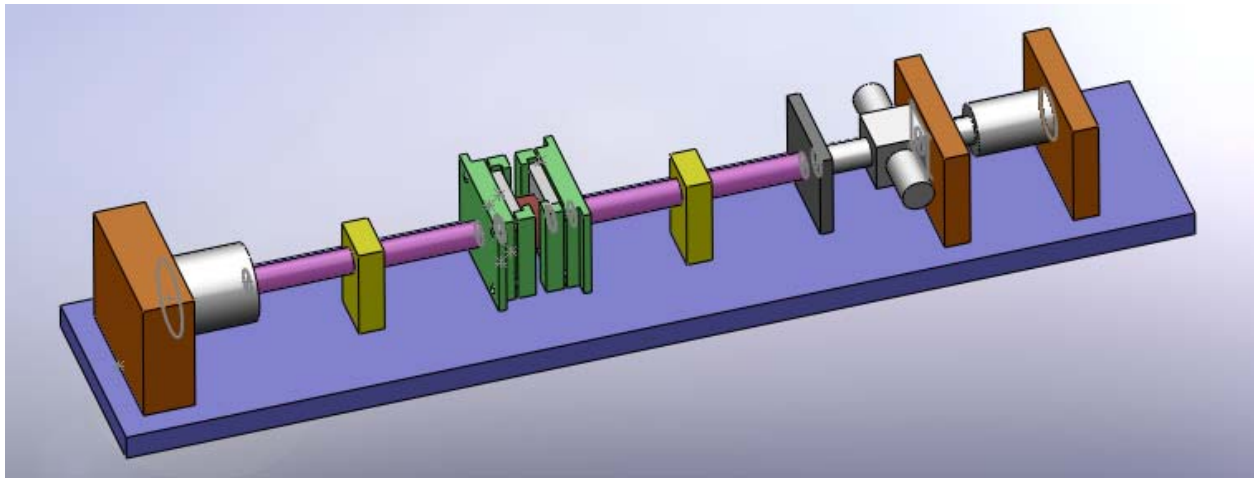


**Figure 5: A picture created in Solidworks 2008 shows one of the design options. The blue shows the base; purple shows the rods; the orange shows the supports; the green shows the grips; the gray shows the PMMA; the red shows the motion segment; the black shows the rotating rectangle; the silver shows the devices (load cell, rotary actuator, hydraulic cylinder); the yellow shows the bearing supports.**

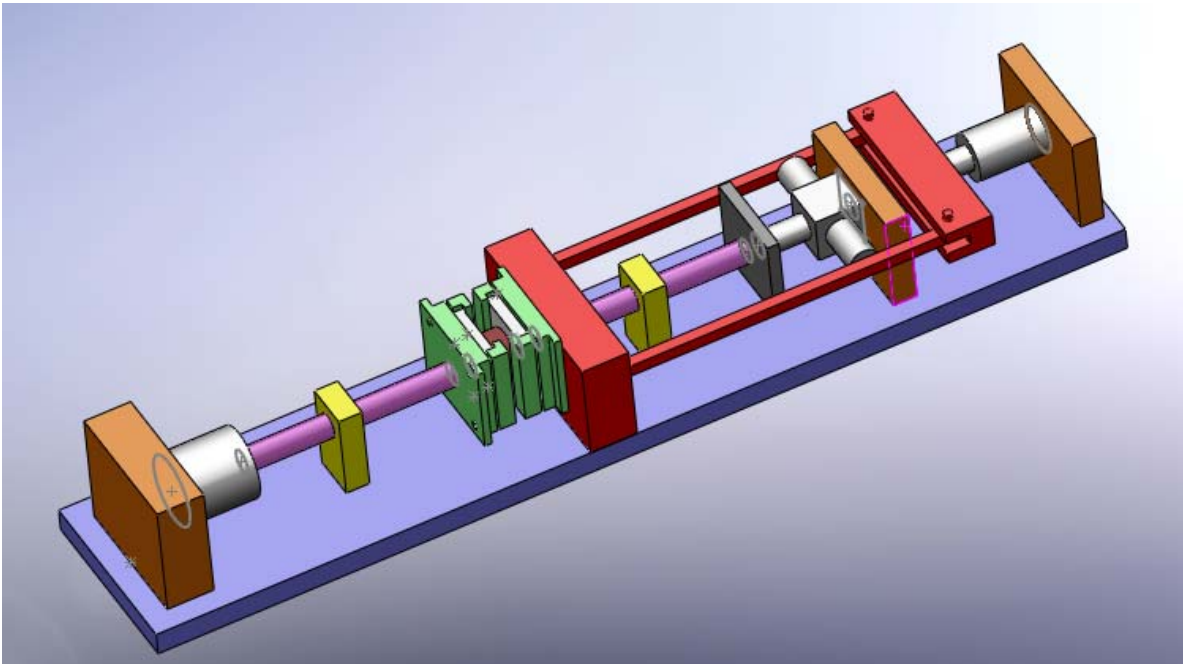


**Figure 6: A picture created in Solidworks 2008 shows a design option with the compressive setup. The blue shows the base; purple shows the rods; the orange shows the supports; the green shows the grips; the gray shows the PMMA; the red shows the motion segment; the black shows the rotating rectangle; the silver shows the devices (load cell, rotary actuator, hydraulic cylinder); the yellow shows the bearing supports; the bright red shows the compression setup.**

The current design, shown in Figure 7, is a combination of the previous two options shown in Figure 5 and Figure 6. The compressive hydraulic cylinder will apply compression to the rotary actuator support. The rotary actuator support will be part of the compressive setup, having the 0.5-inch square rods extending from the rotary actuator support to the PVC rectangular block located adjacent to the grips. This design allows the Delrin rod and the PVC block applying compression, and eliminates the need for the Delrin rod to extend. It is possible that the rotary actuator may be too heavy and try to tip over. If this is the case, a shelf for the rotary actuator support can be attached to the vertical support shown in Figures 5-7. Note that the PBS bath is not shown in any of the figures.

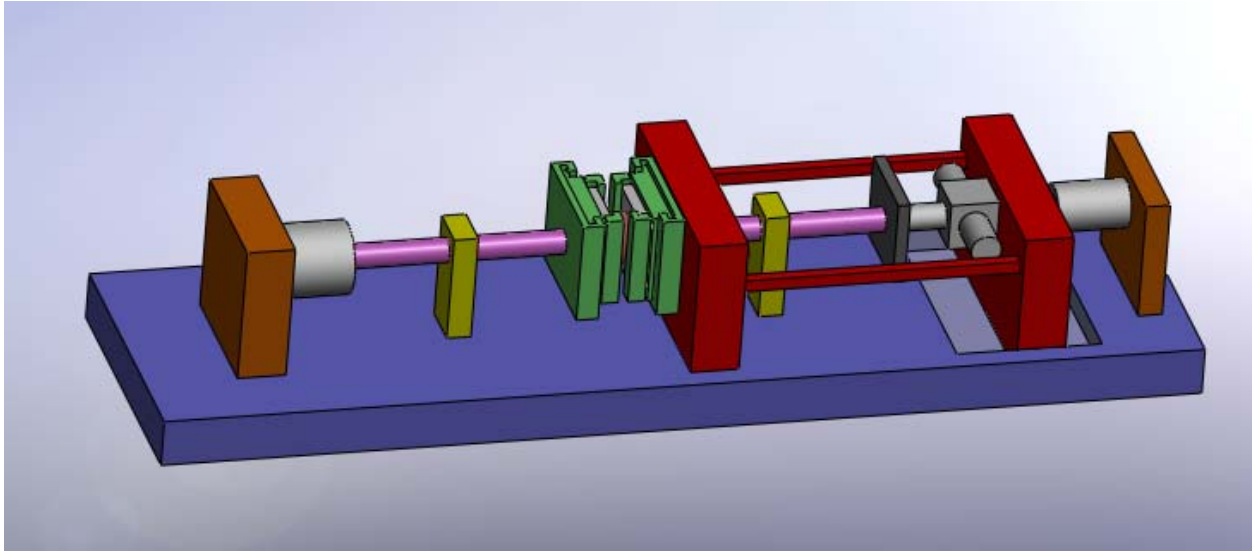


**Figure 7: A picture created in Solidworks 2008 shows the current design option with the compressive setup. The blue shows the base; purple shows the rods; the orange shows the supports; the green shows the grips; the gray shows the PMMA; the red shows the motion segment; the black shows the rotating rectangle; the silver shows the devices (load cell, rotary actuator, hydraulic cylinder); the yellow shows the bearing supports; the bright red shows the compression setup.**

### **3.3 Magnetic Resonance Imaging**

For this study, either a 3T or a 7T MRI scanner (Siemens Medical Solutions) will be used. The 7T would give a better quality images than the 3T, but due to the 7T MRI scanner's intensity, it would make the device larger than desired because the metal devices would have to be placed further away from the specimen. O'Connell *et al.* used a 3T MRI scanner (Trio, Siemens Medical Solutions), and the quality of the images was sufficient for that study's strain analysis [11]. Therefore, the 3T should produce images with a high enough resolution for strain analysis. However, the decision has not been made at this point. The sequence that will be used during the test will be a high resolution. The sequence that will be used will most likely be a high resolution T<sub>2</sub>-weighted turbo spin echo.

Working in collaboration with this project are Alex Wright, PhD and James Gee, PhD from the Radiology department at the University of Pennsylvania. They are both working on ANTS. For pure compression, two-dimensional (2D) images can be taken, and those images will be sufficient for the strain analysis. However, for torsion 3D images will be needed because some of

the points that are in a 2D plane initially will rotate out of the 2D plane when in torsion. In order to measure the strain, it is necessary to have an initial point and be able to trace its motion; therefore, 3D imaging is necessary.

### **3.3.1 Minimal Distance Protocol**

Before the actual testing begins and the designs are finalized, the required minimum distances between the devices and the specimen need to be determined. In order to do this, the exact devices that will be used in the actual testing, as well as the same MRI machine, need to be used in the following protocol. The minimum distances for the devices will be different in the 3T machine than the 7T machine; therefore, it is necessary to use the appropriate machine. Also, the sequence that will be used for the actual testing should be used in this protocol.

A homogenous solution, such as water or PBS, will be placed in the MRI machine in place of a specimen. One of the devices will be placed on the appropriate side of the homogenous solution, in the same orientation that it will be in the device, and then an image will be taken. The image quality will be observed. If there is interference, the device will be moved further away from the solution; if there is no interference, the device should be moved closer to the solution. Another image will be taken, and the image quality will be observed. This process should be repeated until the minimum distance is known for each device. Once the minimum distance has been determined for each device separately, all the devices should be put in the machine with the homogenous solution at the same time on their appropriate sides. Note that either the rotary actuator or the compressive hydraulic cylinder will most likely have to be placed further than their minimum distance in order to have the same order as they would in the actual testing. The rotary actuator should be closer to the solution than the compressive hydraulic cylinder. The distance between the rotary actuator and the hydraulic cylinder depends on the design chosen. If the design has not been chosen, use a gap of approximately 1 inch between the rotary actuator and the rod of the hydraulic cylinder. An inch gap would be the closest the two objects would be together for either design option. An image should be taken with all devices in place to make sure there is no interference. If there is interference, move the appropriate device(s) until there is no interference.

### **3.4 Protocol**

Before testing the specimens begins, the load cell will be calibrated in torsion and compression by applying known forces using an Instron testing machine (Model 8874). The rotary actuator and the hydraulic cylinder will be calibrated by placing a load cell in place of the specimen (Dyancell, Instron). A preload of 750 N will be applied and held for one hour. For a human disc, 750 N corresponds to an average of 0.48 MPa stress; this stress is equivalent to the stress felt during low to moderate activity, such as walking or sitting. After the one-hour hold, 20 sinusoidal cycles from  $\pm 6^\circ$  at 0.5 Hz will be applied while keeping the compressive load constant. The preload and preconditioning will be done using an Instron (Canton, MA) testing machine (Model 8874).

One of the preliminary tests consisted of testing a bovine tail motion segment. The specimen was preloaded to 365 N to achieve a stress of approximately 0.48 MPa. The specimen was preconditioned as previously described. The specimen was then rotated, incrementally, to  $2^\circ$ ,  $4^\circ$ , and  $6^\circ$ . The specimen was allowed to relax at the incremental rotations. This preliminary test was done to determine the time needed for stress-relaxation of the specimen to occur. The specimen needs to have time to “relax” in order to reduce the amount of movement during imaging. Figure 8 below shows a picture of the testing setup, and Figure 9 below shows the stress-relaxation curves for all the displacement holds from this test.



**Figure 8: A picture of the test setup for the preliminary test. This picture does not show the complete PBS bath.**

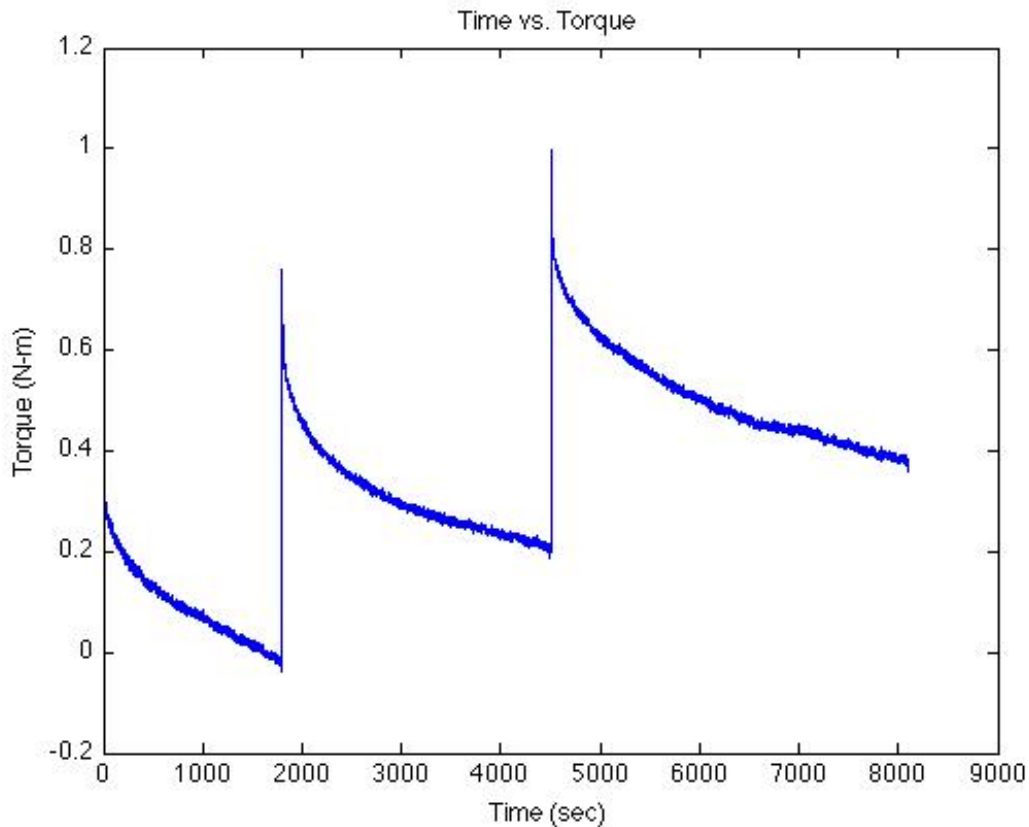


**Figure 9: Stress-relaxation curves for the 2°, 4°, and 6° rotation holds from the preliminary test. Note that the specimen does not fully relax for any of the holds.**

After analyzing the data from the preliminary test and developing Figure 9, it was determined that the specimen did not fully relax for any of the holds. Therefore, the times for the actual test have not been determined. Another preliminary test will be ran that will hold the angle displacements longer in order to determine the equilibrium time.

For the actual test, a constant force of approximately 750 N will be applied by the hydraulic cylinder throughout the duration of the test. The specimen will then be rotated to a displacement of 2°, then 4°, and then 6°. The holding times for each angle displacement will be chosen based on the preliminary test results.

### **3.5 Data Analysis**

While MRI is a useful tool for imaging specimens, it does not output displacement or strain. In a previous study, O'Connell *et al* [11], texture correlation was used to find the displacements between a reference image and a deformed image. The strain can be calculated from the displacement. This method is an accepted method, and has low strain percent error when used with MR images [26]. However, for this study ANTS will be used instead of texture correlation.

## **4. RECOMMENDATIONS**

The goal of this research project is to study the mechanical properties of the disc; therefore, the disc was isolated. Future work could include studying discs that are not isolated. Leaving all the joints and ligaments intact and applying compression and torsion would lead to a better understanding of the properties of the entire spine. If the joints and ligaments are left intact, the amount of torque applied should be increased since the intact structure can resist a larger load than an isolated disc [12]. Knowing the properties of both the isolated and non-isolated disc could be very advantageous in future motion segment studies.

## **5. CONCLUSIONS**

In conclusion, a non-magnetic device has been designed to apply torsion and compression to a specimen, with the exception of some dimensions. The design will not be finalized until the minimum distance for the metal devices have been determined by following the protocol in Section 3.3.1. The device will not be built until the design is finalized and a Delrin rod has been tested to ensure that it can resist the torque that will be applied. A hydraulic cylinder (URR-17-1/2, Clippard Minimatic) will be used to apply the compression, and a custom-built load cell (LXT-920, Cooper Instruments) will be used in the device that will measure the torsion and compression throughout the test. A custom-built rotary actuator (Bimba) is being designed but some details on controlling the amount of rotation are still being worked on before finalizing the design. When these three devices are available, the preliminary distance test can be conducted. Once the device is built, the plan is to proceed to test the specimens with the protocol described in Section 3.4.

## 6. ACKNOWLEDGEMENTS

I would like to thank many organizations and people for their help and support throughout this summer. I would like to thank the SUNFEST program director, Jan Van der Spiegel, the Electrical and Systems Engineering Department at the University of Pennsylvania for hosting the SUNFEST program, and I would also like to thank the National Science Foundation for the grant that funds the SUNFEST program.

I also want to thank the McKay Orthopedic Research Lab, which is the lab that I worked in this summer. Specifically, I would like to thank my advisor Dr. Dawn Elliot, and Jonathon Yoder, a graduate student whom I worked closely with throughout the summer.

## 7. REFERENCES

- [1] M. A. Adams, and P. Dolan. (2005, Oct.). Spine biomechanics. *Journal of Biomechanics*. [Online]. 38 (10), pp. 1972-1983. Available: <http://www.ncbi.nlm.nih.gov/pubmed/15936025>
- [2] M. A. Adams, and P. J. Roughley. (2006, Sept.). What is Intervertebral Disc Degeneration, and What Causes It?. *Spine*. [Online]. 31 (18) pp. 2151-2161. Available: <http://www.medscape.com/viewarticle/543611>
- [3] Degenerative Disc Disease. (2009). Medtronic. [Online]. Available: [http://wwwp.medtronic.com/Newsroom/LinkedItemDetails.do?itemId=1101769745199&itemType=fact\\_sheet&lang=en\\_US](http://wwwp.medtronic.com/Newsroom/LinkedItemDetails.do?itemId=1101769745199&itemType=fact_sheet&lang=en_US)
- [4] American Chiropractic Association. (2009). [Online]. Available: [http://www.acatoday.org/level2\\_css.cfm?T1ID=13&T2ID=68](http://www.acatoday.org/level2_css.cfm?T1ID=13&T2ID=68)
- [5] M. B. Coventry, R. K. Ghormley, and J. W. Kernohan. (1945, Jan.). The Intervertebral Disc: Its Microscopic Anatomy and Pathology. *The Journal of Bone and Joint Surgery*. [Online]. 27 (1) pp. 105-112. Available: <http://www.ejbjs.org/cgi/reprint/27/1/105>
- [6] H. F. Farfan, J. W. Cossette, G. H. Robertson, R. V. Wells, and H. Kraus. (1970, April). The Effects of Torsion on the Lumbar Intervertebral Joints: The Role of Torsion in the Production of Disc Degeneration. *The Journal of Bone and Joint*

- Surgery*. [Online]. 52 (3), pp. 468-497. Available:  
<http://www.ejbjs.org/cgi/content/abstract/52/3/468>
- [7] V. M. Haughton, T. H. Lim, and H. An. (1999, June). Intervertebral Disk Appearance Correlated with Stiffness of Lumbar Spinal Motion Segments. *American Journal of Neuroradiology*. [Online]. 20 (6), pp. 1161-1165. Available:  
<http://www.ajnr.org/cgi/reprint/20/6/1161.pdf>
- [8] T. A. Schmidt, H. S. An, T. H. Lim, B. H. Nowicki, V. M. Haughton. (1998, Oct.). The Stiffness of Lumbar Spinal Motion Segments With a High-Intensity Zone in the Annulus Fibrosis. *Spine*. [Online]. 23 (20), pp. 2167-2173. Available:  
<http://ovid.tx.ovid.com/spa/ovidweb.cgi>
- [9] A. Fujiwara, T. H. Lim, H. S. An, N. Tanaka, C. H. Jeon, G. B. J. Andersson, V. M. Haughton. (2000, Dec.). The Effect of Disc Degeneration and Facet Joint Osteoarthritis on the Segmental Flexibility of the Lumbar Spine. *Spine*. [Online]. 25 (23), pp. 3036-3044. Available: <http://www.ncbi.nlm.nih.gov/pubmed/11145815>
- [10] K. M. McGlashen, J. A. A. Miller, A. B. Schultz, and G. B. J. Andersson. (1987). Load Displacement Behavior of the Human Lumbo-sacral Joint. *Journal of Orthopedic Research*. [Online]. 5 (4), pp. 488-496. Available:  
<http://deepblue.lib.umich.edu/handle/2027.42/50380>
- [11] G. D. O'Connell, W. Johannessen, E. J. Vresilovic, and D. M. Elliot. (2007, Dec.). Human Internal Disc Strains in Axial Compression Measured Noninvasively Using Magnetic Resonance Imaging. *Spine*. [Online]. 32 (25), pp. 2860-2868. Available:  
<http://cat.inist.fr/?aModele=afficheN&cpsidt=19897075>
- [12] M. A. Adams, and W. C. Hutton. (1981, Jun). The relevance of torsion to the mechanical derangement of the lumbar spine. *Spine*. [Online]. 6 (3), pp. 241-248. Available: <http://www.ncbi.nlm.nih.gov/pubmed/7268544>
- [13] D. M. Gillard. (2005). Degenerative Disc Disease (DDD). [Online]. Available:  
[http://www.chirogeek.com/000\\_DDD\\_Page-1\\_Aging.htm](http://www.chirogeek.com/000_DDD_Page-1_Aging.htm)
- [14] A. N. Nguyen, W. Johannessen, J. H. Yoder, A. J. Wheaton, E. J. Vresilovic, A. Borthakur, D. M. Elliot. (2008, April). Noninvasive Quantification of Human Nucleus Pulposus Pressure with Use of T1 $\rho$ -Weighted Magnetic Resonance Imaging. *The Journal of Bone and Joint Surgery*. [Online]. 90 (4), pp. 796-802. Available: <http://www.pubmedcentral.nih.gov/articlerender.fcgi?artid=2657301>
- [15] J. D. Auerbach, W. Johannessen, A. Borthakur, A. J. Wheaton, C. A. Dolinskas, R. A. Balderston, R. Reddy, and D. M. Elliot. (2006, Aug.). In vivo quantification of

- human lumbar disc degeneration using T<sub>1ρ</sub>-weighted magnetic resonance imaging. *Spine*. [Online]. 15 (3), pp. 338-344. Available: <http://www.pubmedcentral.nih.gov/articlerender.fcgi?artid=2335378>
- [16] W. Johannessen, J. D. Auderbach, A. J. Wheaton, A. Kurji, A. Borthakur, R. Reddy, D. M. Elliot. (2006, May). Assessment of Human Disc Degeneration and Proteoglycan Content Using T<sub>1ρ</sub>-weighted Magnetic Resonance Imaging. *Spine* [Online]. 31 (11), pp. 1253-1257. Available: <http://cat.inist.fr/?aModele=afficheN&cpsidt=17811514>
- [17] M. A. Adams, P. Dolan, W. C. Hutton, and R. W. Porter. (1990, Mar.). Diurnal Changes in Spinal Mechanics and Their Clinical Significance. *The Journal of Bone and Joint Surgery*. [Online]. 72 (2), pp. 266-270. Available: <http://www.jbjs.org.uk/cgi/content/abstract/72-B/2/266>
- [18] EURODISC. Intervertebral Disc Degeneration: Interplay of Age, Environmental and Genetic Factors. [Online]. Available: <http://www.physiol.ox.ac.uk/EURODISC>
- [19] B. Ludescher, J. Effelsberg, P. Martiosian, G. Steidle, B. Markert, C. Claussen, and F. Schick. (2008, July). T<sub>2</sub>- and Diffusion-Maps Reveal Diurnal Changes of Intervertebral Disc Composition: An In Vivo MRI Study at 1.5 Tesla. *Journal of Magnetic Resonance Imaging*. [Online]. 28 (1), pp. 252-257. Available: <http://www.ncbi.nlm.nih.gov/pubmed/18581387>
- [20] N. Boos, Å. Wallin, T. Gbedegbegnon, M. Aebi, and C. Boesch. (1993, Aug.) Quantitative MR Imaging of Lumbar Intervertebral Disks and Vertebral Bodies: Influence of Diurnal Water Content Variations. *Radiology*. [Online]. 188 (2), pp. 351-354. Available: <http://radiology.rsna.org/cgi/content/abstract/188/2/351>
- [21] J. R. Ledson, V. Lessoway, L. E. Susak, F. A. Gagnon, R. D. Gagnon, and P. C. Wing. (1996, July). Diurnal Changes in Lumbar Intervertebral Distance, Measured Using Ultrasound. *Spine*. [Online]. 21 (14), pp. 1671-1675. Available: <http://cat.inist.fr/?aModele=afficheN&cpsidt=3174283>
- [22] J. A. Malko, W. C. Hutton, and W. A. Fajman. (1999, May). An *In Vivo* Magnetic Resonance Imaging Study of Changes in the Volume (and Fluid Content) of the Lumbar Intervertebral Discs During a Simulated Diurnal Load Cycle. *Spine*. [Online]. 24 (10), pp. 1015-1022. Available: <http://cat.inist.fr/?aModele=afficheN&cpsidt=1792648>
- [23] N. Boos, A. Wallin, M. Aebi, and C. Boesch. (1996, March). A New Magnetic Resonance Imaging Analysis Method for the Measurement of Disc Height

- Variations. *Spine*. [Online]. *21 (5)*, pp. 563-570. Available:  
<http://www.ncbi.nlm.nih.gov/pubmed/8852310>
- [24] E. J. Chiu, D. C. Newitt, M. R. Segal, S. S. Hu, J. C. Lotz, and S. Majumdar. (2001, March). Magnetic Resonance Imaging Measurement of Relaxation and Water Diffusion in the Human Lumbar Intervertebral Disc Under Compression In Vitro. *Spine*. [Online]. *26 (19)*, pp. E437-E444. Available:  
<http://www.ncbi.nlm.nih.gov/pubmed/11698903>
- [25] M. J. Bey, H. E. Song, F. W. Wehrli, and L. J. Soslowsky. (2002, July). Intratendinous strain fields of the intact supraspinatus tendon: the effect of glenohumeral joint position and tendon region. *Journal of Orthopedic Surgery*. [Online]. *20 (4)*, pp. 869-874. Available:  
<http://cat.inist.fr/?aModele=afficheN&cpsidt=13834515>
- [26] M. J. Bey, H. K. Song, F. W. Wehrli, and L. J. Soslowsky. (2002, April). A Noncontact, Nondestructive Method for Quantifying Intratissue Deformations and Strains. *Journal of Biomechanical Engineering*. [Online]. *124 (2)*, pp. 253-258. Available: <http://www.ncbi.nlm.nih.gov/pubmed/12002136>
- [27] C. L. Gilchrist, W. W. Witvoet-Braam, F. Guilak, and L.A. Setton. (2006, March). Measurement of intracellular strain on deformable substrates with texture correlation. *Journal of Biomechanics*. [Online]. *40 (4)*, pp. 786-794. Available:  
[http://www.jbiomech.com/article/S0021-9290\(06\)00107-2/abstract](http://www.jbiomech.com/article/S0021-9290(06)00107-2/abstract)
- [28] C. L. Gilchrist, J. Q. Xia, L. A. Setton, and E. W. Hsu. (2004, May). High-resolution determination of soft tissue deformations using MRI and first-order texture correlation. *IEEE Transactions on Medical Imaging*. [Online]. *23 (5)*, pp. 546-553. Available: <http://ieeexplore.ieee.org/stamp/stamp.jsp?arnumber=01295075>
- [29] C. W. Pfirrmann, A. Metzendorf, M. Zanetti, J. Hodler, and N. Boos. (2001, Sept.). Magnetic resonance classification of lumbar intervertebral disc degeneration. *Spine*. [Online]. *26 (17)*, pp. 1873-1878. Available:  
<http://www.ncbi.nlm.nih.gov/pubmed/11568697>

# **AMPLIFICATION CIRCUITS AND PATTERNING METHODS OF ORGANIC FIELD-EFFECT TRANSISTORS**

NSF Summer Undergraduate Fellowship in Sensor Technologies

Hank Bink (Electrical and Computer Engineering) – Lafayette College

Advisor: Cherie Kagan

## **ABSTRACT**

Organic transistor technology holds great promise for creating a conformal, human-safe electronic neural interface. These interfaces must amplify the low, microvolt-range brain signals so they can be utilized in analog and digital applications. Brain signals from sensors must be relayed to the transistor's gate through the dielectric and semiconductor layers, as well as through an encapsulant which keeps the device shielded in the aqueous brain environment. In order to test their amplification gains, silicon wafer-based ambipolar organic transistors with a pentacene semiconductor were tested under nitrogen in amplifying configurations including common source and cascode. Gains for common source amplifiers with resistors were up to 3.5V/V. Gains for the cascode setup revealed the same results as common source. Both the common source and cascode topologies exhibited very low bandwidth with -3dB points of 35 and 25 hertz, respectively. Parylene C, a biologically safe polymer, is a leading candidate to encapsulate pentacene transistors and serve as a dielectric layer between the devices and sensing electrodes. We tested etching of this parylene as well as the dielectric materials benzocyclobutene (BCB) and spin-on-glass (SoG) using both oxygen and SF<sub>6</sub> plasma etching. Parylene was etched at a rate of 0.2μm/min with O<sub>2</sub> plasma. BCB and SoG did not exhibit useful etching under O<sub>2</sub> or SF<sub>6</sub> plasma.

## 1. Introduction

The ability to interface electronics with the human brain creates a great potential for countless useful applications. These applications range from sensing neural activity [1] to restoring sensory and/or motor functions to those who have lost them [2]. Current techniques use bulky, rigid subdural grid electrodes with sensors typically around 3mm and spaced 1cm apart [3]. Figure 1 shows a common application of these devices for the purposes of an intracranial electroencephalogram.

Considering there are approximately 146,000 neurons per square millimeter on the cortical surface [5], these 3mm diameter electrodes are not very selective in the signals they sense. Advancing these methods would require devices which are small, able to conform to the brain, and safe in the aqueous brain environment. Organic transistors may be the key to solving these issues. These transistors can be made on the micron scale and on flexible substrates [6]. One area that must be researched is building amplifying circuits with these devices. Since neural signals are on the microvolt scale, amplifiers are essential so the signals can be used in other circuits. Also, since the brain is a very liquid environment, a protective coating must be used which can shield the transistors and still be safe for a human. Devices must be connected through this coating and other layers of the transistor to sensors and other circuitry.

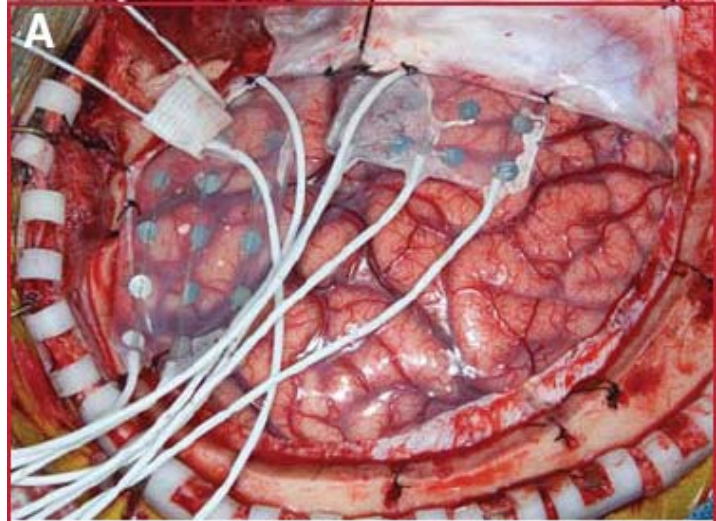


*Figure 1: Subdural grid placed on human brain [4]*

## 2. Background

Contained in this section is the necessary information needed to understand how the problems of making circuits with organic transistors and patterning via holes on them can be solved. The following subsections will outline the following:

- 2.1: Fundamentals of field-effect transistors
- 2.2: Organic field-effect transistors: makeup and characteristics
- 2.3: Organic transistor amplifying and digital circuits
- 2.4: Parylene: use as an encapsulant
- 2.5: Dry etching to create via holes

### 2.1 Fundamentals of Field-Effect Transistors

In field-effect transistors (FETs) the voltage between two terminals, known as the gate and source, electrostatically controls the current flow between the source and the third terminal, known as the drain [7]. FETs can take many forms; however, in all, the source and drain are separated by a semiconductor. Also, there is a dielectric layer separating the gate from the source and drain. One particular setup, known as bottom-gate, bottom-contact, can be seen in Figure 2. The most common type of FET is a metal-oxide semiconductor FET (MOSFET) which typically uses silicon as the semiconductor [6]. There are two types of MOSFETs: NMOS and PMOS. These two transistor types have similar structures, but with different doping of the silicon. NMOS devices work by injecting electrons through the semiconductor, and therefore work with positive gate and drain voltages, whereas PMOS types operate by injecting holes and require negative gate and drain voltages [7].

There are many uses for transistors in digital and analog applications. In certain applications transistors act as switches and make up the digital logic of computers and other solid-state devices. Another application, which is more useful for sensing in the brain, is a transistor's use as an amplifier. In the ideal case, an AC signal is attached to the gate at a certain DC bias, thus causing an amplified version of the input AC signal to appear at the drain at a bias determined by the circuit [7]. The amount of amplification depends on the characteristics of the transistor, the input bias voltage, and the amplifier circuit of which the transistor is part.

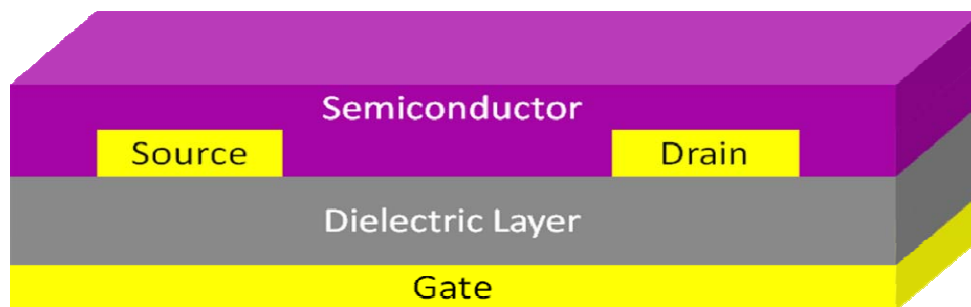


*Figure 2: Bottom gate FET diagram*

## **2.2 Organic Field-Effect Transistors: Makeup and Characteristics**

Organic field-effect transistors (OFETs) are similar to regular FETs except that they have a carbon-based semiconductor rather than the typical silicon semiconductors used in MOSFETs [6]. Many organic materials have exhibited strong qualities as semiconductors for OFETs. Pentacene was used in this project and shows especially strong characteristics in these devices.

### **2.2.1 Pentacene: Use as a Semiconductor**

Pentacene, a chemical compound consisting of five linear fused benzene rings, is one of the most promising candidates for use as a semiconductor in OFETs. This is due to its relative environmental stability and favorable results, such as charge carrier mobility around  $1\text{cm}^2/\text{Vs}$ , when used in a FET [8]. One of the main drawbacks of pentacene is that it is insoluble in organic solvents at room temperature, which means it is hard to deposit on substrates by low cost processes such as spin-coating and ink-jet printing [9]. However, pentacene-based soluble precursors have recently been developed which can be spin-coated on to a substrate. The film formed on the substrate can be converted into pentacene by thermal curing [10].

### **2.2.2 Unipolar and Ambipolar Transistors**

Unipolar OFETs operate similarly to typical inorganic MOSFETs in that there are N-channel and P-channel transistors, which resemble NMOS and PMOS transistors, respectively. The resemblance is that N-channel OFETs work with positive voltages and P-channel OFETs work with negative voltages, even though the inner workings of the organic and MOS devices are quite different. Specifically, OFETs are undoped and work in accumulation mode whereas MOSFETs are doped and operate in the inversion regime [6]. P-channel OFET devices currently have better performance, are more environmentally stable, and therefore, are more prevalent than N-channel.

Another type of OFET is known as ambipolar. This type of device exhibits both N-channel and P-channel characteristics depending on the voltage applied. These devices are not up to the operational ability of current unipolar OFETs [11] but their potential for useful applications is great. Inverters based on these ambipolar transistors could ideally operate similar to complementary-MOS (CMOS) devices, which make up the bulk of digital logic circuits.

### **2.2.3 Advantages and Disadvantages over MOSFETs**

One main advantage of OFETs is that they can be fabricated on thin film substrates such as plastic. This means they can be a cheap and flexible alternative to traditional MOSFETs [6]. Since they have the flexibility of a plastic substrate, as well as a flexible semiconductor in pentacene [8], these devices can conform to the surface on which they are placed. This would be a great advantage for circuitry designed to be put in the brain.

Though OFETs have many promising advantages, they do not currently have as high performance as MOSFETs. The typical drain current measured for OFETs varies from less than one to around thirty microamperes for reasonable gate and drain voltages (see Figure 3 for specific device) [12, 13, 14]. In contrast, most MOSFETs pull a drain current from hundreds of microamperes to tens of milliamperes for similar input voltages [7]. Another comparison is that OFETs have mobility around  $1\text{cm}^2/\text{Vs}$  [8,10] but MOSFETs typically measure close to  $480\text{cm}^2/\text{Vs}$  [7].

## **2.3 Organic Transistor Amplifying and Digital Circuits**

Circuits made with typical MOSFETs can be replicated using OFETs with similar operation. Currently the performance of the OFET-based circuits is much lower than that of their MOSFET counterparts due to the lower device performance of the organic transistors. However, useful analog and digital circuits can still be built. Many amplifier topologies have been shown using unipolar P-channel OFETs, from simple buffers to more complex differential amplifiers [13, 15, 16]. The highest gain from all these was 6.4 V/V for a differential amplifier with a 40V source [16], which is on the order of the typical gain of a simple, one-stage MOSFET amplifier with a 5V source.

Digital circuits have also been constructed, taking advantage of ambipolar OFETs to create a CMOS-like circuit. Inverters are the most commonly shown circuits with ambipolar devices [10, 11, 17, 18] which show proper inversion and gain at the switching state of up to 94 V/V [10]. From these inverters ring oscillators have been made, showing propagation delay time per stage as low as 22 microseconds in a 5-ring setup [18].

## **2.4 Parylene: Use as an Encapsulant**

Parylene is emerging as a promising material with which to coat devices such as OFETs. Parylene is a thermoplastic, transparent polymer which is chemically inert and nonbiodegradable [19, 20], making it biocompatible and a good choice to be placed in the human body. It coats surfaces completely and pinhole-free [19] so it protects the device well. Parylene also acts as a good dielectric barrier [21] and can be used to separate sensor electrodes, which are placed in the brain, from the OFET devices themselves.

## **2.5 Dry Etching to Create Via Holes**

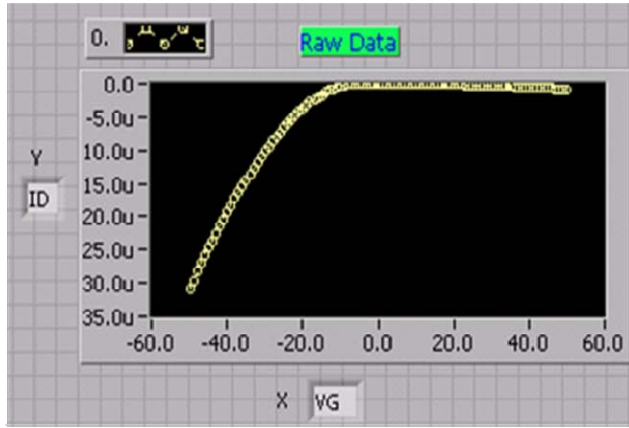
The main problem with encapsulating transistors with parylene is that vias must be made so electrodes can reach the source, drain, and gate of a coated OFET. This is essential for the device to interface with the sensors in the brain and with any further circuitry to which it must pass signals. Because of this, the semiconductor and dielectric layers must also be etched in order to gain access to the gate.

Since parylene is chemically inert, oxygen plasma etching serves as a good method for removal from needed pathways [21]. Tests done by Meng and Tai and Hsu et al. show favorable results from etching parylene using oxygen plasma techniques [20, 21]. Another possible plasma etchant is SF<sub>6</sub>. This can be used for many dielectric materials which can not be etched with oxygen. These materials include benzocyclobutene (BCB) and certain glass polymers which are often used as dielectrics in OFETs.

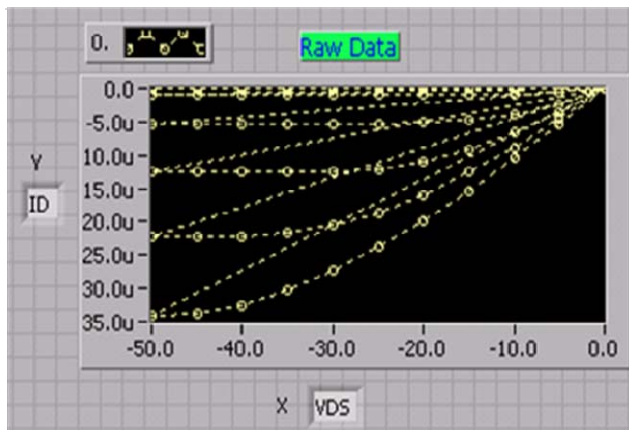
# **3. Experimental Methods**

## **3.1 Amplifying Circuits**

All circuit tests described in this paper were performed with organic transistors in a nitrogen-ambient probe station. Electrical equipment used for the experiments included a Keithley 2420 SourceMeter, an Agilent E3620A power supply, an HP 54601A oscilloscope, an HP 3312A function generator, and an Agilent 4156C parameter analyzer. The organic transistors



(a)



(b)

Figure 3: Typical characteristic curves of organic transistors used (a)  $I_d$ - $V_g$  (b)  $I_d$ - $V_{ds}$

used works best as p-type. Drain resistances used were varied from  $1\text{M}\Omega$  to over  $20\text{M}\Omega$  to make up for the small drain currents. Both the output voltage at the drain and the input small signal were analyzed on an oscilloscope. However, since the input impedance of the scope was  $10\text{M}\Omega$ , on the same order as the drain resistances, a buffer was used to avoid excess loading. The buffer was an LM741CN opamp in the voltage follower configuration and adequately reduced the amount of current drawn from the circuit by the scope.

Figure 4b illustrates the cascode amplifier configuration which was also tested. This setup is similar to the common source but with a second transistor between the drain of the first transistor and the resistor. This second transistor is biased at a certain DC voltage,  $-50\text{V}$  in our tests, to increase the overall gain of the circuit.

used displayed a carrier mobility of around  $0.2\text{cm}^2/\text{Vs}$  and gate-oxide capacitance of  $7.65\text{nF}/\text{cm}^2$ . A typical gate voltage ( $V_g$ ) to drain current ( $I_d$ ) curve is shown in Figure 3a. Figure 3b shows a corresponding drain-to-source voltage ( $V_{ds}$ ) to  $I_d$  curve for varying gate voltages. These transistors were constructed on silicon wafers with a dual dielectric stack of thin silicon dioxide and BCB. Pentacene was the semiconductor in these devices and self-assembled monolayers were applied to the source and drain to enhance ambipolar characteristics. Complete description of these devices can be found in [10].

Several different amplification circuits were tested. The first was the common source amplifier. This geometry is the simplest because it utilizes only one transistor, but can achieve relatively large gains. By definition, the common source amplifier, as shown in Figure 4a, has the source connected to ground, the drain connected to a resistor, and the gate attached to a DC bias with a small AC signal riding on it. The other end of the drain resistor is

attached to a high voltage which supplies the source for the drain current. In this case,  $-50\text{V}$  was used since the ambipolar transistor

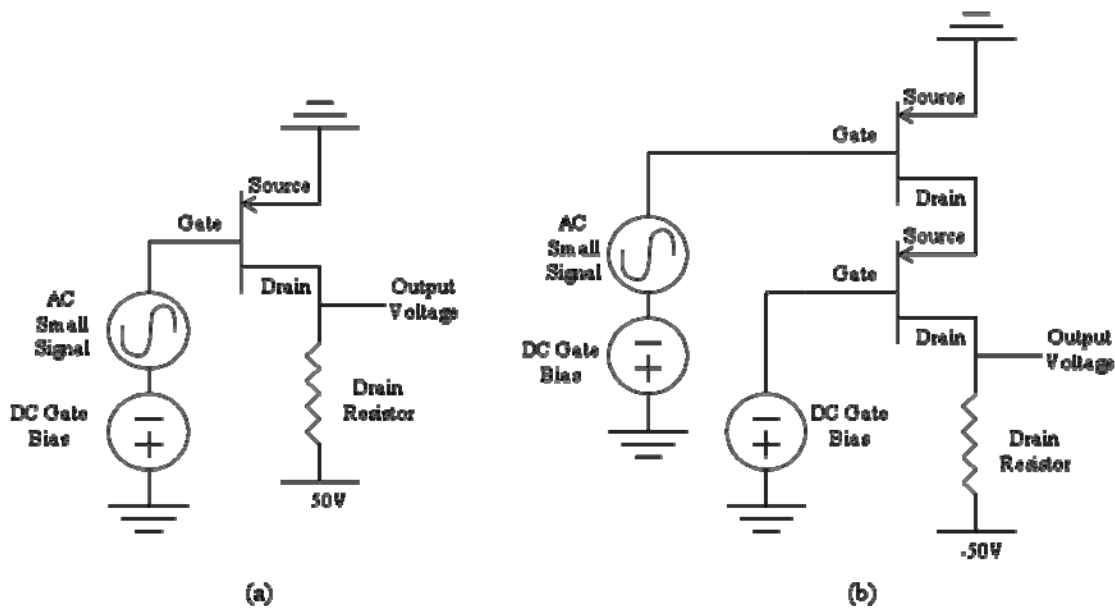


Figure 4: Transistor amplifier topologies (a) common source (b) cascode

### 3.2 Etching Setup

In order to pattern via holes to connect the gates of an organic device to sensing electrodes, etching methods and rates had to be determined for the materials in the device. These materials include parylene-c, which acts as an encapsulant, along with benzocyclobutene (BCB) and spin-on-glass (SoG), which are used as dielectric materials in the transistors. SoG is a glass resin liquid mixture in the silicone family which helps the BCB stick to the device and spin-coat more evenly. It also effectively reduced leakage current between the gate and top electrodes. SoG was spin coated on substrates for 60 seconds at 3000 revolutions per minute then heated for 45 minutes at 200 degrees Celsius. Similarly, BCB was then spin coated on top at 3000 rpm for 30 seconds then cured at 290 degrees for 30 more seconds. A Specialty Coating Systems PDS2010 coater was used for vacuum deposition of parylene. The thickness of parylene on the sample depended on the length of the process and the amount of the parylene monomer used. Typically somewhere between one and four microns were deposited on samples.

The etching process itself was performed on a Technics Planar Etch II parallel-plate Reactive Ion Etching device. This machine was capable of using the plasma of two gases,  $O_2$  and  $SF_6$ , to etch samples. The  $O_2$  was used to etch parylene whereas  $SF_6$  was used to etch BCB and SoG. These organic transistor materials were applied to different substrates including glass, silicon wafer, and Kapton, a type of polyimide, in order to test their etching abilities. The depth of etching was measured using a Tencor Alpha Step 200 profilometer when possible. For some samples the thickness of the material was too small to be accurately measured using the profilometer. For this reason many samples were made using gold-covered silicon wafers and Kapton on which gold gates were deposited. Once the materials were coated and etched off these substrates, subsequent gold strips were deposited. The conductance between the original gold and top-layered gold was tested using the probe station. If the conductance was high

between the two gold areas then it could be concluded that the intermediary substances were sufficiently etched.

## 4. Results and Analysis

### 4.1 Amplification

Based on the characteristics of the organic transistors, gains for the amplifier circuits were first predicted using standard FET equations. The following equation was used for the common source amplifier:

$$|Gain| = g_m R_d = \mu C_{ox} \frac{W}{L} (|V_{gs}| - |V_t|) R_d$$

However, the condition that must be considered when using this equation is that the overdrive voltage ( $|V_{gs}| - |V_t|$ ) must be less than  $V_{ds}$  in order to stay in saturation. So as the gate voltage increases, at a certain point the voltage across the drain resistor becomes too large for the device to stay in saturation. The circuit accounts for this and keeps the drain currents low enough to keep the transistor working in saturation. Considering this, Figure 5 shows the maximum theoretical gains, which would still keep the device in saturation, for various resistances. The curve is close to linear, which makes sense because the equation is linearly based on increasing values of  $R_d$ . However, it can be seen that the gains are starting to level off as the resistances get very high. This is because higher resistances drive the transistor out of saturation more easily.

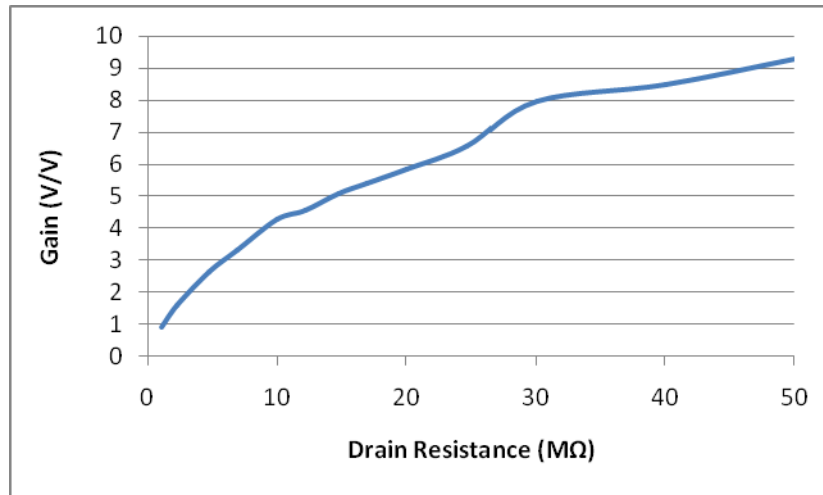


Figure 5: Calculated gain for increasing drain resistance

Next, a DC bias point analysis was performed on the device. Figure 6a shows the curves of varying drain resistances for DC drain voltage versus gate voltage. The point where the slope is greatest in magnitude represents the area for highest gain. The table in Figure 6b shows the slope of the estimated trend line for each resistance. This slope represents the predicted gain for its respective drain resistance.

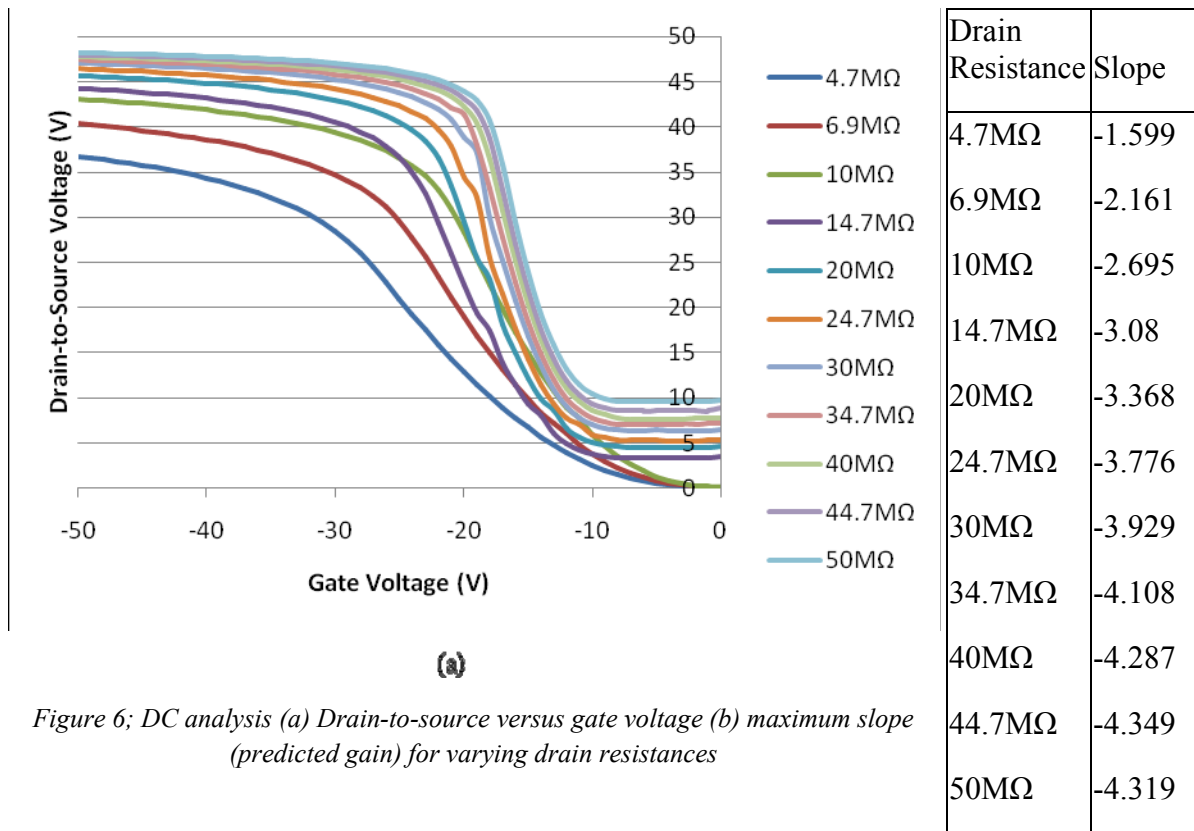


Figure 6; DC analysis (a) Drain-to-source versus gate voltage (b) maximum slope (predicted gain) for varying drain resistances

The  $V_{ds}-V_g$  curves show that the range of highest slope gets shorter closer to zero as the resistance increases. This is because with a higher resistance, the voltage across the drain resistor increases more quickly and pushes the device out of saturation earlier. It can also be seen from Figure 6 that as resistance increases the predicted gain typically increases. This is expected from the calculations, as shown in Figure 5. Another similarity is that both sets of gain predictions appear to be leveling off at high resistances. The gain ceiling is much lower from the DC analysis, however. The calculated gains are based on traditional MOSFET calculations which do not exactly fit the OFETs. For instance, the mobility of organic devices tends to vary with the gate voltage, a phenomenon not accounted for in the calculations. The predicted gains from Figure 6 seem to predict the gains more realistically since they are based specifically on the devices that will be used.

The small signal gain analysis was performed for the same range of resistances. Figure 7 shows a graph of gain versus drain resistance. For each resistance, the gate bias voltage was varied by 1V increments and the input and output waveforms were recorded for each bias voltage. The highest of these recorded gains for each resistance is displayed in Figure 7. These gains were taken for a 15Hz small signal input with a peak-to-peak voltage of 1V.

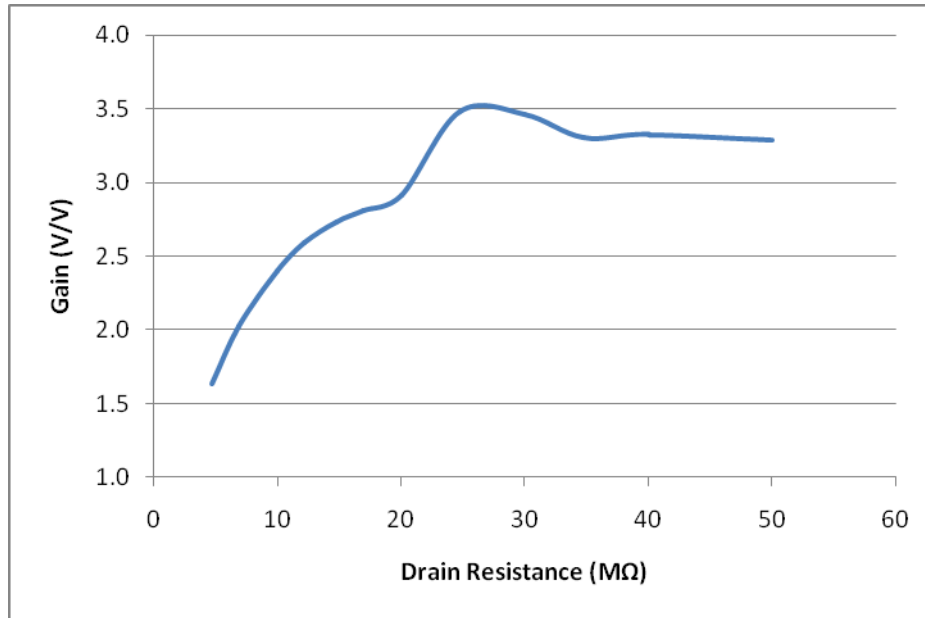
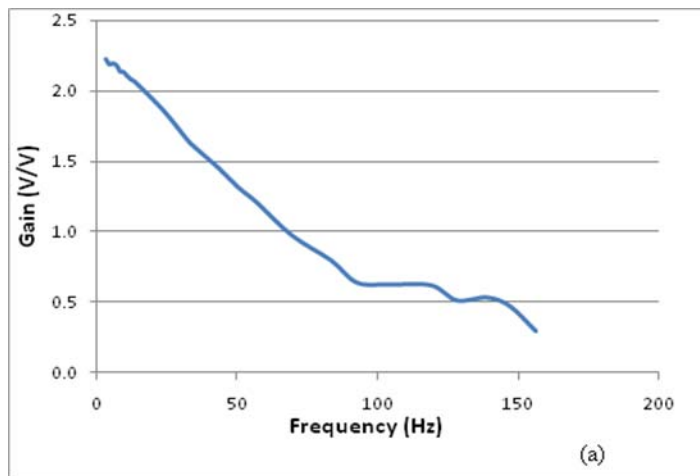


Figure 7: Common source gains for varying drain resistance

The gains found through small signal analysis are seen here reaching 3.5 V/V maximum for resistances around 25MΩ. These gains increase with resistance until they reach a high gain ceiling, just as was seen with the calculation and DC analysis predictions. The actual gains are slightly lower than those predicted by the  $V_{ds}-V_g$  curves. A possibility for this is that the highest gains were passed over as the gate bias was swept. A 1V step is relatively high when dealing



with the small gain range for high resistances. This may also explain why the gain around 25MΩ is slightly higher than the leveling at 35MΩ and above. Another possibility for decreased actual gains is that the 15Hz small signal is too high frequency for the transistor. Since the gate is the entire bottom of the device, the gate capacitances are very large and thus the frequency range for high gain is very small. Figure 8 shows gain with respect to frequency for several drain resistances.

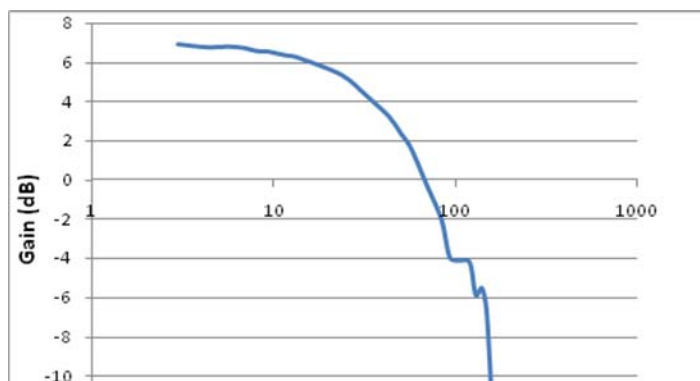


Figure 8: Common source gain vs. frequency (a) in V/V (b) on a log-log plot

It can be seen from Figure 8a that the gains seriously decrease as the frequency of the input signal increases. The system exhibits a maximum gain of about 2.3V/V at 3Hz, the lowest frequency recorded. As soon as the

frequency increases, the gain begins decreasing greatly. By the time 50Hz was reached, the gain had gone down 1V/V. Approaching frequencies over 100Hz, the output became slightly distorted, which could account for the bumps at these values. Figure 8b shows a log-log plot of frequency versus gain in decibels. This graph shows a DC gain approaching about 7V. This gain stays somewhat constant only up to about 8Hz. The -3dB point of this device is about 35Hz. Extrapolating the data, it appears that the gain is falling a bit faster than the typical -20dB/decade exhibited by MOSFETs after the -3dB point.

The very low frequency threshold of the devices used is mostly due to the bottom-gate style it uses. The entire bottom of the sample is a doped silicon gate, thus the capacitance from the gate to the electrodes is very high. This would seriously degrade signals of any measurable AC frequency, as shown in Figure 8. This is problematic for use in a brain-computer interface. The brain impulses are not a consistent AC signal; however they can be sporadic within a short time period. Attempting to get a -3dB point of 500Hz would be ideal. This could be achieved by using small gold gates below the device instead of a large wafer bottom. A smaller gate would decrease the parasitic gate capacitance and increase the frequency limit of the amplifier.

Gains for the cascode device were also measured by small signal gain analysis. The biasing transistor, as seen in Figure 4b, was tied to the -50V power supply to keep it in saturation and give the highest gain. The gain for a cascode device should be close to double that of the common source topology for a typical MOSFET. The gains recorded for the OFET cascode devices, however, were about the same as those of the common source. The maximum gain was around 3.5V/V at a drain resistance of 30M $\Omega$ . This lower gain than expected was caused by the high output resistance of the OFET which was in parallel with the drain resistance. Thus the gain was just the same as the common source since the drain resistance was still equal to the resistor.

Cascode devices should also exhibit a higher bandwidth than their single transistor counterparts. A frequency sweep of the OFET cascode device with a 10M $\Omega$  drain resistance is shown in Figure 9. The -3dB point is around 25Hz, slightly less than the common source -3dB point seen in Figure 8. This is certainly owed to the very large gate to electrode capacitance which destroys the gain of any sizeable AC signal. The gain roll-off after the -3dB point seems to be at a much slower rate than the common source did in Figure 8. The cascode is closer to the 20dB/decade rate seen in MOSFET transistors.

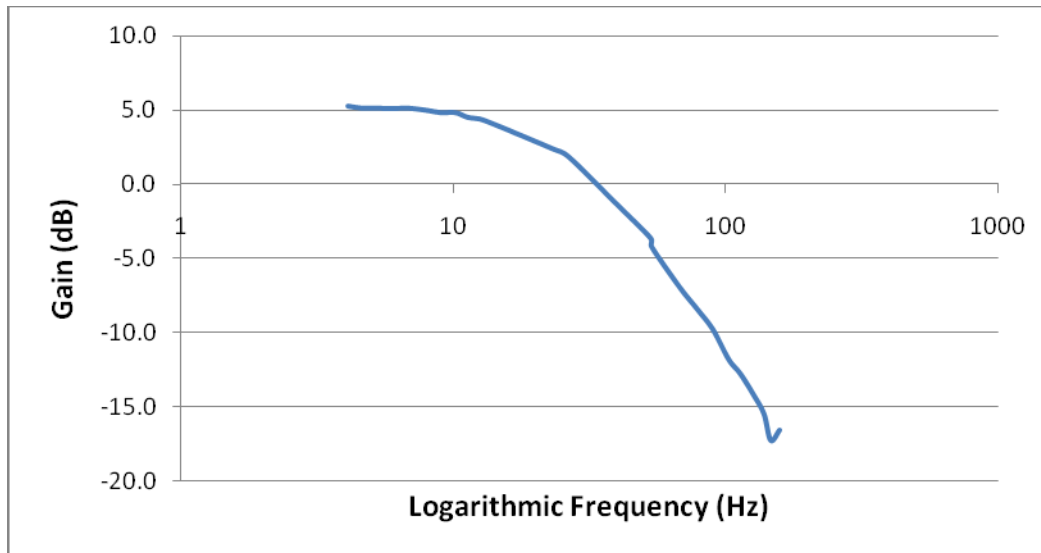


Figure 9: Gain vs. frequency log-log plot for the cascode amplifier

## 4.2 Patterning Methods

Dry etching parylene was performed on several different substrates (glass, silicon, Kapton) for varying thicknesses of parylene.  $O_2$  etching of these samples was performed at a pressure of 500mTorr and an etching power of 100W. The time of etching was varied for all the different samples in order to obtain adequate data. The etch rate of parylene under these conditions was found to be approximately  $0.2\mu\text{m}/\text{min}$  using the profilometer. The samples measured on silicon and glass gave the best results for thickness etched. It was difficult to adequately measure Kapton-based samples under the profilometer due to the non-planarity of the Kapton surface.

BCB and SoG were etched with  $SF_6$  at 500mTorr as well, but the power typically used was 75W. These substances could not be measured well on the profilometer. The SoG was not etched by the  $SF_6$  well and thus would prove difficult for patterning via holes. BCB appeared to be etched, but could not be measured since it was only a few hundred nanometers to begin with.

## 5. Conclusions

Amplifying circuits were set up using pentacene-based organic transistors. Regular common source topologies exhibited gains up to 3.5V/V for resistances near  $25M\Omega$ . These gains were seen over about 10Hz. Cascode was also tested to find the same gains as common source with a slightly lower frequency drop. Parylene was etched using oxygen plasma and exhibited a rate of  $0.2\mu\text{m}/\text{min}$  at 500mTorr and 100W. BCB and SoG were plasma etched using  $SF_6$ , but SoG exhibited no useful etching and BCB appeared etched, but was not able to be measured.

## 6. Recommendations

The biggest difficulty for testing the amplifier circuits was doing so around a glove-box probe station. This limited the amount of devices to two and also inhibited testing to a certain

degree. If devices could be patterned in the circuit form on a substrate using photolithography, higher level topologies could be tested. This would require all transistors as biases since resistors could not be easily put on a chip. This would also further investigate the ambipolar properties of the OFETs created for that purpose.

For the etching process, using a mask to add photoresist to a device in a hole-over-gate fashion could be attempted. This could be done on a transistor itself. After the etching an electrode could be deposited down the hole. The device could then be tested using the electrode as the gate access. This would show that the patterning methods are useful for application on the OFETs. Another possibility for future work on the etching is to use a polyimide dielectric as opposed to SoG and BCB, which were proven to difficult to etch. Polyimide dielectrics have been shown to produce devices with decent characteristics, and may be much easier to etch [22].

## 7. Acknowledgments

I would like Dr. Cherie Kagan, Dr. Jan Van der Spiegel, and Sangam Saudari of the University of Pennsylvania for their support and guidance for this project. I also want to thank David Kim and Yu Jen Lin for their help throughout the summer. Finally I am very grateful to the NSF for giving me the opportunity to experience research as part of the SUNFEST program.

## References

- [1] M. Berggren, A. Richter-Dahlfors, Organic Bioelectronics, *Adv. Mat.*, 19 (2007) 3201-3213.
- [2] R. A. Normann, Microfabricated Electrode Arrays for Restoring Lost Sensory and Motor Functions, *12<sup>th</sup> Int. Conf. on Solid State Sensors, Actuators, and Microsystems*, 2 (2003) 959-962.
- [3] H.M. Hamer, H.H. Morris, E.J. Mascha, M.T. Karafa, W.E. Bingman, M.D. Bej, R.C. Burgess, D.S. Dinner, N.R. Foldvary, J.F. Hahn, P. Kotagal, I. Najm, E. Wyllie, H.O. Lüders, Complications of Invasive Video-EEG Monitoring with Subdural Grid Electrodes, *Neurology*, 58 (2002) 97-103.
- [4] J.J. Van Gompel, G.A. Worrell, M.L. Bell, T.A. Patrick, G.D. Cascino and C. Raffel et al., Intracranial Electroencephalography with Subdural Grid Electrodes: Techniques, Complications, and Outcomes, *Neurosurgery*, 63 (2008) 498–505.
- [5] R. Ornstein, *The Evolution of Consciousness: The Origins of the Way We Think*, New York, Simon & Schuster, 1992, 63.
- [6] J. Zaumseil, H. Sirringhaus, Electron and Ambipolar Transport in Organic Field-Effect Transistors, *Chem. Rev.*, 107 (2007) 1296-1323.
- [7] A. S. Sedra, K. C. Smith, *Microelectronic Circuits*, 4 (1998) 353-395.
- [8] C. R. Kagan, A. Afzali, T. O. Graham, Operational and Environmental Stability of Pentacene Thin-Film Transistors, *Appl. Phys. Lett.* 86 (2005) 193505.

- [9] A. Afzali, C. D. Dimitrakopoulos, T. L. Breen, High-Performance, Solution-Processed Organic Thin Film Transistors from a Novel Pentacene Precursor, *J. Am. Chem. Soc.*, 124 (2002) 8812-8813.
- [10] S. R. Saudari, P. R. Frail, C. R. Kagan, Ambipolar Transport in Solution-Deposited Pentacene Transistors Enhanced by Molecular Engineering of Device Contacts, *Appl. Phys. Lett.*, 95 (2009) 023301.
- [11] T. B. Singh, P. Senkarabacak, N. S. Sariciftci, A. Tanda, C. Lackner, R. Hagelauer, G. Horowitz, Organic Inverter Circuits Employing Ambipolar Pentacene Field-Effect Transistors, *Appl. Phys. Lett.* 89 (2006) 033512.
- [12] M. G. Kane, J. Campi, M. S. Hammond, F. P. Cuomo, B. Greening, C. D. Sheraw, J. A. Nichols, D. J. Gundlach, J. R. Huang, C. C. Kuo, L. Jia, H. Klauk, T. N. Jackson, Analog and Digital Circuits Using Organic Thin-Film Transistors on Polyester Substrates, *IEEE Electron Dev. Lett.*, 21 (2000) 534-536.
- [13] D. M. Binkley, N. Verma, R. L. Crawford, E. Brandon, T. N. Jackson, Design of an Auto-Zeroed, Organic Thin-Film Field-Effect Transistor Amplifier for Sensor Applications, *Proc. Of SPIE – The Int. Soc. For Opt. Eng.*, 5522 (2004) 41-52.
- [14] R. Brederlow, S. Briole, H. Klauk, M. Halik, U. Zschieschang, G. Schmid, J.-M. Gorriz-Saez, C. Pacha, R. Thewes, W. Weber, Evaluation of the Performance Potential of Organic TFT Circuits, *Int. Solid-State Circ. Conf.*, 21 (2003) 21.6.
- [15] N. Gay, W.-J. Fischer, OFET-Based Analog Circuits for Microsystems and RFID-Sensor Transponders, *IEEE Polytronic 2007 Conf.*, 6 (2007) 143-148.
- [16] M. Takamiya, T. Sekitani, Y. Miyamoto, Y. Noguchi, H. Kawaguchi, T. Someya, T. Sakurai, Design for Mixed Circuits of Organic FETs and Plastic MEMS Switches for Wireless Power Transmission Sheet, *Int. Conf. on IC Des. and Tech.*, 4299565 (2007) 168-171.
- [17] T. D. Anthopoulos, D. M. de Leeuw, S. Setayesh, E. Cantatore, C. Tanase, P. W. M. Blom, J. C. Jummelen, Integrated Complementary-Like Circuits Based on Organic Ambipolar Transistors, *Mater. Res. Soc. Symp. Proc.*, 871E (2005) I11.9.1-I11.9.6.
- [18] H. Klauk, M. Halik, U. Zschieschang, G. Schmid, W. Radlik, Polymer Gate Dielectric Pentacene TFTs and Circuits on Flexible Substrates, *Int. Electron Dev. Meet.*, 22.1 (2002) 557-560.
- [19] T. Y. Chang, V. G. Yadav, S. De Leo, A. Mohedas, B. Rajalingam, C.-L. Chen, S. Selvarasah, M. R. Dokmeci, A. Khademhosseini, Cell and Protein Compatibility of Parylene-C Surfaces, *Langmuir*, 23 (2007) 11718-11725.
- [20] E. Meng, Y.-C. Tai, Parylene Etching Techniques for Microfluidics and BioMEMs, *IEEE 2005 MEMS Conf.*, 18 (2005) 568-571.

[21] J.-M. Hsu, L. Reith, R. A. Normann, P. Tathireddy, F. Solzbacher, Encapsulation of an Integrated Neural Interface Device with Parylene C, *IEEE Trans. On Biomed. Eng.*, 56 (2009) 23-29.

[22] H. Kawaguchi , T. Sakurai, High Mobility of Pentacene Field-Effect Transistors with Polyimide Gate Dielectric Layers, *Appl. Phys. Lett.*, 84 (2004) 3789-3791.

# **A VIRTUAL HEART MODEL FOR FORMAL AND FUNCTIONAL MEDICAL DEVICE VERIFICATION**

NSF Summer Undergraduate Fellowship in Sensor Technologies

Allison Connolly, Biomedical Engineering, Johns Hopkins University

Advisor: Rahul Mangharam, Ph.D.

## **ABSTRACT**

Currently, there is no formal method for the development and testing of medical device software, such as that used in pacemakers and implantable cardioverter-defibrillators (ICD). A large majority of device recalls are due to failures in the software that went undiscovered during product testing. For example, safety recalls of pacemakers and implantable cardioverter defibrillators due to firmware (i.e. software) problems between 1990 and 2000 affected over 200,000 devices, comprising 41% of the devices recalled. In order to preempt these failures, the device companies and the regulatory agencies, such as the FDA, need a better way to formally and functionally verify these devices before bringing them to the market. The heart model outlined in this paper is a tool used to simulate, test and validate these devices across multiple modalities in a plug-and-play manner. By synthesizing a large number and variety of intra-cardiac electrogram and derived external electrocardiogram signals, the model will create a database well beyond the scope of the MIT-BIH ECG database, the current standard for most cardiac medical device algorithm testing. This heart model allows for more extensive formal and functional testing of pre-market cardiac medical devices to detect flaws before the devices are implanted in patients.

## 1. INTRODUCTION

As the medical device industry grows, more devices contain software without a person in the loop. However, the Food and Drug Administration (FDA) and other regulatory agencies have no formal method for testing and verifying that the software performs properly and does not malfunction. For this reason, as the medical device industry grows so does the number of medical device recalls. The percentage of device recalls due to software problems is exceptionally high in cardiology and in vitro diagnostics due to the heavy reliance on software in these fields [<sup>i</sup>][<sup>ii</sup>]. Many recalls in cardiac devices are due to inappropriate delivery of treatment or inability to intervene when necessary [<sup>iii</sup>]. According to Compton, 25-33% of implantable cardioverter-defibrillator (ICD) shocks delivered are inappropriate, causing unnecessary pain and damage to the patient [<sup>iv</sup>]. Firmware problems go undiscovered during FDA testing and approval because the algorithms are completely proprietary to the device companies. Each company has its own method for testing and validating its own algorithms, but there is no standardized, formal method that the FDA can utilize to ensure all ICD's deliver shocks appropriately and all pacemakers maintain proper cardiac rhythms.

The development of a virtual heart model (VHM) that can be applied in research and medical environments allows for the betterment of medical device development techniques. The VHM is part of a larger virtual patient model (VPM). Data from every patient entering a hospital and undergoing tests will be stored and used to create an individualized patient model. Incorporating this data into a generic body model, such as the VHM, calls for the creation of interactive signals for use by doctors and researchers alike. Currently, a patient who enters the hospital to have a cardiac ablation procedure for treatment of an arrhythmia undergoes hours of monitoring and several pre-operative tests [<sup>v</sup>]. These data are stored only for the duration of the patient's visit and are discarded afterwards. If this data could be saved and incorporated into a database, it would enhance future patient diagnostics and provide a more extensive database for device validation and verification.

This paper focuses on the development plan for the VHM with the primary aim of testing medical devices for premarket approval. Section 2 provides further background on the growing issue of software failures as well as a summary of current patient models. Section 3 overviews the virtual patient project. Section 4 details the design components of the VHM. Section 5 addresses how the current version of the VHM is implemented. Sections 6 and 7 present conclusions reached during the development of the project as well as future directions. Section 8 lists possible applications of the complete VHM and VPM.

## **2. BACKGROUND**

### ***2.1. Population of Medical Device Users***

Every year, over 100,000 ICD's are implanted in patients throughout the United States [vi]. This number will continue to increase as the baby boomers age and as the rate of obesity-induced cardiac disease climbs, as predicted by [vii] and [viii]. Since 1990, the number of pacemakers implanted has doubled and the number of ICD's implanted has increased 11-fold. These devices are implanted in patients with arrhythmias and those who are at risk of sudden cardiac death. These conditions are usually associated with obesity, diabetes, and hypertension [ix]. It is predicted that 1% or less of the devices that are implanted will malfunction [x]. However, this statistic is surprisingly high when the raw number of deaths is considered. This number will only increase as the number of implanted devices increases in the near future.

### ***2.2. Current Patient Models***

Patient models have many uses, including device testing, medical staff training, and scenario modeling. The MIT-BIH database contains collections of signals from real patients. Some of the waveform data contains simultaneous ECG, blood pressure, arterial pressure, CO2 level, and respiration recordings [xi]. This allow for the analysis of multiple aspects of a patient's health at once, without the presence of an actual patient. These recordings contain all the variability characteristic of real-time signals, but are often too short and do not contain the interaction to be useful in comprehensive device testing. An alternative model is the MedSim300 patient simulator by Fluke [xii]. It is a signal generator that can be used for medical personnel training as well as medical device testing. This device can synthesize signals of cardiac arrhythmias, oxygen levels, respiration, and more. However, these signals are highly simplified and do not contain the variability inherent in true patient data. The virtual patient model outlined in this paper contains the variability of true data with the freedom of a synthesized signal.

### ***2.3. Current Heart Models***

Models of cardiac tissue excitation and contraction have been developed at institutions across the globe. However, many of these are complex, based on intracellular electrical conduction and action potentials. Boulakia et al. have developed a model to simulate external ECG recordings based on the electrical activity across the membranes of a network of interconnected cells [xiii].

Trayanova et al. have modeled the cardiac structure and its response to electrical stimulation, ranging from arrhythmias to depolarization [<sup>xiv</sup>]. These models contain both mechanical and electrical components on the micro level, but are highly complicated and too computationally heavy for real-time processing. The model developed in this paper is on a macro-level, modeling the global electrical activity of the atria and ventricles of the heart.

### **3. VIRTUAL PATIENT**

Creating the virtual patient has a dual purpose, to create a complete medical history for each patient, and to provide a larger number of medical recordings to the public domain for research purposes. This project is developed separately from but has potential to be included in the electronic health record [<sup>xv</sup>].

#### ***3.1. Medical History***

The virtual patient model will compile all medically-relevant information from a patient into a single location to enhance treatment capabilities. Data and results from all tests will be stored here, even if they are not deemed relevant to a specific issue at the time of recording. As medical testing and screening becomes less invasive, even healthy patients will have detailed recordings taken, such as electrophysiology studies of their hearts. The maps created during these tests can be stored in the VPM and provide a healthy baseline for future comparison if the patient develops a heart abnormality.

The medical history will also incorporate details about a patient's lifestyle. This includes physical activity levels, living environment, and daily habits. Previous medical treatments can also be relevant to the VPM. Usage of certain cardio-active drugs affects the performance of the heart and circulatory system. Data such as prescribed drugs, medical treatments or therapies used, the number of hours per week a patient exercises, and the quality of air in the patient's living environment are all important factors that can alter his or her health status, both temporarily and in the long run.

#### ***3.2. Data Storage***

The MIT-BIH database is now the largest and most widely used database for real signals. This data is used to test and verify research-based devices and algorithms as well as devices developed for the market. The database is not the ideal resource for pre-market testing because of the limited number and variety of signals available. One of the main uses of the database is for electrocardiogram (ECG) algorithm testing. However, most of the signals within the

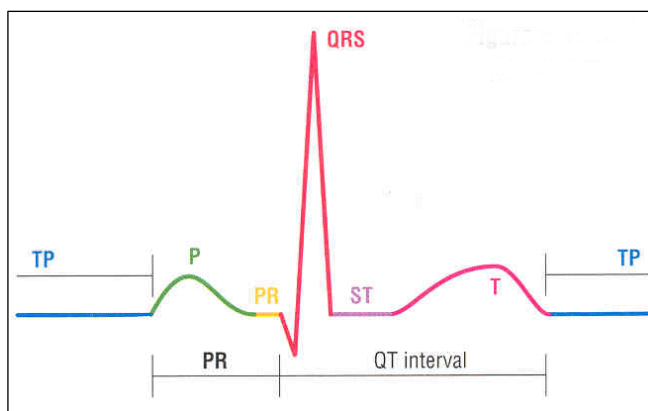
database contain only two leads of pre-recorded data, while standard ECG's contain 12 leads. Doctors are only able to make a satisfactory diagnosis by examining recordings from multiple locations on the patient's chest. Two leads do not contain enough information to make a diagnosis.

When the database was created in the 1980's, it contained a wealth of signals compared to other sources [xvi]. Because the database is not updated regularly, many of these recordings have become outdated and are of low quality compared to those taken with new devices. The data stored in the VPM will be updated regularly as the patient's health is monitored over the years. By making the data stored in the VPM anonymous and available to the public, it will provide a variety of high quality signals for all who desire to use them. The VPM has the potential to be a more powerful algorithm testing tool for all types of medical devices than the MIT-BIH database.

#### 4. DESIGN AND DEVELOPMENT

The first iteration of the virtual heart model was recently developed by the authors for the purpose of virtual and real medical device testing. For this reason, the VHM had to produce electrical signals similar to those recorded by medical devices, namely electrogram and ECG signals. In order to minimize the complexity of the model while making it as rich as possible, it was necessary to translate between the electrogram signals (measured from the interior of the heart) and the ECG signals (measured from the skin on the torso). Transforming electrogram data into multiple-lead ECG signals is known as the forward problem, while transforming the surface signals to the intracardiac signals is known as the inverse problem [xvii]. This iteration of the model utilizes the inverse problem, as ECG signals are more readily available for testing and manipulation.

##### 4.1. Electrophysiology



The electrocardiogram is the most readily available recording of heart activity because it is a non-invasive and relatively inexpensive monitoring procedure. Using ten electrodes placed across the surface of the upper torso, the ECG records the global electrical activation of the heart muscle that

correlates with the contraction of the heart and expulsion of blood. The components of lead II of the standard ECG are shown in Figure 4.1. When the heart is beating in normal sinus rhythm, this pattern is repeated continuously at a constant rate [xviii]. However, when the heart functions abnormally, the morphology of the ECG is altered in relation to the type of arrhythmia.

**Figure 4.1:** Components of the normal ECG. The baseline (blue) corresponds to the time of no electrical activity in the heart. The P wave is atrial depolarization. The QRS complex is ventricular depolarization. The T wave is ventricular

In order to artificially generate ECG signals for the VHM, recordings of normal and arrhythmic signals were taken from the MedSim300 and stored. These signals were parsed into individual heart beats and

then parsed again into the individual components of the beat, namely the P wave, QRS complex, T wave, and baseline, shown in Figure 4.1.

State models for each arrhythmia were generated from the parsed ECG signals. For example, the normal sinus rhythm state model contained P, QRS, T and a baseline of variable length. The length of the baseline was altered to increase or decrease the frequency of the signal and replicate varying heart rates.

#### ***4.2. Inverse Problem***

Although ECG recordings from the body surface are easy to obtain, the traces from the twelve leads are not intuitive and give only limited spatial discrimination inside the heart. A more useful display of the intracardiac excitation levels is through the Frank XYZ leads, which show the projection of the heart vector on the anatomical planes. The inverse Dower matrix was used to map the ECG signals into the XYZ components of the heart vector [xix]. Figure 4.2 shows a tool developed by the author for visualization of the heart vector in three-dimensional space. The heart vector or vectorcardiogram (VCG) is a useful precursor to a complete model of intracardiac excitation because it maps the electrical activity from the surface of the body to the inside of the chest and heart.

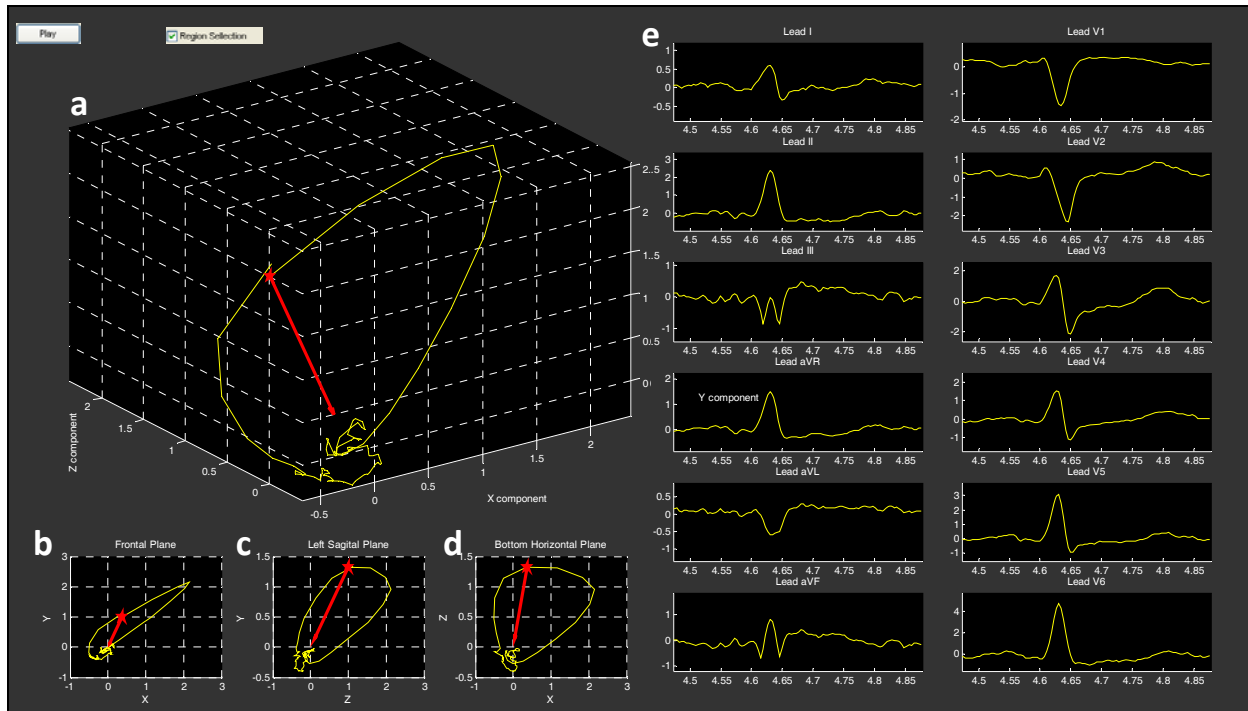


**Figure 4.2:** a) 3D Heart Vector Loop Derived from 12-Lead ECG for one heart beat, b) Projection of the heart vector in the frontal XY plane, c) Projection of the heart vector in the left sagittal YZ plane, d) Projection of the heart vector in the horizontal XZ plane, e) Tracings of the 12 ECG leads for one heart beat.

**4.3. Hardware**

The model was implemented on a programmable hardware platform, allowing the user to directly interface with analog and digital devices. For this project, the VHM was implemented on the National Instrument sbRIO-9641 FPGA board, shown in Figure 4.3 [xx]. The virtual heart model is embedded in the real-time microcontroller. The signals are fed through the FPGA chip to the ADC and DAC onboard, allowing for the transmission of signals between the patient simulator on the computer,

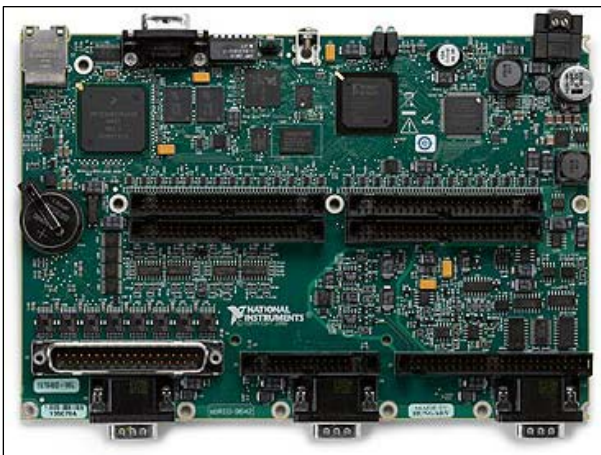


**Figure 4.3:** National Instrument sbRIO-9641 FPGA

the MedSim300, an oscilloscope, and medical devices.

## 5. IMPLEMENTATION

All aspects of the heart model software were created in Labview and embedded in the NI FPGA board. The Labview GUI is shown in Figure 5.1 and the code is shown in appendix D. The heart model responded to three inputs: atrial pacing, ventricular pacing, and an ICD shock. A state diagram of the arrhythmia heart model is depicted in appendix A. The more detailed state diagram of the pieces of sinus rhythm and parts of the ECG are depicted in appendix B.

In this version of the GUI for the heart model, pacing and shocking are manually implemented. This allows for comprehensive testing of the heart model to aid development of the algorithms. For normal sinus rhythm (NSR), the heart rate can be adjusted at the start of signal generation. The construction of the ECG signal in real time is done on the real-time microcontroller. The signal is output through the FPGA board and the DAC to the virtual pacemaker or ICD medical device. The medical device software reacts similarly to how a real medical device would react. The software contains a QRS detector, allowing for heart rate detection and thus identification of the state of the heart. The medical device can then output a pace or shock signal, which is fed back through an ADC to the FPGA and into the heart model.

**a**

**c**

**b**

**d**



**Figure 5.1:** Interactive user interface for the heart model version 1.0.

a) the signal being input from the heart model to the virtual medical device, b) the signal output from the virtual medical device, c) control box for the ICD shocking or pacing functions of the medical device, d) display of the current state of the heart model, either normal sinus rhythm (NSR), bradycardia (BRAD), ventricular tachycardia (VTACH), or ventricular fibrillation (VFIB) and the heart rate measured by QRS detector.

Because the system contains the heart and device in a closed loop, the heart model can react to inputs from the medical devices. This gives the entire system a dynamic nature that one does not find in recorded signals from real patients. For example, if the initial state of the heart is ventricular tachycardia (VTach), the ICD would normally pace in order to restore NSR. However, if the ICD does not detect the VTach for some reason, the state of the heart will degrade to ventricular fibrillation (VFib). For this state, the ICD detects the chaotic rhythm and delivers a shock. This shock causes the heart model to restore NSR.

Not every situation with medical device intervention is ideal, and some can lead to unhealthy results. For example, if the ICD shock or pace is delivered when the ventricles are undergoing repolarization, the heart will not reset to NSR, but will instead go into VFib. This is implemented in the heart model to ensure that the medical device software can detect when the heart is in the T wave (ventricular repolarization), and will thus withhold shock until an appropriate time.

## **6. DISCUSSION**

The virtual heart model was successfully created to interact with actuations from medical devices and medical device software. This actuation will allow for direct testing of medical devices by the FDA and by the medical device companies themselves. The heart model can respond to pacing located in the right atrium and the right ventricle, as well as shocks delivered in the right ventricle. The location of the virtual electrodes that deliver the pace or shock is not variable within the model as it would be in a real patient. Adjusting the location of electrode attachment in the heart wall will need to be incorporated in later iterations of the model.

The current version of the model incorporates a comprehensive set of arrhythmias that are important for medical device testing, namely VTach and VFib. The model does not, however, contain more complex arrhythmias such as heart block or atrial fibrillation, which would be necessary for more in depth analysis and testing of software. Each arrhythmia is represented as a separate state in this version of the model. In order to make the model more physiologically accurate, the model must become based on probabilities and other factors. This can be done using a Hidden Markov process to train the heart model to create more realistic signals.

The use of electrocardiogram signals in the heart model is not realistic for integration with medical devices, as most devices are implanted inside the patient's chest and respond to electrogram signals. For this reason, the use of the vectorcardiogram transform or another inverse model solution is necessary to transform between the external ECG signals and the internal electrogram signals. Once this transformation is made, real medical devices can be plugged in to the model hardware and interact in a closed-loop fashion.

In conclusion, version 1 of the virtual heart model outlined in this paper provides a solid foundation on which to build a more complex and realistic model. The closed loop nature allows for interaction between the heart and devices. A complete model will provide medical device

companies with a tool for proper software development and testing. It will also provide the FDA and other regulatory agencies a method to formally validate and verify this software before approving it for the market. With both the FDA and the device companies working to improve software development, device malfunctions due to software issues are hoped to decrease significantly and reduce the rate of device-related mortality.

## **7. FUTURE WORK**

### ***7.1. Integration of the Virtual Patient Model***

By combining the recorded signals from patients with the synthesized signals from the VHM, the model will be able to create an infinite array of cardiac electrical signals. A purely synthesized signal, such as that created by the MedSim300, is not sufficient for testing and validation of medical devices. Those signals do not contain the variability and unpredictability of signals recorded from real patients.

#### ***7.1.1. Context of Signal***

While standard ECG signals contain useful features due to redundancy and quality of signal, they are limited by the context of the recordings. Because the patient being monitored must be hooked up to the ECG through ten electrodes with connection wires, the patient must remain relatively still. For this reason, nearly all ECG signals are recorded while the patient is stationary. They contain no artifacts due to movement or exercise exertion.

Recordings taken from Holter monitors [xxi] or Loop monitors [xvii] are taken while the patient is ambulatory. This means the signals recorded by these monitors contain artifacts associated with patient motion, environment, and activity level. The VHM will be able to extract these artifacts from recorded signals and superimpose them on the signals produced by the modeling, creating a more realistic and more widely applicable model. Artifacts can arise from activity level, such as running, walking, sleeping, and emotionally and physically stressful situations. The patient's environment and surroundings, such as being underwater, at high altitudes, or at extreme temperatures, can affect the operation of his or her cardiac system. The patient's internal state, such as hormone levels or any drugs that are in his or her system, will also alter the signals, making them more complex for interpretation by software algorithms.

A basic example of artifact integration is breath rate. Breathing causes a baseline variation in the ECG because the distance from the heart to the torso wall changes as lung diameter increases and decreases. The breath rate also introduces variability in heart rate. As the lungs expand, they put pressure on the major veins and arteries in the chest, causing blood pressure to increase, which then triggers heart rate to decrease [xviii]. The VHM must be able to introduce the wandering baseline and the variable heart rate into synthesized signals.

### ***7.1.2. Patient-Specific Signal***

Just as the context artifacts can be integrated into synthesized signals, so can patient specific artifacts. This includes elevations in the ST-level, morphology changes in the P wave, and lengthened PR interval due to diseased conduction pathways. A combination signal containing context and patient artifacts superimposed on the general VHM has uses in medical care. This virtual patient can be used to test medical devices specifically with the patient in mind to see how he or she will respond and if the device will function properly

### ***7.2. Signal Database***

The combination signals give the heart model user the freedom to create a complex signal that will respond to actuation or feedback from an ICD or pacemaker. This provides a better testing environment for software validation and verification than other databases, which are static and provide no response. In addition, multiple forms of cardiac excitation signals need to be generated. This includes ECG, endocardial and epicardial electrograms, and cellular-level action potentials. Using these signals, the heart model can be used to test both implantable and on-body medical devices. Future iterations of the VHM will contain spatial information on the muscular contraction and deformation of the heart, allowing mechanical-based medical devices to be tested as well.

## **8. APPLICATIONS**

The VHM can be used in both research and medical environments. The formal model can be used by the FDA for rapid premarket testing, validation, and certification. The model can be used in clinical trials for cardio-active drugs and other pharmaceuticals. The patient-specific model is useful for pre-operative diagnosis, potentially reducing the number of cardiac procedures. It also has uses in post-operative recovery monitoring, to ensure that treatment was complete and complications do not arise.

### ***8.1. Research and Development***

The heart model can be used by the FDA for rapid premarket testing, validation and verification of medical devices. Currently, the FDA entrusts the validation of medical device software to the companies that make the devices. These companies run the software through a set of signals that was determined by the company itself to be sufficient for testing. The FDA is not involved in choosing the set of signals, so they cannot be sure the device is actually validated or compare performance across different devices.

Examples of devices that require software validation and verification are implantable loop monitors, pacemakers, and ICD's. In conjunction with the design of the heart model, the authors will design an electrocardiogram monitoring adhesive strip. The strip, which will be placed on the patient's chest above the heart, will contain two electrodes for signal acquisition and embedded programmable hardware for arrhythmia detection. The software on the monitoring strip will be verified and validated using the heart model. It will provide useful feedback during the model development to make the model interact properly with device software.

## ***8.2. Medical***

In many situations, insufficient patient history and data are recorded to make a diagnosis. In these cases, the doctor can conduct new tests, which are time consuming and costly, or he or she might perform a procedure or surgery the patient may not need. Integrating a medical history and patient lifestyle with a more general heart model will provide the physician with a predictive tool to diagnose what ailments a patient has without doing invasive testing.

A second medical application is for cardiac ablation surgeries. These surgeries are complicated procedures that require the patient to be under general anesthesia for eight or more hours [xxii]. Much of this time is spent creating an intracardiac map of the excitation timing within the myocardium. If a general map could be produced using the VHM and patient specific data before the procedure, the electrophysiologist would need less time for mapping and thus reduce the overall surgical time.

After the surgery is completed, the patient is at risk for post-operative complications or recurrence of the arrhythmia. The VPM would also have the capability to evaluate the

effectiveness of the ablation procedure and predict the likelihood of a recurrence or transference of the arrhythmia from one site to another [xxiii]. The collection of post-operative recordings from a large number of patients will give the heart model the capability to predict both normal and abnormal outcomes, allowing the doctor to preemptively choose the next step in the patient's treatment.

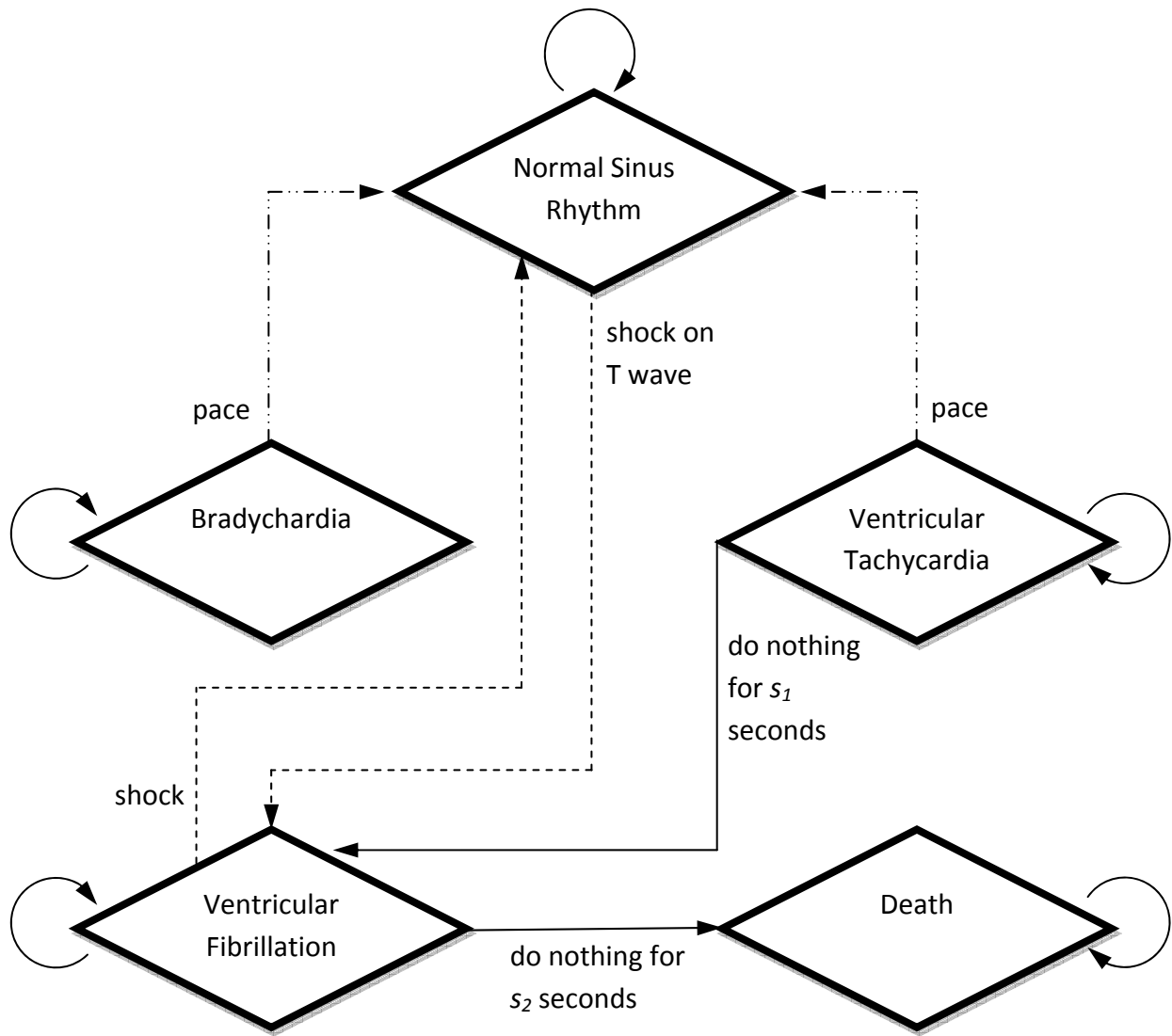
## **9. ACKNOWLEDGEMENTS**

The author would like to thank her advisor, Professor Rahul Mangharam, for his invaluable guidance and advice throughout the summer. She would also like to thank Zhihao Jiang for his long hours of work and dedication to the project and wishes him luck as the project continues. Thanks to all the members of mLab and Dr. Ed Gerstenfeld for their support and collaboration on the project. Finally, thanks to Jan Van der Spiegel and the rest of the SUNFEST administration, along with the National Science Foundation, for providing this opportunity.

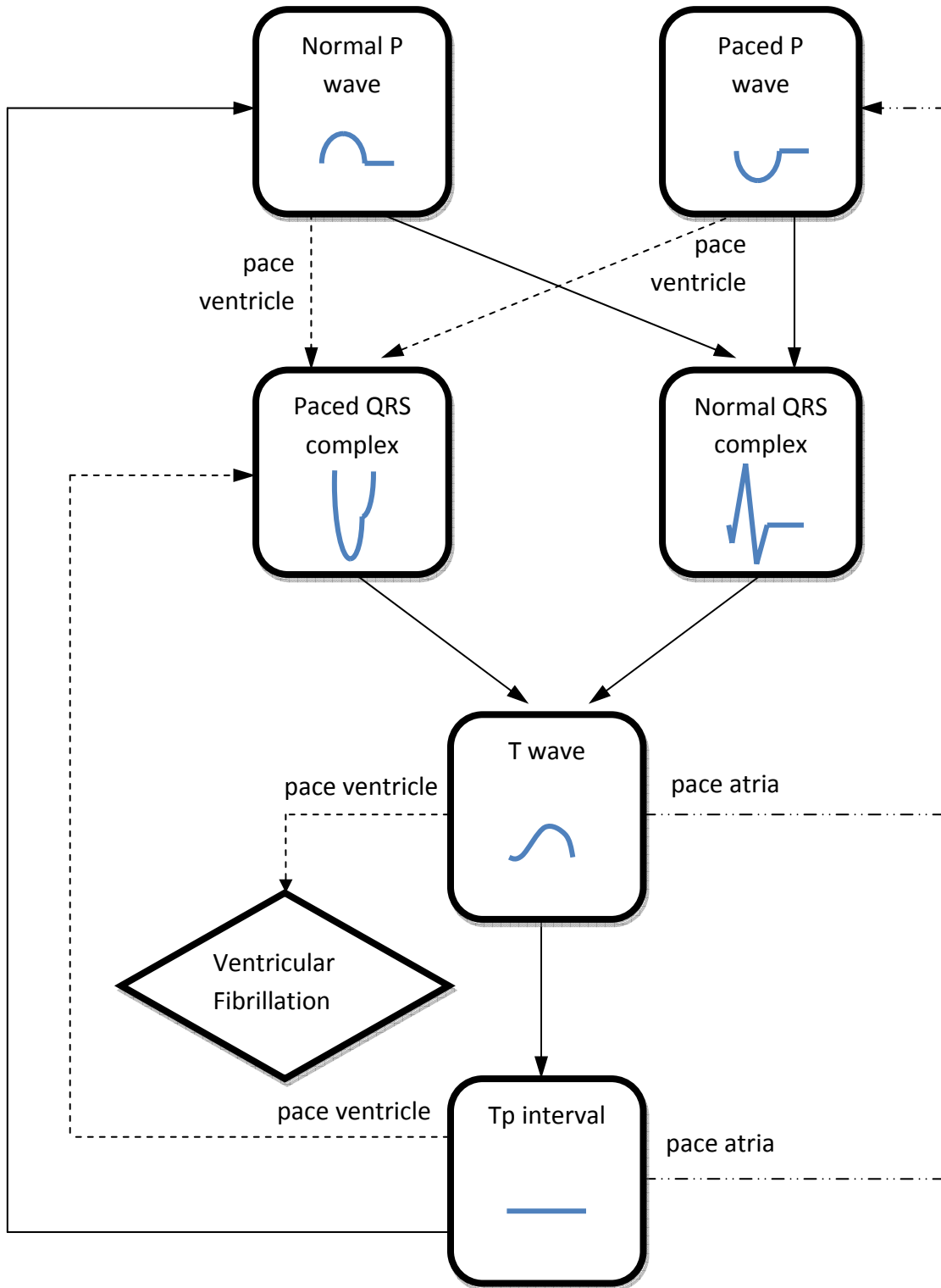
## **10. REFERENCES**

## **11. APPENDICES**

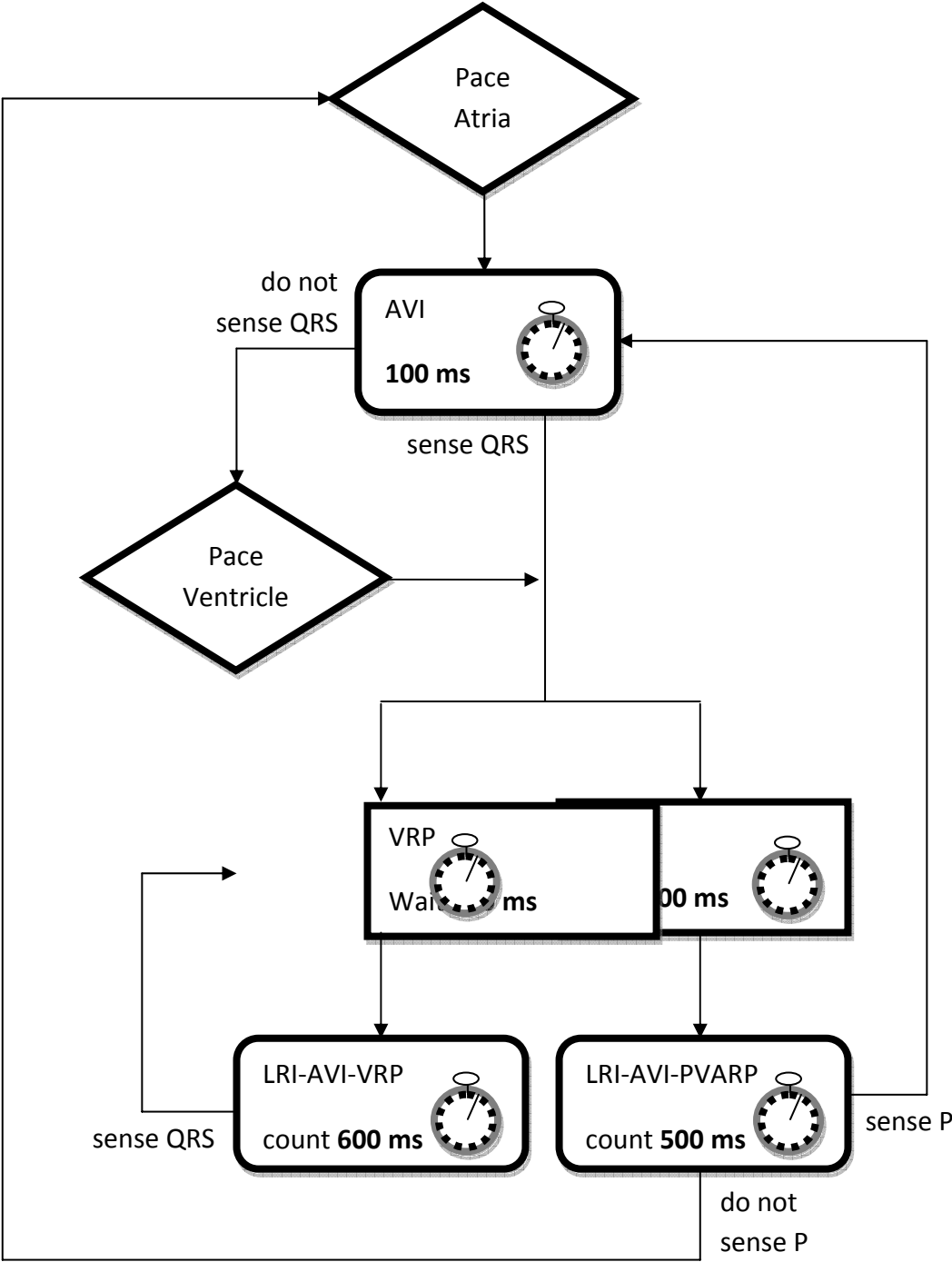
11.1. Appendix A: VHM version 1.0 – Virtual ICD and Heart State Machine



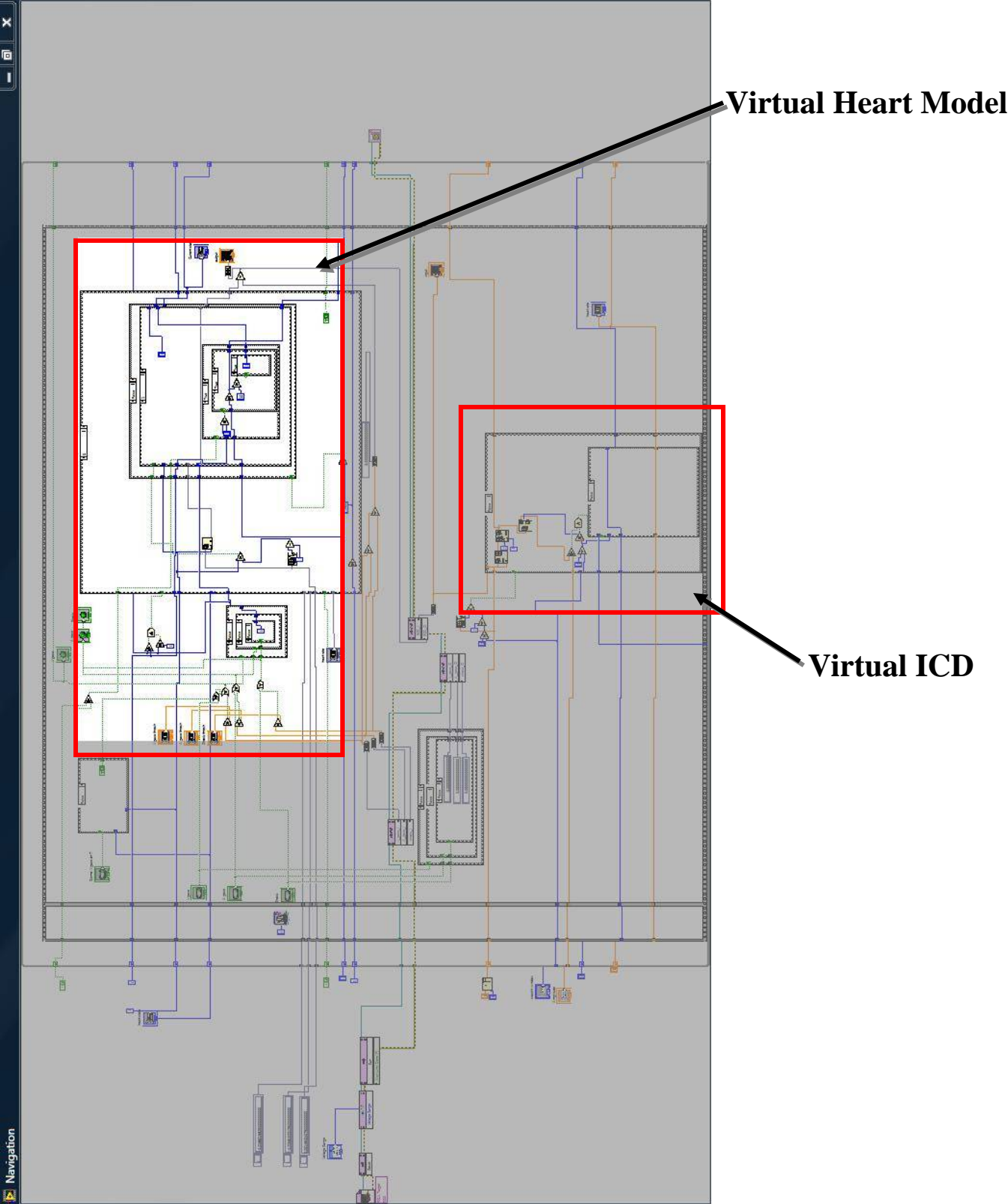
11.2. Appendix B: VHM version 1.1 – Pacemaker/Sinus Rhythm State Diagram



11.3. Appendix C: Pacemaker Flow Diagram



11.4. Appendix D: Labview Code for Heart Model and Virtual Medical Devices



# **AUTONOMIZATION OF A MOBILE HEXAPEDAL ROBOT USING A GPS**

Phillip Dupree (Mechanical Engineering)  
- Columbia University

Advisors: Daniel E. Koditschek, Galen Clark Haynes

## **ABSTRACT**

An important step in the autonomization of robots specifically designed for mobility is autonomous navigation: the ability to navigate from a current position to a programmed point, without the manual control of a human user. The object of this summer research was the autonomization of the robot RHex, a highly mobile hexapodal robot built in the GRASP lab of the University of Pennsylvania, which was accomplished by the integration of a global positioning system (GPS) module into the robot. The GPS module gave the robot the ability to follow a “breadcrumb” path of GPS way-points. Once the GPS data was parsed, the coordinates of both the robot’s location and the path of waypoints were converted into flat-earth approximate Cartesian coordinates, and then inputted into a linear control system. Once this was accomplished, the robot had the ability to “know” its current position and navigate from it to any programmed point, providing there were no obstacles in its path.

## **Introduction**

Robots are becoming more and more visible in daily life, as technological advancements make them capable of performing a variety of tasks. In particular, mobile robots are being used more frequently in everything from domestic purposes, such as mowing the lawn, to military tasks, such as bomb detection. As mobile robots become more advanced, human control is neither convenient nor adequate. More sophisticated robots must move towards autonomy: the ability to perform their tasks without human operation. Mobile robot navigation refers to the robot’s ability to safely move towards the goal using its knowledge and the sensorial information of the surrounding environment. [2]. This can be achieved by using advanced sensors that give a robot the ability to “know” where it needs to go, and collect data on its surrounding environment in order to safely move about and complete its task.

This paper documents the process of making a mobile robot autonomous by integrating a global positioning system (GPS) module. The former is used for global navigation: a higher level of navigation in which the robot both knows its own position and can follow a path of GPS way

points to navigate from its current position to some other position. The latter is used for local navigation: the ability of a robot to “see” its surrounding environment and use this knowledge to avoid obstacles. The ultimate goal of this autonomization is to have the mobile robot follow a “breadcrumb” path of GPS way points, while avoiding immediate obstacles in its path.

## **Background**

### Section 1: Navigation

#### *1.1 Odometry*

Robots use data from sensors on their motor called encoders to calculate how far they have moved in some certain period of time, just as blindfolded humans could guess their approximate position by counting how many steps they have taken. Odometry is the process of estimating the position of a mobile robot using the wheel’s rotational velocity and angular velocity, determined by the encoders[4].

#### *1.2 Dead reckoning*

Dead reckoning is a simple mathematical procedure for determining the present location of a vessel by advancing some previous position through known course and velocity information over a given length of time [6]. Though dead reckoning has a broad meaning, it is typically implemented using odometry data. Dead reckoning is used to compute the position of a robot during path tracking and other behaviors. However, due to cumulative errors in its motor control, a robot that navigates by dead reckoning alone will eventually lose track of its true position [7]. Inertial measurement units, which work by sensing changes in acceleration and calculating change in position over time, are also used for dead reckoning. However, accumulated errors in estimation of displacement over time eventually lead to significant errors. Overall, cumulative errors make dead reckoning a useful yet imprecise measurement of navigation.

#### *1.3 Global Navigation: Global Positioning System*

The Navstar Global Positioning System (GPS) developed as a Joint Services Program by the Department of Defense uses a constellation of 24 satellites (including three spares) orbiting the earth every 12 hours at a height of about 10,900 nautical miles. According to Borenstein and Feng in their essay “Where Am I?”, the absolute three-dimensional location of any GPS receiver is determined through simple trilateration techniques based on time of flight for uniquely coded spread-spectrum radio signals transmitted by the satellites. Knowing the exact distance from the ground receiver to three satellites theoretically allows for calculation of receiver latitude, longitude, and altitude. [5]. GPS gives users their positions whenever and wherever they are

outdoors all over the world. In addition, using GPS, robots can always locate their own position with only one coordinate system that is standardized as latitude/longitude in GPS. This is very helpful to avoid complicated management of coordinate systems [8].

The integration of a GPS into a robot can give the robot the ability to know its current position, and follow a “breadcrumb path” of points from its current position to any determined way point, given an adequate control system. However, the global positioning system has its own set of constraints. GPS cannot be used when users are indoors because the radio waves from satellites cannot penetrate walls [8].

GPS modules give raw data as constant streams of sentences according to protocol (a standard set of rules) defined by the National Marine Electronics Association. The data included in the sentence is defined in the first word, while the individual pieces of data (such as latitude and longitude) are separated by commas. Different sentences give different pieces of data, and modules rotate through outputting these sentences as they constantly update the data they calculate using the satellite signals. In order to utilize the data, a code must be written to *parse* the data: break down each sentence and organize the data into a form useable by whatever device or program means to use it.

## *Section 2: The Robot*

### 2.1 The Body

The RHex robot is a highly mobile hexapodal robot built in the GRASP lab at University of Pennsylvania. The robot’s design consists of a rigid body with six compliant legs, each possessing one independently actuated revolute degree of freedom. The attachment points of the legs as well as the joint orientations are all fixed relative to the body [2].

The legs utilize an alternating tripod phase, with the two “tripods” revolving in anti-phase relative to one another. Each tripod is set to a Buehler clock function with a slow and fast phase. To achieve this, the clock uses a piece-wise linear angle vs. time reference trajectory characterized by four parameters: the total stride or cycle period, the duty factor (the ratio of a single stance period over the cycle period), the leg angle swept during stance, and an angle offset to break symmetry in the gait [11]. Different “gaits” can be designed by altering the parameters of the gait.

### 2.2. Control

A control system, a function used to mathematically compute appropriate commands to move a robot to a desired position, must be put in place to take the GPS data and move the robot along its path of way points. I decided to utilize a basic linear control system, one in which the system being studied can be modeled by linear differential equations [12]. This linear control system

assumes the robot is moving at a constant speed, and alters the orientation over time to steer the robot to its desired position. Such a control system is commonly referred to as a unicycle control system.

## Control System Design

### 1. The Linear Controller

The linear control system (LCS) decided upon is one in which only the orientation of the robot is controlled, and the velocity is assumed constant. Basic trigonometry shows that if this is the case, then if the robot (modeled as a point) moved from point A to point B with a constant velocity, the equations for movement are:

$$x = s \cdot \cos(\theta) + x_0$$

$$y = s \cdot \sin(\theta) + y_0$$

$$s = s$$

$$\theta = \theta$$

Where  $x$ ,  $y$  are displacement in the  $x$  and  $y$  direction, respectively; theta ( $\theta = \arctan(y/x)$ ) is the orientation of the point relative to the origin of a defined coordinate system, and  $x_0, y_0$  are the initial displacements of the point relative to the origin of the defined coordinate system (both zero if the point is initially at the origin). The derivatives of these equations with respect to time are then:

$$x' = s \cdot \cos(\theta)$$

$$y' = s \cdot \sin(\theta)$$

$$s' = 0$$

$$\theta' = \mu$$

The change in speed over time,  $ds/dt$ , is zero because speed is constant. The change in theta,  $\mu$ , is determined later, as it is the only input into the system.

The control system took the form of:

$$X' = [A][X] + [B]$$

Where X is a 4 x 1 matrix consisting of X coordinate displacement, Y coordinate displacement, speed, and orientation; A is the state space equation that describes the state of the system, and B is the input into the system. Using the all ready derived equations we can fill in the state space equation and complete the linear controller:

$$\begin{bmatrix} \dot{x} \\ \dot{y} \\ \dot{s} \\ \dot{\theta} \end{bmatrix} = \begin{bmatrix} 0 & 0 & \cos(\theta) & 0 \\ 0 & 0 & \sin(\theta) & 0 \\ 0 & 0 & 0 & 0 \\ 0 & 0 & 0 & 0 \end{bmatrix} \cdot \begin{bmatrix} x \\ y \\ s \\ \theta \end{bmatrix} + \begin{bmatrix} 0 \\ 0 \\ 0 \\ \mu \end{bmatrix}$$

### 1.2. Closing the Loop – Determining $d\theta/dt$ , the Input into the System

The change in theta with respect to time is the keystone of the controller, as this is what steers the robot from its current position to its destination. In order to come up with an adequate equation, it is necessary not only to know the current orientation of the robot, theta, but also the angle from the robot's current position to the destination point, theta star ( $\theta^* = \arctan(y^*/x^*)$ ). By subtracting these two terms, the difference is the necessary change to alter the orientation of the robot from its current orientation to the direction of the destination point. Therefore, the equation for the change in theta became:

$$\theta' = k_p \cdot [\theta^* - \theta]$$

where  $k_p$  is the gain, a constant that determines how strongly the controller tells the robot to turn per iteration of time. If it is too high, the robot will try to change its orientation faster than it is able, causing errors. If it is too small, the robot will not be able to turn fast enough and will miss the point all together.  $\theta'$  is recalculated each iteration of the controller, constantly updating the robot's orientation theta and recalculating how much the robot needs to turn to align itself with theta star.

With this equation determined, the controller is complete<sup>1</sup>, as shown below.

$$x' = s \cdot \cos(\theta)$$

$$y' = s \cdot \sin(\theta)$$

$$s' = 0$$

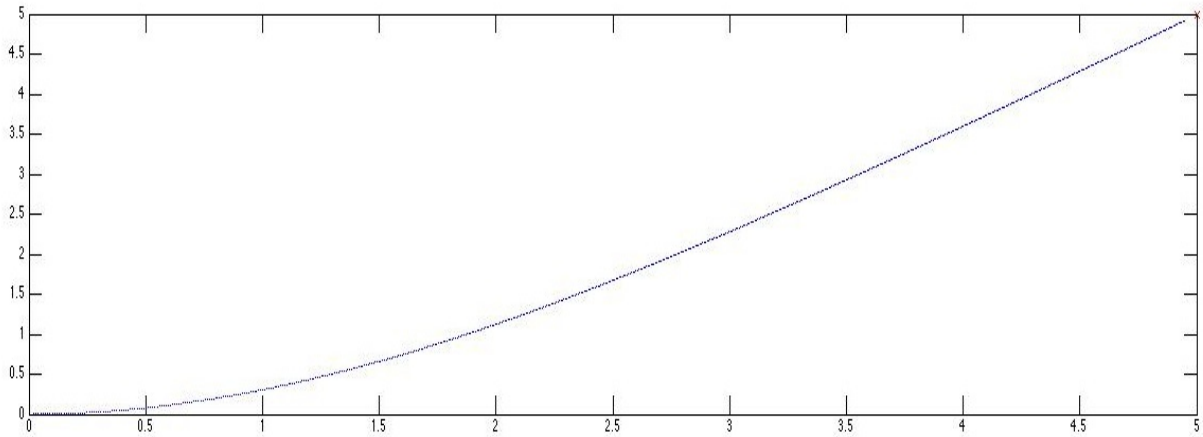
$$\theta' = k_p \cdot [\theta^* - \theta]$$

I then designed a Matlab simulation. The simulation utilized these equations to equate a giant matrix of the incremental changes of x and y of a point moving with some constant speed and changing its orientation according to the equation for  $\theta'$ . After each iteration  $\theta'$  was recalculated using the new values of x and y. The simulation looked like:

*Figure 1: Robot utilizing Basic Controller to move from  $X = 0, Y = 0$  to  $X = 5, Y = 5$*

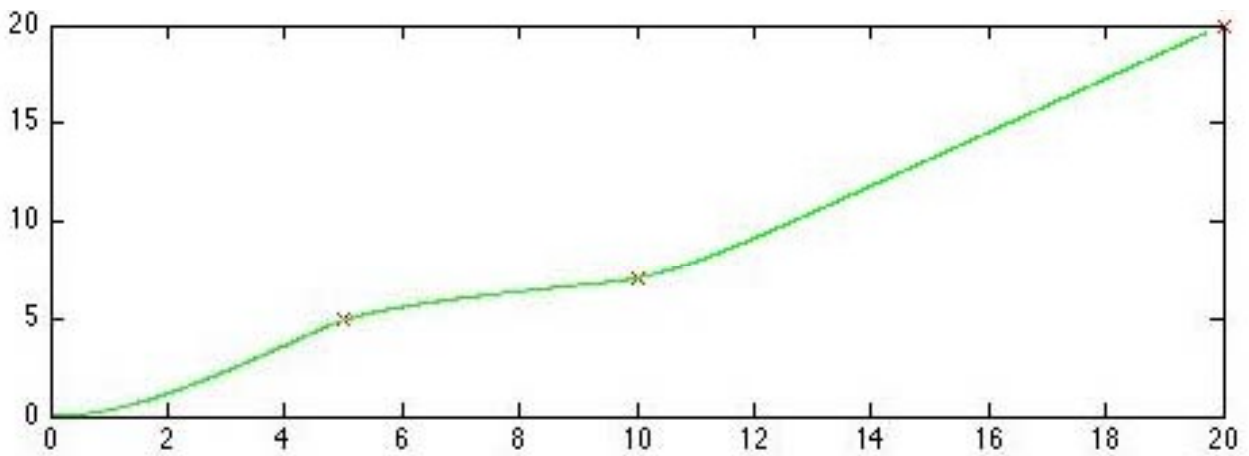
---

<sup>1</sup> See Appendix A for Basic Linear Control System, Matlab simulation code.



The origin is defined as the start point, and coordinate (5,5) as the destination. The robot starts off moving and gradually alters its orientation, ending at the destination point. When modeled with multiple destination waypoints, the controller resembled this:

*Figure 2: Robot utilizing Basic Controller to move to multiple Waypoints.*



The controller reaches some certain distance from its destination point (depending on how accurate the controller needs to be; this value is set. In this case, the value is set at .1 units), and then moves on towards the next point. We call this term proximity.

However, as smooth as the graph may look, in reality such a controller has errors. The robot

reaches its destination and then jerks towards the next point. A smoother, more advanced controller “rounds corners”, beginning to orient itself towards the next point as it nears its first destination. I set about upgrading my control system to smoothly round corners. Considering that change in theta with respect to time,  $d\theta/dt$ , is the only variable controlled in this unicycle control system, the equation for  $\theta'$  had to be altered. In order to have the robot start moving towards the  $(n + 1)^{th}$  destination as it neared the  $n^{th}$ , I needed to put in a  $\theta^*$  term not just from the  $n^{th}$  term, but also the  $(n + 1)^{th}$  term. This  $(n + 1)^{th}$   $\theta^*$  became known as  $\theta^{*2}$ . The equation for  $d\theta/dt$  became:

$$\theta' = k_p \cdot [\theta^* - \theta] + \frac{k_{p2}}{\|X_1 - X\|} \cdot [\theta^{*2} - \theta]$$

Where  $\|x - x_1\|$  is a magnitude term, the displacement between the current position of the robot and the  $n^{th}$  way point. The second gain is divided by this term because this magnitude will get smaller as the robot nears the  $n^{th}$  way point. Therefore, the closer the robot moves towards the  $n^{th}$  way point, the stronger the influence of the second part of the  $\theta'$  equation. If  $k_{p2}$  is too large and the influence of  $\theta^{*2}$  is felt too strongly too early, the robot will not reach the  $n^{th}$  way point before it starts being dragged off course. The robot will loop around several times before eventually reaching proximity (Figure 3). In a worst case, the robot cannot reach proximity, cannot begin to move towards the  $(n+1)^{th}$  point, and the controller will fail as the robot loops infinitely (Figure 4).

*Figure 3: Robot has difficulty reaching Proximity due to a high Gain.*

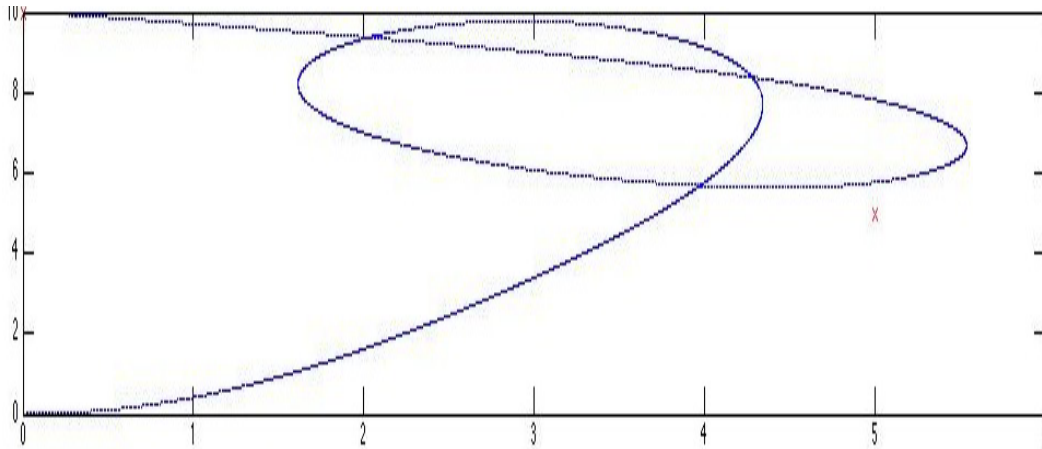
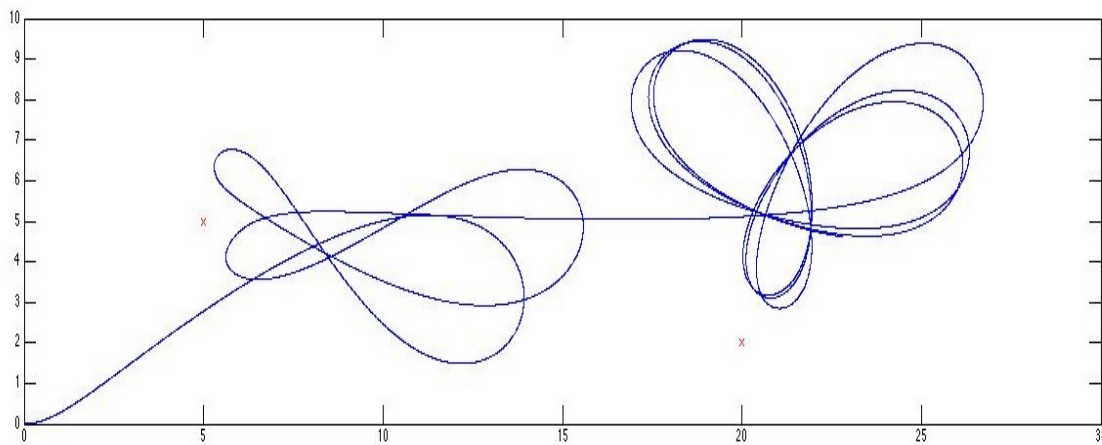


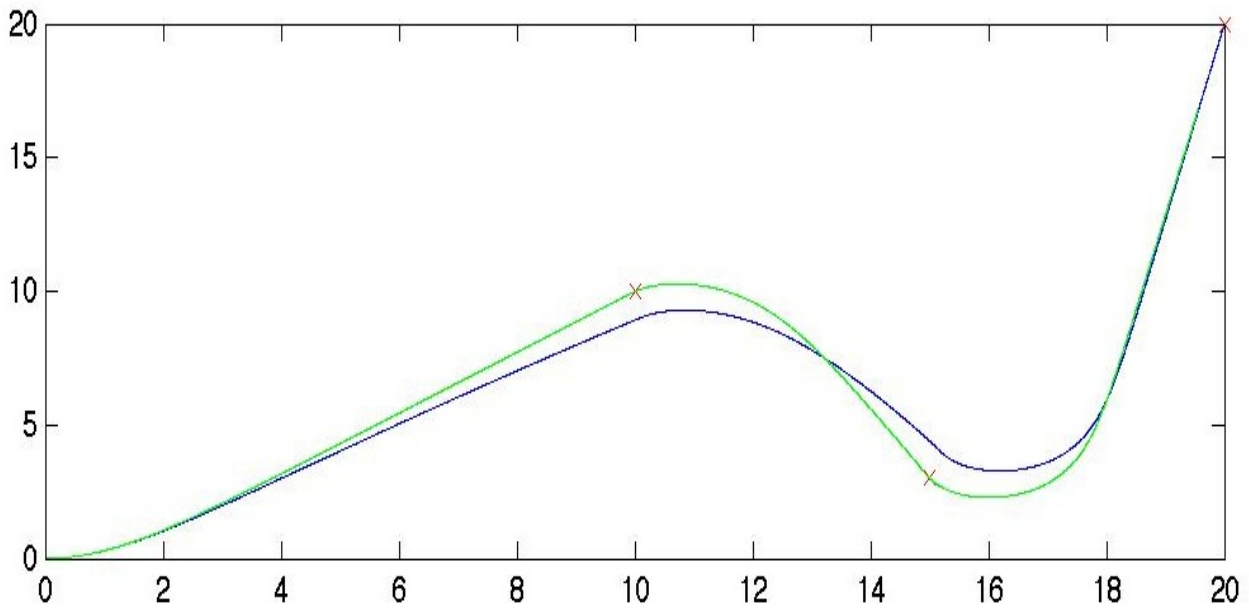
*Figure 4: Robot unable to reach Proximity due to a high Gain.*



However, working normally, the controller gently rounds corners, leading to a more efficient controller<sup>2</sup>. In Figure 5., the basic controller is in green while the advanced controller is in blue:

*Figure 5: Basic Controller (Green) juxtaposed against the Advanced Controller (Blue).*

<sup>2</sup> See Appendix B for Advanced Linear Control System, Matlab simulation code.



The final linear control system, in matrix form, is:

$$\begin{bmatrix} \dot{\hat{x}} \\ \dot{\hat{y}} \\ \dot{\hat{s}} \\ \dot{\hat{\theta}} \end{bmatrix} = \begin{bmatrix} 0 & 0 & \cos(\theta) & 0 \\ 0 & 0 & \sin(\theta) & 0 \\ 0 & 0 & 0 & 0 \\ 0 & 0 & 0 & 0 \end{bmatrix} \cdot \begin{bmatrix} x \\ y \\ s \\ \theta \end{bmatrix} + \begin{bmatrix} 0 \\ 0 \\ 0 \\ k_p \cdot [\theta^* - \theta] + \frac{k_{p2}}{\|X_1 - X\|} \cdot [\theta^{*2} - \theta] \end{bmatrix}$$

### Utilizing the GPS Data

GPS modules give position in terms of latitude and longitude. Latitude and longitude are angular displacements from the equator and prime meridian, respectively. They are angular coordinates that create a grid on a spherical object, and not the simple two dimensional Cartesian coordinates that the linear control system uses to operate. Therefore, directly plugging latitudes and longitudes into the LCS as x and y coordinates would not work. In order to use our control system, we must convert the latitude and longitude given by the GPS into Cartesian coordinates.

These conversions are flat-earth approximations: the formulas draw the angular coordinates onto a flat, two dimensional plane that is, in reality, tangential to the earth's surface. However, due to the large circumference of the earth, flat earth approximations have minimal errors for areas under several hundred kilometers.

The latitude and longitude coordinates were put through these two functions:

$$x = \cos(\phi) \cdot \sqrt{\frac{1}{\left(\frac{\sin(\phi)}{a}\right)^2 + \left(\frac{\cos(\phi)}{c}\right)^2}} \cdot [(longitude2 - longitude1) * \frac{\pi}{180}]$$

$$y = \sqrt{\frac{1}{\left(\frac{\sin(\phi)}{a}\right)^2 + \left(\frac{\cos(\phi)}{c}\right)^2}} \cdot [(latitude2 - latitude1) \cdot \frac{\pi}{180}]$$

where:

$$\phi = \frac{\pi}{2} - \frac{(latitude1 + latitude2)}{2} \cdot \frac{\pi}{180}$$

a = 6378136.6 meters, the equatorial radius of the earth, and c = 6356751.9 meters , the polar radius of the earth. These equations model the earth as a spheroid, instead of simple equations that model the earth as a sphere. This leads to more precise Cartesian approximations, due to a more precise radius of the earth (the radical term).

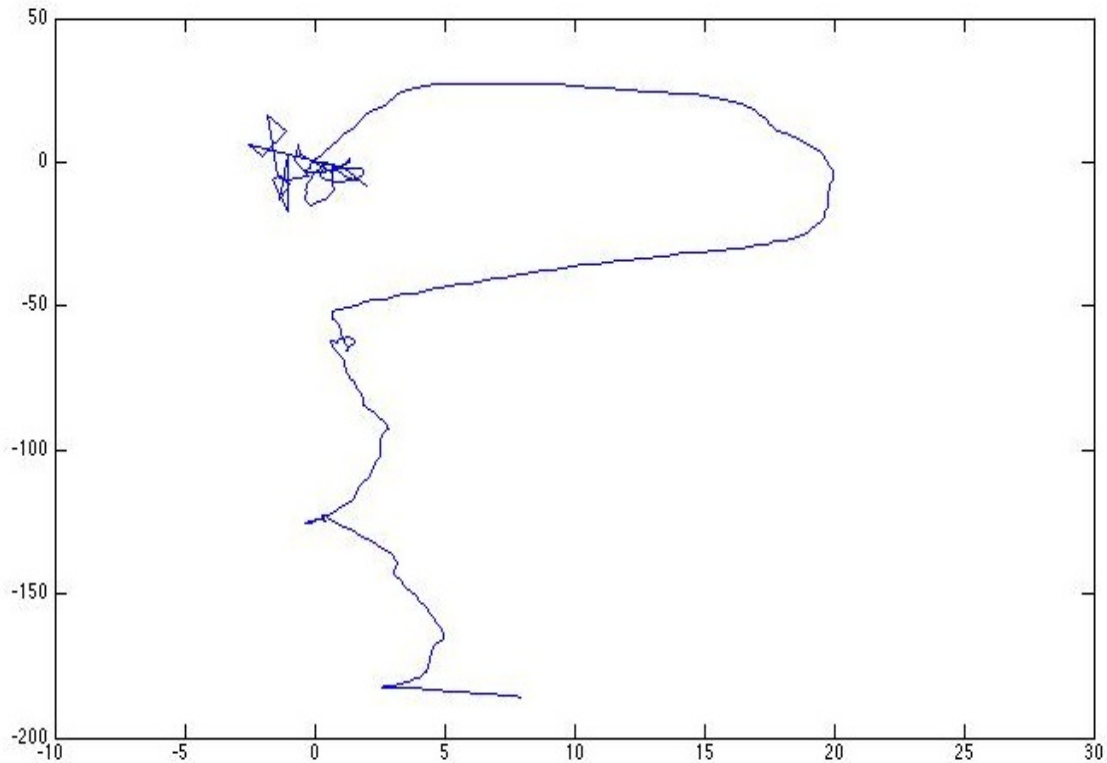
These equations converted a latitude/longitude path that very approximately resembles:

*Figure 6: Approximate Path of Movement on Google Earth.*



Into a Cartesian path of:

*Figure 7: Cartesian Approximation of a path of Latitude/Longitude Points.*



The path is rendered quite precisely in a Cartesian coordinate system<sup>3</sup>. The converted points can now be utilized in the linear control system.

### **Experimental Phase**

The linear control system could not be used directly by the robot; in order to be tested, the controller had to be adapted into a Python code<sup>4</sup> that the robot could utilize. The Python code was only a rough approximation of the sophisticated controls detailed in the previous section. The Gaitrunner code could not tell the robot exactly the angle it needed to turn; instead, it told the robot to turn by a certain speed. The speed of the turn was determined on a -1 to 1 scale, in which -1 told the robot to turn as quickly as possible to the left, and 1 told it to turn as quickly as

---

<sup>3</sup> See Appendix C for parsing/converting code in Python.

<sup>4</sup> See Appendix D for the Robot Controlling Python code.

possible to the right. Giving the robot a value such as -0.5 to .5, or -.1 to .1, would have the robot move far more slowly and gently to the left or right.

The Python code that was eventually used to control the robot first calculated the robot's orientation,  $\theta$ , by basic trigonometry. It took the tangent of the difference on the y axis and the x axis of the robot's last two coordinates. It then calculated the optimal orientation  $\theta^*$ , the angle from the robot's current position to the destination point, also utilizing basic trigonometry. If  $\theta^*$  was greater than  $\theta$  the robot was commanded to turn by -1 (as quickly as possible) to the left, and vice versa. Also by simple trigonometry, the robot calculated the displacement from its current position to the destination point. Once some certain proximity to the destination point was reached, the robot would either start navigating toward the next way point, or sit down if the final way point had been reached. Though the path was inefficient as the robot weaved back and forth,, this basic code allowed the robot to successfully autonomously navigate to multiple GPS way points after it was set down in a field and the points programmed in. The necessary proximity was first set to five meters, then halved to two and a half meters. In both cases the robot reached this proximity and then continued on to the next way point.

## **Conclusion**

There is a great deal of improvement that could be made to the Python code that controls the robot. Ultimately, its level of sophistication needs to rival that of the linear control system on which it was based. Gains on the turn speed must be tuned. Currently, the robot weaves so strongly to the right and left (resembling a sine wave) because even if the orientation  $\theta$  is very close to the optimal orientation, the robot is still told to turn as quickly as possible to the left or right. A gain must be put on the turning speed so that the robot turns quickly when its angle is far from the optimal orientation, and by a very small amount when its angle is near. Once this is done, the code must again be adapted to resemble not just the basic controller, but also the enhanced controller that rounds corners by feeling input from the following point as the robot nears its initial destination.

Secondly, the controller itself could be improved. The enhanced  $\theta'$  equation is nothing more than a poor approximation for a linear spline, one continuous mathematical function that smoothly links together multiple points. Utilizing linear splines in a controller would lead to a simpler, more efficient controller without the need for nearly as much gain tuning.

However, though there are many improvements to be made, the autonomization was ultimately a success. Using a GPS module, a linear control system, and basic trigonometry in the end, a code was designed that, given the absence of obstacles, could autonomously navigate a hexapodal robot from its current position to any set of multiple GPS way points.

## References

- [1] Riisgard, Søren and Blas, Morten Rufus. “SLAM for Dummies: A Tutorial Approach to Simultaneous Localization and Mapping”.
- [2] U. Saranali, M. Buehler, and D.E. Koditschek. “Rhex: A Simple and Highly Mobile Hexapod Robot”. *The International Journal of Robotics Research*, Vol. 20, No.7. pp. 616-631, July 2001.
- [3] Maria Isabel Ribeiro. “Obstacle Avoidance”. Instituto de Sistemas e Robótica, Instituto Superior Técnico, 2005.
- [4] Seung-Hun Kim , Chi-Won Roh , Sung-Chul Kang and Min-Yong Park. “Outdoor Navigation of a Mobile Robot Using Differential GPS and Curb Detection”. 2007 IEEE International Conference on Robotics and Automation. Roma, 2007
- [5] J. Borenstein, H. R. Everett, and L. Feng “Where am I?: Sensors and Methods for Mobile Robot Positioning”. University of Michigan, 1996.
- [6] Dunlap, G.D. and Shufeldt, H.H., Dutton’s Navigation and Piloting, Naval Institute Press, pp. 557-579.
- [7] Jane Yung-Jen Hsu, Der-Chiang, and Lo Shih-Chun Hsu. “Fuzzy Control for Behavior-Based Mobile Robots”. Department of Computer Science and Information Engineering National Taiwan University, 1994.
- [8] Haruhiko Niwa, Kenri Kodaka, Yoshihiro Sakamoto, Masaumi Otake, Seiji Kawaguchi, Kenjiro Fujii, Yuki Kanemori, and Shigeki Sugano. “GPS-based Indoor Positioning

system with Multi-Channel Pseudolite.” 2008 IEEE International Conference on Robotics and Automation Pasadena, 2008.

[9] Sanjiv Singh and Jay West. “Cyclone: A Laser Scanner For Mobile Robot Navigation”. The Robotics Insitute. Carnegie Mellon, 1991.

[10] Robert Ouellette, Kotaro Hirasawa. “A Comparison of SLAM Implementations for Indoor Mobile Robots”. 2007 IEEE/RSJ International Conference on Intelligent Robots and Systems. San Diego, 2007.

[11] J. Seipel and P. Holmes. “A Simple Model for Clock-Actuated Legged Locomotion”. Regular and Chaotic Dynamics, 2007, Vol. 12, No. 5, pp. 502–520. c  
Pleiades Publishing, Ltd., 2007.

## Appendix A

```
function [theta, X] = controller(start_x, start_y, start_angle, end_x, end_y, speed, gain)
```

```
%X is the original state of the system. X = 0, Y = 0, S = .1, theta = 0
```

```
X = [start_x; start_y; speed; start_angle];
```

```
X2 = [end_x; end_y; 0;0];
```

```
xtilda = X2 - X;
```

```
magxtilda = sqrt((X2(1) - X(1))^2 + (X2(2) - X(2))^2);
```

```
i=1;
```

```

while magxtilda > .001
    kp = gain; %gain
    theta = X(4);

    thetastar = atan2(X2(2) - X(2),X2(1) - X(1));
    thetadot = kp*sin(thetastar - theta);

    A = [0,0,cos(theta),0;0,0,sin(theta),0;0,0,0,0;0,0,0,0];
    %State equation.
    B = [0;0;0;thetadot]; %Input
    xdot = A*X + B;
    X = X + xdot*.1;
    magxtilda = sqrt((X2(1) - X(1))^2 + (X2(2) - X(2))^2);

    subplot(2,1,1)
    plot(X(1),X(2), 'b')
    hold on
    plot(end_x,end_y, 'rx')
    hold on

    x(i) = X(1); % x axis data
    y(i) = X(2); % y axis data

```

end

end

## Appendix B

```
function [theta] = newcontroller(start_x, start_y, start_angle, speed, gain)
```

```
    %newcontroller(initial x, initial y, initial orientation, speed, gain)
```

```
    X = [start_x; start_y; speed; start_angle];
```

```
    i = true;
```

```
    j = 1;
```

```
    hold on
```

```
while i == true
```

```
    endx(j) = input('Give the end point on the x axis: ');
```

```
    endy(j) = input('Give the end point on the y axis: ');
```

```
    i = input('Input another set of points? Y=1/N=0: ');
```

```
    j = j+1;
```

```
end
```

```
distance = sqrt((endx(1) - X(1))^2 + (endy(1) - X(2))^2);
```

```

b = 1;

g=1;
while b < j
    while distance > g
        kp = gain; %gain
        kp2=.8*kp;
        theta = X(4);
        thetastar = atan2(endy(b) - X(2),endx(b) - X(1));
        thetastar2 = theta;

        if b+1<j
            thetastar2=atan2(endy(b+1)-X(2),endx(b+1)-X(1));
        end

        diff = thetastar - theta;
        diff2 = thetastar2-theta;
        thetadot1 = kp*(mod(diff + pi, 2*pi) - pi);
        thetadot2 = (kp2/distance)*(mod(diff2+pi, 2*pi)-pi);
        thetadot = kp*sin(diff) + (kp2/distance)*sin(diff2);

A=[0,0,cos(theta),0;0,0,sin(theta),0;0,0,0,0;0,0,0,0]; %State equation.

    B = [0;0;0;thetadot]; %Input

    xdot = A*X + B;

```

```

X = X + xdot*.1;
distance=sqrt((endx(b)-X(1))^2+(endy(b)- X(2))^2);
subplot(2,1,1)
plot(X(1),X(2), 'b', endx(b), endy(b), 'rx')
    hold on
end

b = b+1;
if b == j-1
    g = .1;
end

if b+1>j
    break;
end
distance = sqrt((endx(b)-X(1))^2+(endy(b) - X(2))^2);
end
end

```

## Appendix C

```
import math

# === We begin by creating the Objects ===

#Weird checksum function that no one understands.

def checksum(line):

    sum = 0

    for char in line:

        sum ^= ord(char)

        checksum_manual = "%02X" % sum

    if checksum != checksum_manual:

        print 'bad checksum at line %d' % lineno

    return [checksum_manual]

#Analyzes GPRMC lines of GPS data, gives out latitude, longitude, speed, orientation

def gprmc(line):

    #checksum(line)

    linedata = line.split(',')

    if linedata[3] == "": linedata[3] = float(0)

    lat = int(linedata[3][0:2]) + float(linedata[3][2:]) / 60.0

    lon = int(linedata[5][0:3]) + float(linedata[5][3:]) / 60.0

    speed = float(linedata[7])* 0.514444444 #meters/second
```

```

angle = float(linedata[8])
if linedata[4] == 'S':
    lat = -lat
if linedata[6] == 'W':
    lon = -lon

return [lat, lon, speed, angle]

#Analyzes gpgga lines of data
def gpgga(line):
    #checksum(line)
    linedata = line.split(',')
    #print linedata
    latgga = int(linedata[2][0:2]) + (float(linedata[2][2:]) * 60.0)/3600
    print latgga
    longga = int(linedata[4][0:3]) + (float(linedata[4][3:]) * 60.0)/3600
    if linedata[3] == 'S':
        latgga = -latgga
    if linedata[5] == 'W':
        longga = -longga
    quality = int(linedata[6])
    satnum = int(linedata[7])
    altitude = float(linedata[9])
    return [latgga, longga, quality, satnum, altitude]

```

```

#Analyzes gpgsa lines of data

def gpgsa(line):
    #checksum(line)

    linedata = line.split(',')

    mode = linedata[1]

    #if mode == "A": print "Automatic Mode"
    #elif mode == "M": print "Manual Mode"

    mode2 = int(linedata[2])

    #if mode2 == 1: print "Fix not available"
    #elif mode2 == 2: print "2D fix"
    #elif mode2 == 3: print "3D fix"

    j = 0

    for i in range(3,15):
        if linedata[i] != " ": j=j+1

    print "There are " +str(j)+ " active satellites."

    pdop = linedata[-3]
    hdop = linedata[-2]
    vdop = linedata[-1]

    return [mode, mode2, j, pdop, hdop, vdop]

```

```

#Analyzes gpgsv lines of data

```

```

def gpgsv(line):
    #checksum(line)

```

```
linedata = line.split(',')
number = int(linedata[2])
sentnum = int(linedata[3])
satnumgsv = int(linedata[4])
return [number, sentnum, satnumgsv]
```

```
def getCartesian(lat1, lon1, lat2, lon2):
    #equatorial radius
    a = 6378136.6
    #polar radius
    c = 6356751.9
    phi = (lat1+lat2)/2
    phi = math.pi/2 - (phi*math.pi/180)
    lon_diff = lon2-lon1
    lat_diff = lat2-lat1

    temp = (math.sin(phi)/a)**2 + (math.cos(phi)/c)**2
    r = (1/temp)**0.5

    lon_r = math.cos(phi)*r
    x = lon_r*lon_diff*math.pi/180
    y = r*lat_diff*math.pi/180
    return [x, y]
```

```

# ===== Time to Analyze =====

gpsfile = open('/Users/ryo/GPS2e.txt','r')

lat, lon, speed, angle = [],[],[],[]

latgga, longga, quality, satnum, altitude = [],[],[],[],[]

mode, mode2, j, pdop, hdop, vdop = [],[],[],[],[], []

number, sentum, satnumgsv = [],[],[]

coordinates,x,y,dx,dy=[],[],[],[],[]

lineno = -1

while 1:

    lineno = lineno + 1

    line = gpsfile.readline()

    linesplit = line.split(',')

    if line == "": break

    line = line.strip()

    id = line[0:6]

    (line,checksum) = (line[0:-3],line[-2:])

    if id == '$GPRMC':

        if len(linesplit)<6: break

        data = gprmc(line)

```

```
lat.append(data[0])
lon.append(data[1])
speed.append(data[2])
angle.append(data[3])
elif id == '$GPGGA':
    if len(linesplit)<6: break

    data = gpgga(line)
    if data[0] != 0:
        latgga.append(data[0])
        longga.append(data[1])
        quality.append(data[2])
        satnum.append(data[3])
        altitude.append(data[4])
elif id == '$GPGSA':
    if len(linesplit)<6: break
    data = gpgsa(line)
    mode.append(data[0])
    mode2.append(data[1])
    j.append(data[2])
    pdop.append(data[3])
    hdop.append(data[4])
    vdop.append(data[5])
elif id == '$GPGSV':
```

```

if len(linesplit)<6: break

data = gpgsv(line)

lat.append(data[0])

lon.append(data[1])

speed.append(data[2])

for i in range(0,len(longga)):

    coordinate = [latgga[i], longga[i]]

    coordinates.append(coordinate)

    re = 6371*1000

    y.append(re*(latgga[i]-latgga[0])*math.pi/180)

    x.append(re*(longga[i]-longga[0])*(math.pi/180)*math.cos(longga[0]*math.pi/180))

    ex, ey = getCartesian(latgga[0], longga[0], latgga[i], longga[i])

    if ex < -60:

        print i

        dx.append(ex)

        dy.append(ey)

gpsfile.close()

```

## Appendix D:

```
import math
import dy
import time

dy.init()
dy.network.connect('penn4', 8650)
dy.signal.send('calibrate_start')
time.sleep(5)
dy.signal.send('gaitrunner_start')
time.sleep(5)
dy.signal.send('stand_start')
time.sleep(5)
ds = dy.data.path('penn6')
dyturn = dy.data.create_at(ds, dy.DY_FLOAT, 'gait.turn')
dyspeed = dy.data.create_at(ds, dy.DY_FLOAT, 'gait.speed')
dy.data.set_float(dyspeed, 0,0);
dy.network.push("penn6.gait.speed");
dy.data.set_float(dyturn,0,0)
dy.network.push("penn6.gait.turn");

# === We begin by creating the Objects ===
```

```
#Weird checksum function that no one understands.
```

```
def checksum(line):
```

```
    sum = 0
```

```
    for char in line:
```

```
        sum ^= ord(char)
```

```
    checksum_manual = "%02X" % sum
```

```
    if checksum != checksum_manual:
```

```
        print 'bad checksum at line %d' % lineno
```

```
    return [checksum_manual]
```

```
#Analyzes GPRMC lines of GPS data, gives out latitude, longitude, speed, orientation
```

```
def gprmc(line):
```

```
    #checksum(line)
```

```
    linedata = line.split(',')
```

```
    if linedata[3] == "": linedata[3] = float(0)
```

```
    lat = int(linedata[3][0:2]) + float(linedata[3][2:]) / 60.0
```

```
    lon = int(linedata[5][0:3]) + float(linedata[5][3:]) / 60.0
```

```
    #speed = float(linedata[7])* 0.514444444 #meters/second
```

```
    #angle = float(linedata[8])
```

```
    if linedata[4] == 'S':
```

```
        lat = -lat
```

```
    if linedata[6] == 'W':
```

```
        lon = -lon
```

```
return [lat, lon]
```

```
#Analyzes gpgga lines of data
```

```
def gpgga(line):
```

```
    #checksum(line)
```

```
    linedata = line.split(',')
```

```
    latgga = int(linedata[2][0:2]) + (float(linedata[2][2:]) * 60.0)/3600
```

```
    longga = int(linedata[4][0:3]) + (float(linedata[4][3:]) * 60.0)/3600
```

```
    if linedata[3] == 'S':
```

```
        latgga = -latgga
```

```
    if linedata[5] == 'W':
```

```
        longga = -longga
```

```
    quality = int(linedata[6])
```

```
    satnum = int(linedata[7])
```

```
    altitude = float(linedata[9])
```

```
    return [latgga, longga, quality, satnum, altitude]
```

```
#Analyzes gpgsa lines of data
```

```
def gpgsa(line):
```

```
    #checksum(line)
```

```
    linedata = line.split(',')
```

```
    mode = linedata[1]
```

```
    mode2 = int(linedata[2])
```

```

j = 0
for i in range(3,15):
    if linedata[i] != ": j=j+1
#print "There are " +str(j)+ " active satellites."
pdop = linedata[-3]
hdop = linedata[-2]
vdop = linedata[-1]
return [mode, mode2, j, pdop, hdop, vdop]

#Analyzes gpgsv lines of data
def gpgsv(line):
    #checksum(line)
    linedata = line.split(',')
    number = int(linedata[2])
    sentnum = int(linedata[3])
    satnumgsv = int(linedata[4])
    return [number, sentnum, satnumgsv]

def getCartesian(lat1, lon1, lat2, lon2):
    #equatorial radius
    a = 6378136.6
    #polar radius
    c = 6356751.9
    phi = (lat1+lat2)/2

```

```

phi = math.pi/2 - (phi*math.pi/180)
lon_diff = lon2-lon1
lat_diff = lat2-lat1

temp = (math.sin(phi)/a)**2 + (math.cos(phi)/c)**2
r = (1/temp)**0.5

lon_r = math.cos(phi)*r
x = lon_r*lon_diff*math.pi/180
y = r*lat_diff*math.pi/180
return [x, y]

```

```
# ===== Time to Analyze =====
```

```
gpsfile = open('/dev/ttyS1');
```

```
lat, lon, speed, angle = [],[],[],[]
```

```
latgga, longga, quality, satnum, altitude = [],[],[],[],[]
```

```
mode, mode2, j, pdop, hdop, vdop = [],[],[],[],[], []
```

```
number, sentum, satnumgsv = [],[],[]
```

```
coordinates,x,y,dxx,dyx,endx,endy,pathx, pathy=[],[],[],[],[],[],[],[],[]
```

```
i=1
```

```
j=0;
```

```
b = 0
```

```

while i == 1:
    deg = raw_input('Please give the latitudinal coordinate, degrees.minutes.seconds.hemisphere:
').split('.');
    degx = int(deg[0]) + (float(deg[1]) + (float(deg[2] + "." + deg[3])/60))/60

    if deg[4] == 'S':
        degx = -degx

    deg2 = raw_input('Please give the longitudinal coordinate, degrees.minutes.seconds:
').split('.');
    deg2x = int(deg2[0]) + (float(deg2[1]) + (float(deg2[2] + "." + deg2[3])/60))/60
    if deg2[4] == 'W':
        deg2x = -deg2x
    print degx, deg2x
    endx.append(degx)
    endy.append(deg2x)

    i = raw_input('Would you like to input another set of points? Y=1/N=0: ');
    i = int(i)
    j = j+1;

for i in range(0,j):
    path_x, path_y = getCartesian(39.9535, -75.1916388889, endx[i],endy[i])
    pathx.append(path_x)
    pathy.append(path_y)

```

```

lineno = -1
distance = 100

while b < j:
    while distance > 5:
        lineno = lineno + 1
        line = gpsfile.readline()
        linesplit = line.split(',')
        if line == "": break
        line = line.strip()
        id = line[0:6]
        (line,checksum) = (line[0:-3],line[-2:])
        if id == '$GPGGA' and linesplit[4] != "":

            dy.data.set_float(dyspeed, 1 ,0);
            dy.network.push("penn6.gait.speed" );

            data = gpgga(line)
            latgga.append(data[0])
            longga.append(data[1])
            quality.append(data[2])
            satnum.append(data[3])
            coordinate = [data[0], data[1]]
            coordinates.append(coordinate)

```

```

ex, ey = getCartesian(39.9535, -75.1916388889, data[0], data[1])
dxx.append(ex)
dyx.append(ey)

if len(dyx) > 1:
    delta_y = dyx[len(dyx)-1] - dyx[len(dyx) - 2]
    delta_x = dxx[len(dxx)-1] - dxx[len(dxx) - 2]
    theta = math.atan2(delta_y,delta_x)
    thetax = theta*180/math.pi
    thetastar = math.atan2(pathy[b] - dyx[len(dyx)-1],pathx[b] - dxx[len(dxx) - 1])
    thetastarx = thetastar*180/math.pi
    diff = (((thetastar - theta)+math.pi)%(2*math.pi)) - math.pi

    print thetax, thetastarx
    if diff > 0:
        print "turn left!"
        dy.data.set_float(dyturn,-1,0)
        dy.network.push("penn6.gait.turn");

    elif diff < 0:
        print "turn right!"
        dy.data.set_float(dyturn,1,0)
        dy.network.push("penn6.gait.turn");

```

```
distance = math.sqrt((pathx[b] - dxx[len(dxx)-1])**2 + (pathy[b] - dyx[len(dyx)-
1])**2)
print distance

print "Target Reached!"

b = b+1
if b + 1 > j:
    dy.signal.send('sit_start')
    break

distance = math.sqrt((pathx[b] - dxx[len(dxx)-1])**2 + (pathy[b] - dyx[len(dyx)-1])**2)
print distance
gpsfile.close();
```

## **PEDIATRIC PHYSICAL ACTIVITY DYNAMOMETER**

NSF Summer Undergraduate Fellowship in Sensor Technologies

Katherine Gerasimowicz (Bioengineering) – University of Pennsylvania

Advisors: Dr. Jay N. Zemel, Dr. Babette Zemel

### **ABSTRACT**

Developing strong bones early in life reduces the risk of osteoporosis in the future. Various types of physical activity have been reported to produce osteogenic effects in children. However, current tools used in bone development research are unable to provide convenient and accurate measurements of the loads experienced in long bones throughout a child's regular daily physical activity. We have devised an inconspicuous system that can be embedded in a child's shoe to monitor and store force measurements during the course of a child's normal wakened activity. This in-shoe physical activity dynamometer, Foot-PAD, has been in development since the summer of 2004. The last model prior to the current research consisted of a circuit that amplified and converted electrical signals from polyvinylidene fluoride (PVDF) piezoelectric film sensors into digital force measurements. PVDF sensors are most sensitive to horizontal forces along the surface of the foot rather than forces directly transmitted to the foot. Repeated efforts to convert the normal force to a horizontal force were unsuccessful in the past. The Emfit Ltd. piezoelectret sensor has been developed with similar charge displacement properties but with the ability to measure vertical forces. The primary accomplishment of this development phase, therefore, was the incorporation of piezoelectret sensors into the system and appropriate modification of the circuit design. Tests with a custom-made mechanical testing device and squat jumps confirmed that the piezoelectret sensor could accurately measure vertical forces.

## 1. INTRODUCTION

Osteoporosis is a disease in which bone deteriorates and becomes porous, leading to decreased bone mass and significantly high risk of fracture. Approximately 55% of Americans fifty and older either have or are at severe risk of developing the disease [1]. However, because childhood is a time of rapid growth and peak bone mass is achieved by age twenty, developing strong bones early in life reduces the risk of osteoporosis in the future [2].

Because load-bearing bones are exposed to a significant amount of force from muscle contractions during physical activity, many researchers have studied the relationships between exercise and bone development. One of the hypotheses formed from this area of research is the Mechanostat hypothesis, which states that increasing maximal muscle contraction force from increased loading will have significant effects on bone size and strength [3-6]. Supporters of the Mechanostat hypothesis propose that the mechanical forces to which the bone is exposed ultimately determine its composition and strength.

Various longitudinal studies in children have reported that osteogenic effects vary based on the type of activity. Blimkie et al. and Nichols et al. found that increases in bone mineral content and bone mineral density were not significantly different from controls when examining the effects of resistance training in teenage girls [7, 8]. These resistance training exercises included bicep curl, bench press, triceps press, shoulder press, knee extension, and knee flexion. However, Morris et al. conducted an exercise program involving high-impact activity such as running and jumping in addition to resistance training in ten year old girls and found significant increases in bone geometry and strength compared to controls [9]. Jumping interventions in particular have also reported more substantial effects in increasing bone strength [10] and bone mineral density, even when compared to controls performing other exercise regimens [11, 12].

Although high-impact activity appears to be beneficial for bone development, it is necessary to further characterize the loads experienced in different weight-bearing activities. An ideal way to evaluate different types of activity would be to directly assess the forces experienced in bones during regular daily physical activity. Such measurements would allow researchers to determine an exercise regimen, as well as the intensity and frequency of exercise, which will best improve bone strength. However, the current tools used in bone development research cannot obtain these measurements. Physical activity surveys are highly subjective and only provide an average

measure of the intensity of an activity. A stationary force plate, while extremely accurate, can only take single measurements and provide discrete, occasional observations such as impact after a squat jump. An accelerometer, while mobile, only measures the magnitude and rate of body motion but does not capture the loading of long bones of the legs.

## 2. BACKGROUND

The development of an in-shoe physical activity dynamometer, Foot-PAD, began during the SUNFEST program in 2004 and continued with various senior design teams and SUNFEST Fellows through the summer of 2007. The last model prior to the current research consisted of two polyvinylidene fluoride (PVDF) sensors connected to a 1.25" × 1.265" printed circuit board (PCB) with a 3.3V lithium battery, an instrumentation amplifier, a microcontroller, and flash memory. The sensors were positioned in the ball and heel of a shoe and mounted on small springs. During each step, currents were generated, amplified, converted to digital signals, and processed to obtain peak force, average force, and duration of every step.

PVDF is a piezoelectric polymer film in which an electric potential is produced after the application of a mechanical force. When the film is bent, charges shift to the surface, generating a current (I) proportional to the strain along the horizontal axis. The charge displacement can be described by the following equation:

$$Q_z = d_{zx} \cdot F_x \quad (\text{Eq. 1})$$

$Q_z$  is the charge displaced across the planar surface,  $d_{zx}$  is the piezo stress tensor coefficient, and  $F_x$  is the force along the x-axis (Figure 1). The disadvantage of using PVDF sensors is that applying a compressive force in the thickness direction does not generate a strong current across the two surfaces. Due to the major tensor component, current can only be detected across the two surfaces if the sensor is bent, but integrating the current ( $I = dQ/dt$ ) produces a measure of the force applied along the horizontal axis rather than the force directly transmitted to the child's foot. Several attempts were made to normalize measurements from PVDF sensors, but no reproducible measurements could be obtained.

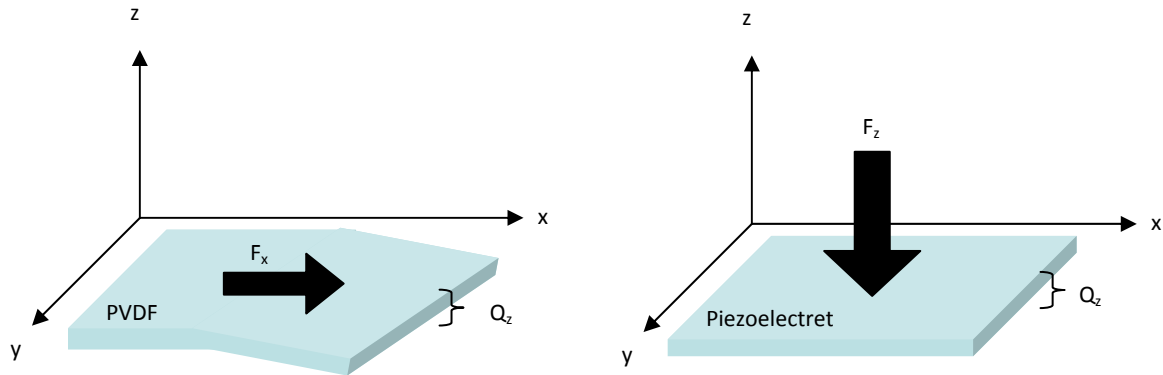


**Figure 1 (left):** PVDF sensor force-charge relation; **(right):** Piezoelectret sensor force-charge relation.

Emfit Ltd. has designed a new piezoelectret sensor, a film with permanently induced dipoles across small air voids [13]. When a force is applied to the film, the air voids compress, causing polar charges to rearrange and induce a current. The fundamental difference between the piezoelectret and the PVDF sensors is that the charge displacement in the piezoelectret film is governed by the equation:

$$Q_z = d_{zz} \cdot F_z \quad (\text{Eq. 2})$$

In this equation,  $d_{zz}$  is the piezo stress tensor coefficient, and  $F_z$  is the force along the z-axis (Figure 1). Unlike in PVDF, the charge displacement is controlled to be entirely in the z-direction. Charges are oriented on opposite surfaces of the air voids, and a compressive force in the thickness direction compresses the voids, drawing the charges closer together without causing them to spread in the horizontal direction (Figure 2). A force in the thickness direction would generate a signal, as is the case with force plates currently in use. Thus, the piezoelectret sensor would directly measure the impulse exerted on a child's load-bearing bones.

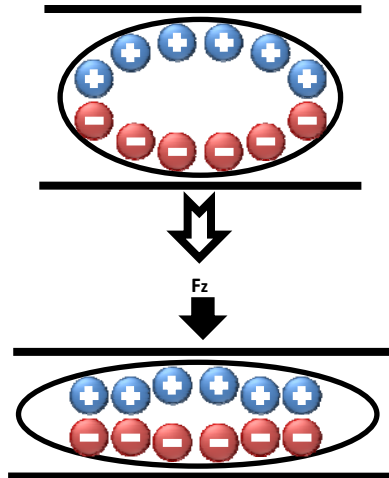


**Figure 2:** Air voids within the piezoelectret prevent charges from spreading in the horizontal direction, thus limiting charge displacement to the z-direction.

### 3. GOALS

An ideal measurement system should have the accuracy of a force plate but should also be conveniently transported. To better understand the effects of physical activity on bone development in children, we have devised the elements of an inconspicuous system that can be embedded in a child's shoe to monitor and store data during the course of a child's normal wakened activity.

Our ultimate goal is to develop a complete, mobile, free-standing force plate device (Foot-PAD) which may be used by Dr. Babette Zemel, the Director of the Nutrition and Growth Laboratory at the Children's Hospital of Philadelphia, in her studies of forces on child bone development.

The following improvements were made in the Foot-PAD device so that data could be collected from healthy children:

1. Designing and incorporating piezoelectret sensors into the Foot-PAD device

2. Finding a suitable battery to power the system
3. Constructing a device to apply periodic loads to test the piezoelectret sensors
4. Confirming that vertical forces could be measured during physical activity.

## **4. FOOT-PAD DESIGN**

Modifications were made to the last PCB design in order to replace the PVDF sensors with piezoelectret sensors. Furthermore, because Foot-PAD needs to be unobtrusive and obtain measurements for an extended period of time, improvements were continuously made to the PCB design to make it more compact and consume as little battery power as possible.

### **4.1 Overview**

A schematic of the various components and connections within the Foot-PAD device is shown in Appendix A. Two piezoelectret sensors are inserted in a shoe to measure impulses in the ball and heel of the foot. The sensors generate a current proportional to the applied force and are loaded with shunt resistors to generate a voltage signal. The voltage signal is then inputted into and amplified by an instrumentation amplifier. The output from the instrumentation amplifier is transmitted to the microcontroller's analog-to-digital converter (ADC) to be converted to digital signals and processed to obtain peak force, average force, time, and time duration of a step. The digital information is then written to a flash memory and can be transferred to a computer through a USB-to-serial connection for data analysis.

### **4.2 Piezoelectret Sensor**

The inability to obtain accurate measurements of downward forces from PVDF sensors in previous versions of Foot-PAD led to the implementation of piezoelectret sensors. The fundamental mechanical and charge displacement properties of piezoelectret sensors were discussed in Section 2. The structure of the film, the calculations performed to obtain force measurements, and the new sensor design are detailed in Sections 4.2.1, 4.2.2, and 4.2.3.

### 4.2.1 Structure of the Emfit Film

The piezoelectret sensor selected for the Foot-PAD is the Emfit Ltd. Ferro-Electret Film (Figure 3). Emfit manufactures the piezoelectret by biaxially stretching layers of polyolefin polymer into a film approximately 65 – 80  $\mu\text{m}$  in thickness. Air voids are made by compounding small particles and swelling the film through a high-pressure gas-diffusion-expansion process. The air voids are charged through the process of corona charging, in which a high electric field is applied across the material. The film is then coated with an aluminum-polyester laminate and laminated.

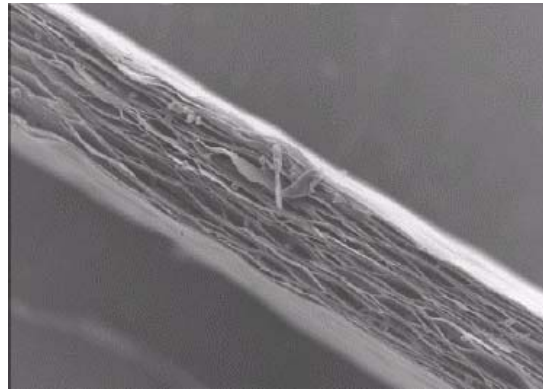


**Figure 3:** Emfit Ferro-Electret Film as captured by a scanning electron microscope. Layers of polyolefin have been swelled to form many small air voids inside of the film [13].

### 4.2.2 Force Calculations

Because charge displacement is limited to the space in between the air voids, the force-charge relationship in the piezoelectret film becomes Eq. 2. A current is produced from the piezoelectret film in response to the application of a force over a period of time. The current is then converted into a voltage by loading the sensor with a shunt resistor. Therefore, the output from the

piezoelectret sensor becomes:

$$V(t) = R_{shunt} \cdot \frac{dQ_z(t)}{dt} = R_{shunt} \cdot d_{zz} \cdot g(Area) \cdot \frac{dF_z(t)}{dt} \quad (\text{Eq. 3})$$

The first relationship is a statement of Ohm's Law. Because  $Q_z \propto F_z$ , the current is proportional to the impulse, or change in force over time. The major tensor component, shunt resistance, and the area of the sensor are also included as constants in the force-charge relationship. Thus, a measurement of the force can be obtained by integrating the voltage:

$$\int_{t_{start}}^{t_{end}} V(t) dt = R_{shunt} \cdot d_{zz} \cdot g(Area) \cdot \int_{t_{start}}^{t_{end}} \frac{dF_z(t)}{dt} dt \quad (\text{Eq. 4})$$

### 4.2.3 Sensor Design

Two samples of piezoelectret material were purchased from Emfit Ltd. (Figure 4). The circular region had a diameter of 1.49 cm and the long strip was 21.64 cm  $\times$  0.346 cm. The total area of the sample sensor was approximately 9.23 cm<sup>2</sup>. The sensors could be placed under the lining of a shoe and still be connected to the PCB or a breadboard, and thus were a convenient length to perform testing.



**Figure 4:** Sample piezoelectret sensor used in tests.

An appropriate output for the ADC was generated when the sensor was loaded with a 10 K $\Omega$  shunt resistor and a gain resistor of 3 K $\Omega$  was used in the instrumentation amplifier. (Refer to

Section 4.3.2 for the experimental protocol used to determine these resistances.) With such a small area, a high-value shunt resistor needed to be used for the voltage signal to have detectable amplitude. However, due to the high resistance, the output signal contained noise with a peak-to-peak of 156.25 mV (+ 93.75 mV and -62.5 mV from ground). Later testing showed that this noise was not significant and a signal could still be detected.

Larger sensors were cut from a sheet of Emfit material provided by Dr. M. Thompson of MSI Inc. (Figure 5). Two sensors were designed in the shape of the ball and heel of a shoeprint to ensure that forces could be measured across the entire ball and heel of the foot, including the toes. The sensors were designed to be placed under the inner lining in a Women's size 7.5 right athletic shoe. A 1.5" strip from the back of the heel sensor and a 3" strip from the back of the ball sensor were also cut in order to make a connection between the sensors and the PCB.



**Figure 5:** Two larger area piezoelectret sensors to be incorporated into the Foot-PAD device.

### 4.3 Instrumentation Amplifier

The instrumentation amplifier chosen for the Foot-PAD device was the INA2126 from Burr-Brown Products of Texas Instruments, Inc. The INA2126 contains two op-amps, and thus has the ability to amplify the signal from each piezoelectret sensor separately. Each op-amp has an adjustable gain which can be set with external gain resistors according to the equation:

$$Gain = 5 + \frac{80k\Omega}{R_G} \quad (\text{Eq. 5})$$

$R_G$  is the resistance of the gain resistor [14]. In addition to amplifying the signal, the INA2126 can also generate an output relative to a reference voltage. Because the input voltage to the microcontroller must be positive, a voltage of +1.25 V was supplied to the INA2126 to ensure a nonnegative output. The INA2126 operates between a voltage of +1.35 V and +18 V, which is suitable for the lithium ion battery selected to power the Foot-PAD.

The INA2126 has also been laser trimmed to have a low voltage offset drift. This property is critical for the Foot-PAD, because any voltage drift in the signal would cause force measurements to rise or fall infinitely far after integration (Eq. 4). In order to confirm that there would be an insignificant amount of drift in the signal, I stood on the sensor for 500 seconds, the maximum amount of time that measurements could be captured on the oscilloscope. When comparing the beginning and end of the signal, no drift could be detected.

#### **4.3.1 Modification of INA2126 Circuitry**

Additional modifications were made to the circuitry to generate a suitable (i.e. non-saturated) output from the instrumentation amplifier. Because the INA2126 has a high input impedance, a bias current path consisting of two 50 K $\Omega$  resistors was placed across the inputs to prevent them from floating to too high of a potential and saturating the output. The return path also needed to be directed to the reference voltage, rather than to the ground, in order for the system to operate with a single supply voltage.

#### **4.3.2 Selection of Gain Resistor**

The INA2126 can amplify signals with gains as low as 5 and as high as 10000. Thus, any resistance between  $\sim 8\Omega$  and infinity (i.e. no gain resistor) may be selected as an external gain resistor. However, because the maximum voltage which can be outputted from the INA2126 is +2.25 V (0.75 V less than  $V_+$  or the positive supply voltage of 3 V), an appropriate gain is

needed to ensure that the output of the instrumentation amplifier has a significantly greater amplitude than the noise without saturating the signal.

Breadboard tests with the INA2126 and the sensor were conducted to find optimal shunt and gain resistors. For the original sample sensor, three types of shunt resistors—10 K $\Omega$ , 100 K $\Omega$ , & 1 M $\Omega$ —were tested with different gain resistors ranging from 1 K $\Omega$  to 77 K $\Omega$  (gain between 6 and 85). The circular region of the sensor was securely positioned under the lining of a shoe in the heel. The long strip was wound behind the heel and out of the shoe to be connected to the breadboard circuit. The shoe was worn and forces were applied to the sensor in two ways: (1) applying weight to the right leg three times and stomping on the sensor three times, and (2) marching three times and then hopping once. As stated previously, a 10 K $\Omega$  shunt resistor and a 3 K $\Omega$  gain resistor (gain = 31.67) produced a suitable output.

In the future, the same tests should be repeated for the new sensors. An electronic scale should also be used to monitor and control the amount of weight applied to the new sensors. Furthermore, because the areas of the new sensors differed, these tests should be performed in both the ball and heel of the foot.

#### **4.4 Microcontroller**

The Foot-PAD also has a PIC18F14K50 20-pin USB microcontroller from Microchip Technology Inc. The PIC operates at up to +5.5 V as well as +3 V (single-supply) for in-circuit serial programming. Two of the nine channels which function as ADC's with 10-bit resolution receive and process the outputs from the instrumentation amplifier. The PIC is capable of long-term storage of program data with 256 bytes of EEPROM (electrically erasable programmable read-only memory). The microcontroller functions in SPI mode, which allows 8 bits of data to be transferred to and received from the flash memory simultaneously through the serial clock, serial data out (SDO), and serial data in (SDI) in pins 11, 9, and 13, respectively. The Enhanced Universal Synchronous Asynchronous Receiver Transmitter (EUSART) allows the microcontroller to communicate with a computer via RS-232 protocol through the input pin Rx and the output pin Tx (pins 12 and 14, respectively).

#### **4.5 Flash Memory**

The M25P16 16 Mbit serial flash memory from Numonyx was incorporated into the PCB design. It operates on a single supply voltage between 2.7 and 3.6 V and can draw up to 15 mA of current. The M25P16 communicates with the microcontroller through SDO, SDI, and the serial clock (pins 2, 5, and 6, respectively). The flash memory also has a chip select mechanism (connected to PIC pin 8 from pin 1) which controls whether the flash memory is powered, in standby, or powered down. A major improvement in its design is that bulk erase can be completed in approximately 13 seconds at 10 mA. Therefore in addition to its reduced size, this flash memory draws significantly less current than the previous flash memory, which required 25 mA of current to erase. The M25P16 is therefore better able to preserve battery life of the Foot-PAD.

#### **4.6 Battery**

The UltraLife U10007 Thin Cell is the optimal battery to power the Foot-PAD device. Measuring merely 3.88 cm × 3.14 cm and only 1.91 mm in thickness, it is small enough to be placed on top of or alongside the PCB. The U10007 Thin Cell has a voltage range of 1.5 V to 3.3 V, with an average voltage of 3 V. The maximum discharge is 25 mA, which is far greater than the maximum amount of current needed to erase the flash memory. Most importantly, the specifications sheet indicates that battery can operate at 6 mA to 1.5 V for 400 mAh. For the Foot-PAD device, the U10007 Thin Cell will be able to provide power for ideally 36 hours—greater than the length of time set in the project goals.

#### **4.7 Final Printed Circuit Board**

The prototype was milled on the T-Tech 5000 CNC milling machine according to the schematics in Figure 6. It was then populated with the surface-mount technology components described in the previous sections. The single pinheads are used to connect to the battery, and the sensors plug into the dual pinheads. The final populated PCB is shown in Figure 7. Due to the small size of the PCB (Figure 8), it took a significant amount of time to ensure that all connections were correct and that there were no shorts across the PCB.

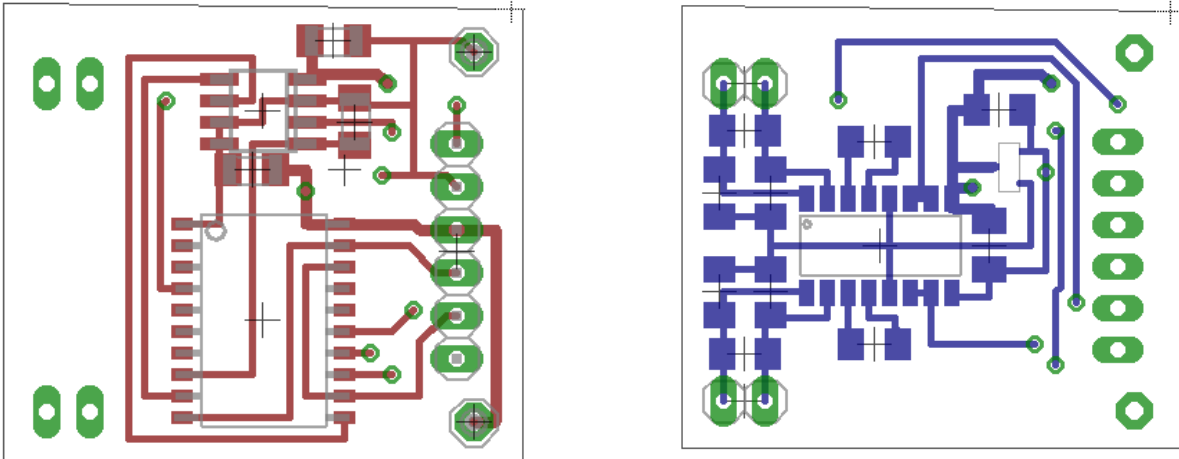


**Figure 6 (left):** Top view of PCB showing wires, pinhead locations, and components; **(right):** Bottom view of PCB showing wires, pinhead locations, and components.

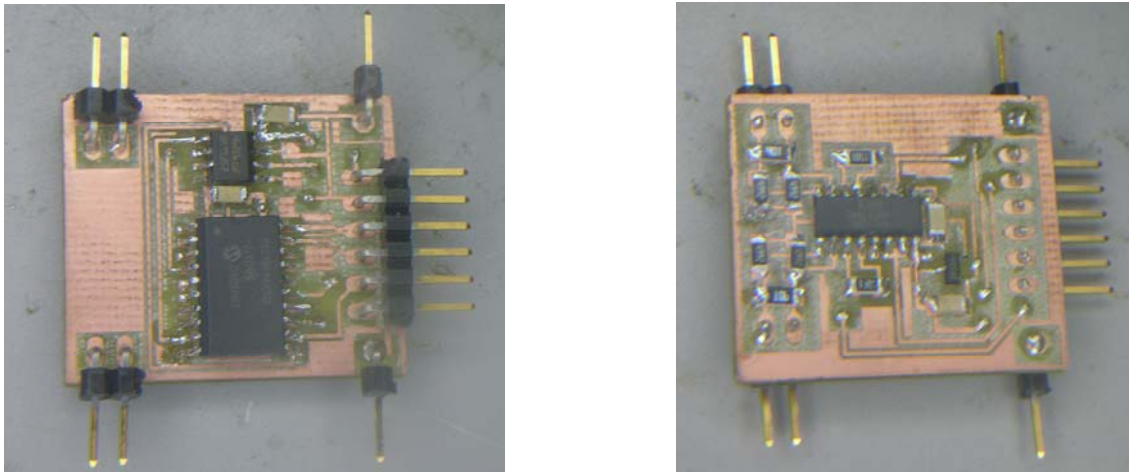


**Figure 7 (left):** Top of populated PCB with flash memory (top chip) and microcontroller (bottom chip); **(right):** Bottom of populated PCB with instrumentation amplifier.

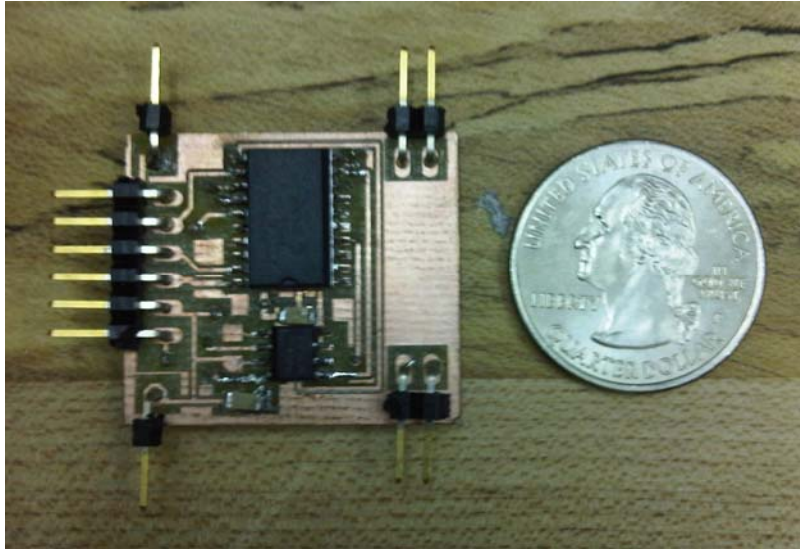


**Figure 8:** Comparison of Foot-PAD with quarter to demonstrate its small size.

#### **4.8 Inserting Device Inside a Shoe**

After populating the circuit and conducting mechanical testing, the device was placed inside a Women's size 7.5 right shoe (Figure 9). The heel was cut open to a depth of 0.325", with a sufficient amount of room to insert the PCB. The PCB was coated with adhesive to protect the components. Although not shown in the figure, wires extended from the single pinheads on the PCB to the battery, which rested in front of the PCB. Wires also extended from the battery through the top of the shoe to a switch which turned the device on and off. A ribbon wire connector was also designed to plug into the USB-to-serial connection and wind through the back lining of the shoe, as shown in Figure 9. The sensors were directed from the sole of the shoe to the top of the sole and taped underneath the lining. When the lining was placed back inside of the shoe, no parts of the device protruded or provided significant discomfort to the wearer.

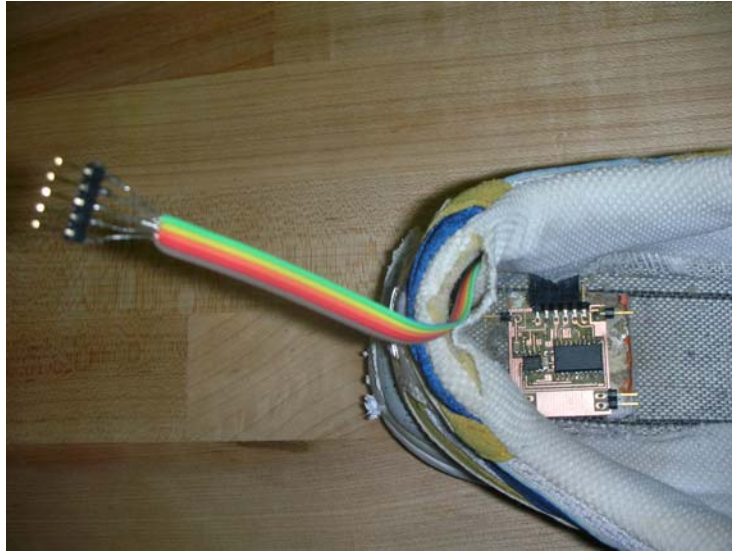


**Figure 9:** Foot-PAD device inside the sole of a shoe.

## **5. TESTING THE PIEZOELECTRET SENSOR**

After the PCB was completed, two tests were conducted with the Foot-PAD in order to assess whether the piezoelectret could accurately measure vertical forces. First, a constant, light load was applied periodically to the sensor through a mechanical testing device. Next, the sensor was placed under the lining of a shoe and I performed a squat jump, an example of a high impact activity which the sensor will later be used to measure.

### **5.1 Designing a Mechanical Testing Device**

A previous SUNFEST Fellow had designed a sensor calibration device for the Foot-PAD [15]. A pulley system controlled by a clock motor periodically lifted and dropped a mass of 21.5 pounds connected to a tubular instrument scale. This device gave reproducible signals when testing PVDF, but it was later misplaced. A simpler mechanical testing device was designed instead for testing the piezoelectret.

The new device consisted of a Dremel drill press and two cylindrical blocks (Figure 10). A cylindrical aluminum block was inserted into the top of the drill press and held in place with a small rectangular block. A small cylindrical block rested loosely on top of a stiff piece of foam. During testing, the sensor was placed in between the cylindrical block and the foam. The top cylinder was lowered directly into the center of the loose cylindrical block. The foam acted as a spring and allowed a gradual application of the force due to its elasticity. The amount of load applied was easily controlled by the lever of the Dremel drill press.



**Figure 10 (left):** Front view of mechanical testing device; **(right):** Side view of mechanical testing device.

This device could generate reproducible measurements, but should not be considered a calibrator because it did not have the same accuracy and level of control as the sensor calibrator. In addition to variations in the way the lever was pulled, occasionally the rectangular block would shift out of place when the load was applied. More accurate sensor calibration will need to be conducted in the future with a higher accuracy device such as a force plate.

Because a small weight was applied to the sensor during testing, a 1 M $\Omega$  shunt resistor was soldered to the PCB so a sufficiently large voltage signal would be generated. The gain across the instrumentation amplifier was kept at 31.67.

## 5.2 Mechanical Device Test Results

The output from the mechanical testing device is shown in Figure 11. The voltage output from the PCB is the impulse (Eq. 3) and the force was obtained by integrating the voltage (Eq. 4). Typically after integration, the signal drifted significantly upward or downward. The offset drift was calculated by dividing the final voltage value by the final time and was subtracted from the raw data during integration. After removing the offset drift, the average force signal was centered around zero.

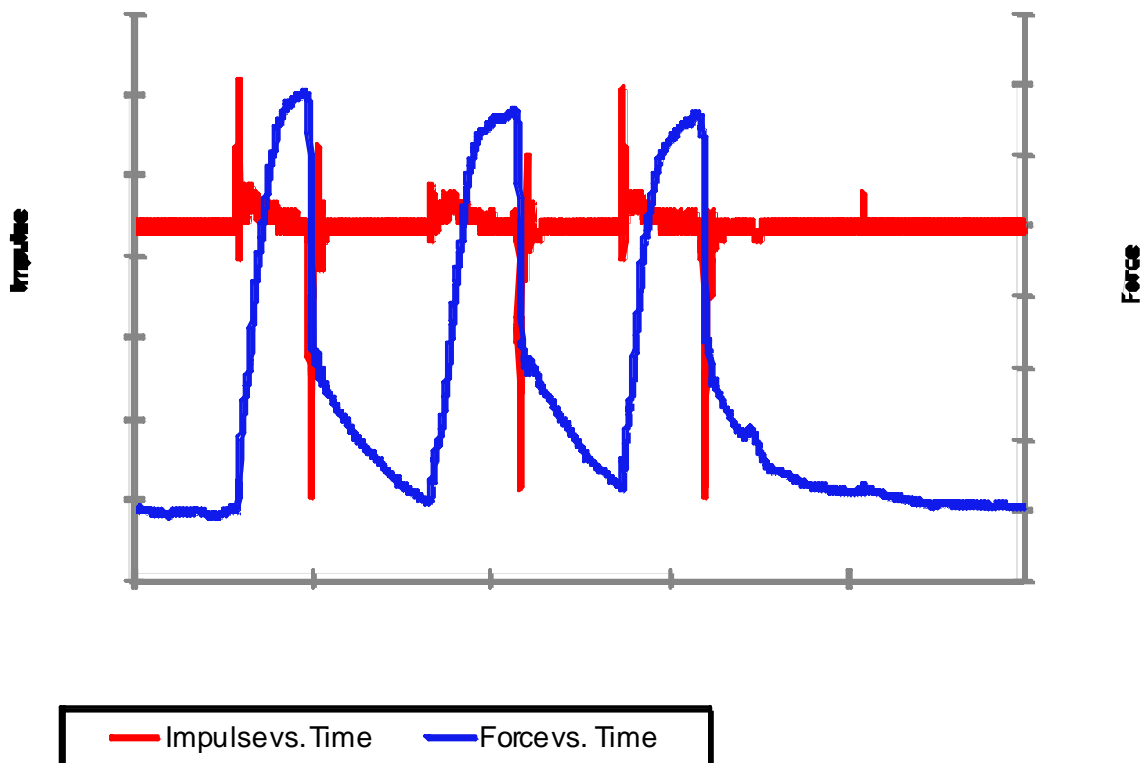


**Figure 11:** Impulse and force measurements from sensor in mechanical testing device.

In the impulse vs. time plot, a positive signal was generated when the sensor was in compression as the weight was being applied. Conversely, a negative signal was produced when the weight was released and the film stretched back to its natural thickness. During testing, the lever was pulled down slowly and the weight was gradually applied to the sensor. The lever was then instantly released rather than slowly being lifted up. This difference in the rate at which the force was applied and removed was reflected in the impulse vs. time plot, which showed a negative peak with a greater magnitude than the positive peak.

In the force vs. time plot, the force increased and decreased with the positive and negative impulse peaks. The force was initially zero and rose quickly to a positive value. Then the force remained at approximately the same magnitude as the weight was in contact with the sensor. The force tapered off more gradually to zero as the foam the sensor was attached to deformed back to its natural state. The most significant feature of the force vs. time plot was that the maximum force and duration of force was approximately the same each time the force was applied to the sensor.

The results from the mechanical device test confirmed not only that reproducible measurements could be obtained from the device, but also that the piezoelectret sensor is able to detect constant, vertical forces.

### **5.3 Physical Activity Test Results**

To assess whether the piezoelectret would generate appropriate outputs during physical activity, squat jumps were performed while the sensor was placed underneath the lining of a shoe in either the heel or the ball of the foot. Wires were directed from the sensor to the PCB, which was held in a vice grip outside of the shoe. The squat jump was selected because it is frequently performed in force plate tests to assess forces in high impact physical activity.

The results from the physical activity tests are shown in Figure 12. Both the impulse and force plots are very comparable to the mechanical device test. The positive impulse peaks have a lower magnitude than the negative impulse peaks because the rate at which force is applied to the sensor during a squat is far less than the rate at which force is applied when springing up to jump.

The sensor also successfully detected the forces in each jump. When the sensor was placed in the ball of the foot, I jumped to a lower height on the first jump and, therefore, exerted less force. The fact that the jump required less force is reflected in the lower magnitude peak in Figure 11. The rest of the jumps were all taken to maximal height and, most importantly, all of the force measurements have approximately the same magnitude. Therefore, the sensor can be positioned in either the ball or heel of the foot because the sensor will be able to quantify the forces transmitted to the load-bearing bones in either location.

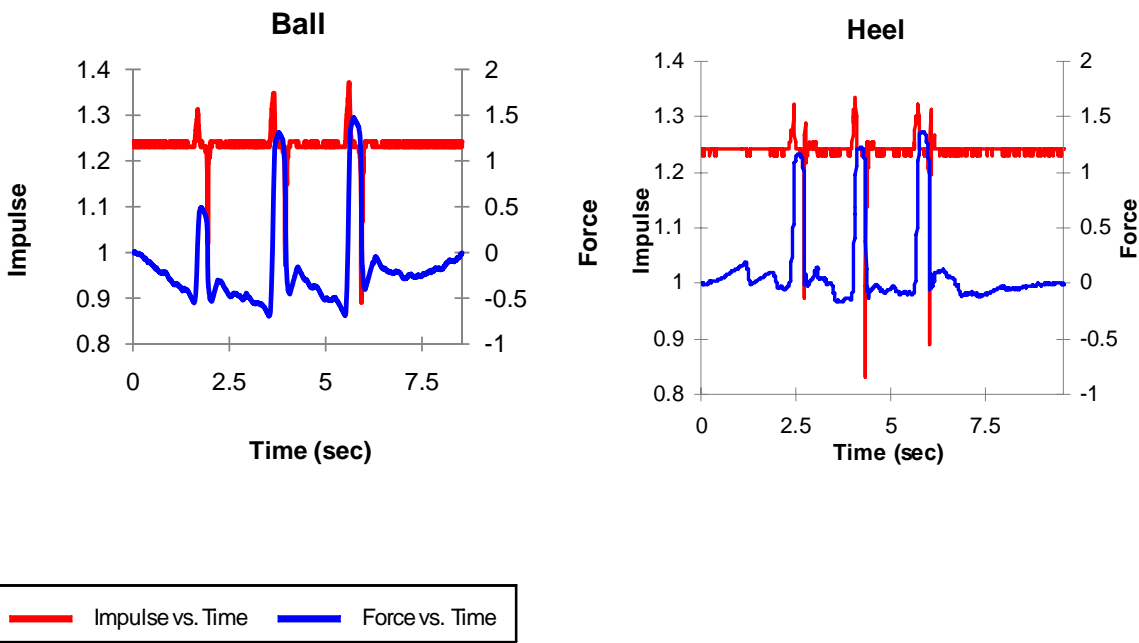


**Figure 12 (left):** Impulse vs. Time and Force vs. Time plots from ball of foot during squat jumps; **(right):** Impulse vs. Time and Force vs. Time plots from heel during squat jumps.

## 6. CONCLUSIONS

For the first time since the start of the project in 2004, the Foot-PAD device was able to measure the forces transmitted to the feet and load-bearing bones. The most significant improvement in the Foot-PAD device was the replacement of PVDF piezoelectric sensors limited to measuring

horizontal forces with piezoelectret sensors capable of measuring vertical forces. Tests on the piezoelectret sensor confirmed that these sensors could measure vertical forces during high impact activity. Furthermore, a complete prototype of the Foot-PAD device, including the new sensor and battery, was built during the summer and will serve as the fundamental design for the device. The device will only require minor improvements in the future before it can be used in clinical research to obtain data from children during physical activity.

## **7. RECOMMENDATIONS**

### **7.1 Incorporating System into Shoe**

The Foot-PAD was inserted into a shoe as described in Section 4.8. However, once the shoe was worn, data could not be collected or downloaded due to leakage in the PCB. The PCB also could not be repaired after it was removed from the shoe. Once a new PCB is milled and populated, more investigation will be needed to determine how best to coat the PCB and secure its connections so the PCB will work inside of the shoe. Furthermore, it may be beneficial to do more rubout or increase the dimensions of the PCB to prevent leakage and shorts.

### **7.2 Calibration with Force Plate**

As seen in Figures 11 and 12, the force measurements were not presented with units because integrating the voltage output does not directly give a force measurement. Other constants such as the shunt resistance, area of the sensor, and stress tensor coefficient must be factored into the calculations. To determine the proportionality constant between current and force, the sensors will need to be calibrated. A simple calibration device was previously designed for the PVDF sensors, but calibration with a Kistler force plate would be the most suitable since the Foot-PAD will ultimately function as a mobile force plate.

### **7.3 New Sensor Design**

As stated in Section 4.2.3, larger area sensors should be designed to measure forces across the entire ball and heel of the foot. Furthermore, although the signal could be easily detected with the original sensors, even less noise would be present in larger area sensors because a lower shunt resistance would be needed. A simple design in the shape of a shoe print was cut but not laminated. This shoe print design will need further testing to determine whether it is an optimal design and, if so, which shunt resistor and gain resistor would be needed to convert and amplify the sensor output.

#### **7.4 Logarithmic Amplifier**

A logarithmic amplifier might be better for the Foot-PAD than an instrumentation amplifier because low voltages could be easily detected without large voltages becoming saturated. However, most logarithmic amplifiers currently in the market operate on a single supply of +5 V. A TPS60241 zero-ripple switched cap buck-boost 2.7 V to 5.5 V input to 5 V output converter may be used to generate the +5 V necessary to operate the log amplifier from a +3V power supply. However, although these chips can receive inputs up to 10 mA, nonlinearity increases if currents rise above 3.5 mA. Logarithmic amplifiers currently in the market would not be suitable for Foot-PAD, although they should continue to be investigated in the future.

#### **7.5 Long-term Physical Activity Data Collection**

Data only needed to be collected for less than one minute to conduct the tests in Sections 5.2 and 5.3. The current system was unable to collect data for more than a few minutes. Adding a capacitor across the clock of the microcontroller and flash memory increased the length of time data collection occurred, but additional modifications may be needed in the hardware to collect data for an extended period of time. Once a final prototype of the Foot-PAD is created, it should be inserted inside of a shoe with a battery and worn for multiple hours. If data collection continues throughout the entire time and always produces accurate force measurements, the Foot-PAD is then ready to be inserted in children's size shoes and distributed to the Children's Hospital of Philadelphia. Children in various bone development studies will wear these shoes to measure forces during their daily activity.

## 8. ACKNOWLEDGEMENTS

I would like to thank my advisor, Dr. Jay Zemel, for his guidance throughout the course of the project, his willingness to thoroughly teach any concepts I was not clear on, and a few short and simple adages which I will always keep in mind throughout my research career. I would also like to thank my other advisor, Dr. Babette Zemel, for teaching me the necessary medical and biomechanics background for the project and the overall need for bone research. Thanks to Sanket Doshi who, even though this was not his project, helped me so much with coding and any issues with the electronics. Finally, thank you to Dr. Van der Spiegel and the SUNFEST staff for running this wonderful program, and to the National Science Foundation for their financial support.

## 9. REFERENCES

1. National Osteoporosis Foundation. *NOF – Bone Mass Measurement*. [Online]. Available: <http://www.nof.org/osteoporosis/diseasefacts.htm>.
2. International Osteoporosis Foundation. *Bone Development in Young People*. [Online]. Available: <http://www.iofbonehealth.org/patients-public/more-topics/bone-development-in-young-people.html>.
3. S. L. Bass, P. Eser, R. Daly, “The effect of exercise and nutrition on the mechanostat,” *J. Musculoskelet. Neuronal. Interact.*, vol. 5, no. 3, pp. 239 – 254, Apr. 2005.
4. F. Rauch, “Bone growth in length and width: the Yin and Yang of bone stability,” *J. Musculoskelet. Neuronal. Interact.*, vol. 5, no. 3: pp. 194 – 201, Apr. 2005.
5. F. Rauch, E. Schoenau, “The developing bone: slave or master of its cells and molecules?” *Pediatric Research*, vol. 50, no. 3: pp. 309 – 314, Jan. 2001.

6. E. Schoenau, "Muscular system is the driver of skeletal development," *Ann Nestlé*, vol. 64: pp. 55 – 61, 2006.
  
7. C. J. R. Blimkie, S. Rice, C. E. Webber, J. Martin, D. Levy, C. L. Gordon, "Effects of resistance training on bone mineral content and density in adolescent females," *Can. J. Physio. Pharmacol.*, vol. 74, pp. 1025 – 1033, Apr. 1996.
  
8. D. L. Nichols, C. F. Sanborn, A. M. Love, "Resistance training and bone mineral density in adolescent females," *J. Pediatr.*, vol. 139, pp. 494 – 500, Apr. 2001.
  
9. F. L. Morris, G. A. Naughton, J. L. Gibbs, J. S. Carlson, J. D. Wark, "Prospective ten-month exercise intervention in premenarcheal girls: positive effects on bone and lean mass," *J. Bone Miner. Res.*, vol. 12, pp. 1453 – 1462, Mar. 1997.
  
10. H. M. MacDonald, S. A. Kontulainen, K. M. Khan, H. A. McKay, "Is a school-based physical activity intervention effective for increasing tibial bone strength in boys and girls?" *J. Bone Miner. Res.*, vol. 22, pp. 434 – 446, Dec. 2006.
  
11. R. Fuchs, J. Bauer, C. Snow, "Jumping improves hip and lumbar spine bone mass in prepubescent children: a randomized controlled trial," *J. Bone Miner. Res.*, vol. 16, pp. 148 – 156, Aug. 2000.
  
12. H. A. McKay, M. A. Petit, R. W. Schutz, J. C. Prior, S. I. Barr, K. M. Khan, "Augmented trochanteric bone mineral density after modified physical education classes: a randomized school-based exercise intervention in prepubescent and early pubescent children," *J. Pediatr.*, vol. 136, pp. 156 – 162, Sept. 1999.
  
13. Emfit Ferro-Electret Film. [Online]. Available:  
[http://www.emfit.com/sensors/sensors\\_products/emfit-film/](http://www.emfit.com/sensors/sensors_products/emfit-film/).

14. INA2126 Datasheet pdf. [Online]. Available:  
[http://www.datasheetcatalog.com/datasheets\\_pdf/I/N/A/2/INA2126.shtml](http://www.datasheetcatalog.com/datasheets_pdf/I/N/A/2/INA2126.shtml).

15. O. Tsai, “Dynamometer—The New Activity Monitor,” SUNFEST 2004, Center for Sensor Technologies, University of Pennsylvania, 2004.



# **STABILITY CONTROL SYSTEM FOR THE BIOLOID HUMANOID ROBOT**

NSF Summer Undergraduate Fellowship in Sensor Technologies  
Willie W Gonzalez (EE) – University of Puerto Rico Mayagüez campus

Advisor: Dr. Daniel D. Lee

## **ABSTRACT**

A key characteristic in any autonomous system is stability. Without stability robots could not work properly. To achieve stability first the robot needs the means to know its position with respect with its original so that a correction in position can be obtained if necessary. This is true for the type of INS (inertial navigation system) known as dead reckoning. In this INS the current position of the robot or system is calculated from measurements of the acceleration and knowledge of its original position. Some IMUs (inertial navigational units) consist of a couple of accelerometers and gyroscopes. With this IMU acceleration can be obtained. On Strap-down navigational system, this IMU are directly attached to the system so that their measurements correlates with those of the system, so that they can be used to calculate the position of the system. Throughout this document a method on how to obtain the necessary measurements from the IMU and how to apply them, will be discuses.

## **1. Introduction**

The creation of autonomous robots is a task that many have undertaken for military, medical or other reasons. But no matter the reason, measurements of the position of the system relative to its environments are needed for it to act accordingly without an external intervention. A technique that humans have used to navigate through their environment is dead reckoning [1]. This approach consists of the calculation of current position with the use of the following: knowledge of an initial position, and measurements of speed and direction. The inertial navigation system (INS) uses an equivalent approach with the help of Newton's laws. These laws, which relate velocity, acceleration, and position, enable us to calculate the change in position. With knowledge of the position of a part of an autonomous system and some inverse kinematics, the position of every part of the system can be calculated. With this information an accurate displacement of each part can be achieved.

How do we obtain these measurements? To measure the acceleration of a body, inertial sensors are used: accelerometers and gyroscopes. The accelerometer is used to measure acceleration in a single direction. By placing three accelerometers orthogonally to each other we can sense the acceleration in any direction [2]. From the gyroscope we can obtain the angular velocity on a single axis. These two inertial sensors together can help to identify the change of position of a system. Inertial sensors are often attached to a fixed part of the vehicle or system so that the measurements that it senses are due to the system movement and not the movement of the sensor itself. This type of configuration is called Strap-down INS[1] Many types of this inertial sensor are well documented [3] but they come with some limitations: noise and drift on the measurement readings can disturb the outcome of the calculations.

This paper explores ways of eliminating or attenuating those limitations by using complementary filters. We created a control loop that used the readings of the IMU to allow the platform to return to its original position. Some application for this type of system could be a platform that holds a camera so that in case of undesired movements the camera continues filming in the same direction.

## **2. Background**

### **2.1 Inertial navigation system (INS)**

The inertial navigation system was first developed in the early 1950 by the Sperry Gyroscope Corp. Their objective was to be able to create a navigation system that did not require ground beacons. In time of wars these beacons can be jammed or destroyed [4]. Their main applications are in missile, aircraft, marine and land vehicles.

Inertial navigation systems used the force laws postulated by Isaac Newton to estimate the current position and orientation of an object [1]. Using force equations that relate angles, forces, velocity, position and acceleration, the current position and orientation of an object can be

determined. But before we are able to apply these equations we need to have devices that can measure the acceleration of the system and for that inertial sensors are needed.

Inertial sensors are external sensors that can measure the acceleration of a system and make almost no references to the external world. Inertial sensors are often used to refer to accelerometers and gyroscopes that can measure acceleration in a single axis and angular acceleration respectively. These types of sensors are commonly used in Strap-down INS.

## **2.2 Strap-down INS**

Strap-down INS are like any other INS; the difference is that instead of having a big platform holding the INS, the inertial measurement unit (IMU) is attached or strapped down to the system. This results in a lighter, smaller and cheaper Inertial Navigation System. But for this type of system to work more accurate sensors and higher computational equipment are needed [1]. Thanks to the advance in technology these needs have been satisfied.

## **2.3 Inertial measurement unit**

An IMU consists of the set of sensors that will be used in a certain application to retrieve the information needed to calculate the position and orientation of the body of a robot or any system. This project used the IDG300 gyroscope and the ADXL330 accelerometers IC's which are both located on the Inertia Measurement Unit developed by SPARK FUN

### **2.3.1 Gyroscope**

Gyroscope can sense the angular rate of turn or angular acceleration about a single axis. There are many types of gyroscope with different applications depending on the environment and the accuracy needed.

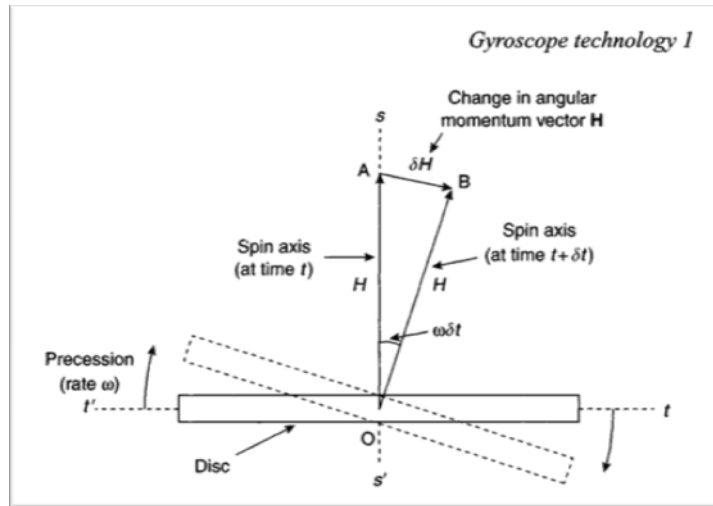


**Figure 10 Gyroscope technology [7]**

A component normal to the rotation axis appears, the precession  $\omega$ , to try to align the spin axis with the torque axis.  $T = \omega H$  where  $T$  (torque) and  $H$  (angular momentum) this is [5], also known as the gyroscope law. If a torque is applied to keep it's spin axis aligned with a direction then the measurement of this torque will provide the angular movement of the object to which the gyroscope is attach.

### 2.3.2 Accelerometer

Accelerometers allow the measurement of the acceleration on a single axis to be ascertainable thanks to Newton's second law  $F=ma$  where  $a$  could be represented as the sum of  $g$  (gravitational forces) and  $f$ , the acceleration produced by external forces of the object, thus  $a=g+f$ . Typically in NS there are three accelerometers orthogonal to each other to provide the acceleration reading in three different directions. It is not practical to use the entire mass of a system to determine its acceleration. Instead, a proof mass connected to a set of springs is used to measure the acceleration is found to be more efficient in discerning the acceleration. With the help of the Hook law  $F=x*k$  where  $k$  is a constant, a property of the spring and  $x$  it's the stretch displacement of the spring the acceleration of the object on a single axis can be measured. This is the simplest type of accelerometers there far more accurate and expensive accelerometers that involve technology such as Solid-state ferroelectric accelerometer and Solution electrolytic accelerometer [6].

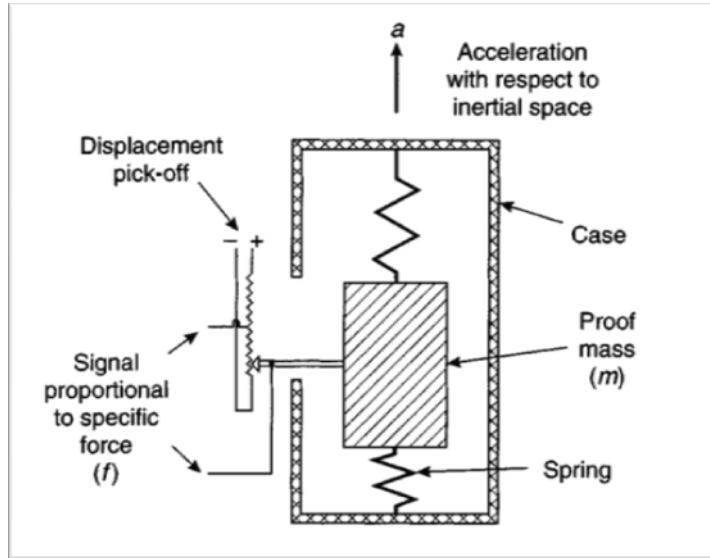


Figure 2 Accelerometer technology [8]

### 3. Calculation and application method

#### 3.1 Equations and approach

With both the accelerometer and the gyroscope, a displacement angle can be calculated using the following equations.

$$\theta \approx \int w(\text{angular rate}) dt$$

$$\theta \approx \sin^{-1} \left( \frac{\text{accel output}}{g} \right)$$

Both of the equation can be used to determine the angle but each one has a drawback. The first equation is not suited for long periods of time because it could cause saturation in your reading for its growth characteristic through time due to the integration, but it's excellent with fast movements in short period of time. The second equation doesn't have the problem of saturation but in fast movement the accelerometer output contain the acceleration of external forces and that can cause error in readings, but its preferable in calculations involving long periods of time and slows movements. We must attempt to obtain the beneficial information from each equation whilst eliminating the erroneous data found in each equation. For that a complementary filter can be used.

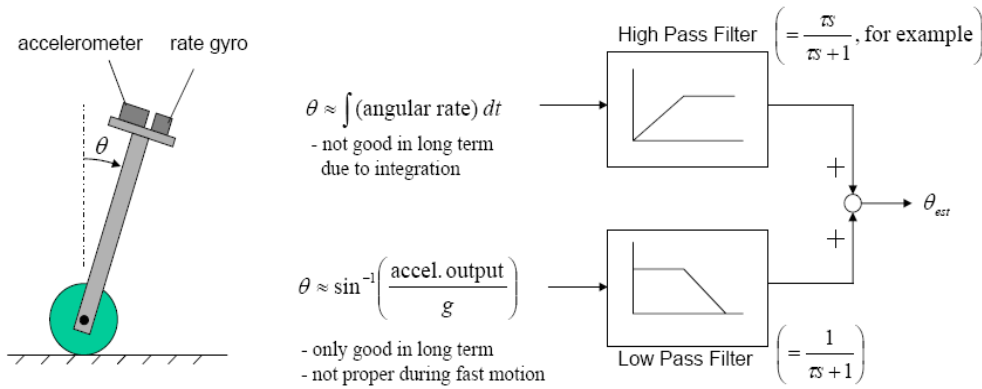


**Figure 3 Complementary filter [9]**

By passing the integration equation by a high pass filter we will obtain only the peaks in the graph of the integration representing the fast movement of the object in which the gyroscope is reliable and get rid of the saturation problem. When we pass the other equation through a low pass filter we will obtain only the measurements during last periods of times and get rid of momentary movement that can alter the readings for the accelerometer. Then by adding the two outputs of each filters the measurement of the accelerometers is going to be a bias reading and the gyroscope will then be the peaks that result from the fast movement, in other words, we have theoretically obtained the best of both reading and gotten rid of their drawbacks.

### 3.2 Complementary filter

A complementary filter consists of two filters, commonly a high pass and a low pass filter. If the sum of two filters in the phase is zero and the magnitude is one, they are complementary to each other. A good way to verify this is to pass some data through both filters and the sum should yield the original data. In other words, the original graph minus the sum should be zero.

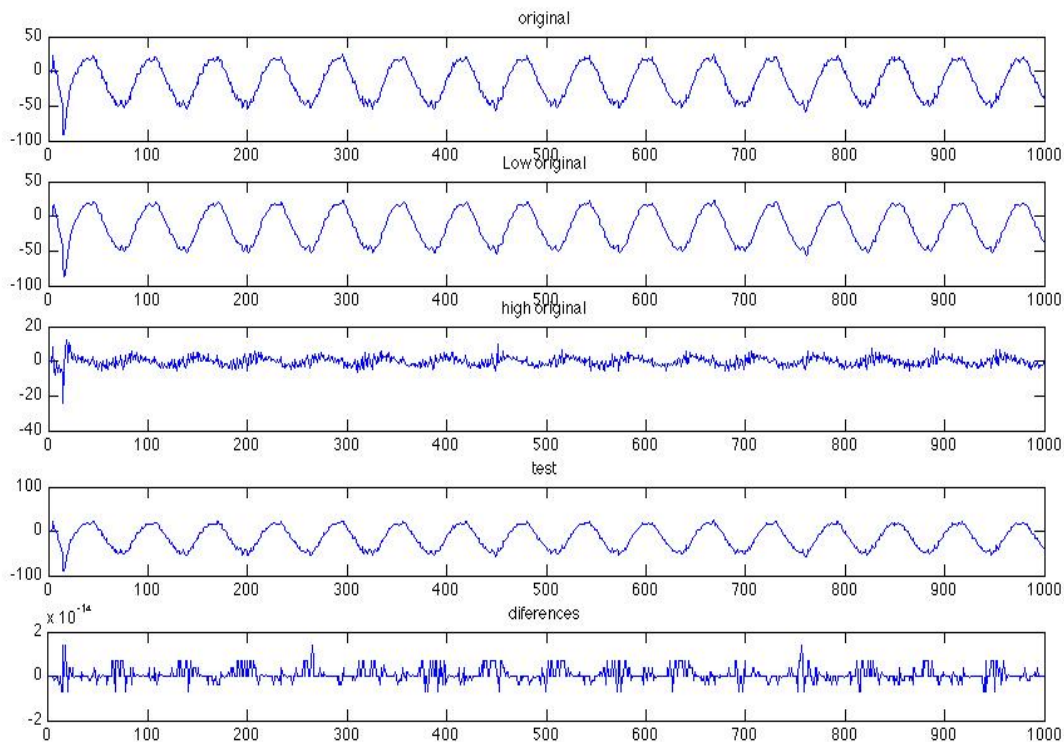
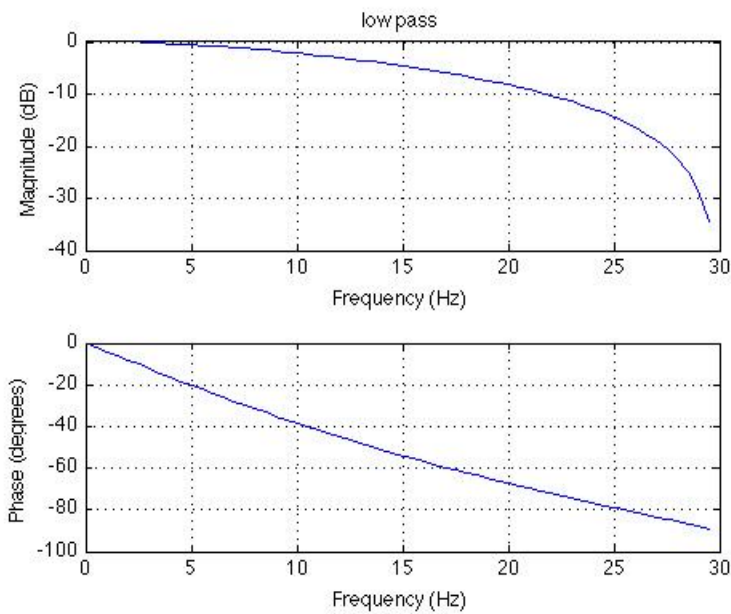


### Figure 4 Complementary Filter Corroboration

In Figure 4 the data retrieved from the accelerometer can be seen in the top of it. That data was filter through both high pass and low pass filters and their sum is graph in the third plot. The differences of the original and sum is in the order of  $10^{-14}$  which can be considered to be zero. The frequency of the complementary filter was not arbitrary chosen but was chosen after some test.



The first frequency to be chosen was 25% of the sampling rate for the low pass and the same for the high pass. The one yielding better result on the measurements was approximately %12.5 percent of the sampling rate. The sampling rate was around 60 HZ. Figure 5 shows the low pass filter.

Figure 5 Low pass

filters

### 3.3 Gyroscope and accelerometer before and after the filter

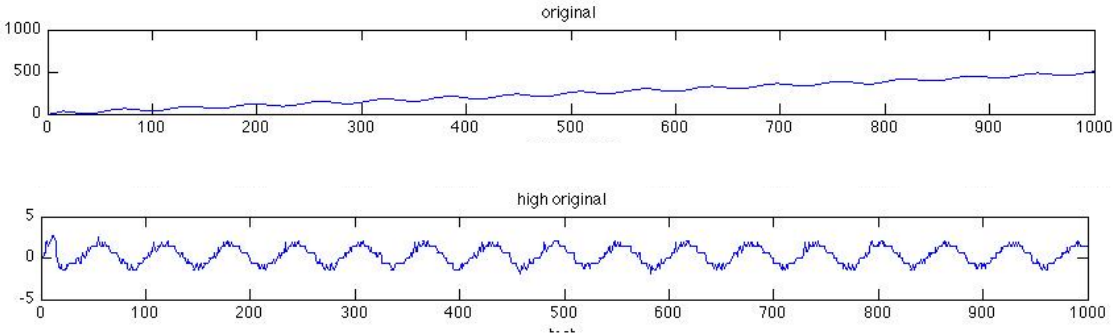


**Figure 6 Gyroscope response**

In figure 6 we can see the response to a sine wave movement by the motors in the readings of the gyroscope. In the first plot the saturation problems with the gyroscope are visible when the measurement continues to increase over time after performing the integration. The second plot shows the actual response after passing the data through the high pass filter.

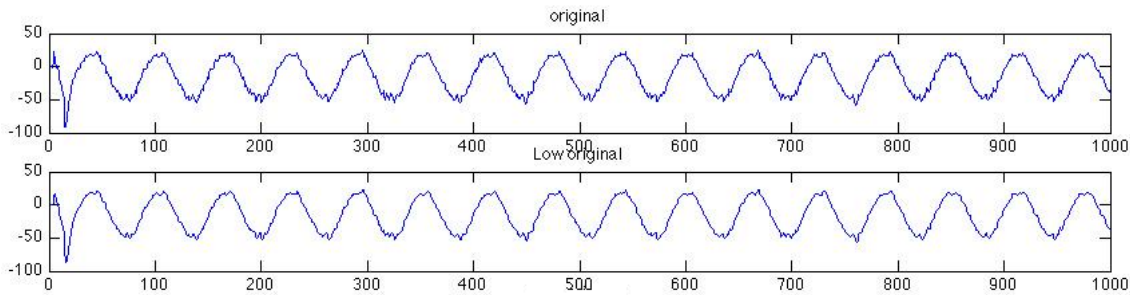


**Figure 6 accelerometer response**

In figure 6 we can see the response to a sine wave movement by the motors in the readings of the accelerometer. After passing the data through the low pass filter the sine wave becomes smoother and the graph gets rid of the high frequency noise it once had.

### 3.3 Gyroscope plus accelerometer and tracking of angle movement

After the filters adding the two signals yield the estimated angle of the (IMU). which translate to the angle of the system where the IMU have been strap down. To be able to check if the measurements are correct we need a point of references. The motors that we are using are the Dynamixel AX-12, which have an angle range from 0 degree to 300 degree, depending on the signal position that goes from 0 to 0x3ff (1023). The theoretical angle can be calculated from this relationship assuming a linear equation with an intercept in 0. The equation turns out to be  $y=m*x$  where  $y$  is the angle  $x$  is the signal and  $m$  is  $(300/1023)$ . If we assume that the angle can vary from (150 to -150) making the 0 perpendicular to the surface of the motor platform. The equation turns out to be  $y=m*(x-511)$ . The number 511 is the theoretical value of the signal to 150 degrees. It is important to notices that the equation  $y=(300/1023)*x$  does not hold truth for both angles 300 and 150 degrees with 1023 and 511 as respective signals hence  $m$  is not

constant, but it doesn't vary that much and it is a good approximation. Now the text was to send a sine wave signal and see how well does the reading follows the theoretical response.

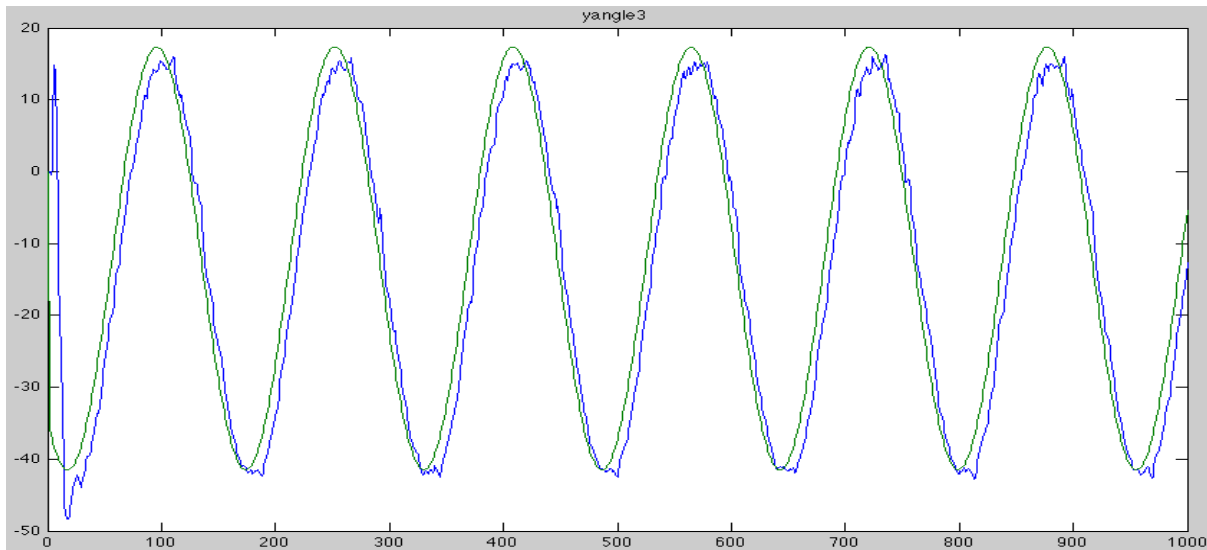


**Figure 7: Accelerometer Reading VS. Theoretical Response**

On figure 7 we can see how the angle reading (blue line) follows the theoretical response with some lag. The source of the lag is a result of two things; a lag caused by the filters because it's averaging data, and the delay that the motors have on getting to the designated position when the signal is sent. This was achieved for low frequencies, from .1 to 1 HZ beyond that the measurements don't follow the theoretical responses for two major reasons. For one, the accelerometers readings are not reliable because of the constant fast movement making it so that even if you pass a whole set of data that is wrong through the filter, the outcome will not be reliable, Also at some point the motors can't keep up with the sine wave, the other major reason for it's failure.

### 3.3 Feedback loop

A simple proportional (P) feedback was created for the platform. This kind of feedback takes the differences between the riding and the settling point, the error, and multiplies it by a constant  $p$  to send the signal to the system. In this case this constant was not calculated but rather it was found experimentally.

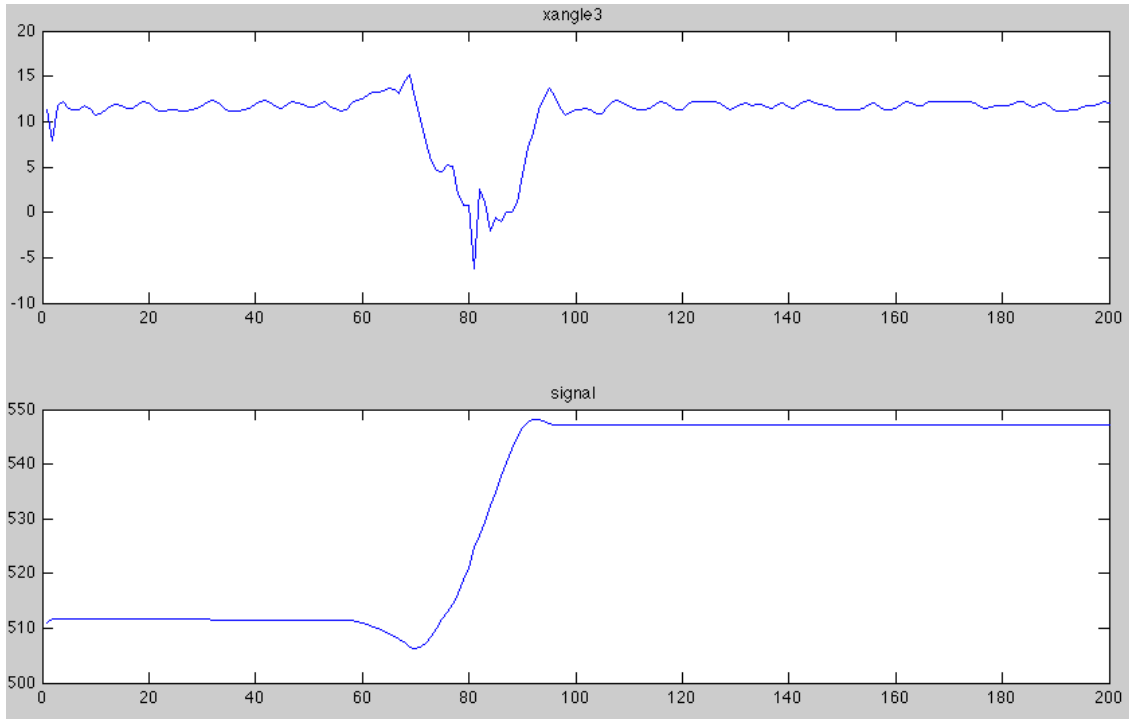


**Figure 8 control loop response**

In figure 8 we can see the control loop response to disturbances and how a change on the angle reading affects the control signal. Notice that even if the angle reading is not a flat line in some part, the control signal doesn't change. This is due to the implementation of a threshold on the error or differences of 1 degree. That threshold was implemented because during a stationary state without any movements, the angle reading is not a flat line (as can be seen on figure 9).

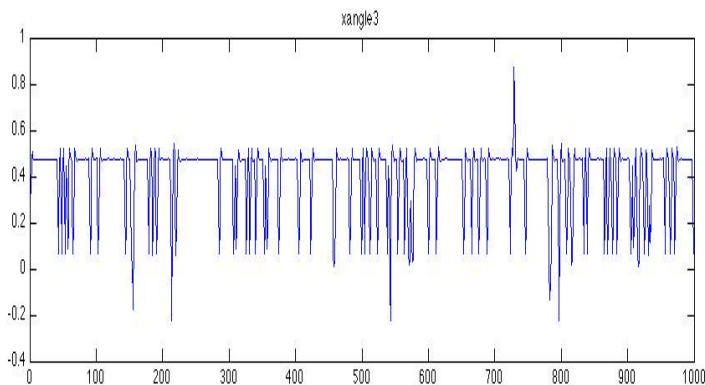


Figure 9 shows the readings of the sensors when there is no movement on the platform. There is an offset or noise of approximately 0.4 degrees on the upper bound and 0.7 degrees to the lower bound, assuming the center of the line is exactly at .5 degrees. For that reason a threshold of 1 degree to each bound was implemented.

**Figure 9: Noise In The Reading**

### Future work

- 1) Try to improve the calculation of the angle readings. Currently working on a way to determine whether the accelerometer readings are reliable or not.

## Approach

The readings of a 3 axis accelerometer are basically vectors in each direction; the value of each vector should go up to around 9.81. Because the only acceleration that counts is the gravity, higher numbers imply that the acceleration has another component due to external forces. Nevertheless there are three vectors, one on each axis and they are all measuring gravity. Hence all of them are a component of the G vector of which the magnitude should be 9.81. If denominated, each vector  $g_x$ ,  $g_y$  and  $g_z$  a component of G then:

$$|G| = \sqrt{g_x^2 + g_y^2 + g_z^2} \cong 9.81$$

With these criteria we can determine if the readings are reliable or not. Also, there will be a margin of error for the readings in which case a threshold around 9.81 on which the readings can be considered reliable.

These equations have been already implemented in the code, but the question of what will be better to do if the readings of the accelerometer are not reliable is still without an answer.

- 2) Implement a PD or PID feedback loop to improve the response of the control system.

## References

- [1] D. Titterton and J. Weston, "Introduction," in *Strapdown Inertial Navigation Technology*, 2th ed. The American Institute of Aeronautics and Astronautics, 2004. pp1-5
- [2] G. Dudek and M. Jenkin "Nonvisual Sensor Algorithms", in *Computational Principle of Mobile Robotics*. 1th ed. Cambridge University Press 2000. 56-58
- [3] D. Titterton and J. Weston, *Strapdown Inertial Navigation Technology*, 2th ed. The American Institute of Aeronautics and Astronautics, 2004.
- [4] Shaw, Brian, [International Journal of Electrical Engineering Education](http://findarticles.com/p/articles/mi_qa3792/is_199901/ai_n8842342/), Jan 1999
- [5] D. Titterton and J. Weston, "Gyroscope technology," in *Strapdown Inertial Navigation Technology*, 2th ed. The American Institute of Aeronautics and Astronautics, 2004. pp1-26 (of the 4 chapter)
- [6] D. Titterton and J. Weston, "Accelerometer and multi-sensor technology," in *Strapdown Inertial Navigation Technology*, 2th ed. The American Institute of Aeronautics and Astronautics, 2004. pp 21 (of the 6 chapter)
- [7] D. Titterton and J. Weston, "Gyroscope technology," in *Strapdown Inertial Navigation Technology*, 2th ed. The American Institute of Aeronautics and Astronautics, 2004. Pp 65 (7 of chapter 4)
- [8] D. Titterton and J. Weston, "Accelerometer and multi-sensor technology," in *Strapdown*

*Inertial Navigation Technology*, 2th ed. The American Institute of Aeronautics and Astronautics, 2004. pp 154(2 of the 6 chapter)

[9] Sanghyuk Park and Jonathan How, Examples of Estimation Filters from Recent Aircraft Projects at MIT November 2004, [http://ocw.mit.edu/NR/rdonlyres/Aeronautics-and-Astronautics/16-333Fall-2004/67AC5F9B-4FC0-4F62-9A4A-3921AA27A5FB/0/115\\_filter\\_examp.pdf](http://ocw.mit.edu/NR/rdonlyres/Aeronautics-and-Astronautics/16-333Fall-2004/67AC5F9B-4FC0-4F62-9A4A-3921AA27A5FB/0/115_filter_examp.pdf)

## Appendixes

Control system with angle reading.

```
%{
The I\ ID of 120

IMU Bytes
-----
#define CONTROL_FORWARDS_ACCEL_LOW 26 //z
#define CONTROL_FORWARDS_ACCEL_HIGH 27
#define CONTROL_SIDEWAYS_ACCEL_LOW 28 //y
#define CONTROL_SIDEWAYS_ACCEL_HIGH 29
#define CONTROL_VERTICAL_ACCEL_LOW 30 //x
#define CONTROL_VERTICAL_ACCEL_HIGH 31
#define CONTROL_PITCH_RATE_LOW 32 //y rate
#define CONTROL_PITCH_RATE_HIGH 33
#define CONTROL_ROLL_RATE_LOW 34 //x rate
#define CONTROL_ROLL_RATE_HIGH 35
#define CONTROL_YAW_RATE_LOW 36
#define CONTROL_YAW_RATE_HIGH 37
%}

clc

imu_id = 120;
timeout = .1; %Really arbitrary
x_addr = 30;
y_addr = 28;
z_addr = 26;
x_rate_addr = 34;
y_rate_addr = 32;
phi = 0;
zeta = 0;
%Reading bounds
start_addr = z_addr;
```

```
stop_addr = x_rate_addr+1;
length = stop_addr-start_addr+1;
num_points = 200;
```

```
factor=1024/300;
alfa=511;
```

```
-----
x=(factor)*(0)+alfa;    %set the initial angle
```

```
y=(factor)*(0)+alfa;
-----
```

```
if ~exist('fid'),
    fid = dynamixelOpen();    %open the comunication to the motors
end
```

```
[b,a] = butter(2,.3999,'low');
[d,c] = butter(2,.3999,'high');
```

```
for i=1:500
    dynamixelMove(16,y, 1023);
    dynamixelMove(18,x, 1023);
end
```

```
% initializes all vectors to prevent boundaries problems
```

```
x_accel = zeros(num_points,1);
y_accel = zeros(num_points,1);
z_accel = zeros(num_points,1);
x_rate = zeros(num_points,1);
y_rate = zeros(num_points,1);
timestamp = zeros(num_points,1);
```

```
x_phi1 = zeros(num_points,1);
y_phi1 = zeros(num_points,1);
```

```
x_phi2 = zeros(num_points,1);
y_phi2 = zeros(num_points,1);
```

```
x_phi2a = zeros(num_points,1);  
y_phi2a = zeros(num_points,1);
```

```
x_phi1a = zeros(num_points,1);  
y_phi1a = zeros(num_points,1);
```

```
x_angle = zeros(num_points,1);  
y_angle = zeros(num_points,1);
```

```
x_angle1 = zeros(num_points,1);  
y_angle1 = zeros(num_points,1);
```

```
x_rate_2 = zeros(num_points,1);  
y_rate_2 = zeros(num_points,1);
```

```
xangle =zeros(num_points,1);  
yangle =zeros(num_points,1);  
pre_angle=zeros(num_points,1);  
pre_angley=zeros(num_points,1);  
signal =zeros(num_points,1);
```

```
x_phi2ab = zeros(num_points,1);  
y_phi2ab = zeros(num_points,1);
```

```
x_phi1ab = zeros(num_points,1);  
y_phi1ab =zeros(num_points,1);
```

```
x_angle2 = zeros(num_points,1);  
y_angle2 =zeros(num_points,1);
```

```
x_angle12 = zeros(num_points,1);  
y_angle12 = zeros(num_points,1);  
xangle2=zeros(num_points,1);  
yangle2=zeros(num_points,1);  
x_phi1b=zeros(num_points,1);  
y_phi1b=zeros(num_points,1);  
x_phi2b=zeros(num_points,1);  
y_phi2b=zeros(num_points,1);  
xangle3= zeros(num_points,1);  
yangle3= zeros(num_points,1);
```

```
xsignal=zeros(num_points,1);  
ysignal=zeros(num_points,1);
```

```

x1= 0;
y1= 0;
z1= 0;
xp1= 0;
yp1= 0;

j=1;
k=1;
count=0;

tic;
%profile on
for i=1:num_points

%-----

%-----

imu = dynamixelReadData(imu_id, start_addr, length);
if(size(imu,2)==length)
    x_accel(i) = (imu(5)+imu(6)*256);
    y_accel(i) = (imu(3)+imu(4)*256);
    z_accel(i) = (imu(1)+imu(2)*256);
    x_rate(i) = (imu(9)+imu(10)*256);
    y_rate(i) = (imu(7)+imu(8)*256);
    timestamp(i) = toc;

end
while ( x_accel(i)==0 ) && ( y_accel(i)==0 ) && ( z_accel(i)==0 ) && ( x_rate(i)==0 ) &&
(y_rate(i)==0)
    count=count+1;

imu = dynamixelReadData(imu_id, start_addr, length);
if(size(imu,2)==length)
    x_accel(i) = (imu(5)+imu(6)*256);
    y_accel(i) = (imu(3)+imu(4)*256);
    z_accel(i) = (imu(1)+imu(2)*256);
    x_rate(i) = (imu(9)+imu(10)*256);
    y_rate(i) = (imu(7)+imu(8)*256);
    timestamp(i) = toc;
end

end
end

```

```

%if i>1

    g=gravity( x_accel(i), y_accel(i),z_accel(i));
    g1(j:j+3,1)=g;
    g4=g(1,1);
    if j==1
        g3=g
    end
if i>1
    if (g4>9.87||g4<9.5)

        g=g1(j-4:j-1,1) ;

    end
end
g1(j:j+3,1)=g;
g7(i)=g(1,1);

%-----
% its suppose tu calculate the angle from the gyroscope reading

if i==1

    x_phi1(i) = x_rate(i)-x_rate(1);
    y_phi1(i) = y_rate(i)-y_rate(1);

    x_phi2(i) =atan2( g(2,1),g(4,1))*180/pi;
    y_phi2(i) =atan2( g(3,1),g(4,1))*180/pi;

    % x_phi2(i) =real(asin( g(2,1)/9.81)*180/pi);
    % y_phi2(i) =real(asin( g(3,1)/9.81)*180/pi);

    x_angle2(i) = (x_phi2(i));
    y_angle2(i) = (y_phi2(i));

    x_angle12(i) = (x_phi1(i))/3.41;
    y_angle12(i) = (y_phi1(i))/3.41;

```

```
xangle3(i)= x_angle2(i)+y_angle12(i);  
yangle3(i)= y_angle2(i)+x_angle12(i);
```

```
else
```

```
x_rate_2(i) = x_rate(i)-x_rate(1);  
y_rate_2(i) = y_rate(i)-y_rate(1);
```

```
x_phi1(i) = x_rate_2(i)+ x_phi1(i-1); %perform integral  
y_phi1(i) = y_rate_2(i)+ y_phi1(i-1);
```

```
x_phi2(i) =atan2( g(2,1),g(4,1))*180/pi;  
y_phi2(i) =atan2( g(3,1),g(4,1))*180/pi;
```

```
% x_phi2(i) =real(asin( g(2,1)/9.81)*180/pi);  
% y_phi2(i) =real(asin( g(3,1)/9.81)*180/pi);
```

```
%-----
```

```
x_phi2ab = filter(b,a,x_phi2);  
y_phi2ab = filter(b,a,y_phi2);
```

```
x_phi1ab = filter(d,c,x_phi1);  
y_phi1ab = filter(d,c,y_phi1);
```

```
x_angle2(i) = (x_phi2ab(i));  
y_angle2(i) = (y_phi2ab(i));
```

```
x_angle12(i) = (x_phi1ab(i))/3.41;  
y_angle12(i) = (y_phi1ab(i))/3.41;
```

```
xangle3(i)= x_angle2(i)+y_angle12(i);  
yangle3(i)= y_angle2(i)+x_angle12(i);
```

```
end
```

```

%-----
%{Control loop/ part that change on the sine wave code
  if i>1

      if (xangle3(i)>(xangle3(1)+1))||(xangle3(i)<(xangle3(1)-1))
          landa=(xangle3(i)-xangle3(1));
          delta=(xangle3(i)-xangle3(i-1));
          x=(x-((landa)/4.5));

          if x<325
              x=325;
          end
          if x>625
              x=625;
          end

          % x=560;
          dynamixelMove(18,x, 1023);
      end

      %-----

      if (yangle3(i)>(yangle3(1)+1))||(yangle3(i)<(yangle3(1)-1))
          landa=(yangle3(i)-yangle3(1));
          % delta=(yangle3(i)-yangle3(i-1));
          y=(y-((landa)/4.5));
          if y<240
              y=240;
          end
          if y>599
              y=599;
          end

          % y=511;
          dynamixelMove(16,y, 1023);
      end
  end
}
%-----
xsignal(i)=x;

ysignal(i)=y;

pre_angle(i)=((x-alfa)/factor);

```

```

pre_angley(i)=(y-alfa)/factor);
j=j+4;
k=k+10;

end
toc;

-----
xint= x_phi1;
yint= y_phi1;      %record data to simulate in filters without roning the entire program

xatan= x_phi2;
yatan=y_phi2;
-----
%profile viewer

% Plot the angles readings

figure(1)
subplot(2,1,1);
plot(yangle3);
title('yangle3')

%subplot(4,1,2);
%plot(yangle3);
%title('yangle3')

subplot(2,1,2);
plot(ysignal);
title('signal')

%subplot(3,1,3);
%plot(pre_angley);
%title('spre_angley')

figure(2)
subplot(2,1,1);
plot(xangle3);

```

```
title('xangle3')
```

```
%subplot(4,1,2);  
%plot(xangle3);  
%title('xangle3')
```

```
subplot(2,1,2);  
plot(xsignal);  
title('signal')
```

```
%subplot(3,1,3);  
%plot( pre_angle);  
%title(' pre_angle')
```

---

```
% sine wave for either y axis or x axis  
t=clock;
```

```
pre_angle(i)=$((x-alfa)/factor);  
pre_angley(i)=$((y-alfa)/factor);
```

```
%x=100*sin(w*t(6)*f)+511;  
%signal(i)=x;  
%dynamixelMove(18,x, 1023);
```

```
y=100*sin(w*t(6)*f)+470;  
signal(i)=y;  
dynamixelMove(16,y, 1023);
```

```
    j=j+4;  
    k=k+10;
```

---

```
%things that needs to be initializes for the sin wave code  
f=.5;  
F=f*ones(num_points,1);  
w = 2*pi;
```

---

# **AUTOMATED GAIT OPTIMIZATION FOR A CENTIPEDEINSPIRED MODULAR ROBOT**

NSF Summer Undergraduate Fellowship in Sensor Technologies

Sarah Koehler (Mechanical Engineering) - Cornell University

Advisor: Dr. Mark Yim, Dr. Daniel E. Koditschek

## **ABSTRACT**

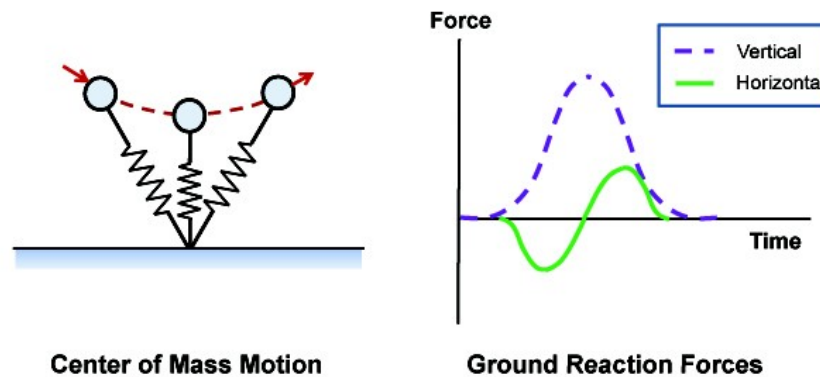
Manually tuning a biologically inspired robot's gait so that it can walk quickly and efficiently is a time-consuming and tedious task. For this project, CKBot (a modular robot system) has been configured into a centipede-inspired configuration with six legs. The project started with a few manually tuned gaits which follow an alternating tripod pattern. The purpose of this project is to automate tuning of the robot's gait such that it optimizes a factor such as specific resistance, speed, or power. Most of the effort in this project has gone into setting up the framework for such optimization trials. This set up included creating and building the Matlab optimization code, a 7.4 V regulator, a Vicon ball tracking piece. Other code was also created for interaction with the current sensor, communication with the robot, and interface with the Vicon. Each optimization trial runs the centipede back and forth and adjusts the six parameters that change the robot's gait by using the Nelder Mead optimization method. The end result after optimization is a gait with minimal specific resistance, maximum speed, or some other optimal factor. Successful tests were completed that maximized speed of the centipede robot.

## 1. INTRODUCTION

Modular robots can be reconfigured into many different shapes. For example, modular robot systems such as Polybot can be reconfigured into a snake-like robot [7] or a dynamic rolling loop [8]. Because of this versatility, a modular robot system such as CKBot [1] is well suited for the study of different kinds of locomotion. We are particularly interested in dynamic locomotion. Dynamic locomotion has been previously studied in modular robotics in systems such as the YaMoR modular robot system [5] and in bio-inspired robotics such as RHex [2]. This project is a synthesis of those two ideas.

For this project, we are studying a template of legged locomotion found in nature called SLIP (Spring Loaded Inverted Pendulum) [6]. A template is a simplified version of a more complex system that portrays the same behavior [12]. The SLIP template is a dynamical template, so it portrays the same movement behavior as the more complex leg. The SLIP model treats a single leg as a spring attached to a mass point. The mass and spring system act as an inverted pendulum that pivots around the leg's contact point with the ground (see Figure 1). The corresponding force versus time graph shows the forces pushing vertically and horizontally against the leg in the given two-dimensional space.

Our purpose in studying the SLIP template is that many different kinds of animals – from cockroaches to humans to elephants – portray this kind of motion [10]. We are interested in mimicking this motion because animals are good at maneuvering on rough terrain. The general idea is that if we can get the robot to move like these animals, then it too will be able to move around better on various terrains [11].



1: SLIP Model [3]

The long-term purpose of this project is to tune multiple parameters in the gait for specific resistance and perhaps power, speed, or hopping height. Tuning these factors affects the leg trajectory and the timing of the strides. The main effort in this project is in setting up the infrastructure that enables us to automate running the robot back and forth while changing the gait parameters. The next section will introduce the robot and the optimization method. The following sections will outline the setups of the computer-to-robot connections that allow separate systems (laptop, Vicon, power supply, sensors, and robot) to communicate with one another. Finally, there will be conclusions with a few test results that demonstrate that the optimization

process works.

## 2. BACKGROUND



*Figure 2: The centipede-inspired robot [3]*

### 2.1 Configuration and Movement of the Centipede Robot

The configuration we are using in this project is one in which the SLIP model and the modular robot system are combined. It is a centipede-inspired configuration consisting of six modules and three pairs of legs [3] (see Figure 2). Altogether there are six actuated degrees of freedom which are collapsed down to two degrees of freedom in the control. The two degrees of freedom are in the two twist directions of the legs. The first is each leg's angle in the transverse plane (denoted as  $\theta$ ), and the second is each leg's angle in the coronal plane (denoted as  $\phi$ ) (see Figure 3). Each leg's angle in the two planes are mirrored to be the same so that all legs have the same angle in the same plane. The image on the left-hand side is of the transverse plane, and the image on the right-hand side is of the coronal plane. Note that each square represents a module of the centipede and that only one module and one pair of legs are shown in the coronal plane.

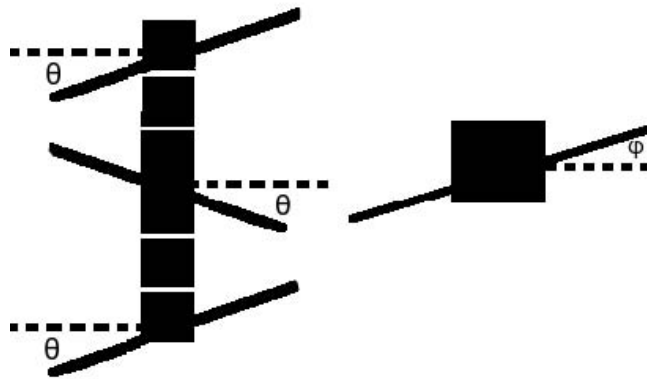


Figure 3: The two degrees of freedom denoted by  $\theta$  and  $\phi$

The gait used with the centipede is an alternating tripod gait. A gait can be described as the pattern and frequency of footsteps on the ground. The alternating tripod gait is one in which the front and back legs of one side of the centipede make contact with the ground at the same time as the middle leg on the opposing side does. The two tripods then act like two legs on a walking bipedal – one tripod supports the body while the other tripod swings forward to take the next supporting stance.

We can create this alternating tripod gait by using six parameters:  $\theta_1$ ,  $\theta_2$ ,  $\phi_1$ ,  $\phi_2$ ,  $dt_1$ , and  $dt_2$ . The two  $\theta$  parameters are two  $\theta$  angles in the transverse plane, the two  $\phi$  parameters are likewise two  $\phi$  angles in the coronal plane, and the two “ $dt$ ” parameters are the time it takes to move onto the next angle. An example gait parameter table is shown in Table 1 with parameters set as  $\theta_1 = 20$  degrees,  $\theta_2 = 20$  degrees,  $\phi_1 = 20$  degrees,  $\phi_2 = 30$  degrees, and the  $dt$  parameters are not shown. Modules 1, 3, 4, and 6 change between positive  $\theta_1$  and  $\theta_2$  angles whereas modules 2 and 5 go through the  $\phi_1$  and  $\phi_2$  angles (as indicated by the written parameters in parentheses). Each line of the gait table is a segment of the gait; the first and third segments take “ $dt_1$ ” seconds (e.g. 0.100 seconds) to execute completely and the second and fourth segments take “ $dt_2$ ” seconds to execute. Each line occurs immediately after the previous line is completed. Once the robot has gone through one gait table as shown below, it has essentially taken two full steps. Each gait can be tuned by changing any of the six parameters.

Module 1	Module 2	Module 3	Module 4	Module 5	Module 6
-20 (- $\theta_2$ )	-20 (- $\phi_1$ )	-20	20	20	20
20 ( $\theta_1$ )	-30 (- $\phi_2$ )	20	-20	30	-20
20 ( $\theta_2$ )	20 ( $\phi_1$ )	20	-20	-20	-20
-20 (- $\theta_1$ )	30 ( $\phi_2$ )	-20	20	-30	20

Table 1: A gait parameter table

## 2.2 Optimization

While we have some idea of the pattern and frequency of the footfall of the robot we are using, we can only tune a few of these gaits manually. Tuning gaits by hand is a time-consuming and tedious process, and there is no way of knowing if the gait could make the centipede go faster, or jump higher for example. Thus, there is much usefulness and practicality of an optimization process for tuning gaits.

Many different optimization algorithms have been used for gait optimization, including a genetic algorithm-based optimization for bipedal robots [9], and optimization from a central pattern generator using the Powell optimization method for modular robots [5]. Our approach is to use the Nelder Mead optimization method, similar to an approach done with the RHex robot [4]. According to recent research, this method improves specific resistance by a factor of three, and increased speed by a factor of five in comparison with the fastest manually tuned speed [4].

Nelder Mead is a simplex based optimization algorithm. Given  $n$  parameters (in our case, six parameters), Nelder Mead begins with a  $n+1$  simplex, and uses a cost function to evaluate and replace the points in the simplex until it finds an effective minimum. A cost function we would use with our robot is inverse speed to maximize speed, or specific resistance (power/mgv) to maximize power efficiency. Nelder Mead is a good method to use in our optimization because it is a direct search (i.e. it does not require derivatives) which is useful when the cost function relies on variables that are prone to error and noise. One such variable is current because its value is not constant for the entirety of the experiment; even averaging the current over a trial run does not get rid of spikes in the current.

## 3. GENERAL SET UP

This project utilizes Matlab code that implements the Nelder Mead Optimization method. The code was previously set up for the Nelder Mead Optimization with Edubot for automated tuning of that robot's gaits [4]. The main focus of this project was editing and fitting the code to the Centipede robot's dynamism, or the software that controls the robot. The code was set up on a 32-bit Linux Ubuntu Operating System.

The general process for the optimization experimentation requires several systems to be set up. First, the robot must receive power. The robot could be powered either wirelessly using batteries or through a wired connection to a power supply. A wired connection through a power supply is preferred because the current sensor can only read current through a wired connection. The current is useful to know for calculating certain cost functions (power, specific resistance) in the optimization process. A tradeoff for using a wired power supply is that the cable may affect the robot's movements by pulling on it or placing other forces on it.

Second, the robot must receive communication from a computer. The robot will use a CAN bus line for easy changeability because the robot's gait will be updated each trial, and there can be up to 100 or 200 trials. Again, a tradeoff is that the CAN requires a wired connection, which could place forces on the robot. However, a wireless communication would have made it much more difficult to change the gait as much as it is necessary for the optimization process. Finally, a current sensor is attached to the power line and to the computer through a Phidget Interface Kit. The robot is placed within the field of vision of the Vicon camera three dimensional tracking system, and the optimization process can begin.

Once the above configuration is set up, the Matlab code prompts the user to set up the

two end zones for the robot in the Vicon tracking system. Then, the code sends the robot across this field, collecting speed and current data. Then, the cost function is calculated from appropriate data such as current (usually specific resistance, which is a kind of power efficiency normalized according to weight). The Nelder Mead method then adjusts the parameters ( $\theta_1$ ,  $\theta_2$ ,  $\phi_1$ ,  $\phi_2$ ,  $dt_1$ , and  $dt_2$ ) for the centipede and runs the centipede across the field again using the newly tuned parameters. This process repeats until the Nelder Mead algorithm can find a good minimum in the cost function. See Appendix A for the `run_across.m` function that provides the main commands for sending the robot across the Vicon field and calculates cost.

#### 4. POWER SUPPLY

The power supply that can be used with the voltage regulators is a 28A maximum cumulative current DC regulated power supply. The other option to power the robot is to use 7.4 V batteries. A wired power supply is preferred because the current sensor cannot connect to the batteries.

In order to read the current being supplied to the robot, a Phidgets ([www.phidgets.com](http://www.phidgets.com)) current sensor is attached in series to the robot and the power supply. Each module in the robot typically draws about 3 amps of current, up to a maximum of about 5 amps.



*Figure 4: Phidgets Current Sensor  
[http://www.emmeshop.it/images//  
phidgets/1119.jpg](http://www.emmeshop.it/images//phidgets/1119.jpg)*

Although the hardware is provided to read the current from the the Phidget board, the drivers that interface the hardware with the computer do not run on Matlab in Linux. Since the optimization code was written in Matlab and in Linux Ubuntu, it was necessary to find a way to port the information through to Matlab. The Phidget board does interface with the C language in Linux, so we are using C mex files to port the current sensor information to the Matlab code. A mex file that reads the current from the sensor can be found in Appendix B.

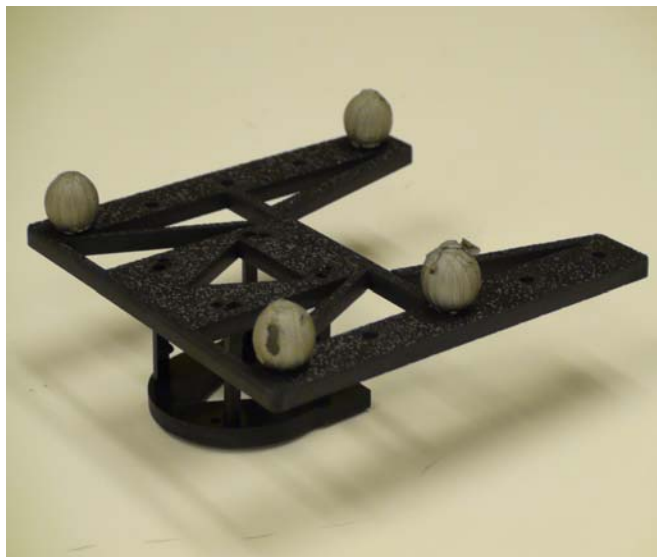
## 5. TRACKING SYSTEM

The Nelder Mead optimization setup requires that we know the position and speed of the robot. Also, if we wanted to optimize for a factor such as hopping height, we would need to be able to collect the position data. The GRASP lab at the University of Pennsylvania has a six-camera Vicon three-dimensional tracking system which allows us to track and record the position of the robot in real time. The system collects data from multiple reflective balls on the body of interest. In order to accurately track the body, it is generally best to have at least four reflective balls in an antisymmetric layout (four balls are required because it tracks in three dimensions, and an antisymmetric layout can allow the camera to differentiate between the front and back of the robot).

### 5.1 Mechanical Design of Ball Holder

In order to track the robot in the Vicon camera system, the robot must have four reflective balls rigidly attached to it. Because the centipede is modular and only the center two modules stay rigid with respect to one another, a ball holder was created in order to support the balls. The balls could not be attached to the legs because the legs move with respect to one another.

Other considerations that were taken into account when designing the ball tracker for the centipede were that it should be lightweight so the ball tracking piece was designed with many holes cut out of it and was made out of ABS plastic. The piece had to attach to the top of the centipede such that not balls would be obstructed from the camera's view. It also had to be designed to hold the balls slightly above the main body of the centipede so that it would not interfere with the twisting motions of the modules or the legs.



## 6. VOLTAGE REGULATORS

In order to use the centipede in connection with a power line, voltage regulators had to be created so that enough current could run through the robot while simultaneously providing the correct amount of voltage to each module. Each module takes about 2-3 Amps on average to run. Each servo in the modules is also specified to take 7.4 V to work correctly. See Figure 6 for a photo of the Voltage Regulator.

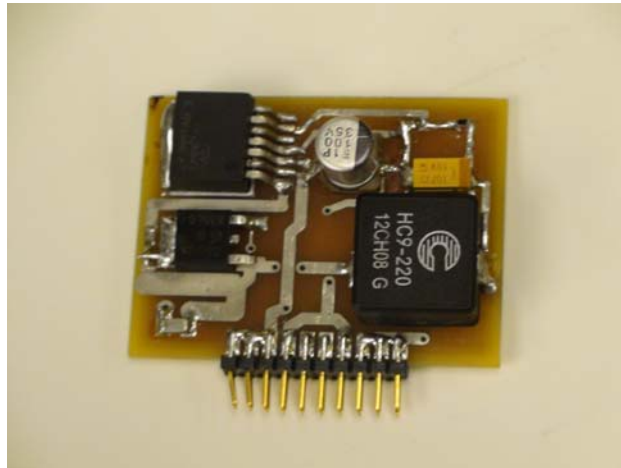


*Figure 6: Voltage Regulator*

### 6.1 Design of the Voltage Regulator

The voltage regulator was designed using a LM2677 Step-down Switch. The board was designed to allow a maximum of 5 A to run through it and provide 7.4 V output from a 24 V input. The board also had several size restrictions because it had to fit inside the module (See Figure 7). The board's first design was constrained to be 3 cm x 4 cm with a maximum height of 8 mm. Finally, it was important to keep the input capacitor as close as possible to the switch in order for the board to work correctly.

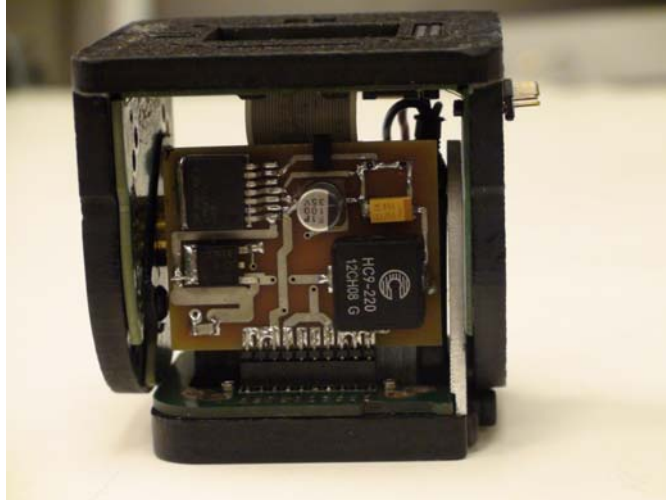


Figure 7: A Voltage Regulator in the module

A few calculations were done in order to determine which resistors and which capacitors to get. Using the suggested feedback voltage of 1.21 V and a suggested resistance of 1 k $\Omega$  for the first resistor (noted as R1 in Figure 8), a resistance for resistor 2 (R2 in Figure 8) was calculated as follows:

$$R_2 = R_1 \cdot \frac{V_{OUT} - V_{FB}}{V_{FB}} = 1 \text{ k}\Omega \cdot \frac{7.4 - 1.21}{1.21} = 5.12 \text{ k}\Omega$$

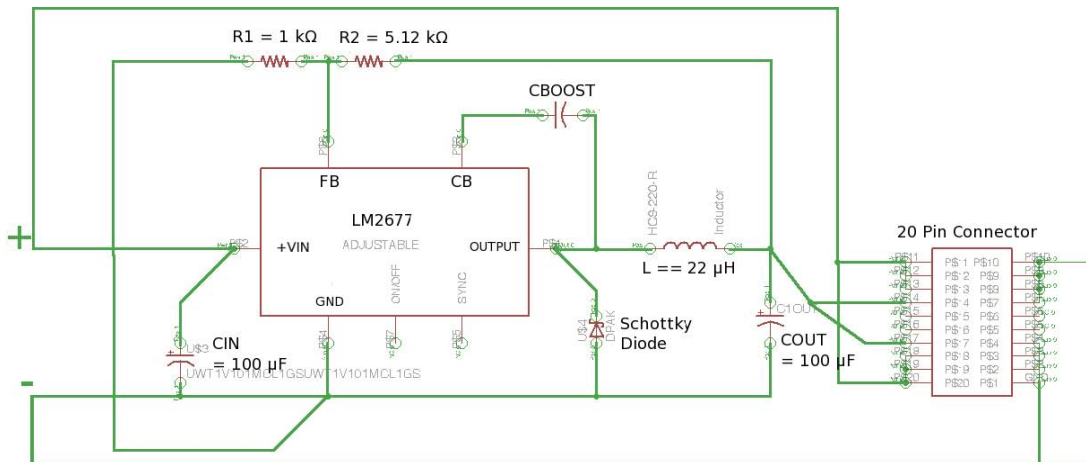


Figure 8: Electrical Schematic

The other electrical components were chosen to handle a maximum current of 5 Amps. Most selections were guided by the LM2677 data sheet recommendations. The inductor selected has inductance of 22  $\mu H$ , the output capacitor would handle 10 V and 100  $\mu F$ , the input capacitor would handle 35 V and 100  $\mu F$ . A Schottky diode was selected in order to keep

current flowing in the correct direction, and a boost capacitor would make sure that the voltage regulator would fully turn on.

The board layout is illustrated in Figure 9, with pads placed for the 20 pin connectors that the modules use. The inductor was placed towards the bottom of the voltage regulator for minimal interference with the module while in motion. Wires for the input and output were made as thick as possible in order to carry the maximum current of 5 Amps as well as the high input and output voltages.

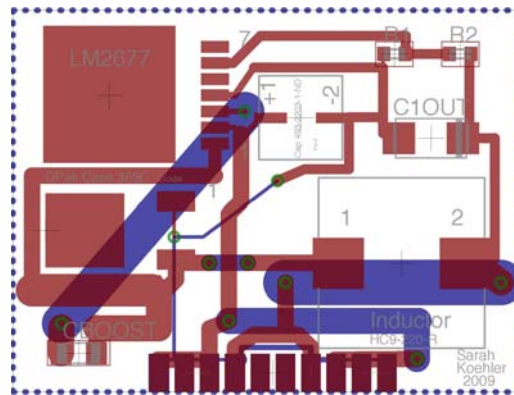
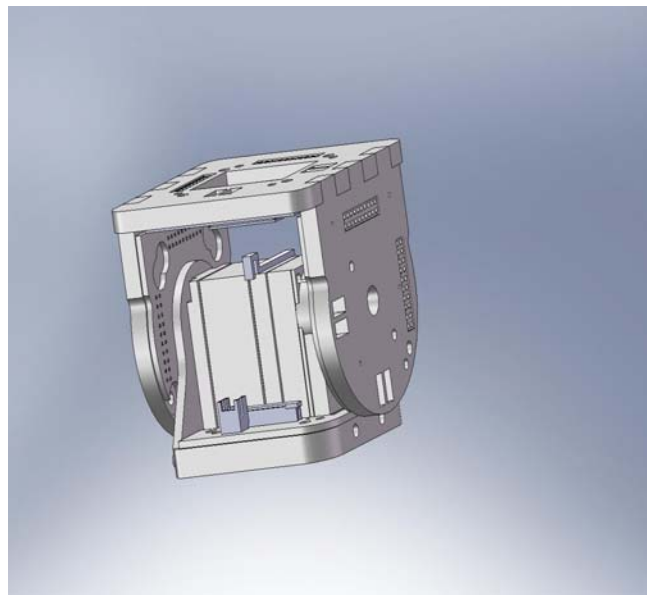


Figure 9: Board Layout

## 6.2 Problems

Though the design does work and provides the correct voltage output, the voltage regulator is still currently causing problems when interacting with the robot. One small problem is that on some of the modules, the input capacitor (about 8 mm tall) and the LM2677 switch do not fit in the module. To temporarily solve the problem, clips were designed to attach the boards to the servos they were sitting on (See Figure 10).



A more serious problem with the voltage regulator involves the circuitry, and has not

been resolved at this point. The direct problem with the robot is that sometimes the robot does not respond to CAN bus messages, or messages that tell it to move. In other words, the robot does not always move when it is supposed to. Currently, it appears that the problem causing this could be the voltage regulator's noisy output. That is, the voltage regulator does not provide a continuous output voltage, but an uneven voltage with spikes. The noisy output causes another voltage regulator for the micro-controller in the modules to go into low power mode, causing the micro-controller to not be able to function properly. The inductor and output capacitor are essential for “quieting” the noise, or smoothening the voltage output. It seems that the voltage regulator may need a larger output capacitor (one with a higher capacitance). This problem is still to be resolved.

## 7. RESULTS AND CONCLUSIONS

A few tests have been done far, but there is still a good amount of troubleshooting to be done. The tests were only done with  $\text{cost} = 1/\text{speed}$  and with the centipede powered by battery because the voltage regulators are still causing problems. There seems to be a problem with the communication, because the centipede generally stops responding to Matlab CAN messages after running back and forth in the experiment a few times. The most runs back and forth that we could achieve were 20 runs, and according to the similar Edubot optimization experiments, the optimization process should take 100-200 runs in total.

A large part of the problem with present optimization runs is that oftentimes the centipede does not run straight. This is most likely a cause of error with the communications. The Matlab code has been set so that if the robot does not run straight for a particular gait, that gait has to be run again until it does go straight.

Our most recent results show that the centipede sped up when it was run through the Nelder Mead process. Plotting the cost versus the trial number, it is evident that cost decreased over time (see Figure 11).

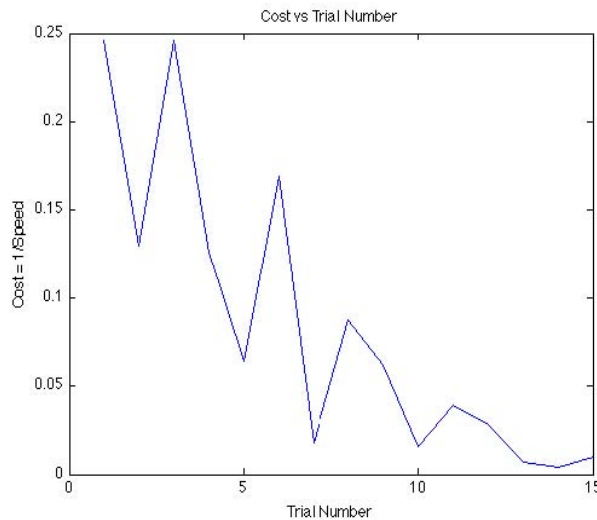


Figure 11: Cost decreases over time

Results from this latest run show an increase in velocity, but the timing was not quite accurately measured. Although the velocity data is not correct, the cost vs trial number graph depicted in Figure 11 still shows that Nelder Mead does work correctly. In the latest run, only the two time parameters were optimized with the other parameters set as:

theta1 = 30 degrees  
theta2 = 30 degrees  
phi1 = 20 degrees  
phi2 = 80 degrees.

The movement of the centipede was of interest – it did not appear to portray a SLIP-like behavior because the robot just slid its legs along the ground very quickly without lifting them up at all. An error that may be occurring is that the centipede does not reach the full theta or phi angles as it should.

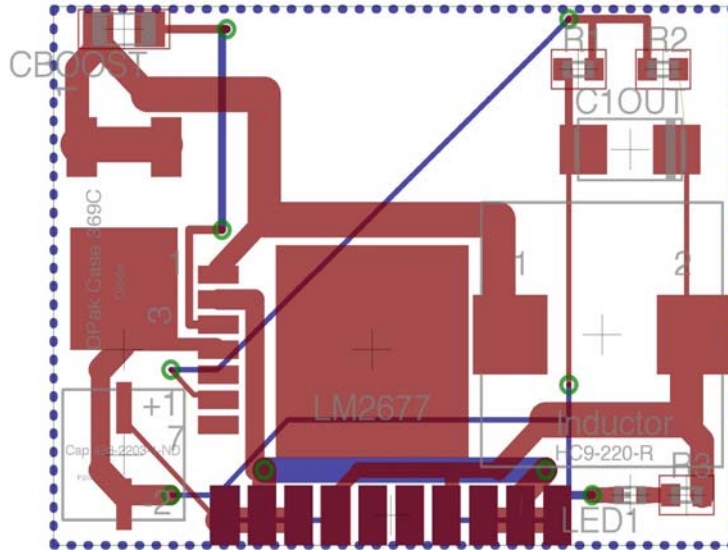
## **8. RECOMMENDATIONS**

The next steps in the process will be to optimize the robot for other factors. Fixing the voltage regulators and getting them to work correctly with the power supply and robot will be useful for any future work with the CKBot modular robot system.

Once more of the robot's gaits have been well tuned, it will be interesting to develop a dynamical model of each of the robots movements (e.g. hopping, walking, running). A long-term goal would be to embed the SLIP template in such a dynamical model in order to make the Centipede robot much more dynamically similar to an actual centipede, as well as to many other animals.

### **8.1 Voltage Regulators**

To permanently solve the problem of fitting in the modules, a new board layout was created with the tall pieces (switch, capacitor, inductor, and diode) as close as possible to the bottom of the board where there is the least likelihood of the pieces interfering with module movement (See Figure 11). The board was also reduced in size to be the same width and height of the servo since the board sometimes also hit small pieces like screw tops when the module was moving. Finally, an LED was added on the output side of regulator in order to show when the voltage regulator is working.



## 9. ACKNOWLEDGMENTS

I would like to thank my advisors, Dr. Mark Yim and Dr. Daniel Koditschek, for selecting me to participate in this exciting research program. I would especially like to thank Dr. Yim for getting me interested in modular robotics and also Dr. Koditschek for pushing me intellectually beyond the basic scope of my project this summer. I'd also like to thank Jimmy Sastra for working extensively with me this summer and I'd like to thank the rest of both labs for providing a friendly and encouraging workspace. Finally, I would like to thank the National Science Foundation for their support through an NSFREU grant and Microsoft Corporation for their financial support.

## 10. REFERENCES

- [1] M. Park, S. Chitta, A. Teichman, and M. Yim, "Automatic Configuration Recognition Methods in Modular Robots," *Intl. J. of Robotics Research* Invited, Nov. 2006
- [2] R. Altendorfer, N. Moore, H. Komsuoglu, M. Buehler, H. B. Brown Jr., D. McMordie, U. Saranli, R. Full, and D. E. Koditschek, "Rhex: A biologically inspired hexapod runner," *Autonomous Robots*, vol. 11, pp. 207–213, 2001.
- [3] J. Sastra, W. G. Bernal Heredia, J. Clark, and M. Yim, "A biologically-inspired dynamic legged locomotion with a modular reconfigurable robot," in the ASME 2008 Dynamic Systems and Control Conf., Ann Arbor, MI.
- [4] J. D. Weingarten, G. A. D. Lopes, M. Buehler, R. E. Groff, and D. E. Koditschek, "Automated Gait Adaptation for Legged Robots," in *2004 IEEE Int. Conf. Robotics and Automation*, New Orleans, LA, pp. 2153-2158.
- [5] A. Sproewitz, R. Moeckel, J. Maye, A. J. Ijspeert, "Learning to Move in Modular Robots using Central Pattern Generators and Online Optimization," *Int. J Robotics Research*, vol. 27, pp. 423-443, 2008. Available: <http://ijr.sagepub.com/cgi/content/abstract/27/3-4/423>
- [6] G. A. Cavagna, N. C. Heglund, and C. R. Taylor, "Mechanical work in terrestrial

- locomotion: Two basic mechanisms for minimizing energy expenditure, ” *American J of Physiology*, vol. 233 (5), R243-R261, 1977. Available: <http://ajpregu.physiology.org/>
- [7] Yim, M., Duff, D.G., Roufas, K.D., 2002. "Walk on the wild side," *IEEE Robotics & Automation Magazine*, vol. 9(4), pp. 49-53, December 2002.
- [8] J. Sastra, S. Chitta, and M. Yim, "Dynamic Rolling for a modular loop robot," *Proc. of the Intl. Symp. on Experimental Robotics*, Rio de Janerio, 2006.
- [9] G. Dip, V. Prahlad, P. D. Kien, "Genetic algorithm-based optimal bipedal walking gait synthesis considering tradeoff between stability margin and speed," *Robotica*, vol. 27, pp. 355-365, 2009. DOI: 10.1017/S026357470800475X
- [10] R. Blickhan and R. J. Full, "Similarity in multilegged locomotion: Bounding like a monopod". *J of Comparative Physiology*, 173(5), pp. 509–517, 1993.
- [11] U. Saranli, "Dynamic locomotion with a Hexapod Robot." Ph.D. diss., University of Michigan, 2002.
- [12] R. J. Full and D. E. Koditschek, "Templates and Anchors: Neuromechanical hypotheses of legged locomotion on land," *J. of Experimental Biology*, vol. 202, pp. 3325-3332, 1999.

## APPENDIX A

```
function [cost,vel, total_time, lost] =
run_across(robotname, field_setup)

% Run across

global cent

% FIXME - the robot mass in kg ... need to actually weigh
robot
% !!!!!!!!!!!!!!!!!!!!!!!!!!!!!!!!!!!!!!!!!!!!!!!!!!!!!!!!!!!!!!!
!!!!!!!! %%

robot_mass = 3.31;

% grab vicon position, put into planar version

[s,t,trans,rot,lost] = grab_data_force(robotname);
[x,y,theta] = planar_state(trans,rot);

% transform to "field coordinates"

newcoord = field_coord(field_setup,[x,y,theta]);

% compare distances to either endzone to figure out which
direction we're running

d1 = newcoord(1);
d2 = field_setup.track_length - newcoord(1);

if d1 > d2
    disp('running to endzone 1')
    goal_id = 1;
    goal = field_setup.mark1;
else
    disp('running to endzone 2')
    goal_id = 2;
```

```

    goal = field_setup.mark2;

end

% Initialize current, i, sensIdx, starting
% current = zeros(1,5);
% i = 1;
% sensIdx = 4; % Where the phidget is attached to the
current sensor

starting = 1;

canhandle = Open_canmex;
pause(5)
cent.canhandle = canhandle;

while 1

    % get robot position and update plot

    [s,t,trans,rot,lost] = grab_data_force(robotname);
    [x,y,theta] = planar_state(trans,rot);
    newcoord = field_coord(field_setup,[x,y,theta]);
    plot_field(field_setup.track_length,newcoord)

    % if we're starting, check if we've crossed the start
line
    if (starting)
        if (goal_id == 1)
            if newcoord(1) <
                field_setup.track_length
                    starting = 0;

            end
        end
        if (goal_id == 2)
            if newcoord(1) > 0
                starting = 0;
            end
        end
    end
end

```

```

        end
    end
    if (starting == 0)

        % START the robot!

        disp('Starting the robot!');
        tic;

    end
end

% Go through one gait table

goCentipede(canhandle)

% Collect Current
% current(i) = readCurrent(sensIdx);
% i = i + 1;

% check if we have reached the goal

if (goal_id == 1)
    if newcoord(1) < 0.0

        % stop integrating and break from the while loop

        disp('reached end zone 1')
        break;

    end
end
if (goal_id == 2)

    % stop integrating and break from the while loop

    if newcoord(1) > field_setup.track_length
        disp('reached end zone 2')
        break;

    end
end
end

```

```

% If we lose the robot, we need to start this gait over

if lost
    disp('Robot is lost. Restart this gait')

    break
end

end

% dummy parameters so that program doesn't crash

if lost

    cost = 999;
    vel = 999;
    total_time = 999;
    disp('Put Robot back where it just started!');

    return
end

% if we exited the while loop, we finished our integration.
Stop recording time and stop robot.

total_time = toc;
disp('Robot is stopping!');
relax(canhandle);
pause(5)
Close_canmex(canhandle);
[s,t,trans,rot,lost] = grab_data_force(robotname);
[x,y,theta] = planar_state(trans,rot);
newcoord = field_coord(field_setup,[x,y,theta]);
plot_field(field_setup.track_length,newcoord)

% if robot made it to the end line, it's not lost!

lost = 0;

```

```

dist = field_setup.track_length;
vel = dist / total_time;
cost = 1/vel;
fprintf('velocity is %f',vel);

% % grab the average power and voltage
% avgcurrent = mean(current);
% avgvoltage = 7.4; % Volts
% avgpower = avgcurrent*avgvoltage;
%
%
% % specific resistance
%
% % % method A: normal specific resistance
% cost = avgpower / (robot_mass * 9.81 * dist/total_time);

% method B: modified with factors
% cost = avgpower / (robot_mass * 9.81 *
(dist/total_time)^3);

% method C: use of just average power results in
underpowered gaits
% cost = avgpower;

```

## APPENDIX B

/\* readCurrent.c MEX MEX MEX MEX MEX Read the sensor value from the phidget board. Convert it from "phidget" units (which reads the current value as anywhere between 0 and 1000) to Amps. Matlab syntax: current = readCurrent(index,ifKit) where current is a double that contains current value in Amps, index is the number of the sensor you are using (0-7), and ifKit is the integer ID of the interfaceKit that you have opened\*/

```
#include "matrix.h" #include  
<phidget21.h> #include "mex.h"
```

```
double read_current(int idx, int ifKit)  
{ int result, numSensors, i, sensorValue; const char *err; double current;  
  
    /*open the interfacekit for device connections*/  
    CPhidget_open((CPhidgetHandle)ifKit, -1);  
  
    /*get the program to wait for an interface kit device to be attached*/ if((result =  
    CPhidget_waitForAttachment((CPhidgetHandle)ifKit, 10000)) {  
        CPhidget_getErrorDescription(result, &err); mexPrintf("Problem  
        waiting for attachment: %s\n", err); return 0;  
    } CPhidgetInterfaceKit_getSensorValue((CPhidgetInterfaceKitHandle)  
ifKit,idx,&sensorValue); current = sensorValue/1000.0*50-25; mexPrintf("Sensor %d has  
    current of %f Amps\n",idx,current);  
  
    return current; }
```

```
void mexFunction(int nlhs, mxArray *plhs[], int nrhs, const mxArray *prhs[])  
{ /*All code and internal function calls go in here!*/ int idx; double current; int ifKit;  
    /*Get input variable*/  
    idx = (int)mxGetScalar(prhs[0]);  
    ifKit = (int) mxGetScalar(prhs[1]);  
  
    /* Call function to read current */  
    current = read_current(idx,ifKit);  
  
    /* Set output to the current */  
    plhs[0] = mxCreateScalarDouble(current);  
  
    return; }
```

## **MODULAR PHOTOVOLTAIC-MILLIFLUIDIC ALGAL BIOREACTOR SYSTEM**

NSF Summer Undergraduate Fellowship in Sensor Technologies

Linda McLaughlin, Electrical Engineering, Community College of Philadelphia

Advisors: Jay Zemel, Jorge Santiago, David Graves, Michael Mauk

### **ABSTRACT**

Photovoltaic cells and biofuel technologies have never been fused together to the best of our knowledge. The long term goal of this project is to use these two technologies to develop a prototype to convert the sun's radiation to different forms of power. The purpose of this present study is to design a PBR that provides light and dark periods the algae need in their photosynthetic process to increase algal growth. For this reason, light shielding (dark regions) was supplied by separated solar cells placed periodically over the PBR. Flat PBRs were constructed. A control PBR without photovoltaic cells providing dark periods was set up and exposed to sun radiation. Data obtained was compared with the one that had solar cells upon it. Cell concentration decreased in the system without solar cells (control) on a sunny day. Preliminary observations suggest that the Light/dark period PBR system led to an increase of cell growth under the same conditions. Yet, because of minimal data acquisition and presence of limiting factors such as CO<sub>2</sub> depletion, feedstock supply, degassing system, and temperature control, future investigation will be needed. Further studies, in which photovoltaic cells will be used with this dual purpose: converting light into electrical energy and provide the light shielding the algae need to improve growth, will need to be done.

## **1. Introduction**

The long term goal of this project is to convert solar radiation into useful power through the fusion of two technologies: photobioreactor and solar cells. The PBR will be used to grow and harvest algae to produce biofuels and byproducts. The other goal is to use the solar cells to provide power for the bioreactor in order to achieve its basic functions like mixing and gassing-degassing. In order to approach the photobioreactor design, the first step was to understand the algae photosynthetic process, which in future research will implement the conditions required for maximum algal growth. Work this summer has explored a hybrid system, using a flat photobioreactor and solar cells placed over it. Prior research has suggested that light/dark cycles using the flashing light method [1] can increase growth over constant illumination. Our major goal was to test this hypothesis.

## **2. Background**

### **2.1 Algae and Photosynthesis:**

Algae are a natural choice for maximum yield of biofuels because they [1]:

- Intrinsically offer the greatest flux tolerance and photosynthetic efficiency as a consequence of a minimum of internally competitive plant functions.
- Enjoy fast reproductive cycles.
- Have limited nutrient requirements.
- Can readily be exposed to temporal and spectral irradiation distributions and intensities that are not encountered in nature but appear to be optimal for bioproductivity via cleverly crafted photonic systems.

Photosynthetic organisms (PO), such as algae, transform visible light in the 400-700 nm part of the solar spectrum [2]. The energy in the form of biomass that can be obtained via photosynthesis depends on the level of PAR (Photosynthetic Active Radiation), meaning light useful to photosynthesis. Understanding the algae photosynthetic process is a necessary first step in designing a bioreactor. The theory clearly states that photoinhibition at noon is almost impossible to prevent. Mutual shading, i.e. the continuous change between light and dark phases, represents a serious problem for ultrahigh population densities [10] and there will be limitation of growth. Experiments have been conducted using the flashing light method as well

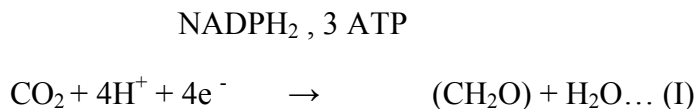
as incorporating mixing effects in the PBR. Flashing light is the imposing of on-off character to a continuous light source [1]. According to Gordon [1], experiments with dense culture combined with short light/dark cycle times produced increase of algae cells. Gordon's experiments used flow rates that allowed average light/dark cycle times of the order of tens of milliseconds. His experiments has produced  $\sim 17 \text{ gm}^{-2} \text{ h}^{-1}$  at flux values up to  $\sim 8000 \text{ } \mu\text{mol photons m}^{-2} \text{ s}^{-1}$  using the flashing light effects. Gordon stated that this elevated productivity was a consequence of hydrodynamically shortening the average light exposure time  $\tau_{\text{exp}}$  to the order of milliseconds. This value of  $\tau_{\text{exp}}$  is closer to the  $\tau_{\text{dark}}$  of the order to ten to hundreds of microseconds. Consequently, he concluded that the optimal bioreactor strategy must combine rapid algae transit times with optimal flashed light. For simplicity, the use of flashing lights periods haven't been used in our experimentation. Mixing effects haven't been used either to avoid turbulence. Instead, photocells have been placed over the PBR to give the shielding (Dark periods) and spacing between the photocells (light periods) the algae need to grow. Laminar fluid dynamics is the base of the PBR design. Reynolds numbers lesser than 2000 ensures laminar flows; thereby low velocities are achieved.

## 2.2 Algal Photosynthetic process:

Photosynthesis represents a unique process of solar energy conversion. Algae photosynthesis is expressed as a redox reaction driven by light energy (harvested by chlorophyll molecules), in which carbon dioxide, water and nutrients are converted into lipids, carbohydrates, proteins, and oxygen. The conversion is divided into two stages, the so-called *light reactions* and *dark reactions* [3].

- Light reactions: Light reactions occur on photosynthetic membranes, in which the light energy is converted to chemical energy providing a biochemical reductant  $\text{NADPH}_2$ , and ATP, a high energy compound [3].

- Dark reactions: Dark reactions take place in the stroma, in which  $\text{NADPH}_2$  and ATP are utilized in the sequential biochemical reduction of carbon dioxide [3]. In order to fix one molecule of  $\text{CO}_2$ , three molecules of ATP are required [3]



## 2.3 Algae and its growth requirements:

Algae's growth conditions require careful measures in order to keep algal culture chemically and biologically clean, as well as allowing exchange of CO<sub>2</sub> and O<sub>2</sub> between medium and atmosphere [4]. In this project, we examined the growth condition of algae culture in a closed environment (bioreactor).

The general nutrient requirements for optimal algal growth are [5]:

- I) The total salt content, which is determined by the habitat from where the algae originates.
- II) Nutrients such as K<sup>+</sup>, Mg<sup>2+</sup>, Na<sup>+</sup>, Ca<sup>2+</sup>, SO<sub>4</sub><sup>-</sup> and Cl
- III) Nitrogen sources, specially nitrate, ammonia and urea.
- IV) pH
- V) Trace elements and some chelating agent such as EDTA (ethylenediamine-tetraacetic acid). It is added because it complexes with elements such as iron, making them more soluble and readily available to the cells.
- VI) Vitamins and CO<sub>2</sub> supply.

## **2.4 Processes that algae undergoes during photosynthesis:**

### **2.4.1 Photoinhibition:**

Photoinhibition is defined as a light-induced decay of photosynthesis, and it is manifested as a decrease in the maximum quantum yield of photosynthesis [6]. Technically, photoinhibition is associated with prolonged exposure of the algal culture to excessive light, producing damage to photosystem II (PSII) thereby affecting the algal productivity.

### **2.4.2 Photorespiration:**

Photorespiration is the process where the organic carbon is converted into CO<sub>2</sub> without any metabolic gain. Photorespiration is stimulated by a high O<sub>2</sub>/CO<sub>2</sub> ratio. For optimal yields in microalgal mass cultures, it is necessary to minimize the effects of oxygen photorespiration. Therefore, a higher ratio of CO<sub>2</sub>/O<sub>2</sub> is necessary. Research has shown that oxygen accumulation in the culture is an obstacle to the development of closed bioreactors requiring. Therefore; an efficient degassing system will be needed [7].

### **2.4.3 Effect of suboptimal temperature on photoinhibition and culture productivity:**

Algal cultures that are grown outdoors are exposed to environmental stress such as non-optimal temperature. Increased susceptibility to photoinhibition can be caused by several mechanisms associated with temperature variations; for instance, low temperatures will [7]:

- Slow the rate of CO<sub>2</sub> fixation, thus causing reduction of electron transport compounds (in Photosynthesis)

Inhibit the PS II repair cycle during photoinhibition.

- In order to reduce such stresses, a system to regulate temperature in the bioreactor will be needed.

## **2.5 Photovoltaic Cells**

Photovoltaic cells are a relatively mature source of electrical power with conversion efficiencies in 14-20% range. Photovoltaic cells are used to convert solar radiation to electricity. They are made of semiconductor materials such as silicon. Silicon is an excellent material for solar cells. It is the most popular used. In principle, all that is needed to generate electricity is an excited state or states, in which a carrier can be excited from the ground state by photon absorption [8]. A solar cell consists of a layer of semiconductor materials with different electronic properties [9]. Essentially, a slab or film of Si is *n*-doped and *p*-doped in its surface regions (forming an *n*-*p* junction). This structure is positioned between a transparent front electrode arrangement and an opaque metallic back electrode. The device is supported by glass or polymeric foil [8]. Light consists of particles called photons. When light hits the solar cells, some of the photons are absorbed in the region of the junction and are free to move through the silicon and into the external circuit [8]. Since not all the light is absorbed, antireflective coating is used to decrease reflection of light.

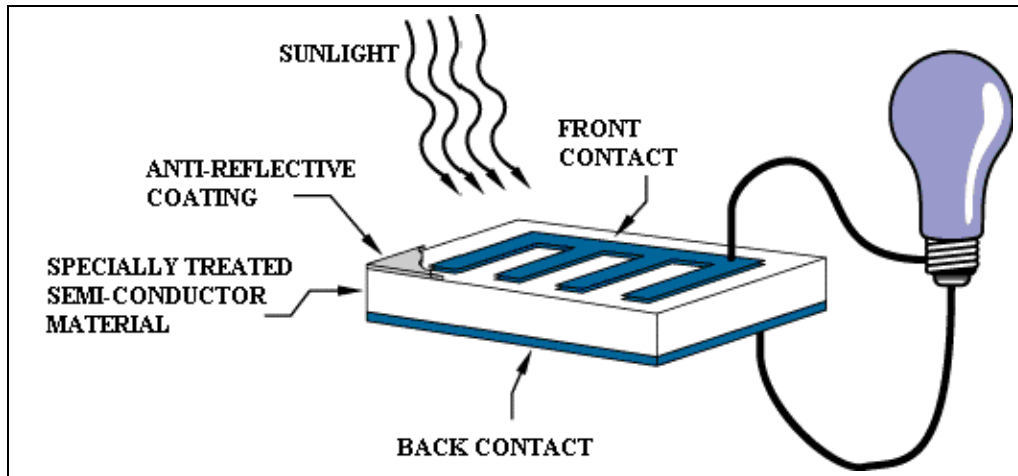


Fig 1: Photovoltaic cell

Source: <http://science.nasa.gov/headlines/y2002/solarcells.htm>

### 3. Approach and Methods

Section 2 describes the many factors in the production of algae. A major focus of this summer's effort was to address the photo-bleaching or photoinhibition problem. An alternative would be to provide to the system both shading and the light-dark periods the algal culture requires to grow efficiently.

#### 3.1 The Parallel PhotoBioreactor Approach:

As stated previously, photobleaching represents a problem, especially at midday. For this reason, our PBR uses photovoltaic cells to shield portions of the reactor from the solar light (solar cells over the PBR).

#### 3.2 The following solutions are being explored:

- Prototype of a flat bioreactor that provides dark and light cycles for efficient algal production.
- Photobleaching
- Types of alga used
- The PBR design.

### 3.2.1 The Bioreactor Construction:

A flat bioreactor model has been designed, using laminar fluids for simplicity. Laminar flows are characterized by smooth and constant fluid motion. In fluid mechanics, Reynolds number  $Re$  is a dimensionless number that give the measure of the ratio of inertial forces to viscous forces. It is used to characterize different flow regimes, such as laminar or turbulent flow. Laminar flow occurs at low Reynolds number, where viscous forces are dominant, and it's characterized by smooth, constant fluid motion. If we were to work with turbulent fluids, more energy would be needed to maintain the system, and the complication of the system will go far beyond scope to be solved now.

#### Laminar flow

- $Re < 2000$  ( See appendix c for formula)
- 'low' velocity
- Fluid particles move in straight lines
- Simple mathematical analysis possible

Reynolds number:

$$Re = \frac{\rho u d}{\mu} \quad \dots(1)$$

$$D_h = \frac{4LW}{2(L+W)} = \frac{2LW}{L+W} \quad \dots(2)$$

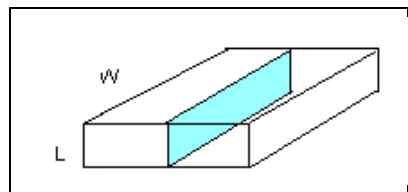


Fig 2: Cross section of Rectangular duct

Where  $D_h$  represents the hydraulic diameter of the PBR. In our case  $W$  is the dimension of the length of the solar cell: 39 mm, and  $L$  is the height of the PBR (See Fig2). Since dealing with laminar fluids simplified our calculations. It is assumed that  $D_h$  is not greater or lesser than  $2L$ . Various Reynolds numbers have been chosen to get the average velocity.

For instance, in Fig. 2, two different  $Re$  have been chosen to get the average velocity  $V$

Reynolds Number	Hydraulic Diameter d(mm) ~ 2L	D. Viscosity (mm <sup>2</sup> /sec)	T ( C)	V(mm/sec)
360	10	1.002	20.0000	36.072
365	10	1.002	20.0000	36.573

Table 1: Data obtained using equation 1

With this understanding, the specifics for our PBR were obtained. Refer to Appendix D

The velocity of the system was calculated using equation 1.

The height of the PBR has been calculated using equation 2.

Our initial approach of the Photobioreactor :( Refer to Appendix A to see all materials used)

Acrylic material was chosen because of its transparent properties. Our first PBR design (See Appendix D) was designed in AutoCAD. To glue the parts, methyl methacrylate-methanol solution MMA, an organic solvent material, was used. Four pieces were glued together: The dimensions, based on Reynolds number calculations were 230x98x5.4mm. The thickness of the PBR was decided to be 1cm. According to the literature, *Chlorella* grows well under a 1cm. thickness. The height of the PBR was kept to 5.4 mm. The calculation based on laminar flows gave us the chance to choose the hydraulic diameter, and height. The width of the PBR was kept a constant: 78 mm, which was the width dimension of two small solar cells. Using Reynolds numbers lesser than 700 gave us dimensions of 5.4 mm of height for the PBR. One Inlet hole of 3.1mm of diameter was drilled on each side of the model for tube connection. Unfortunately, the system couldn't withstand the preliminary leakage water testing. Leakage was detected in the middle part. It was decided then to reduce the width of the PBR to 39mm, keeping the same height (see Fig 3) and tube inlet dimensions. In the same fashion, this system was cut and glued. This PBR was tested for water leakage. The testing was successful. This model was used as a control. It was exposed to full sun radiation to observe photobleaching. Reynolds number calculations indicated that the flow was 6.27mL/s, which gave us a velocity of approximately 36mm /s, but the system, could not withstand the required pressure to sustain this flow. If velocities were increased in the PBR, air bubbles formed and the pressures would have caused the PBR components to separate. As a result, this system was used with a velocity of approximately 29 mm/s. So, two more inlet holes were added to the sides with the purpose to decrease pressure drops .Fig 2, 6, 7 show an implementation of the control model.

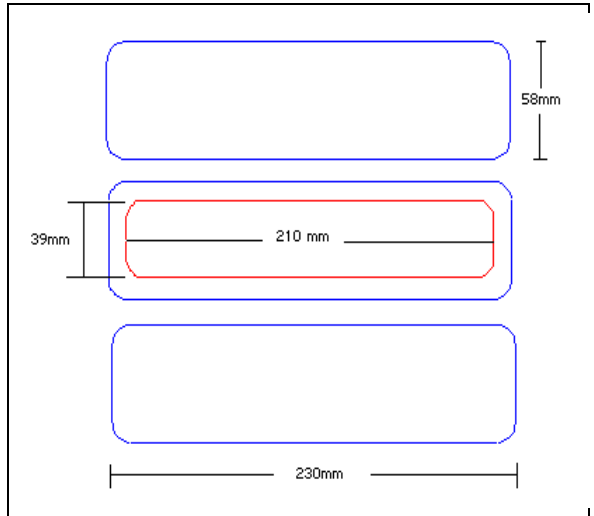


Fig. 3: Our PBR design

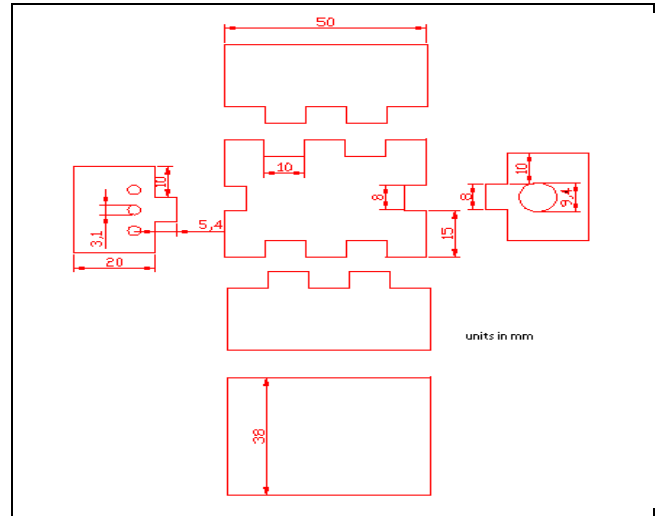


Fig. 4: Tanks to connect tubes between the three inlet holes of the PBR to a one tube



Fig 5: Control Model Exposed to sun radiation

The two additional holes added to each side of the PBR helped to decrease pressure drop, but still achieve a velocity of approximately 36 mm/s. This improved model was used to test the light and dark reaction periods. An arrangement of nine solar cells was placed upon each PBR. Each solar cell was separated given 0.1(Dark spacing+ light spacing). Our dark spacing was 23mm, the width of each solar cell. Specifically, a light spacing/dark spacing of 1/10 ratio was used. The light spacing was calculated to be 2.33mm

Fig. 6-7 show our improved model.



Fig 6: Implementation of control model

Fig 7: 1/10 Light/Dark cycle PBR

length(mm)	Fraction open	Velocity mm/s	Light time-sec	Dark time-sec	Pressure(Pa)
2.33	0.1	35.715	0.006523869523	0.05871483	0.638
2.33	0.1	36.072	0.006459303615	0.05813373	0.651
2.33	0.1	37.575	0.006200931470	0.05580838	0.706
2.33	0.1	75.150	0.003100465735	0.02790419	2.824

Table 2: Light/dark periods

The calculation of time was done using the velocity obtained with Reynolds numbers. The light spacing for a 1/10 ratio was 2.33 and taking the velocity 35.715 then the time the fluid will take to past the light region will be :  $\text{time} = \text{space} / \text{velocity} = 2.33 / 35.715 = 0.00653 \text{ sec}$  ( see table 5 above), the light time-sec obtained is lesser than the dark time each cell undergoes under laminar average velocity. The purpose is to have the cells moving in a continuous flow, so they can get the sunlight but don't get overexposed to it.

### 3.2.2 Pump Choice:

Two types of pump were available: syringe, or peristaltic. It was decided to use a peristaltic pump because different flow rates could be achieved. The syringe pump emptied the cell culture too fast. For instance, for our control model, syringe pump emptied in approximately 9.57 seconds and then reversed the direction with a velocity of 29.77mm/s. Furthermore, achieving high flow rates was difficult. On the other hand, it was worrisome that peristaltic pump could possibly crush the cell walls of the cell. Therefore, trials were run to observe the effect on algae cell wall breakage. A peristaltic pump was used to pump the cells for 18 and 36 hours. The samples were centrifuged them at about 10 rev/min for 10 minutes each. The results are shown in Fig 8.



Fig 8: Comparison of cells sample after centrifugation

On the left: algal sample, no pump used, in the middle: sample pumped y a peristaltic pump during 18 hours in the peristaltic pump, and on the right: sample pumped during 36 hours.

#### **4. Preliminary experimentation:**

##### **4.1 Algae Choice:**

Three algae sample algal culture were chosen: *Chlorella*, *Anabena*, and *Euglena gracilis*. In order to have an idea of alage growth under different conditions, the next steps have been followed:

1. Samples of the *Chlorella*, *Anabena*, and *Euglena gracilis* have been placed in Petri dishes, using 10 ml fertilizer diluted in water (tap or distilled water) of concentration 0.98g/L as nutrients.

2. *Chlorella* sample was exposed to sunlight from 10 am to 4 pm at an average temperature of 27°C and exposed the halogen lamp. *Anabena* was exposed to artificial light from 9:30 to 4:00 pm. at room temperature, using an iluminator-Fiber-lite lamp.

3. The sample of *Anabena gracilis* algae was exposed to sunlight from 8:00a m to 11:30pm on a sunny day and taken away from the sun at noon and placed to a shaded area. The sample was returned to light from 2:00 pm to 5:00 pm. The average temperature was around 30° C. Another sample of the same species of algae was exposed to artificial light, using a 40 Watts sunbeam bulb in a lamp.

Results for these first preliminary experiments:

**First group** (*Chlorella*, *Anabena*, and *Euglena gracilis*): Sun light exposure.

Optometer reported on a cloudy day: 17.5 kCd/m<sup>2</sup>

This group didn't survive to light exposure. We actually did another trial, using the same kind of culture without success. It was evident that sunlight and temperature factors are crucial problems to solve.

**Second group** (*Chlorella*, *Anabena*, and *Euglena gracilis*): Exposed to Fiber optic illuminator. Optometer reading reported: 30.5 kCd/m<sup>2</sup>

*Chlorella* was exposed to artificial light at 7cm. of distance, using the Fiber optic illuminator-Fiber-lite lamp (Model 190 120VAC, 60Hz, and 50 Watts). Tap water was used to dilute the fertilizer. The culture didn't show any discoloration as in the first group exposed to sunlight. For the rest of the week, we noticed that it was alive (green color present), but growth was not noticeable. The Fiber optic lamp used didn't heat the sample, which stayed at ambient temperature all the time.

The other two: *Anabena* and *Euglena gracilis* samples were exposed by the Halogen lamp (12V max X 50 Watts 60Hz.) No improvement noticed. Photobleaching of the samples followed, and finally we concluded they died. The lamp seemed to produce too much heat. We noticed that the Petri dishes were hot to the touch.

Third Sample: *Euglena Gracilis*

Optometer reported: 26.3 kCd/m<sup>2</sup> on sunlight and 4.3 kCd/m<sup>2</sup> on artificial light.

A sample of *Euglena gracilis* was exposed to sunlight from 8:00am to 11:30am on a hot day. Average temperature: 80 degrees. The sample was taken away from the sun and placed in a shaded area, but returned to sunlight from 2:00pm to 5:00pm. At this time, discoloration of the sample was noted (green to transparent), and by night, I concluded the algal sample had died. Another sample was exposed to artificial light, using the 40 Watts sunbeam bulb in a lamp from 8:00 am to 5:00pm and didn't show discoloration, remaining green. The sample didn't seem to show increment of temperature which remained at a constant 21 Celsius temperature. This sample has remained alive for three days at present. For this experiment, distilled water is used to dilute the fertilizer.

*Chlorella* was chosen because after inspection *Anabena* clumped together, *Euglena gracilis* seemed too big in comparison to *chlorella* according to available literature.

#### **4.2 Experiment: Measurement of solar cell's voltage:**

These measurements have been done in order to compare the luminance obtained using different kinds of lamps and solar radiation. It was also necessary to know how transparent acrylic or Plexiglas materials were to let the light get through. The next steps were followed:

1. A solar cell is exposed to sun and artificial light and measurements of the voltage are taken. The solar cell is now placed underneath of an empty Petri dish and the measurement of voltage is taken. The Petri dish is now filled with fertilizer diluted in water, and again we proceeded to measure the voltage. Finally, the algae culture is added on the Petri dishes, and we measured voltage again.
2. Using an optometer, which is placed perpendicular to the light, measurements of the luminance (cd /m<sup>2</sup>) are taken for all samples in the stated conditions.

Data obtained using a solution of water and fertilizer and a 40 Watts sunbeam bulb in a lamp:

	Voltage (V)
S. cell exposed to the lamp's light	0.4540
S. cell underneath an empty petri dish exposed to the lamp's light	0.4490
S. cell underneath a petri dish that contains a solution water&fertilizer	0.4490
S. cell underneath a petri dish that contains algae and solution water&fertiliz	0.4460

Table 3: Solar cell's voltage reading

$$\% \text{ change in voltage} = (0.4540 - 0.4460)/0.4540 \times 100 = 1.76 \%$$

Measurements obtained using the Fiber optic lamp: using *Chlorella* for the last voltage's measurement:

	Voltage (V)
Solar cell exposed to the lamp's light	0.4890
S. cell underneath an empty petri dish exposed to light	0.4870
S. cell underneath a petri dish that contains a solution water&fertilizer	0.4890
S. cell underneath a petri dish that contains algae and solution water&fertiliz	0.4860

Table 4: Solar cell's voltage reading using a Fiber Optic lamp as a source of light

$$\% \text{ change in Voltage} = (0.4890 - 0.4860)/0.4890 \times 100 = 0.6\%$$

Using *Euglena Gracilis* on sunlight:

	Trial 1	Trial 2	Trial 3	Average
	Voltage (V)			V
S cell exposed to sunlight at 1:25 pm	0.5450	0.5350	0.5400	0.5400
S. cell underneath an empty petri dish exposed to sun light	0.5000	0.4890	0.4930	0.494
S. cell underneath a petri dish that contains a solution water&fertilizer	0.5050	0.4910	0.5040	0.500

Solar cells exposed to sunlight: (control sample), T = 80 degrees. Sunny day about 1000w/m<sup>2</sup>

Table 5: Solar cell's voltage reading using sunlight as a source of light

% change =  $(0.04)/0.54 \times 100 = 7.407\%$  (decrease in efficiency comparing to 0.54V initially measured)

This would seem to indicate that placing PV cells under the reactor would not seriously decrease their electrical power generation capability.

## 5. Photobleaching and growth yield experiments

Two different experiments were conducted. The first one was a control (no dark/light periods.) This PBR was exposed to sunlight using range approximate velocities of 23-30mm/s. Flow rates of 4.86-6.27 mL/s were calculated based on the settings of the peristaltic pump. For the second experiment, the 2 PBRs system with the solar cells laid upon them were used with Light and dark cycles of 1/10 ratio. The two systems were run simultaneously. The basic idea was to compare yields. Recording of temperature and luminance were done about every 1-2 hours. Cell counting was done before and after the experiments.

## 6: Results

Unfortunately, due to amount of rainy days and deadline time, we were unable to collect a substantial data. During the days of sun exposure, our control system had increased cell growth when the sample was analyzed. We noticed that those days were cloudy and with illuminance reading below 37Kcd/m<sup>2</sup>. (See Appendix B). A second control system indicated cell decrease on a sunny day. The midday temperature reported was above 50° C. The illuminance reading upper bound was about 46 Kcd/m<sup>2</sup> for this last case; we have the hypothesis that photobleaching was the cause of cell death, but further experimentation will need to be done. Finally, cell concentration from the light/dark PBR was analyzed after and before sun exposure. Our minimal data acquisition indicated an increase on cell numbers on a particular sunny day.

The higher illuminance reading was reported about 70 kcd/m<sup>2</sup>, followed but a decrease of cell concentration on a cloudy day. Limiting factors such as CO<sub>2</sub> depletion, feedstock requirements, and high temperatures are suspected to be the cause of this decrease in cell concentration. For detailed data information refers to appendix B.

## **7. Conclusion**

Our minimal data acquisition did not yield enough results to have conclusions regarding cell growth and photobleaching. More experimentation will be needed. Limiting factors such as CO<sub>2</sub>, feedstock supply, temperature control systems will need to be controlled while each factor is examined. We hypothesize CO<sub>2</sub> depletion was the critical nutrient and that everything else was limited by the supply of this nutrient. Nevertheless, we were able to approach and construct our PBR design.

## **8. Future work section**

Different light/dark cycle regions will need to be used and compared with a control (PBR without solar cells upon it), both exposed on full sun radiation. For instance, using light and dark cycles regions of 2/10 ratio, and so on. Cell concentration counting will need to be done in trials for each sample to obtain accurate data. The following limiting factors will need to be studied:

- Surface- to-volume ratio of Flat PBR.
- CO<sub>2</sub> supply system
- PBR Orientation and inclination.
- Mixing and degassing devices.
- Systems for cleaning and temperature regulations.
- Transparencies and durability of the material.
- Type of algae
- Feedstock system.

In this study, it is suspected that uncontrolled limiting factors are the reasons of death cells. Consequently, research and experimentation on each one will be crucial to achieve high algae

productivity. Finally, when these limiting factors are known to be controlled, high efficiency solar cells will need to be implemented into the system. The goal is to operate our light/ dark period PBR using minimum power. Therefore, the systems that will control the PBR processes will need to be engineered effectively to high efficiencies. The excess power (produced by solar cells, but not used for the PBR) will be stored for use elsewhere.

## **9. Acknowledgments**

I would like to thank Jay Zemel who has afforded me the opportunity to participate in this research. I would also like to thank Michael Mauk, David Graves, and Jorge Santiago, with whom I worked closely for the construction and completion of this project. Lastly, I would like to acknowledge and thank Dr. Jan Van der Spiegel and the NSF-funded SUNFEST Program for their research support

## **10. References**

[1] J. Gordon, "Ultrahigh bioproductivity from algae," *Appl. Microbiol Biot*

*chnol* (2007) 76 : 969-975,971

DOI 10.1007/s00253-007-1102-x, July 2007.

[2] K. Dimitrov, " GreenFuel Technologies: A Case of Study from Industrial Photosynthetic Energy Capture,"p. 4[online].

Available: <http://www.nanostring.net/Algae/CaseStudy.pdf>

[3] J. Masojidek, " Microalgal Culture,"in *Photosynthesis in Microalgae*, edited by A. Richmond, Ed. Blackwell Science Ltd, 2004, pp. 20-21, p. 30

[4] I. Probert, "Microalgal Culturing," Basic concepts,[Online].

Available: [http:// www. Nhm.ac.uk/hosted \\_sites/ina/CODENET/culturenotes.htm](http://www.Nhm.ac.uk/hosted_sites/ina/CODENET/culturenotes.htm)

[5] J. Grobbelar, “Algal Nutrition,” edited by A. Richmond, Ed. Blackwell Science Ltd, 2004, p. 98

[6] M. Tredici, “Mass production of Microalgae: Photobioreactors,” edited by A. Richmond, Ed. Blackwell Science Ltd, 2004, p. 98.

[7] A. Vonshak&G. Torzillo, “ Environmental Stress Physiology,” edited by A. Richmond, Ed. Blackwell Science Ltd, 2004, p. 72, p. 64, p 69.

[8]C. Granqvist, “ The Radiation Around us& How it can be used: Review of Solar Energy Materials,” presented on a Workshop on “ Physics for Renewable Energy,” The Angstrom Laboratory, Uppsala University, Sweden, October 17-25, 2005,p 9-10

[9] PennState, office of Physical Plant, “ Solar PV(photovoltaic). Source retrieved from <http://energy.opp.psu.edu/projects/ecms/solar-pv-photovoltaic> on August 7, 2009.

[10] A. Gitelson, “Photic Volume in PhotoBioreactors Supporting Ultrahigh population Densities of the Photoautotroph *Spirulina Platensis*,” Applied and Environmental Microbiology, May 1996, p. 1570-1573 0099-2240/96/\$04.00 + 0, Copyright 1996, American Society for Microbiology, p.1.

#### **Appendix A:** Material used for the PBR-solar cells construction

1- Peristaltic Pump (Master Flex, Cole-Parmer, Model Number 7553-71, and Motor: System model N 75530-70, 6-600 RPM)

2- Organic solvent methyl methacrylate(*MMA*)

3- Optometer( Model GO 352 by GRASEBY OPTRONICS)

- 4- Solar cell 21mm X 39mm (7% efficient)
- 5- Halogen lamp (12V max X 50watts 60Hz)
- 6- Fiber optic illuminator-Fiber-lite lamp (Model 190 120VAC, 60Hz, 50 Watts)
- 7- 40 Watts sunbeam bulb, 305 lumens, in a lamp.
- 8-Algae: *Chlorella*, *Euglena Gracilis*, wild algae.
- 9- Fertilizer dissolved in distilled water with concentration: 0.98 g/L

The fertilizer (Rose Plant Food by Miracle-Gro) contains:

- Total nitrogen 18%:
  - 2.4 % Ammoniacal Nitrogen
  - 15.6 % Urea Nitrogen
- Available Phosphate (  $P_2O_5$  ) : 24%
- Soluble Potash (  $K_2O$  ) : 16%
- Copper ( Cu ) : 0.05 %
- Iron (Fe) : 0.10%
- Manganese (Mn) : 0.05%
- Zinc (zn) : 0.05%

10- Voltmeter.

11- Acrylic plastic 5.4mm of thickness.

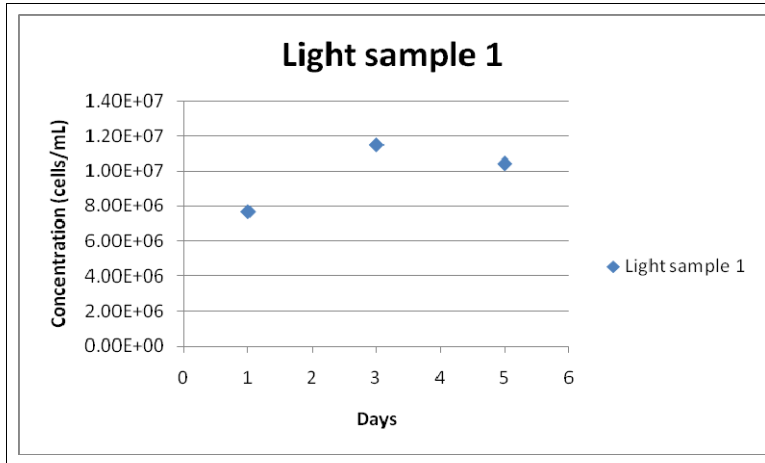
12-Plastic tubes: -1/4" in OD, wall 1/16 in, 3/8" OD, # 14-169-1J

- 1/8" OD, 1/32" wall, # 14-169-1B

## **Appendix B:** Cell counting Data

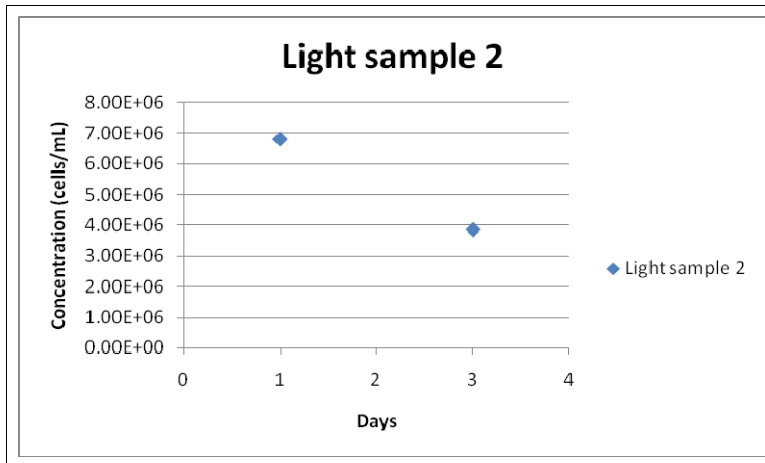
1. Control PBR

Day	Light sample 1
1	7.67E+06
3	1.15E+07
5	1.05E+07



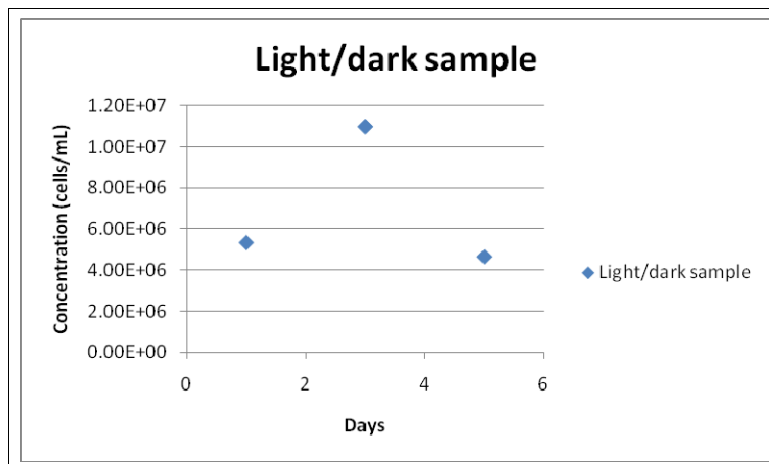
2. Second run for our Control sample :

Day	Light sample 2
1	6.83E+06
3	3.85E+06
5	0



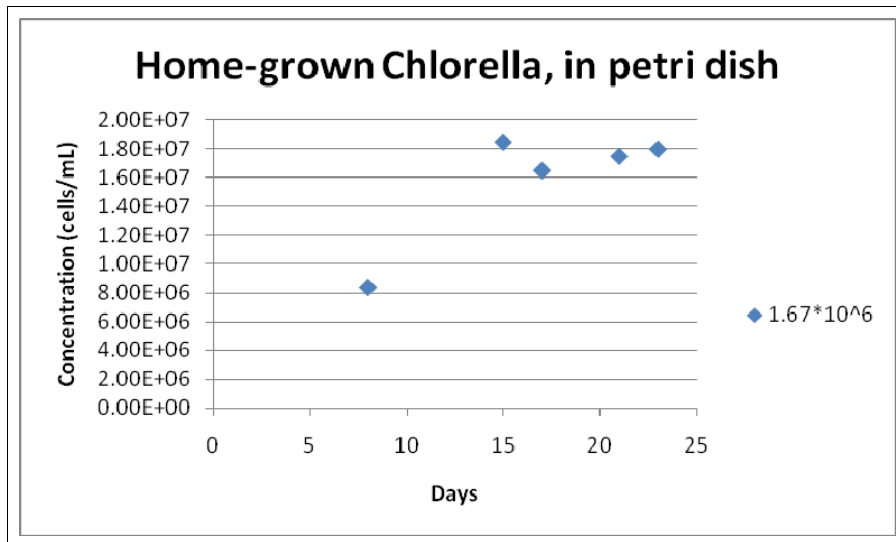
### 3. Light/Dark Cycle PBR experiment

<i>Day</i>	<i>Light/dark sample</i>
<i>1</i>	<i>5.34E+06</i>



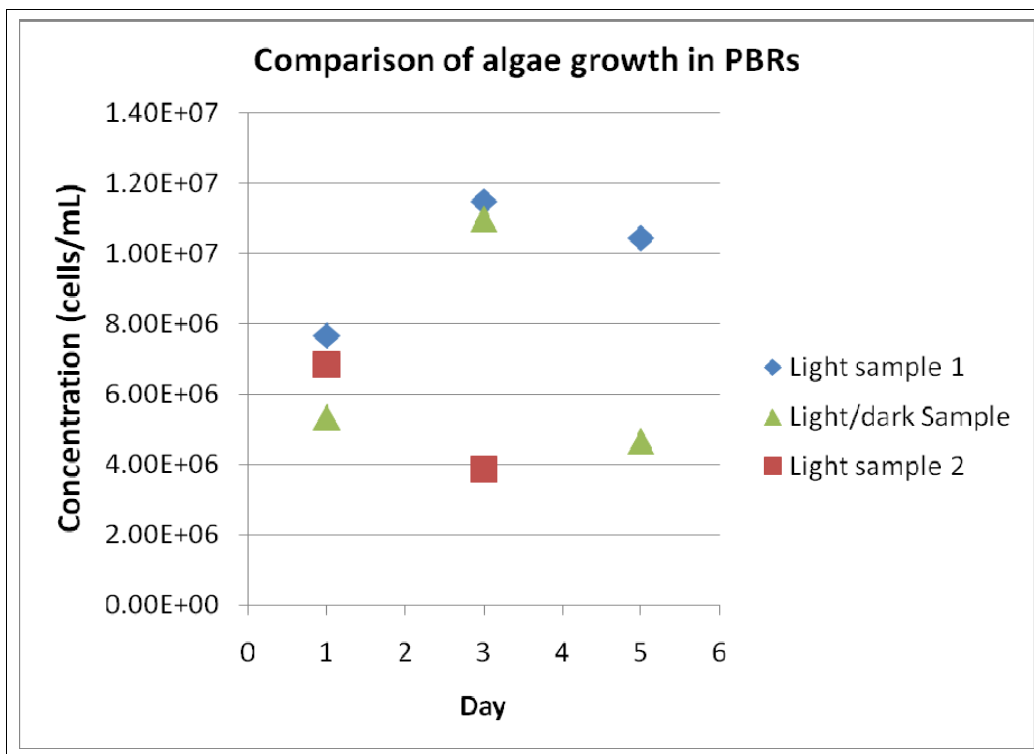
4. Chlorella grown indoors under temperatures 25-30° C, at 4 Kcd/m<sup>2</sup>

day	1	8	15	17	21	23
Cell concentration	1.67*10 <sup>6</sup>	8.35E+06	1.85E+07	1.65E+07	1.75E+07	1.80E+07



5. Comparison of algae concentration of all samples:

Day	Light sample 1	Light sample 2	Light/dark sample
1	7.67E+06	6.83E+06	5.34E+06



### Appendix C: Reynolds number and laminar fluids

Reynolds number:

$$Re = \frac{\rho u d}{\mu}$$

Laminar flow:  $Re < 2000$

Transitional flow:  $2000 < Re < 4000$

Turbulent flow:  $Re > 4000$

### Appendix D: specifics for the first PBR design

Reynolds numbers: 360 (This number was chosen, and many other Reynolds number will give different values of average velocity)

$D_H = 10.1$  mm (hydraulic diameter)

$\nu = 1.002$  mm<sup>2</sup>/s (Dynamic viscosity of water)

Temperature = 20 °C

Velocity = 35.715 mm/s

Reactor length = 210mm

Reactor width = 78mm

Solar cell = 21mm X 39mm

PBR height = 5.4 mm

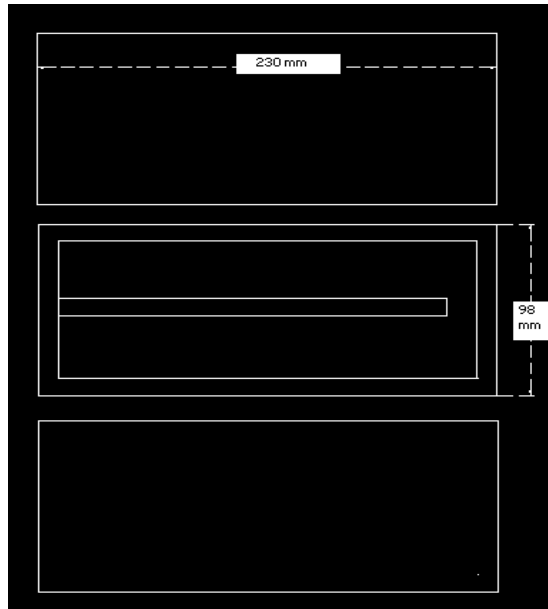


Fig: First PBR design

## **ANALYSIS OF DARK AND LIGHT CYCLES ON CHLORELLA GROWTH**

NSF Summer Undergraduate Fellowship in Sensor Technologies

Ieva Narkeviciute, Chemical Engineering, University of Massachusetts Amherst

Advisor: Jay Zemel, Jorge Santiago, David Graves, Michael Mauk

### **ABSTRACT**

Photovoltaic (PV) cells and photobioreactors that grow algae for the production of biodiesel have never been combined in a hybrid system even though they both use the sun as a source of energy. The goal of this study was to design a photobioreactor that combines modular PV panels for dark and light (DL) periods to increase algal photosynthesis. Simultaneously, the PV panels produce electrical energy that will power the system and any excess power could be fed to the electrical grid. Two bioreactors were constructed. One reactor was not covered by solar cells and served as a control for the experiment. The second reactor had 90% of its surface covered by solar cells to provide dark periods. One goal was to reach comparable or higher yields for the DL reactor in comparison to the uncovered reactor. Another was to examine whether short, cyclic DL periods increase growth. Data acquisition was minimal, but preliminary results show that the system without DL periods had a longer doubling time than the one with the DL periods, proving that the cycles increase growth.

## 1. INTRODUCTION

Photovoltaics and algae utilize solar radiation to provide energy for algae growth and photovoltaic generation of electricity.

Factors to be considered when building a photobioreactor to use for the study include:

- High surface area to volume ratio [4]
- Orientation and inclination of the bioreactor towards the sun [4]
- Degassing of oxygen in the system [4]
- Supply of carbon dioxide [4]
- Mixing of the algae slurry[4]
- Temperature control [4]
- Species of algae used [4]
- Modulated intervals of the solar panels placed on top

The main goal of the experiment was to design a photobioreactor to investigate the hypothesis that short term DL cycles can produce economically adequate algae growth and prevent photobleaching. The modulated light effect was achieved by placing solar panels periodically in a planar array onto a photobioreactor while moving the algae inside the photobioreactor in a linear flow. Thus, as the algae traveled through the reactor, they were exposed to light when they were in a region between solar panels, then to dark when they were underneath a solar panel. Furthermore, the effects of varying types of light on algae were investigated.

## 2. BACKGROUND

Solar power is a mature field that has made progress within the last 50 years. Its technological strides went from 6% conversion efficiency in 1955 up to a record 35% efficiency in recent years. Most of today's commercially produced photovoltaic panels range in the 14-20% conversion of sunlight into energy [1,2].

Biofuel is usually produced from vegetable oils, animal fats, waste vegetable oils and certain types of algae. Vegetable oils that can be used are rapeseed, soybean, mustard and sunflower. Animal fats include tallow, lard, yellow grease and chicken. The most popular form of biofuel is biodiesel and it can be produced by "transesterification." Transesterification is mixing fatty acids with methanol and a catalyst (like alkali metals or acids) to get a mixture of methyl esters and glycerol. The methyl esters are the biodiesel, and glycerol is a byproduct.

Biofuels are beneficial because their feedstock usually mitigates carbon dioxide. This feedstock only includes photosynthetic plants such as algae. Carbon dioxide, water, and sunlight are the main reactants in the photosynthetic reaction that produces glucose and oxygen. A feedstock of

biodiesel could be grown in a place where carbon emissions are high and that way mitigate carbon dioxide.

Algae are a popular feedstock for biodiesel because they reproduce fast, have small land requirements, can be farmed in bioreactors in unproductive land instead of arable land and have minimum nutrient requirements [3].

Research has been conducted to improve algae yields, but further studies must be done. Different bioreactors were used ranging from open ponds to tubular reactors, from sac reactors to flat reactors. All of them had drawbacks. Flat bioreactors overheated easily, and had problems with photobleaching. Pond reactors became easily contaminated with bacteria and other foreign organisms. Tubular reactors have problems with optimal light exposure and thick algae. Despite the associated problems, the most promising design is the flat bioreactor because it can easily be tilted to face the sun and still maximize productivity per unit volume and per unit of illuminated surface of the reactor [3]. Flat reactors can also be closely packed together, using minimal land area. They are easy to degas and mix by bubbling gases.

Light flashing experiments have been done to see whether algae exposed to short DL periods would grow faster. Studies by J. Gordon and J. Polle claim that intense light photon flux pulsing for extremely short periods of time can increase the production from the average 2-3 g dry weight  $\text{m}^{-2} \text{h}^{-1}$  to 100  $\text{g m}^{-2} \text{h}^{-1}$ [4]. Additionally, K. Terry asserts that introducing a fan to provide flashing of DL intervals can increase productivity by a factor of two [5].

### 3. METHODS

To analyze the effects of dark periods on algal growth, a clear photobioreactor with intermittently spaced solar cells laid on top of it to provide shading for the algae growing in the PBR underneath them was designed. A control PBR was also used without any shading.

#### 3.1 ALGAE GROWTH TRIALS

Algae was chosen from ten samples. The choices were *Anabaena*, *Closterium*, *Oscillatoria*, *Volvox*, *Chlamydomonas*, *Euglena Gracilis*, *Spirogyra*, *Chlorella*, *Oedogonium*, *Synedra*. After inspecting the characteristics of the algae such as tendency to clump together and relative size (not on a microscopic level) three types of algae were chosen to try to cultivate: *Anabaena*, *Euglena Gracilis*, and *Chlorella*. We added about 10 mL of Miracle-Gro Rose Plant Food fertilizer at a concentration of .98 g/L to about 2 mL of algae sample. The algae were stored in a petri dish at a sample thickness of about 2-5 mm.

All three types of algae were placed under a halogen lamp. The halogen lamp, at a close distance of 9 cm, gave luminance readings of 19.7 kilocandelas/ $\text{m}^2$ , and at a farther distance of 37 cm read 0.7  $\text{kCd/m}^2$ . Initially, the halogen lamp was held at the closer range because it compared to

the luminance values of a cloudy day (17.5 kCd/m<sup>2</sup>). Unfortunately, halogen lamps get extremely hot, and this high temperature may have killed all three types of algae because they died within several days of exposure. Instead of having a characteristic green color, they became whitish. The optimal temperature for growth of *Anabaena* is 40-45° C, for *Euglena Gracilis* it is 29° C, and for *Chlorella* it is 25° C. The temperature of the room was about 25° C, and the temperature of the samples was not recorded but empirically observed to definitely be higher than the temperature of the samples at room temperature.

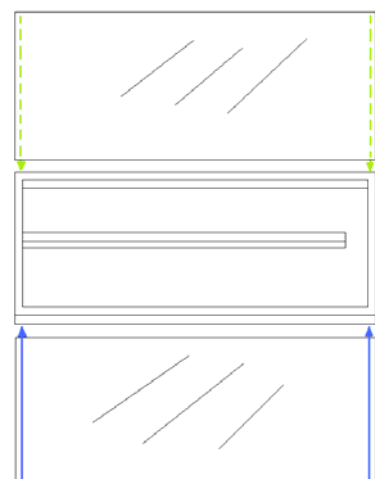
Because the halogen lamp was unsuccessful, the algae were grown outdoors. All three types of algae were exposed to direct sunlight (luminance values of ~60 kCd/m<sup>2</sup>) for periods as little as 3 hours and as long as 7. All of the samples died. Even on cloudy days with luminance values of ranging from 15 to 20 kCd/m<sup>2</sup> the samples died. Temperature was probably a factor in the death of the algae because they should be able to withstand cloudy day luminance values. Temperatures reaching the high 80s and direct sunlight easily heat up a thin layer of algae sample and kill it.

*Chlorella* was then grown indoors under a Fiber-Lite fiber-optic illuminator at a distance of 7 cm which produces a luminance of 30.5 kCd/m<sup>2</sup>. The *Chlorella* grew well with these conditions. However, the illuminator did not illuminate a large area because it was a thin beam of light. The surface that this beam illuminated was about 3 cm in diameter. Thus, all of the algae outside the range of this particular beam received minimal illumination, and the *Chlorella* under this beam grew well. Then the light was switched to an energy saving (40 W) incandescent lamp with a luminance of 4.3 kCd/m<sup>2</sup>. A sample of *Chlorella* growing under this light increased in concentration from 8.3x 10<sup>6</sup> cells/mL to 1.185 x 10<sup>7</sup> cells/mL in a week. However, this lamp still heated up the algae, so the bulb was switched to a 4 Watt LED light that had a luminance of ~131 kCd/m<sup>2</sup>. Under this light, the *Chlorella* went from a concentration of 2.96 x 10<sup>6</sup> cells/mL to 1.6 x 10<sup>7</sup> cells/mL in a week.

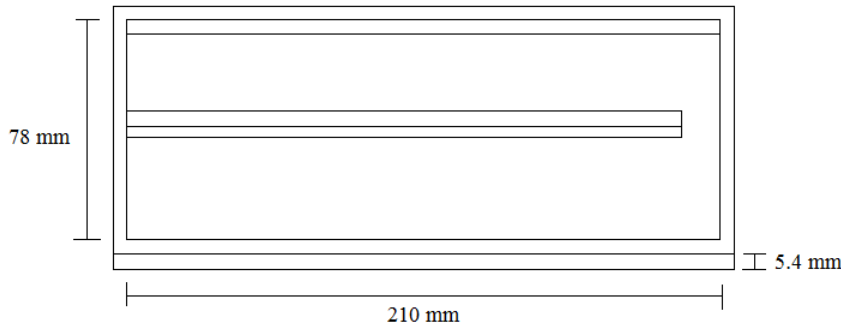
Among the algae that grew well, *Chlorella* was chosen for further study. It is suitable for the experiment because it is a small, unicellular spherical alga with a diameter ranging from 2-10µm that does not clump together.

### 3.2 PHOTOBIOREACTOR DESIGN

The PBR was made out of acrylic because it is a clear plastic that is easy to cut and glue together. To fuse the plastic together, a methyl methacrylate-methanol solution was used. To build the PBR, two thin pieces that make up the top and bottom were bonded with the center-piece that determined the internal diameter (Figure 1, 3). *Chlorella* grows well in thicknesses of about 1 cm. The thickness of the PBR was .54 cm to ensure that



all of the sun's rays penetrate the culture. The first PBR's internal width was the length of two photovoltaic cells connected in series. The dimensions of the photovoltaic cells were 21 mm wide by 39 mm long, so the width of our reactor became 78 mm. Figure 1. Construction of PBR The length of the reactor was 210 mm to allow a fraction of .5 for dark periods with 5 DL



periods. The internal dimensions of the first PBR were 5.4 mm high by 78 mm wide by 210 mm long (Figure 2). This PBR also had a strip in the middle to provide a travel path that is not 78 mm wide but

Figure 2. Dimensions of first PBR design

instead 37 mm to allow lower flow rates (Figure 2). However, the middle separator could not withstand the pressure that built up inside of the PBR and collapsed, allowing water to freely float about the reactor without following the specified path. Due to these drawbacks, the reactor width was scaled down to 39 mm.

The dimensions of the second PBR design were were: 5.4 mm high, 39 mm wide, and 210 mm long (Figure 4). This reactor only broke when a considerable amount of pressure was put on it (flow rates exceeding 6.3 mL/s). The second PBR design was the chosen design. Improvements made to the system include having 3 instead of 1 inlet and outlet streams. This decreased the pressure inside of the reactor so flow rates as high as 8.4 mL/s could be achieved.

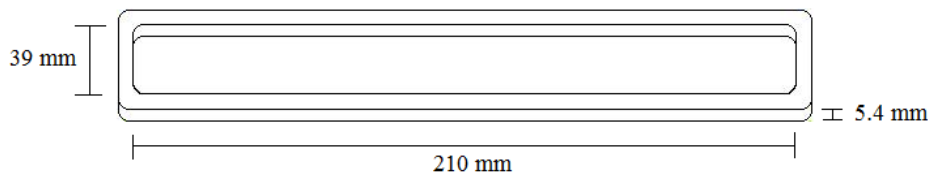


Figure 4. Dimensions of second PBR

### 3.1 DL PERIODS

The photovoltaic cells, which have a width of 21 mm, are the dark period for algal photosynthesis. The light period length can be altered. For the DL reactor a 1:10 ratio of light to dark cycles was used.

To calculate the speed of the algae, the Reynold's equation,  $Re = \rho D_H V / \mu < 2300$ , was used.  $\rho$  is the density of the liquid,  $D_H$  is the hydraulic diameter of the reactor,  $V$  is the velocity of the liquid, and  $\mu$  is the dynamic viscosity of the liquid. The following parameters were used to determine velocity:

Temperature = 35° C

Re = 500

$D_H = 9.425 \text{ mm}$

$\mu = .69 \text{ mm}^2/\text{s}$

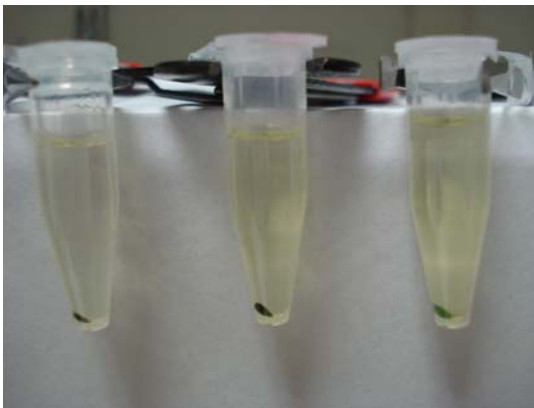
$\rho = 1 \text{ kg/m}^2$  (assume it to be the same as water)

The velocity of the algae is 36.6 mm/s. Hydraulic diameter was determined by:  $D_H = 4\text{Area}/\text{Perimeter}$  of a cross-section of the PBR perpendicular to the direction of flow. To find the amount of time that the cells are exposed to light if they are traveling at a certain speed, the length of open space was divided by the velocity. For the dark periods, the fraction of length of the reactor that is open (i.e. .1) was subtracted from 1 (to get a dark fraction of .9), then multiplied by the length of open space and divided that product by the velocity.

The length of the dark periods was predetermined to be 21 mm, and a light fraction of 0.1 was used. With these parameters, the length of light exposure is 2.33 mm. With a speed of 36.6 mm/s, the amount of time algae are exposed to light at every light period is .0064 s, and every dark period lasts .057 s. According to Gordon and Polle, for high sunlight intensity values, it is desirable to achieve exposure times that are to the order of milliseconds to avoid photobleaching and maximize growth [3].

### 3.2 PUMPING

There were two choices of pumps: syringe pumps or peristaltic pumps. The problems that arose from a syringe pump are that it empties too fast. For example, if the width of the PBR is 39 mm, and the speed of the algae is 36.6 mm/s, then a 60 mL syringe would have to empty in 7.78 seconds and then reverse direction. Furthermore, it would have a lot of trouble achieving such high flow rates.



On the other hand, a peristaltic pump has drawbacks because it could crush the cell walls of the algae. To analyze this, a sample of algae was put into a centrifuge to see the extent of the green tint of the water from the broken cells in the slurry. It was slightly green (Figure 5). The algae was then pumped with a peristaltic pump for 18 and 36 hours, centrifuged, and compared. The color of the “crushed” samples was similar to the color of the zero-hour sample. The samples were in fact greener,

Figure 5. after 0, 18, and 36 hours, respectively but very slightly (Figure 5). Unfortunately, these characteristics were only observed with the naked eye, instead of a spectrophotometer. Therefore, it became clear that using a peristaltic pump instead of a syringe pump was more practical.

### 3.3 OVERALL EXPERIMENT

Two PBRs were run, one with DL (Figure 6) periods and one without (control). The reactor constantly exposed to sunlight ran at linear flow velocities of about 23-30 mm/s. This system was run simultaneously with the system that had both DL cycles to see how algae yields compare. The second system was run at 36.6 mm/s except it had 2 PBRs, with 9 solar panels on top of each PBR placed 2.33 mm apart. The algae in the second PBR were therefore exposed to 18 DL cycles. The cultures were kept outside in sunlight for about 7 hours a day and temperature and luminance of the sun were recorded every 1-2 hours. The concentration of the cells was recorded every other day.

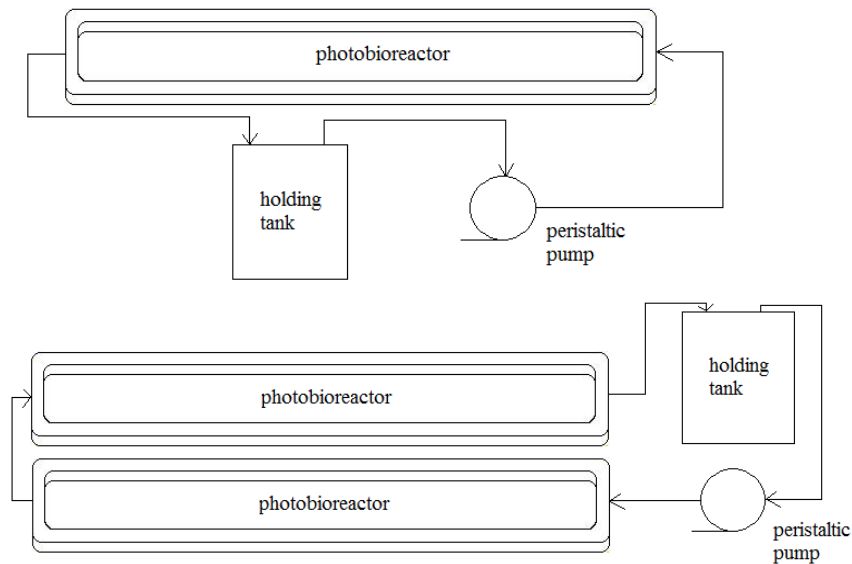
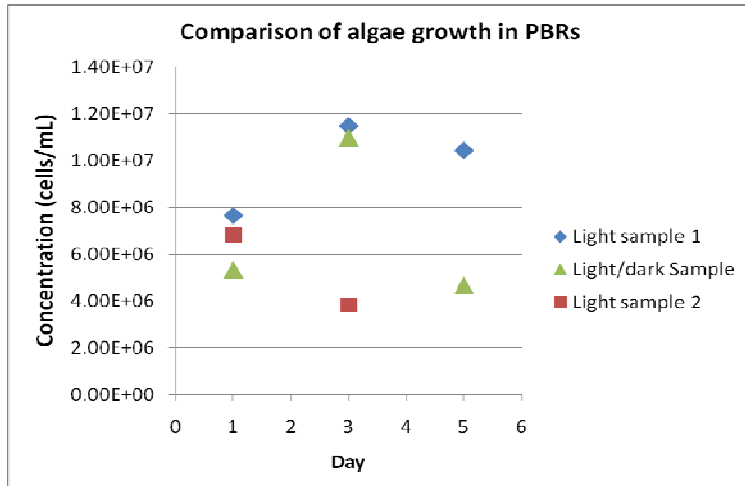


Figure 6. System which is constantly exposed to light (top), system which has DL periods (bottom)

## 4. RESULTS



Cell growth increased in two of the three samples tested, and then dropped in both of them. In the third sample, cell concentration simply decreased. The cell concentration of the light reactor 1 increased from  $7.67 \times 10^6$  cells/mL to  $1.15 \times 10^7$  in only two days with luminance values ranging from 7.5 to 36 kCd/m<sup>2</sup>. The temperature during that time hovered around 34° C. However, the concentration then dropped to  $1.05 \times 10^7$  in two days of light

Figure 7. Cell growth in three different reactors exposure. The luminance on those days ranged from 6.6 to 50 kCd/m<sup>2</sup>. The temperature went from a low of 36.5° C to a high of 53° C. Light reactor 2 simply had a drop in concentration from  $6.83 \times 10^6$  cells/mL to  $3.85 \times 10^6$  in only one day. The luminance was 14.2-44 kCd/m<sup>2</sup> with temperatures reaching 44° C. Lastly, the DL reactor doubled in concentration from  $5.34 \times 10^6$  cells/mL to  $1.10 \times 10^7$  in two days. These two days had a very high luminance values reaching 71.8 kCd/m<sup>2</sup>. But this sample of algae also decreased in concentration to  $4.65 \times 10^6$ . During the decrease in concentration, the luminance was 14.2-44 kCd/m<sup>2</sup>. For full description of conditions refer to appendix A and for cell concentrations listed in a table see appendix B.

## 5. CONCLUSION

Data acquisition was very minimal for the experiments conducted. Each reactor was only kept outside for 3-5 days and assumptions are being made from the readings made on those days. All of the conclusions listed below are loosely based off of the results and there must be a lot of further experimentation done to prove the hypothesis that DL cycles at high luminance values improve growth or at least are comparable in growth to uncovered reactors.

Regarding light reactor 1, cells grew well on day 2 because the luminance was low (7.5-36 kCd/m<sup>2</sup>) and the temperature was moderate (30-37° C). They then began to die on days 3 and 4 because luminance reached high values like 50 kCd/m<sup>2</sup> and temperatures were hot, maintaining values as high as 50° C in the midday sun. Thus a reactor without any dark periods grows its algae best in low luminance and low-moderate temperature because then it does not get photobleached.

Light reactor 2 has insufficient data. But the drop in growth was probably due to somewhat high intensities for an uncovered PBR (14.2-44 kCd/m<sup>2</sup>).

The DL reactor had strong growth at high intensities of  $71.8 \text{ kCd/m}^2$ . On the other hand, it grew poorly when light intensities were low and only reached  $44 \text{ kCd/m}^2$ . It is concluded that a DL PBR needs high luminance values to grow well because low luminance values do not provide enough light to support the dark regions.

Therefore, to maintain increasing growth in a light photobioreactor, low luminance values must be used. And to increase growth in a DL reactor, very high luminance values must be attained. Furthermore, nutrient and carbon dioxide replenishment is crucial for increased growth.

According to the results a DL ratio of 1:10 works properly for increased growth. However, this may not be the optimum fraction for the photobioreactors used in this experiment. Also, it is clear that algae do not need long periods of light exposure when they are in high luminance conditions. These conditions may only photobleach them.

## **6. RECOMMENDATIONS**

For future work, other fractions of light exposure should be investigated. The fraction used for this study was .1, but other fractions like .2, .3, .4 and .5 should also be explored to find an optimum.

The photobioreactor system should also become more automated and continuous by factoring in a degassing system, a nutrient replenishment system and a carbon dioxide feed. The methods used in this experiment were crude and elementary. Carbon dioxide was added in the form of seltzer water with a pipette. The required amount of a fertilizer was also added manually. Also, the degassing system used was simply and uncovered holding tank. All of these things should be upgraded to more automated systems.

## **7. ACKNOWLEDGEMENTS**

I would like to thank all four of my advisers: Jay Zemel, Michael Mauk, Jorge Santiago, and David Graves for their instruction, help, and continued support. Without them, our project would not have been possible. I would also like to thank Ken Chen for always letting us use his chemical engineering senior lab. Also, I want to thank Jan Van der Spiegel and SUNFEST for accepting me to this amazing, eye-opening program. And lastly NSF for supporting REU experiences all over the nation and providing grants for these very useful and rewarding experiences.

References:

[1] A. Luque and S. Hegedus, *Handbook of Photovoltaic Science and Engineering*. England: Wiley, 2003, pp. 11-19.

[2] G. Knier, "How do photovoltaics work?" *Science@NASA*, Jun. 19, 2009. [Online]. Available: <http://science.nasa.gov/headlines/y2002/solarcells.htm>. [Accessed: Jun. 1, 2009].

[3] J. Gordon and J. Polle, "Ultra-high bioproductivity from algae," *Applied Microbiology and Biotechnology*, vol. 76, pp. 969-975, Jun. 2007.

[4] A. Richmond, *Handbook of Microalgal Culture*. Australia: Blackwell Science, 2004, pp. [need to check]

[5] K. Terry, "Photosynthesis in modulated light: quantitative dependence of photosynthetic enhancement on flashing rate," *Biotechnology and Bioengineering*, vol. 28, pp. 998-995, 1986.

Appendix A.

Wednesday, 07/29

Time	Luminance	Temp	Conditions
10:12	10	30	
10:28	14	31	
10:32	17.47	32	
10:33	18.16	32	
12:00	18	36	mostly
1:40	18.7	34	cloudy
1:42	36	34	
1:53	24.1	37	
2:16	7.5	34.5	
3:41	10	35	

Thursday, 07/30

Time	Luminance	Temp	Conditions
10:58	24.5	40	
11:00	15.7	42	sunny
12:00	43.2	50-53	
1:25	50	45	sunny
1:25	6.6	45	cloudy
3:35	8.7	36.5	

Friday, 07/31

Time	Luminance	Temp	Conditions
8:00	3.2		cloudy
3:35	2.5	35	cloudy

all day was very cloudy

Saturday, 08/01

Time	Luminance	Temp	Conditions
12:30	71.8		very sunny
1:30	similar		very sunny

Monday, 08/02

Time	Luminance	Temp	Conditions
9:18	5.3	29	cloudy
10:05	16.6	29	sunny
11:00	8.5	46.5	sunny
12:09	36.5	50	sunny
2:46	18	46	sunny
4:47	4		cloudy

Tuesday, 08/02

Time	Luminance	Temp	Conditions
12:05	38	38	cloudy
12:06	44	41	sunny
4:00	14.2		cloudy

Wednesday, 08/03

Time	Luminance	Temp	Conditions
2:00	25	32	cloudy

Appendix B

Day	Light sample 1	Light sample 2	Light/dark sample
1	7.67E+06	6.83E+06	5.34E+06
3	1.15E+07	3.85E+06	1.10E+07
5	1.05E+07	0	4.65E+06

# **MICROMECHANICAL IMAGING ANALYSIS OF BULK VS. LOCAL PROPERTIES CONCERNING MESENCHYMAL STEM CELL HETEROGENEITY**

NSF Summer Undergraduate Fellowship in Sensor Technologies

Jeffrey Perreira (Mechanical Engineering) – Lehigh University

Advisor: Dr. Robert Mauck

Graduate Student: Megan Farrell

## **ABSTRACT**

Mesenchymal stem cells (MSCs) harvested from bone marrow tri-differentiation potential into osteoblasts, adipocytes, and chondrocytes along with portraying a variety of phenotypes. MSCs are a promising cell source for cartilage tissue engineering, but MSC seeded constructs have yet to match the mechanical properties of chondrocyte seeded constructs. The basis of this study is to use imaging techniques on MSCs that have already been developed to analyze chondrocytes and native articular cartilage to provide information on matrix production, cell response to load, and cell mechanical properties. This paper displays two studies. The first study used micromechanical analysis with florescent microscopy on MSCs and cartilage to study the local and bulk mechanical properties and development of the cells' extra cellular matrix (ECM). The hypothesis was that comparing the local mechanical properties to the bulk properties of MSCs and chondrocytes will explain why the MSC constructs are weaker than the chondrocyte constructs. The second part of the study used confocal microscopy to analyze cell deformation as a function of matrix production over time. The cell deformations were analyzed via a customized Matlab (Mathworks) program to act as a standardized analysis method. Analysis when complete of cell, local, and bulk tissue mechanics is expected to provide insight into the subpar bulk mechanics found in MSC constructs and determine the heterogeneity of local matrix properties.

## **INTRODUCTION**

Mesenchymal Stem Cells (MSCs) harvested from bone marrow possesses the ability to differentiate into adipocytes, chondrocytes, myocytes, and osteoblasts [1 Pittenger]. This is significant because many adult stem cells have the ability to repair a variety of tissues after injury. In the area of cartilage, MSCs serve as a potential source of cells to reconstruct damaged or diseased cartilage tissue. Finding an effective method to heal cartilage has proven difficult due to the inherent nature of cartilage [2 Csak]. The slow healing rate of cartilage has contributed to the fact that its damage affects more than 20 million Americans. Thus there is a strong demand for a method to more rapidly repair cartilage. MSCs show potential to be used as a cell source for tissue engineering cartilage due to their ability to differentiate into cartilage; however, there is a problem with MSCs due to their weaker mechanical properties and heterogeneity, meaning the cells display different phenotypes and have varying likelihoods of cell differentiation. In an effort to study these unexplained problems this paper focuses on studying the micromechanical properties and bulk properties of MSCs and chondrocytes. Analysis, when complete is expected to prove that the varying likelihoods of MSC differentiation can be analyzed via the micromechanical properties of the cells and give insight into the deformation chondrocytes and MSCs experience with mechanical stimulation on a microscopic and macroscopic scale.

## **8. BACKGROUND**

### **8.1 NATURAL CARTILAGE HEALING**

Articular cartilage, the cartilage that coats the bones at joints, can handle extreme compressive, cyclic, and static loads due to its structure. However, its structure also causes it to heal slowly once damaged. The first reason for its slow repair rate is that articular cartilage is only 1% tissue by volume, while the other 99% is an extracellular matrix [3 Shulz]. The second reason that cartilage grows slowly is that it lacks both capillary and nerve connections throughout the tissue which slows down the distribution of nutrients [2 Csak]. When the cartilage matrix is damaged and the damage does not reach the bone, the adjacent chondrocytes multiply and repair the extracellular matrix [3 Shulz]. After a long period of repair, the cartilage appears the same as the rest of the tissue. When cartilage has trauma that reaches the bone, MSCs flow from the bone to the damaged site. The MSCs replace the articular cartilage with Type I and Type II cartilage. After a few weeks the MSCs differentiate into cartilage tissue that resembles the original cartilage, but has weaker mechanical properties. When the bone is ruptured from the trauma the injury receives the help of the nutrients brought by blood in

addition to the MSCs to increase the rate of healing. After a few weeks the new cartilage resembles the previous tissue; however, again the tissue has weaker properties because of the MSCs that were used to make the new cartilage. Cartilage normally has the ability to withstand and repair itself under extreme dynamic loads; however, under certain circumstances cartilage loses the ability to fix itself.

## **8.2 OSTEOARTHRITIS**

Osteoarthritis is the inflammation of a joint caused by the breakdown of cartilage. Osteoarthritis is technically a repair process because as the articular cartilage is damaged new bone is formed to fill in for the lost tissue. A paper published by the British College of Physicians describes osteoarthritis as a ‘slow but efficient repair process that often compensates for the initial trauma resulting in a structurally altered, but symptom free joint’ [4 Osteoarthritis]. Osteoarthritis becomes a debilitating disease when the cartilage cannot ever make a complete recovery of its damage. Osteoarthritis is caused by obesity, age, and repetitive trauma. Primarily the disease is highly correlated to age because as we grow older the water percentage of cartilage increases while the protein percentage decreases [5 Shiel]. This trend weakens cartilage and allows it to flake or crack.

## **8.3 CURRENT PRACTICES**

Currently options for cartilage problems include arthroscopic surgery, joint replacements, and tissue transplantation. There are 1,500,000 arthroscopic operations annually to repair torn tissue such as tendons, menisci, or cartilage [3 Shulz]. However, these surgeries were deemed to be ineffective for osteoarthritis in a 2002 study at a Houston Veterans Affairs Medical Center [6 Moseley]. Joint replacements are performed to replace arthritic, damaged, or cancerous points of the joint. A total of \$15 billion worth of complete joint replacement surgeries are performed annually [3 Shulz]. Both the large costs involved in cartilage repair and demands for cartilage disease solutions are the reasons people are studying tissue engineering.

## **8.4 TISSUE ENGINEERING USING MSCs**

Many scientists in the field of tissue engineering hold high hopes for MSCs as a method to repair cartilage tissue in the human body. MSCs have the potential to differentiate into adipocytes, osteocytes, and chondrocytes. [7 Mareddy] MSCs can be isolated from many sources

in the body such as liposuction fat and bone marrow. [8 Huang] [9 Guilak] This means that cartilage tissue from the body will not need to be sacrificed for cells to repair the damaged cartilage. MSCs can be relatively easily cultured and expanded while keeping their many phenotypes. The identification of a suitable cell source such as MSCs is a major step in the advancement of tissue engineering.

## **8.5 PROBLEMS WITH MSCs**

Before MSCs can be utilized for cartilage repair many steps must be taken to improve the cells' deficiencies. First of all the standard practice for harvesting and collecting MSCs involves adhering MSCs to plastic which most other cells do not adhere. [10 Vogel] [8 Huang] This method of collecting MSCs provides a mixture of MSC phenotypes and other cell types, which creates a large hurdle when attempting to grow a homogenous population of cells. Second, MSCs lack unique cell surface markers that can be utilized to recognize the varying phenotypes of MSCs. Third, MSC constructs have yet to be produced that match the mechanical properties of cartilage based constructs and ultimately native cartilage.

## **9. METHODS**

Bovine MSCs and chondrocytes were harvested from three donors' femurs and tibias. The cells were then encapsulated in 2% agarose constructs 4mm in diameter and 2.25mm in thickness with density of 20million cells per mL. The cells were then cultured in a chemically defined media with or without TGF- $\beta$ 3 (CM+ or CM-). At time points of weeks 0, 1, 3, 6, and 9 the constructs were tested for biochemistry mechanical properties, and with histology. Constructs at each time point were tested for biochemistry after mechanical testing. The sGAG amount was tested with dimethylmethylene blue dye binding. The collagen amount was tested with hydroxyproline assay. The DNA was tested using PicoGreen. Three constructs were tested with an unconfined compression device from our lab at each time point to find the modulus of elasticity for constructs. One construct was fixed to 4% paraformaldehyde inside of paraffin wax used for histology at each time point. Three constructs were tested with the microscope straining device seen in Figure 1. The device has a micrometer for precise adjustments to the linear stage, load cell that can measure between  $\pm 250$ gF with precision of 0.1gF, cover slip to lay the construct, water tight PBS bath, and two platens to strain the construct. The construct was cut in half and laid on its cut portion so that the cells could be imaged by the microscope. The layout of the construct can be seen in Figure 2. The constructs were imaged at strains from 0% to 20% by increments of 4%. This means that the constructs were strained five times with 80 seconds of

straining and 500 seconds of stress relation before the load reading was taken. Images were taken using a Nikon florescent microscope of the Hoechst die stain constructs while operating the microscope straining device. For more details on the microscope straining device protocol see Appendix A. The images were then stitched together using a program called Autostitch. The protocol for Autostitch can be seen in Appendix B. The stitched images were then analyzed using Vic-2D which texture-maps and compares a reference image for each sample to a strained image. This analysis technique allowed for the displacements and strains of the stress to be compared between the time points and between Chondrocytes and MSCs. In other words this method allowed for the study of the ECM by viewing the cells' strain.

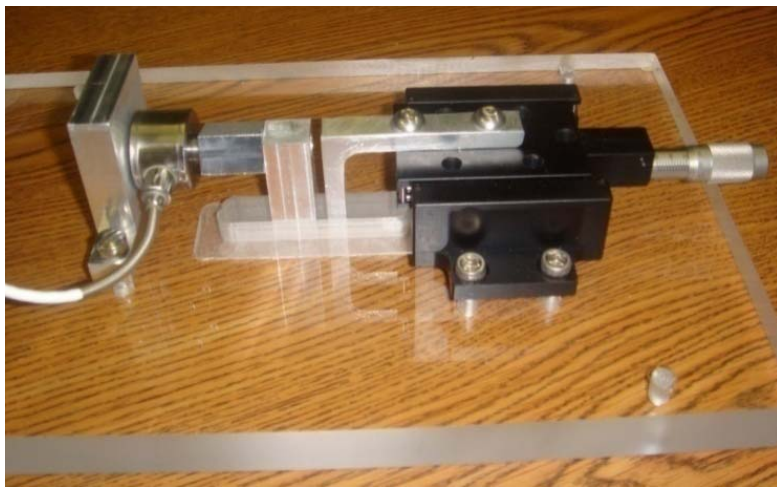
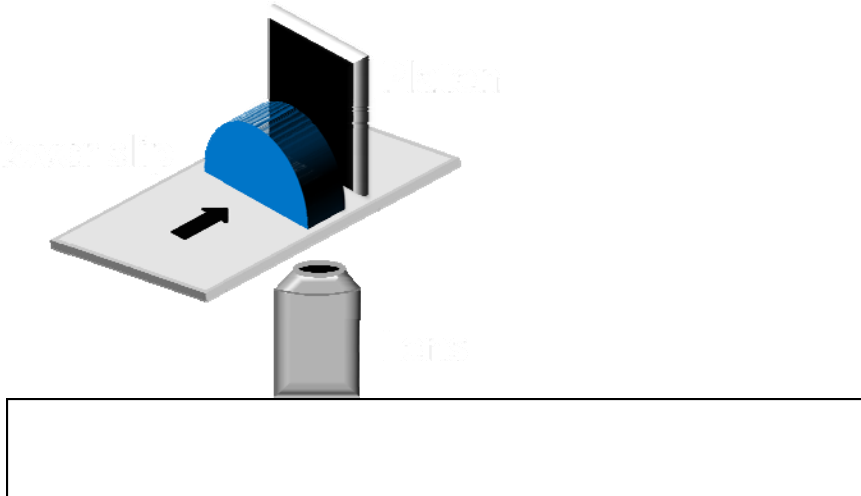


Figure 11: The microscope straining device used on the Florescent Microscope. The Constructs are placed in between the aluminum platens. The load cell is on the left and the linear stage with the ball micrometer is on the right.

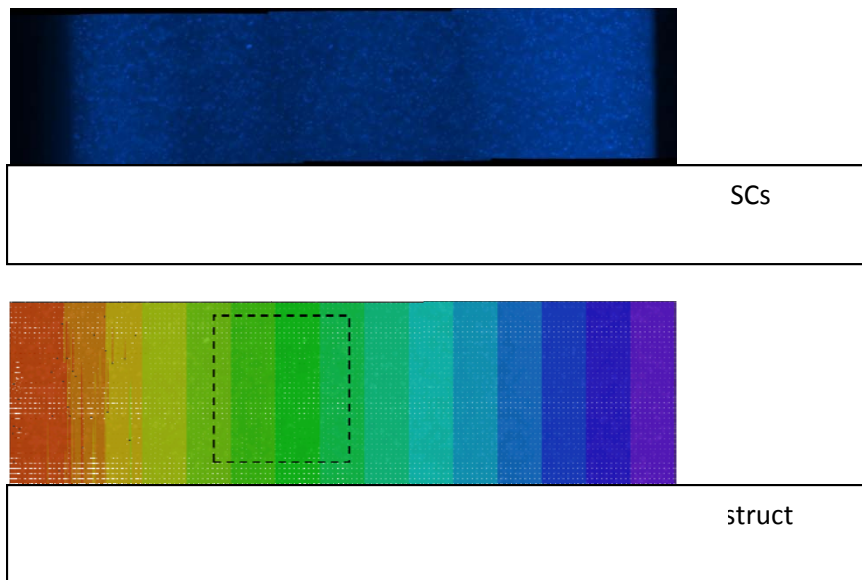


In the second part of the study, similar constructs were analyzed using confocal microscopy. Strained and unstrained constructs were imaged with a 60x objective. The images were then analyzed with a customized Matlab program seen in Appendix C. The program threshed the image via the light intensity, area size, and eccentricity. The light intensity was threshed using the Otsu method which makes an image binary by assigning each grayscale pixel a 1 or 0 in a way that minimizes the variance of each class. The area was threshed via a minimum threshold and by an upper and lower standard deviation. The eccentricity is the distance between the foci divided by the length, which was useful in filtering out the scale bar in images and non cells that were essentially lines. These methods eliminate non-cells, cells that were touching, and cells on the edge of the image. The program then outputted each of the region's orientation, major axis (length), minor axis (width), eccentricity, and aspect ratio. It is important to clarify that the major axis is the longest axis of the ellipse, the minor axis is the width of the ellipse perpendicular to the major axis, and the orientation is the angle in degrees between the positive x-axis to the major axis. It is also important to define eccentricity as the distance between the foci of the area regions divided by the length and aspect ratio is length divided by width. This analysis method allowed for the cell deformations to be analyzed at different time points as the ECM developed.

## 10. RESULTS

NOTE: All the results are not present because the experiments have not been completed.

The results will include a comparison between bulk mechanical properties to local mechanical properties of chondrocytes and MSCs at the time points of 0, 1, 3, 6, and 9 weeks. An example of an Autostitched hoescht stained image at 10x can be seen in Figure 3. Images like this exist for each of the strain increments for each fluorescent microscope imaged construct. The strained images were then tested with respect to an unstrained image from the construct. An example of an analysis of the strain of a construct can be seen in Figure 4. Images like this will allow the bulk properties of chondrocyte and MSC constructs to be analyzed. Figure 5 then shows that the displacement across the construct in Figure 4 is uniform across the construct. Figure 6 shows that the local displacements in the construct are not uniform from right to left even though Figure 5 showed a uniform displacement. Comparing these two types of images for chondrocytes and MSCs at various time points will allow us to compare local versus bulk properties.



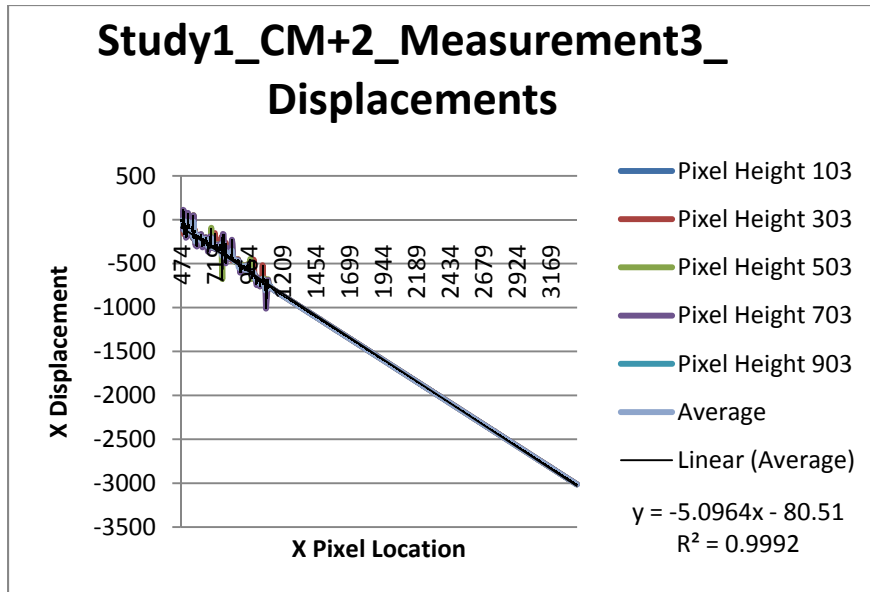


Figure 15: Analysis of Figure 14 at different y-pixel heights showing that the x-displacement across the construct is linear.

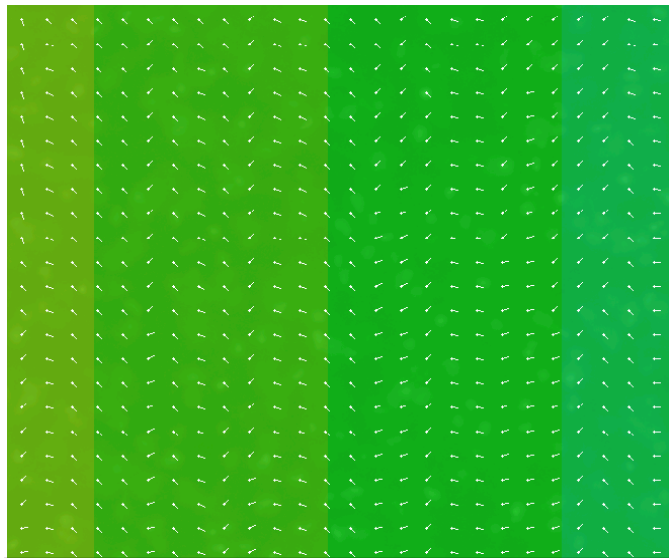
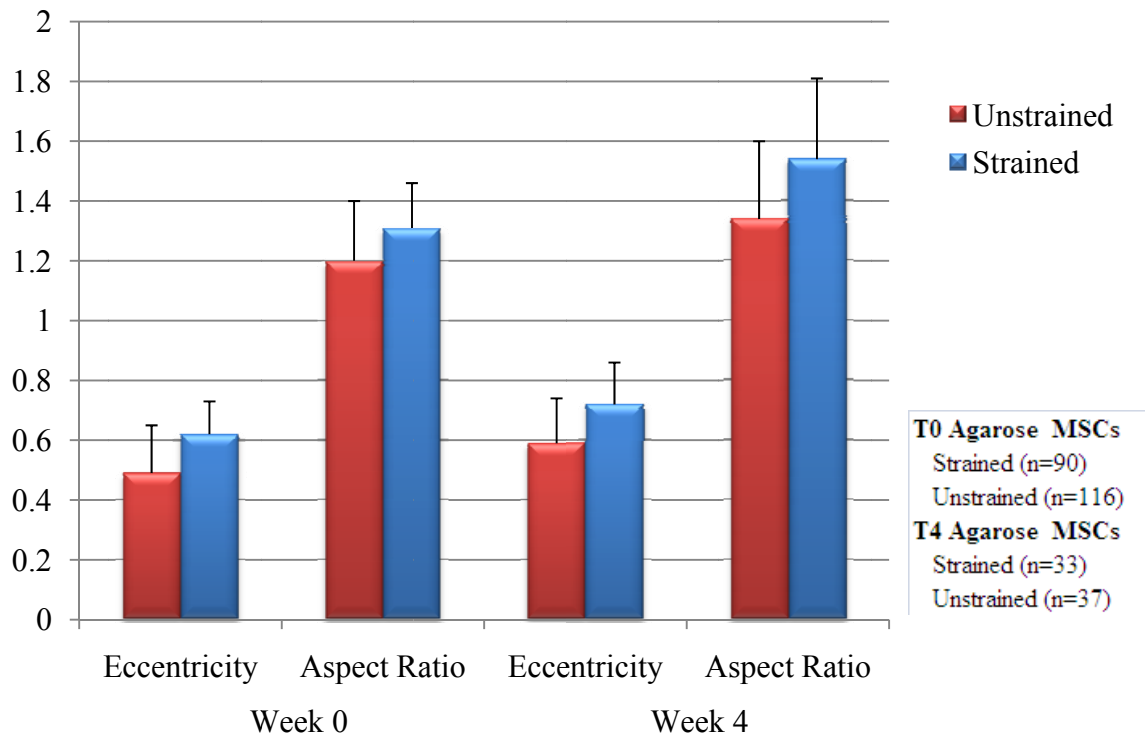


Figure 16: A zoomed in image of Figure 14 with the arrows showing the direction of maximum displacement.

The data in this section will allow us to assess cell deformation as a function of matrix production over time. There will be the average eccentricities, aspect ratios, and orientation of cells at various time points using the confocal microscope and the customized Matlab program in Appendix C. An example of a completely analyzed image sample can be seen in Appendix D. Figure 7 then shows the cumulated data for many analyzed MSC agarose constructs from weeks 0 and 4.



at  
for week

## 11. DISCUSSION AND CONCLUSIONS

The results from the first part of the study with the microscope straining device will allow for comparing the local and bulk micromechanical properties of MSCs to chondrocytes. The local properties will be observed with the help of Vic-2D and the bulk properties will be observed with the help of an unconfined-compression device. Comparing the local properties to the bulk properties will hopefully explain why the MSCs have a lower module of elasticity than the chondrocytes.

The results from the second part of the study will allow for assessing the cell deformation as a function of matrix production over time. This portion of the study will also show the effects of stress shielding. Stress shielding normally occurs within weeks 0 and 8 weeks when the ECM protects the cells from deformations. The ECM prevents the cells from deforming because the

ECM is stiffer than the agarose in which the cells reside. This is of interest because stress shielding prevents the cells from receiving some of the loading signals during mechanical stimulation in bioreactors. Loading signals are extremely important with cartilage and MSCs because they tell the cells to produce different proteins. This portion of the study will also give insight into the experience of the deforming cells during mechanical stimulation.

## **12. RECOMMENDATIONS**

I recommend that in the future the florescent microscope straining device be redesigned. The platens should be flush to the bottom of the PBS bath so that soft constructs do not seep between the platens and cover slip. The micrometer should be motorized so that there is no human error with adjusting the strain on the constructs. Adjustments to the PBS bath should be made so that it is easier to place the constructs in between the platens. The load cell on the microscope straining device should be attached to a DAQ so that the readings are accurately recorded. This redesigned device will be more precise and allow for more representative comparisons between time trials and samples.

I recommend that in the future a confocal microscope straining device be created. Currently the strain is placed on the construct by placing the construct in between two slides and squeezing the construct with a rubber band. A device similar to the florescent microscope straining device should be made for the confocal microscope so that the strain can be adjusted during imaging. This device would allow for tracking cells while they are strained and during stress relaxation.

## **13. ACKNOWLEDGMENTS**

I would first like to thank the Penn McKay Orthopedic Research Laboratory, my advisor Dr. Robert Mauck and my supervising graduate Megan Farrell. I would like to thank the University of Pennsylvania's SUNFEST program run by Dr. Jan Van der Spiegel for giving me this opportunity to research this summer. I would also like to thank the National Science Foundation for their support through an NSF-REU grant.

## 14. REFERENCES

1. Pittenger M. F., A. M. Mackay, S. C. Beck, R. K. Jaiswal, R. Douglas, J. D. Mosca, M. A. Moorman, D. W. Simonetti, S. Craig, and D. R. Marshak. (1999, Apr.). Multilineage Potential of Mesenchymal Stem Cells. *Science*. [Online]. Vol. 284, pp. 143-147.  
Available: <http://www.sciencemag.org/>  
a. [1 Pittenger]
2. Csaki C., P. R. A. Schneider, and M. Shakibaei. (2008, Jul.). Mesenchymal Stem Cells as a Potential Pool for Cartilage Tissue Engineering. *Elsevier*. [Online]. pp. 395-412.  
Available: <http://www.sciencedirect.com/>  
a. [2 Csaki]
3. Schulz R. M. and A. Bader. (2007, Feb.). Cartilage Tissue Engineering and Bioreactor Systems for the Cultivation and Stimulation of Chondrocytes. *Eur Biophys J.* (36), pp. 539-568.  
a. [3 Schulz]
4. *Osteoarthritis*. London, UK: Royal College of Physicians, 2008.  
a. [4 Osteoarthritis]
5. Shiel W. C.. (2009). Osteoarthritis. *MedicineNet*. [Online]. Available: <http://www.medicinenet.com/osteoarthritis/article.htm>.  
a. [5 Shiel]
6. Moseley J. B., K. O'Malley, N. J. Petersen, T. J. Menke, B. A. Brody, D. H. Kuykendall, J. C. Hollingsworth, C. M. Ashton, and N. P. Wray. A Controlled Trial of Arthroscopic Surgery for Osteoarthritis of the Knee. (2002, Jul.) *N Engl J Med.* 347(2). pp. 81-88.  
a. [6 Moseley]
7. Mareddy, S., R. Crawford, G. Brooke and Y. Xiao (2007). "Clonal isolation and characterization of bone marrow stromal cells from patients with osteoarthritis." *Tissue Eng* **13**(4): 819-29.  
a. [7 Mareddy]
8. Huang, Alice H., Megan J. Farrell, Robert L. Mauck. "Mechanics and Mechanobiology of Mesenchymal Stem Cell-Based Engineered Cartilage," unpublished.  
a. [8 Huang]
9. Guilak, F., K. E. Lott, H. A. Awad, Q. Cao, K. C. Hicok, B. Fermor and J. M. Gimple (2006). "Clonal analysis of the differentiation potential of human adipose-derived adult stem cells." *J Cell Physiol* **206**(1): 229-37.  
a. [9 Guilak]
10. Vogel, W., F. Grunebach, C. A. Messam, L. Kanz, W. Brugger and H. J. Buhring (2003). "Heterogeneity among human bone marrow-derived mesenchymal stem cells and neural progenitor cells." *Haematologica* **88**(2): 126-33.  
a. [10 Vogel]

## APPENDIX A: MICROSCOPE IMAGING PROTOCOL

This protocol is utilized to study how MSCs and cartilage cells grown in constructs deform under strain at various time points. The time points will be weeks 0, 1, 3, 6, and 9. At each time trial there will be three CM- and three CM+ constructs tested.

### Step A: Hoescht Stain

1. Measure the diameter and thickness of the construct.
2. Cut the construct in half across the diameter.
3. Measure the radius of each of the halves.
4. Place the two halves of the construct in separate capsules
5. Add 1mL of PBS to each capsule.
6. Add 2 $\mu$ L of Hoescht stain to the capsules.
7. Wait 30 minutes for stain to set. Wrap the capsules in aluminum foil.
8. Remove the stain from the capsules via pipette.
9. Add 1mL of PBS to the capsules. Wrap the capsule in aluminum foil.

### Step B: Microscope Imaging

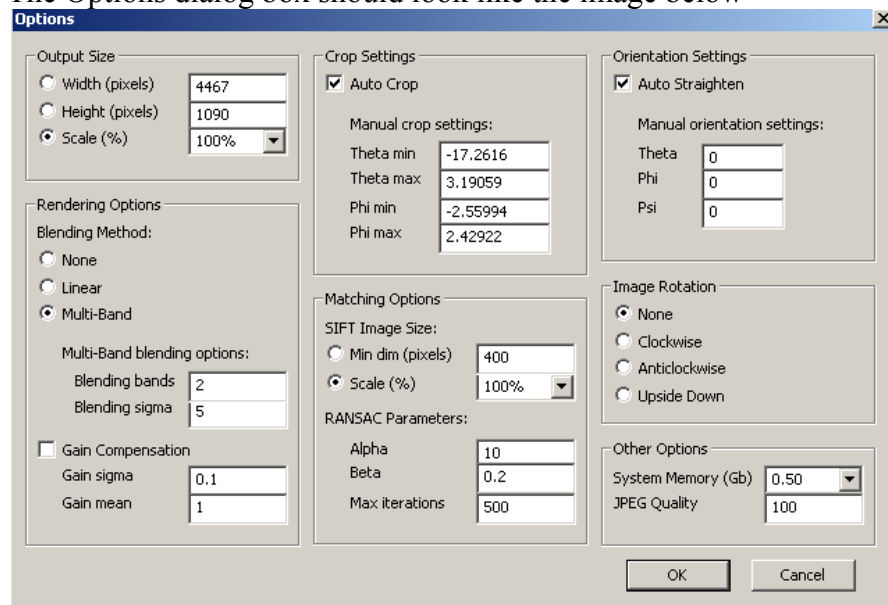
1. Fill the microscope straining device's (MSD's) water bath with PBS.
2. Lay the cut edge of the construct in the MSD.
3. Screw the MSD to the microscope stage.
4. Plug in the load cell display.
5. Record the load cell zero.
6. Screw the micrometer so that the plungers just touch the construct.
  - a. This is done by adjusting the micrometer until the load reading decreases below the load cell zero.
7. Take a "Series of Pictures" to get reference images
  - a. At 10x take Florescent DAPI setting images across the construct.
    - i. Adjust the exposure time of the microscope each time the magnification of the microscope or displacement of the construct changes by clicking Auto Exposure in the middle of the construct.
    - ii. Ensure that there is overlap of 1/8<sup>th</sup> of the image after each time the microscope stage is moved so that the image stitching software can operate effectively.
  - b. At 2x take a Florescent DAPI setting image of the construct.
  - c. At 2x take a Phase image of the construct.
    - i. Do not turn off the lamp until the end of the experiment.
  - d. After all the pictures, block the light source so that photo bleaching is prevented.

8. Adjust the micrometer by 0.10mm over an 80 second time period, which is approximately 4% strain.
9. After 8 minutes 20seconds from adjusting the micrometer, record the load cell reading.
10. Take another "Series of Pictures"
11. Repeat steps 8-10 five times (until 20% strain is achieved) this means that there are a total of 6 image series

## APPENDIX B: AUTOSTITCH IMAGING PROTOCOL

This protocol is used to prepare the images from the Microscope Imaging Protocol for Vic-2D analysis. The directions must be followed so that the images maintain the highest resolution possible and to allow for accurate Vic-2D analysis.

1. Download the Windows Demo Version of Autostitch from [www.cs.ubc.ca/~mbrown/autostitch/autostitch.html](http://www.cs.ubc.ca/~mbrown/autostitch/autostitch.html)
2. Close all other programs. This program takes a lot of memory when working with large image files
3. Click *Edit* and then *Options*
  - a. Under *Output Size*-select *Scale %* and change the drop down menu to **100%**
  - b. Under *Matching Options* and *SIFT Image Size* and change the drop down menu to **100%**
  - c. Under *Other Options* change *System Memory (Gb)* to **.50**
  - d. Under *Other Options* change *JPEG Quality* to **100**
  - e. The Options dialog box should look like the image below



4. Click *File* and then *Open*
  - a. Open images (.jpg) in order that you want to stitch together
5. Save the stitched image for Vic-2D analysis.
6. Trouble shooting
  - a. If the stitched image does not look correct then retry step 4

## APPENDIX C: CONFOCAL IMAGING ANALYSIS CODE

```

%-----
%Jeffrey Perreira
%UPENN ORL
%Strain Analysis
%This program takes a jpg, thresholds areas by statistics, thresholds
%eccentricities, finds statistics on cells, saves the image file, and
%writes statistics to a specified XLS file in a sheet named the image name
%StrainAnalysis_07-28-09_BlobAnalysis_Methods.m
%-----
clc
clear all
close all
%-----
%Step 1: Modify Each Time

%Specify File to Write To
XLSfilename='t0 1% HA';
XLSfilename=char(XLSfilename);

```

%SPECIFY METHOD

%Column 1: Intensity Threshold

%Column 2: Minimum Area

%Column 3: Lower Area Std.

%Column 4: Higher Area Std.,

%Column 5: Eccentricity Threshold

%Column 6: Region definition for Area threshold

%Column 7: ConvexArea Threshold

%Method 1:

Method(1,:)= [1.000, 50.000, 2.000, 2.000, 1.000, 8.000, 5.000];

%Method 2:

Method(2,:)= [1.500, 90.000, 1.000, 2.000, 1.000, 4.000, 5.000];

%Method 3: Same as Method 1 with eccentricity threshold

Method(3,:)= [1.000, 50.000, 2.000, 2.000, 0.925, 8.000, 5.000];

%Method 4: Same as Method 2 with eccentricity threshold

Method(4,:)= [1.500, 90.000, 1.000, 2.000, 0.925, 4.000, 5.000];

%Method 5: Best blob analysis method as of 7/11/09

Method(5,:)= [1.250, 90.000, 1.000, 3.000, 0.925, 8.000, 1.000];

%Method 6: Created for Greg's microsphere analysis

Method(6,:)= [1.000, 40.000, 1.000, 5.000, 0.925, 8.000, 1.000];

%Select a method

M=Method(5,:);

```

%-----
% STEP 2: OPEN FILE

% open file prompt
[filename, pathname, filterindex] = uigetfile('*.*jpg', 'Open Image File');

% if user hits cancel, exits script
if filterindex == 0
    returnL
else
    name = strcat(pathname,filename)
end

% open the file
img = imread(name);

%Find image pixel height and width
pictureSize=size(img);
pictureW=pictureSize(2);
pictureH=pictureSize(1);

%-----
% STEP 3: EDIT IMAGE

```

```

% Create grayscale image
img = rgb2gray(img);
figure(1)
imshow(img);
title('Grayscale')

% Create black and white image
% Create a threshold level
level = M(1)*graythresh(img);
%Instances of 1 are the cell, 0 is the background
img = im2bw(img,level);
figure(2)
imshow(img)
title('Thresholded Using Otsu Method')

%Threshold image's small areas
%M(6) for either 8 or 4
img2=bwlabel(img,M(6));
Area0=regionprops(img2,'area');
indxb = find([Area0.Area] > M(2));
img3 = ismember(img2,indxb);
figure(3)
imshow(img3);
title('Eliminated Bottom Areas')

```

```

%Histogram of Areas

img4=bwlabel(img3,8);
Area0=regionprops(img4,'area');
Area1=struct2cell(Area0);
Area1=cell2mat(Area1);
StandardDev=std(Area1);
Average=mean(Area1);
y=hist(Area1,20);
MIN=min(Area1);
MAX=max(Area1);
x=(MIN+(MAX-MIN)/20):(MAX-MIN)/20:MAX;

figure(4)
bar(x,y)
title('Histogram of Areas')
xlabel('Areas')
ylabel('Quantity of Occurances')

%Upper and Lower Bounds

%Lowerbound area
indxl = find([Area0.Area] > Average-M(3)*StandardDev);
img5 = ismember(img4,indxl);

figure(5)
imshow(img5)

```

```

title('Eliminated Lower Standard Deviation')

%Upperbound area
img6=bwlabel(img5,8);
Area0=regionprops(img6,'area');
indxu = find([Area0.Area] < Average+M(4)*StandardDev);
img7 = ismember(img6,indxu);
figure(6)
imshow(img7)
title('Eliminated Upper Standard Deviation')

%Eliminate cells on border of image
img8=bwlabel(img7,8);
indx=[img8(1,:),img8(pictureH,:),img8(:,1),img8(:,pictureW)'];
indx=sort(indx,'ascend');
indx=unique(indx);
img9 = ~ismember(img8,indx);
figure(7)
imshow(img9)
title('Eliminated Border Areas')

%Eliminate cells with high eccentricities
img10=bwlabel(img9, 8);
Eccentricity0=regionprops(img10, 'eccentricity');
indx = find([Eccentricity0.Eccentricity] < M(5));

```

```

img11 = ismember(img10,indx);
figure(8)
imshow(img11)
title('Eliminated High Eccentricities')

%Eliminate cells with holes, abnormal outshoots, or multiple cells
img12=bwlabel(img11, 8);
ConvexArea0=regionprops(img10, 'ConvexArea');
Area0=regionprops(img10, 'Area');
indx = find([ConvexArea0.ConvexArea] < [Area0.Area]*M(7)*4/pi);
img13 = ismember(img12,indx);
figure(9)
imshow(img13)
title('Eliminated via ConvexArea')

%-----
%STEP 4: ANALYZE BLOBS

%Label each cell with a different number
img14=bwlabel(img13,8);
Area=regionprops(img14,'area');
Image=img14;
imview(Image);

```

```

%Regionprops measures a set of properties for each labeled region
%Length in pixels of major axis
Length=regionprops(Image,'majoraxislength');
Length=[Length.MajorAxisLength]';
%Length in pixels of minor axis
Width=regionprops(Image,'minoraxislength');
Width=[Width.MinorAxisLength]';
%Eccentricity is the ratio of the foci and the major axis length. 0=circle
Eccentricity=regionprops(Image,'Eccentricity');
Eccentricity=[Eccentricity.Eccentricity]';
%Orientation is the angle (degrees) between the x-axis and the major axis
Orientation=regionprops(Image,'Orientation');
Orientation=[Orientation.Orientation]';
%Aspect Ratio is the long side divided by the short side
AspectRatio=Length./Width;%
% %-----
% %Step(5)
%
%Consolidate data
SUM(:,1)=Length;
SUM(:,2)=Width;
SUM(:,3)=Eccentricity;
SUM(:,4)=Orientation;
SUM(:,5)=AspectRatio;

```

```
%Print data to file

characters=size(filename);
characters=characters-4;
XLSsheet=filename(1:characters(2));
xlswrite(XLSfilename,SUM,XLSsheet);

%Print image to a .xsl file
s=' Matlab.jpg';
s=char(s);
AfterImageFilename=[filename(1:characters(2)),s];
imwrite(Image, AfterImageFilename, 'jpg');
```

## Appendix D: Matlab Imaging Analysis Example

Appendix D shows an example analysis of a confocal image utilizing the customized Matlab program in Appendix C. Figure 8 shows a strained MSC construct at week 0 in 2% Agarose gel. Figure 9 shows the outputted Matlab image after Figure 8 has been analyzed by Matlab. Figure 10 labels the cells seen in Figure 9. The program then outputs the length, width, eccentricity, orientation, and aspect ratio of each cell as seen in Table 1.

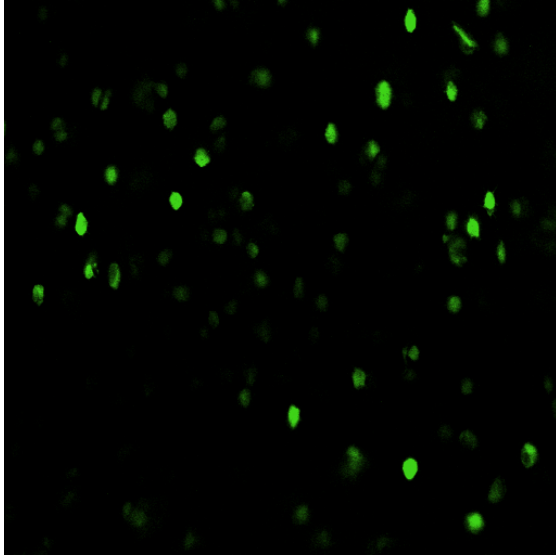


Figure 18

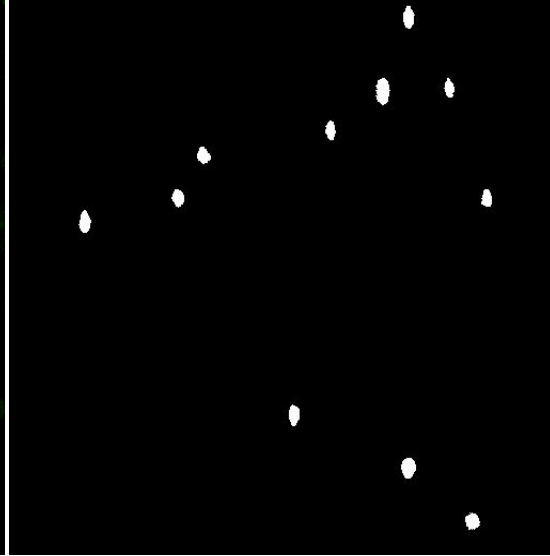


Figure 19

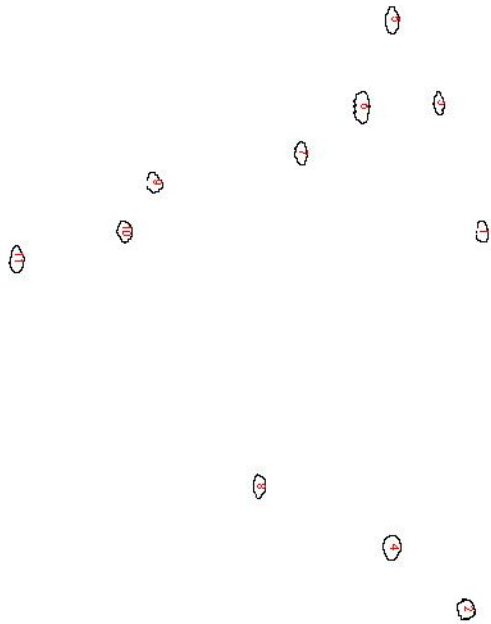


Figure 20

Table 1

Cell #	Length	Width	Eccentricity	Orientation	Aspect Ratio
1	20.67	10.57	0.86	89.86	1.96
2	16.25	11.31	0.72	82.22	1.44
3	15.61	12.00	0.64	69.42	1.3
4	19.29	10.29	0.85	89.42	1.87
5	17.95	9.29	0.86	87.39	1.93
6	25.02	12.87	0.86	89.99	1.94
7	19.2	13.67	0.7	87.25	1.4
8	20.84	10.29	0.87	89.19	2.03
9	17.58	8.93	0.86	83.25	1.97
10	15.38	13.62	0.46	77.78	1.13
11	16.8	9.89	0.81	88.34	1.7
Average	18.60	11.16	0.77	84.92	1.70
Standard Deviation	2.84	1.67	0.13	6.43	0.32

# **VIBRATIONAL ENERGY HARVESTING USING MEMS PIEZOELECTRIC GENERATORS**

Andrew Townley – Electrical Engineering, University of Pennsylvania

Advisor: Gianluca Piazza

## **ABSTRACT**

In recent years, energy harvesting using piezoelectric materials has become a very popular research topic. Various device sizes and structures have been tested, but it is difficult to compare power measurements as device fabrication and experimental methods vary from paper to paper. In an effort to standardize comparisons in spite of these changing parameters, the dependence of generator power output on device dimensions has been investigated. Though MEMS scale devices have been produced, comparatively little work has been done using aluminum nitride (AlN). This project utilizes AlN due to its ease in processing and potential for on-chip integration. By operating at a MEMS scale, the benefit is that arrays of piezo generators can be placed on the same die. With the process advantages of AlN, a long term goal of an integrated power-harvesting chip becomes feasible. However, theoretical results of scaling predict that raw power output and even power per unit volume will decrease with scaling. This indicates that a single large generator, taking up the same area as several small generators, would produce a noticeably larger power output. Due to time constraints, no new generators could be fabricated within the time span of the project. An existing piezoelectric cantilever was used to verify the theoretical predictions of resonant frequency and static deflections under applied voltage. These predictions agreed quite closely with the observed results. However, no measurable electrical response could be found while exciting the beam with an electromagnetic shaker device. A similar experiment was performed using an AFM to directly excite the beam, but again the electrical response was difficult to characterize. While the results of the experiments were not optimal, the difficulty in measuring the electrical response of the beam demonstrates the design challenges involved with energy harvesting on a small scale. Piezoelectric generators rely on resonance to generate useful quantities of power, and power output is highly sensitive to the frequency of the physical vibrations applied. While generators of this type could be useful if targeted to a specific application if the frequency of environmental vibrations is known, a more versatile approach would use a different design to reduce the frequency sensitivity. Broad-band designs, using either non-resonant or self-tuning structures, would be able to harvest energy much more efficiently in changing environments.

## **1. INTRODUCTION**

Low-power wireless distributed sensor networks are becoming attractive for monitoring different variables – such as temperature, strain in a material, or air pressure – over a wide area. However, one drawback of these networks is the power each node draws, though recent work has shown this can be lowered considerably [1]. Batteries can be used to power nodes for extended periods of time, but they have a limited life cycle and eventually need to be replaced. As this can be a costly and time consuming procedure for networks with many nodes, a means of powering the devices indefinitely would be a more practical solution.

Solar power provides a considerable amount of energy per area and volume, but unfortunately is limited to applications that are reliably sunlit [2]. A promising alternative takes advantage of the energy in ambient vibrations and converts it to electrical power. This approach compares very favorably with batteries, providing equal or greater power per unit volume.

There are multiple techniques for converting vibrational energy to electrical energy. The most prevalent three are electrostatic, electromagnetic, and piezoelectric conversion [3]. A majority of current research has been done on piezoelectric conversion due to the low complexity of its analysis and fabrication. Most research, however, has targeted a specific device scale [4-7]. Little research comparing power output across different scales has been done for piezo harvesters, though scaling effects have been discussed briefly in some works [4,8].

This paper aims to develop a theoretical understanding behind the scaling of piezoelectric cantilever generators, and to recommend a direction for future research in this area based on the conclusions.

## **2. BACKGROUND**

### **2.1 The Piezoelectric Effect**

The piezoelectric effect, in essence, is the separation of charge within a material as a result of an applied strain. This charge separation effectively creates an electric field within the material and is known as the direct piezoelectric effect. The converse piezoelectric effect is the same process

in reverse: the formation of stresses and strains in a material as a result of an applied electric field.

The IEEE standard on piezoelectricity lists several different forms for the piezoelectric constitutive equations [9]. The form used here is known as the d-form, and the equations are as follows:

$$S = s^E T + dE$$
$$D = dT + \varepsilon^T E$$

These equations, known as the “coupled” equations, reduce to the well-known stress-strain relationship at zero electric field, and the electric field and charge displacement relationship at zero stress.

### **2.1.1 Piezoelectric Materials**

A majority of piezoelectric generators that have been fabricated and tested use some variation of lead zirconate titanate (PZT). Typically, PZT is used for piezoelectric energy harvesters because of its large piezoelectric coefficient and dielectric constant, allowing it to produce more power for a given input acceleration [10]. Another less common material is aluminum nitride (AlN). Though it has a smaller piezoelectric coefficient and dielectric constant, aluminum nitride has advantages in material deposition and in compatibility with the standard CMOS processes used for fabrication of integrated circuits [6]. This makes the possibility of an integrated “power chip” realizable. Because of these advantages, the project will focus on the use of AlN as the piezoelectric material of choice. However, for future optimizations, the change in output power from switching to a different material should be investigated.

### **2.1.2 Anisotropic Effects and Coupling Modes**

Piezoelectric materials have a built-in polarization, and therefore respond differently to stresses depending on the direction. There are two primary modes of electromechanical coupling for piezoelectric materials: the 3-1 mode and the 3-3 mode. In the 3-1 mode (Figure 2.1a), the

electric field is produced on an axis orthogonal to the axis of applied strain, but in the 3-3 mode (Figure 2.1b), the electric field produced is on the same axis as the applied strain.

Figure 2.1a:

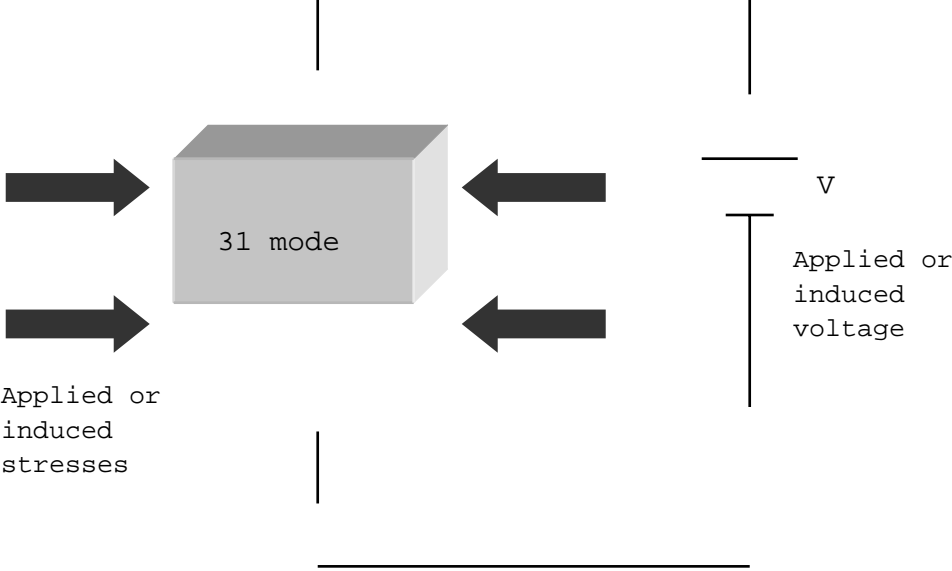
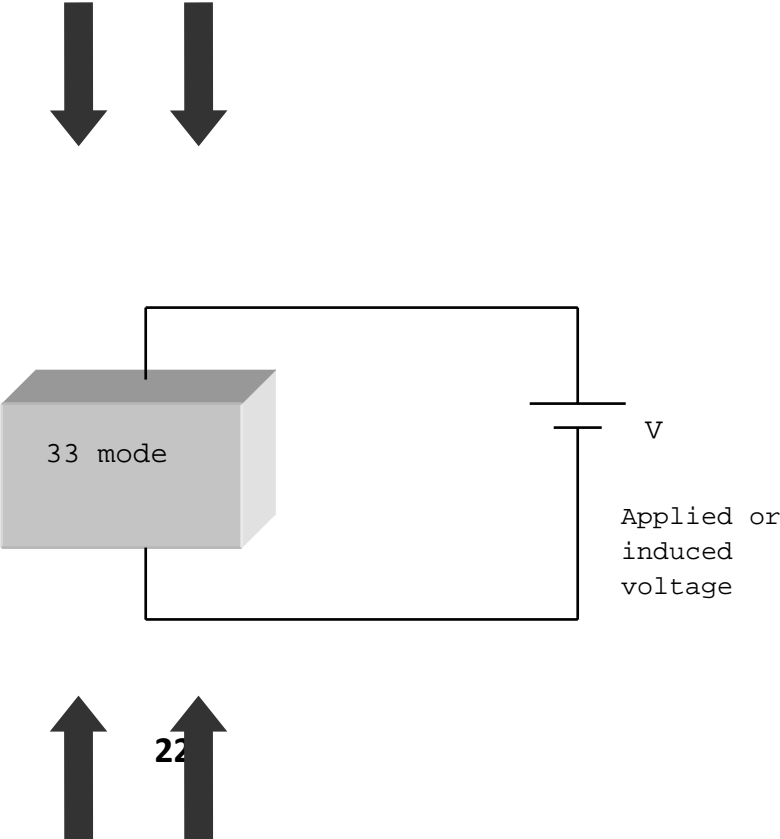
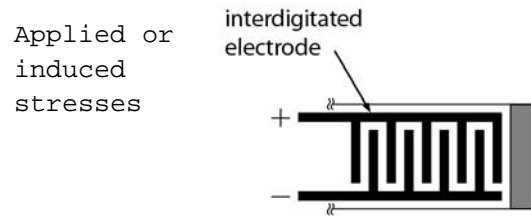


Figure 2.1b:





**Figure 2.2: an example of an IDE pattern [7]**

While the piezoelectric coefficient is higher in the 3-3 mode for most materials, taking advantage of the larger coefficient requires a much more complex design. Instead of simple planar electrodes, a series of interdigitated electrodes (IDE) can be used to take advantage of the 3-3 coupling mode [7]. However, this approach leads to a very small device capacitance and therefore a high output impedance, making load matching difficult [11]. Another disadvantage is that the IDE approach only works for electrically-poled piezoelectrics such as PZT. In AlN, the direction of polarization of the material is set during deposition, so fabrication of a 3-3 mode device would be prohibitively complex. For this reason, the devices analyzed in this report will only utilize the 3-1 coupling mode.

## 2.2 Device Configuration

The vast majority of piezoelectric energy harvesting devices use a cantilever beam structure. A cantilever beam, by definition, is a beam with a support only one end, and is often referred to as a “fixed-free” beam. When the generator is subjected to vibrations in the vertical direction, the

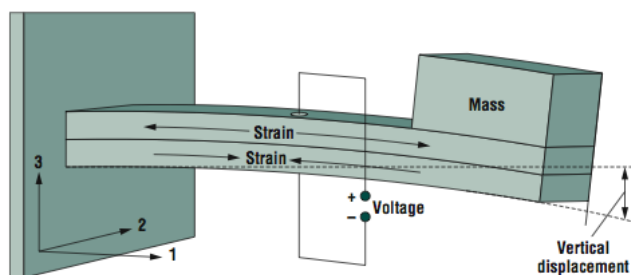


**Figure 2.3: note that strain is generated along the length of the beam, hence the use of the 3-1 mode**

support structure will move up and down in sync with the external acceleration. The vibration of the beam is induced by its own inertia; since the beam is not perfectly rigid, it tends to deflect when the base support is moving up and down (see Figure 2.3). Typically, a proof mass is added to the free end of the beam to increase that deflection amount. This lowers the resonant frequency of the beam and increases the deflection of the beam as it vibrates. The larger deflection

leads to more stress, strain, and consequently a higher output voltage and power [5].

Electrodes covering a portion of the cantilever beam are used to conduct the electric charges produced to an electrical circuit, where they can be utilized to charge a capacitor or drive a load. Different electrode lengths or shapes have been shown to affect the output voltage, since strain is not uniform across the beam [12].

### 2.3 Modes of Vibration and Resonance

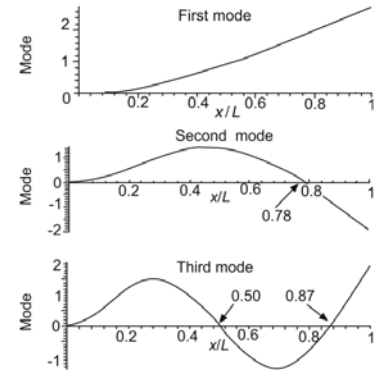


**Figure 2.4: Different mode shapes of a vibrating beam. (Figure from [14])**

A cantilever beam can have many different modes of vibration, each with a different resonant frequency. The first mode of vibration has the lowest resonant frequency, and typically provides the most deflection and therefore electrical energy. A lower resonant frequency is desirable, since it is closer in frequency to physical vibration sources and generally more power is produced at lower frequencies [5]. Therefore, energy harvesters are generally designed to operate in the first resonant mode.

Each mode of vibration has a characteristic mode shape. This describes the deflection of the beam along its length. Figure 2.4 shows some examples of mode shapes for the first three vibrational modes of a beam. When a beam is vibrating in a particular mode, the deflection will vary sinusoidally with time, with the amplitude of the sine wave along the length of the beam given by the mode shape. The points where the mode shape is zero are stationary and are referred to as nodes. In general, the  $n$ th vibrational mode will have  $n$  nodes.

## **2.4 Physical Vibration Sources**

The frequency and amplitude characteristics of ambient vibration sources have been analyzed in Roundy *et al* [2]. They concluded that most ambient vibration sources have relatively low frequencies (under 200 Hz) and widely varying acceleration levels. As a representative source, they chose the 120 Hz,  $2.5 \text{ m/s}^2$  acceleration measured from a microwave oven.

## **2.5 Rectification and Storage**

To convert the AC output voltage to a more useful DC voltage, some form of rectification must be used. One group has come up with a generator that produces DC voltage directly, without the need for rectification, but it is still in the development phase [15]. Typically, low-power or small signal diodes are used to form a bridge rectifier [4-7]. Novel approaches have included the use of custom low-power diodes and voltage multipliers [6].

After rectification, the DC voltage is used to charge a capacitor or battery. This allows the device to draw more power over a short period than the harvester is able to provide. DC-DC conversion schemes have also been explored and have been shown to charge batteries far more efficiently [16].

# **3. THEORETICAL PREDICTIONS**

## **3.1 Estimation of Resonant Frequency**

The following estimates assume that beams are homogenous, composed of a single uniform material, and of constant cross section. However, equivalent values for Young's modulus and density can be calculated for composite beams by using a weighted average method [17]. The resulting equations describing the resonant frequencies are much more compact, making the scaling analysis far more straightforward.

### 3.1.1 Using the Beam Equation<sup>5</sup>

The resonant frequencies of a beam can be estimated using Euler-Bernoulli beam theory [14]. By solving the Euler-Bernoulli beam equation with the appropriate boundary conditions, the eigenvalues of the system can be determined, which then allow for the calculation of the resonant frequencies. The differential equation describing the motion of an Euler-Bernoulli beam is:

$$\frac{\partial^4 \delta}{\partial x^4} + \frac{\rho A}{EI} \frac{\partial^2 \delta}{\partial t^2} = 0,$$

where  $\delta$  is the beam deflection as a function of position along the beam and time,  $\rho$  is the density,  $A$  is the area of the cross section of the beam,  $E$  is the Young's modulus, and  $I$  is the area moment of inertia. For a beam of rectangular cross section, the relevant moment is  $I = \frac{1}{12} wt^3$ .

The general solution for sinusoidal vibration is as follows, with the constants and eigenvalues determined by the boundary conditions.

$$\delta(x, t) = (c_1 \sin \beta x + c_2 \cos \beta x + c_3 \sinh \beta x + c_4 \cosh \beta x) \cdot \sin \omega t$$

where

$$\beta^4 = \frac{\rho A \omega^2}{EI}$$

For a fixed-free beam with no proof mass, the relevant boundary conditions for a beam of length  $L$  are:  $\delta(0, t) = \delta_x(0, t) = 0$  and  $\delta_{xx}(L, t) = \delta_{xxx}(L, t) = 0$ . These first two boundary conditions

---

<sup>5</sup> This information is paraphrased from "The Encyclopedia of Vibration", pages 137-143.

indicate that the fixed end of the beam is stationary, and that the beam is flat at the point of attachment. The free end conditions mean that there are no forces applied at that point and no bending moment. The first nontrivial eigenvalue of this system is  $\beta L \approx 1.875$ , so the equation for the resonant frequency of the first mode is:

$$f = \frac{\omega}{2\pi} = \frac{1.875^2}{2\pi L^2} \sqrt{\frac{EI}{\rho A}}$$

By rewriting  $I$  and  $A$  in terms of the beam dimensions, the widths cancel and the expression reduces to:

$$f = \left( \frac{1.875^2}{2\pi} \sqrt{\frac{E}{12\rho}} \right) \frac{t}{L^2}$$

For a beam with a proof mass added on the tip, the mass can be modeled as a point load on the tip. The fourth boundary condition then becomes

$$\delta_{.xxx}(L,t) = -\frac{m\omega^2}{EI} \delta(L,t),$$

where  $m$  is the mass of the beam. The calculation of eigenvalues in this case depends on the ratio of the added mass to the mass of the beam.

### 3.1.2 Using Stiffness and Effective Mass

If we model the beam deflection as a 1<sup>st</sup> order spring-mass system, then the resonant frequency can be estimated as

$$f_o = \frac{1}{2\pi} \sqrt{\frac{k_{eff}}{m_{eff}}}$$

The effective mass of the beam itself is approximately 0.236 times the beam's actual mass [18], and if the proof mass is modeled a point load at the tip, the total effective mass is approximately:

$$m_{eff} = 0.236\rho AL + m_{proof}$$

The stiffness of a rectangular beam is  $k_{eff} = \frac{3EI}{L^3}$ , so for a beam with no proof mass:

$$f = \left( \frac{1}{2\pi} \sqrt{\frac{E}{0.236 \cdot 4\rho}} \right) \frac{t}{L^2}$$

Assuming the added mass on the tip is much larger than the mass of the beam itself leads to this expression for the resonant frequency (assuming the stiffness is unaffected):

$$f = \left( \frac{1}{2\pi} \sqrt{\frac{3E}{m_{proof}}} \right) \sqrt{\frac{wt^3}{L^3}}$$

To model the effects of the distributed mass loading, rather than tip loading, of the proof mass,  $L_{eff} = L_{beam} - 0.5L_{proof}$  can be substituted for the length.

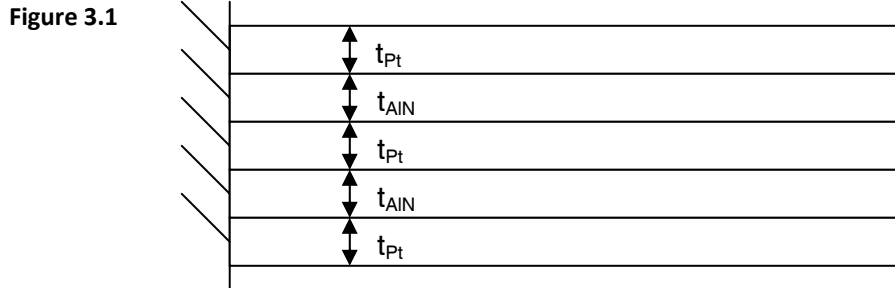
Both approaches for calculating the resonant frequency arrive at similar results when the proof mass is not taken into consideration, differing by only about 1%. When the proof mass is also considered, the stiffness approach is mathematically simpler, and will be used to estimate the structure size needed to take advantage of ambient vibration sources.

## 3.2 Modeling of Piezoelectric Generators

### 3.2.1 Static Deflections

For the modeling of static deflections of beams, a simple equation was derived from the piezoelectric constitutive relationship. DeVoe and Pisano [19] developed a model for multilayer actuators by equating strain at the boundaries of each layer. For this specific beam, a simpler model can be developed exploiting the symmetry of the fabricated structure.

The beams tested have a “sandwich” structure, consisting of alternating layers of aluminum nitride and platinum, as shown in Figure 3.1.



To derive a relationship between deflection of the beam and applied voltage, we start by computing stress based on a known tip deflection. If the tip is deflected downward by some amount  $\delta_t$  then the deflection along the length of the beam – assuming constant curvature – becomes

$$\delta(x) = -\frac{\delta_t}{L^2} x^2$$

where L is the length of the beam, so that the deflection at  $x=L$  is  $\delta_t$  in the downward direction.

Strain is a linear function of distance from the neutral axis, and is written as

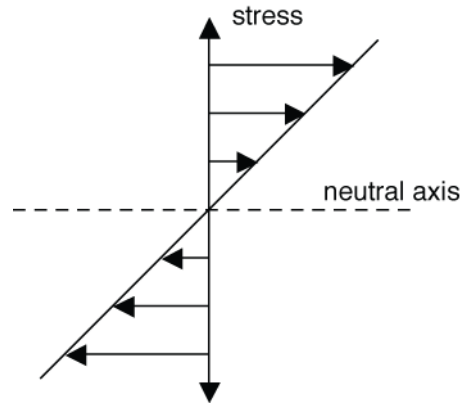
$$S = \frac{M}{EI} y = -\frac{\partial^2 \delta}{\partial x^2} y = \frac{2\delta_t}{L^2} y$$

Figure 3.2 shows this strain variation with respect to the distance from the neutral axis. Using the piezoelectric equation  $S = sT + d_{31}E$ , evaluated at  $T = 0$ , gives the following relationship between the strain,  $S$ , and the applied voltage,  $V$ .

$$S = \frac{2\delta_t}{L^2} \cdot \frac{1}{2}(t_{Pt} + t_{AIN}) = d_{31}E = d_{31} \frac{V}{2t_{AIN}}$$

The average distance from the neutral axis is used in place of  $y$  to arrive at a value for average stress. In a bending beam, the neutral axis is the line along the beam where no stress is experienced. Because of the symmetric nature of the structure, the neutral axis will be centered vertically.

**Figure 3.2**



Solving for deflection in terms of voltage gives

$$\delta_t(V) = \frac{d_{31}L^2V}{2t_{AIN}(t_{Pt} + t_{AIN})}$$

So deflection as a function of length is then

$$\delta_t(x, V) = \frac{d_{31}x^2V}{2t_{AIN}(t_{Pt} + t_{AIN})}$$

Smits and Dalke [20] develop a similar model using energy density to calculate deflection, which reduces to the following for this structure:

$$\delta_t(x, V) = \frac{3d_{31}x^2V}{8t_{AIN}^2}$$

The predictions of the two models and the experimental results are compared in Section 4.2.

### 3.2.2 Dynamic Deflections

Many different approaches have been used to model the mechanical and electrical behavior of piezoelectric cantilever beam generators when excited by external vibrations [3,5,21,22]. Basic models represent the system as a spring-mass-damper mechanical system, with the electrical output coupled to some physical parameter of the system [3]. More sophisticated models take into account the additional damping and backward coupling effects of the electrical load on the mechanical system [5,21]. Even more accurate models use multiple degrees of freedom to model the effect of multiple modes of resonance of the system [22].

For this report, the model of Roundy & Wright [5] was chosen for its simplicity and demonstrated success in modeling. A multiple degree of freedom model would provide more accurate results at frequencies far from the first resonant frequency, but near resonance the two should have similar results.

Roundy's model for voltage output across a resistive load, as a function of excitation frequency, is listed below. It is assumed that the two piezoelectric layers are wired in series.

$$|V(\omega)| = \omega^2 \frac{2c_p d_{31} t_c A_{in}}{\varepsilon k_2} \left\{ \left[ \frac{\omega_n^2}{RC_b} - \left( \frac{1}{RC_b} + 2\zeta\omega_n \right) \omega^2 \right]^2 + \omega^2 \left[ \omega_n^2 (1 + k_{31}^2) + \frac{2\zeta\omega_n}{RC_b} - \omega^2 \right]^2 \right\}^{-1/2}$$

The constants in the equation are described in Table 3.1, at the end of this section.

Assuming operation at resonance, Roundy also derives this relationship:

$$|V| = \frac{2\omega c_p d_{31} t_c A_{in}}{\varepsilon k_2} \left\{ \omega^2 \left( \omega^2 k_{31}^2 + \frac{2\zeta\omega}{RC_b} \right)^2 + 4\zeta^2 \omega^6 \right\}^{-1/2}$$

Instantaneous power dissipation is then

$$P = \frac{V_{rms}^2}{R} = \frac{|V|^2}{2R} = \frac{1}{2\omega^2} \frac{RC_b^2 \left( \frac{2c_p d_{31} t_c}{k_2 \varepsilon} \right)^2 A_{in}^2}{(4\zeta^2 + k_{31}^4)(RC_b \omega)^2 + 4\zeta k_{31}^2 (RC_b \omega) + 4\zeta^2}$$

With an optimal load resistance ( $R = 1/\omega C_b$ ), the power expression becomes

$$P = \frac{1}{2\omega^3} \frac{C_b \left( \frac{2c_p d_{31} t_c}{k_2 \varepsilon} \right)^2 A_{in}^2}{(8\zeta^2 + 4\zeta k_{31}^2 + k_{31}^4)}$$

**Table 3.1:**

$\omega$	Driving frequency (in rad/s)
$c_p$	Young's modulus of piezo layer
$t_c$	Thickness of piezo layer
$A_{in}$	Magnitude of input acceleration
$\varepsilon$	Permittivity of piezo layer
$k_2$	Relates tip deflection to stress:

	$k_2 = \frac{L^2}{\frac{3}{2}(t_{Pt} + t_{AlN})} \frac{2L + \frac{3}{2}L_{mass}}{2L + L_{mass} - L_{electrode}}$
$\omega_n$	Resonant frequency of generator
R	Load resistance
$C_b$	Capacitance of beam
$\zeta$	Damping ratio
$k_{31}$	Coupling coefficient: $k_{31}^2 = \frac{d_{31}^2 C_P}{\epsilon}$

### 3.3 Effects of Scaling

Roundy & Wright briefly discuss the dependence of power output on device scale, and verify that a larger generator will produce a larger power output [5]. However, they do not investigate the full dependence of power generation on device scale.

To understand how power and scale are related, a relation between device size and resonant frequency must first be derived. From section 3.1.2 we see that for devices with a large tip mass:

$$\omega_o \propto \sqrt{\frac{wt^3}{mL^3}}$$

The other parameters in the power equation have the following dependences on scale:

$$C_b \propto \frac{wL}{t}, t_c \propto t \text{ and } k_2 \propto \frac{L^2}{t}$$

So then the final power dependence on scale is

$$P \propto \left( \frac{wt^3}{mL^3} \right)^{-3/2} \frac{wL}{t} \left( \frac{t}{\frac{L^2}{t}} \right)^2 = \sqrt{\frac{1}{w} \left( \frac{mL}{t} \right)^3} = w^{-1/2} L^{3/2} t^{-3/2} m^{3/2}$$

This brief scaling study shows that a long, thin beam with a large proof mass will yield the most power. Another interesting result is to consider a base design, with a standardized length, width, thickness, and proof mass size, and investigate what happens when each dimension is scaled linearly. Mathematically, this can be emulated by replacing each linear dimension by a factor of  $k$ , and the mass by  $k^3$ , since mass is proportional to volume, which is measured in the cube of linear dimensions. It is then derived that power is proportional to the fourth power of the linear dimension of the device, i.e. that

$$P \propto k^4.$$

This also means that power per unit area and volume will both decrease when devices are scaled down, since area and volume are proportional to  $k^2$  and  $k^3$ . Kasyap [8] arrives at a similar conclusion and verifies it with finite-element method (FEM) simulations.

## 4. EXPERIMENTAL RESULTS

### 4.1 Experimental Setup

For testing purposes, the die containing the cantilevers to be tested was attached to a PCB approximately 4cm by 4cm with carbon tape. Two leads were soldered to the PCB, and the contacts connected to the electrodes on the surface of the beam were wire-bonded to the PCB. On the device itself, the top and bottom electrodes share a single pad on the die, and the second pad is connected to the middle electrode. A hole was drilled in the center of the PCB and threaded for attachment to the mount on the vibration shaker.

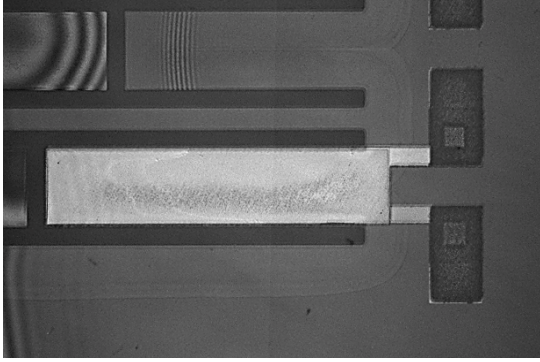


Figure 4.1a: an overhead view of one of the 400 $\mu$ m beams

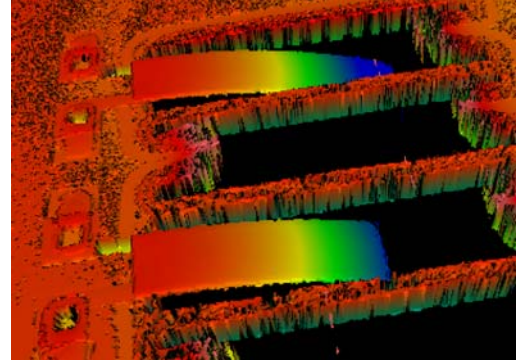


Figure 4.1b: a side view of two beams showing the bending caused by the mass of the beam

Due to the time constraints, the design and fabrication of a generator was not feasible. Instead, a cantilever on an older wafer was chosen for analysis. The cantilever to be tested is approximately 400 $\mu$ m long and 100 $\mu$ m wide, with  $t_{Pt} = 0.2\mu$ m and  $t_{AlN} = 1\mu$ m (see Figure 3.1). There is actually a series of cantilevers, with lengths of 400, 300, 200, and 100  $\mu$ m. However, the longest cantilever would exhibit the greatest response, so the 400 $\mu$ m was chosen for testing. Since the cantilevers were not designed with energy harvesting in mind, they lack proof masses. This design is not optimal, but it does serve to illustrate many of the characteristics that would need to be taken into account. The relevant material properties used in estimates can be seen in Table 4.1.

Table 4.1:

$E_{AlN}$ (in plane)	292 GPa [23]
$\rho_{AlN}$	3200 kg/m <sup>3</sup> [17]
$d_{31}$ (AlN)	-1.98 pC/N [23]
$E_{Pt}$	168 GPa [17]
$\rho_{Pt}$	21450 kg/m <sup>3</sup> [17]

## 4.2 Resonant frequency verification

To verify the estimates for the resonant frequency, the impedance of the device was measured across a range of frequencies using an Agilent impedance analyzer. The impedance measurements were done in a vacuum, as damping due to air would severely reduce the beam's movement at atmospheric pressure and make the resonance peak difficult to discern.

The following measurement was made for the beam measuring 400 $\mu\text{m}$  long by 100  $\mu\text{m}$  wide:

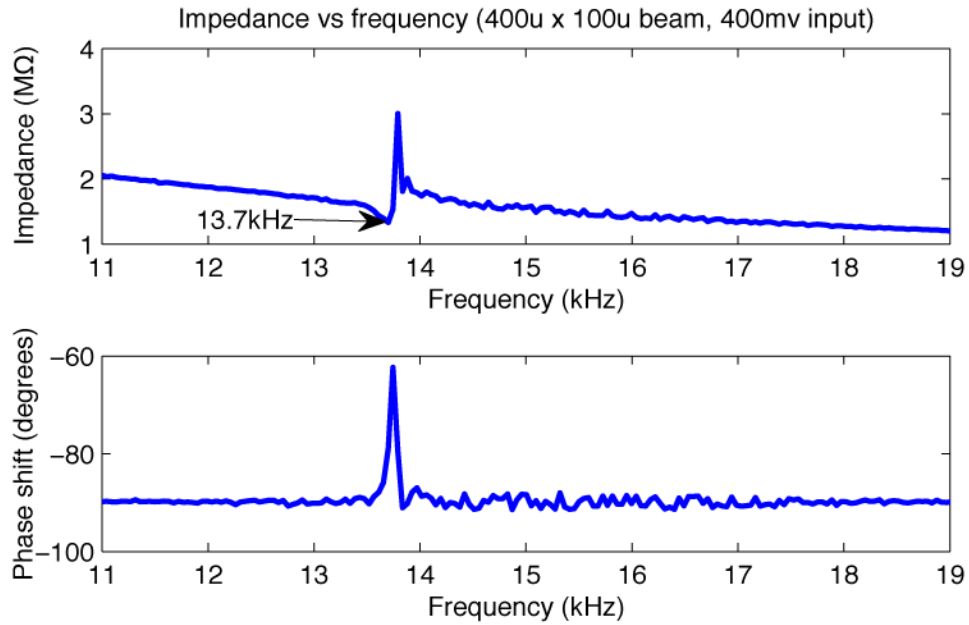


**Figure 4.2**

Using the approximate relationships derived in section 3.1, the calculated resonant frequencies are 15.6 kHz (beam equation approach) and 15.9 kHz (stiffness approach). This represents errors of 13% and 15%, respectively. For comparison purposes, another impedance measurement was made of a 300 $\mu\text{m}$  by 100 $\mu\text{m}$  beam on the same die:

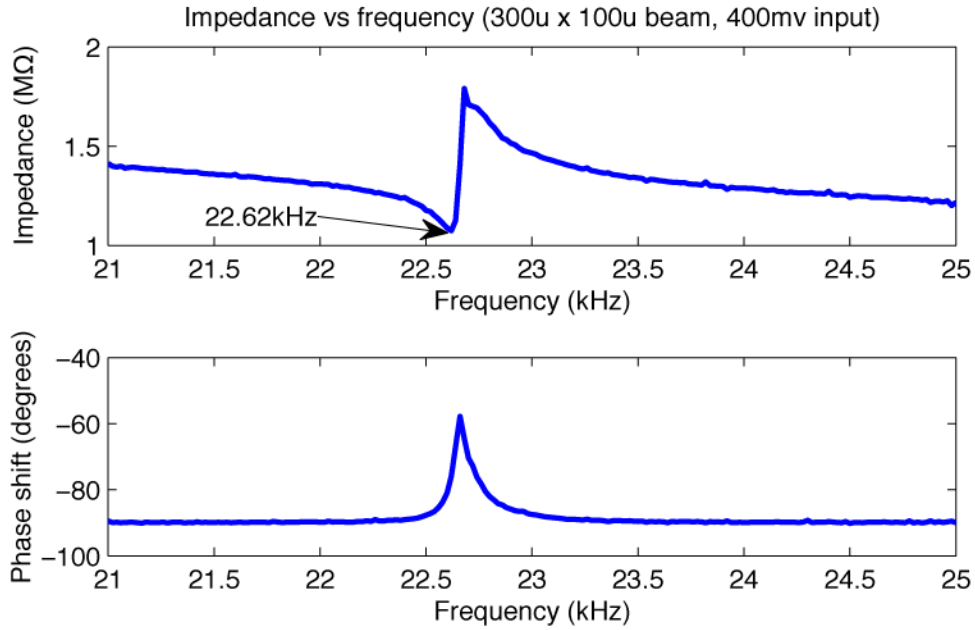


**Figure 4.3**

In this case, the calculated resonant frequencies are 27.8 kHz (beam equation) and 28.2 kHz (stiffness), and the relative errors are 22% and 25%.

Since the relative error increases significantly when a shorter beam is used, this suggests that the derived models are not as accurate for shorter beams. In fact, one of the assumptions of the Euler-Bernoulli beam equation is that the length is significantly larger than the width and thickness. Keeping all other factors constant, better agreement would be expected with longer beams.

## 4.2 Static Deflection

To verify the actuation response of the beam, a voltage was applied across the electrodes of the beam and the deflection response measured (see figure 4.4). The measurements were made using a Zygo laser interferometer.

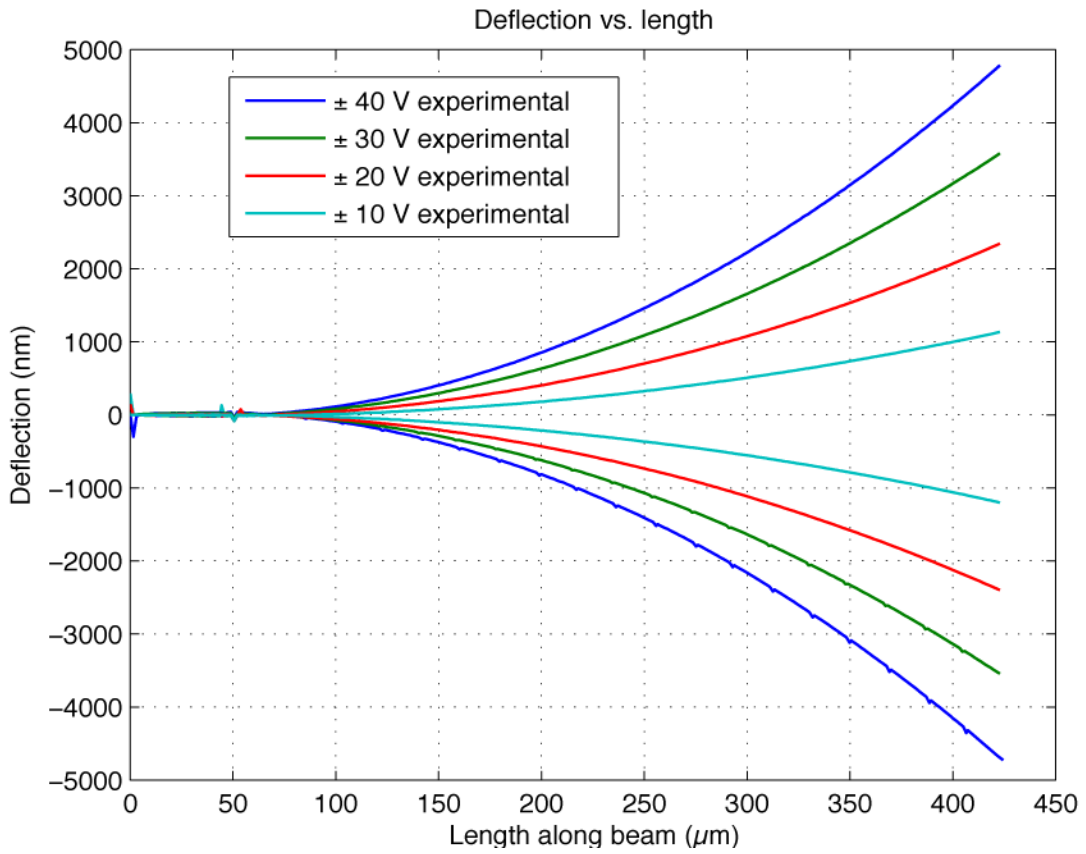


**Figure 4.4**

Comparing tip deflection between experimental measurements and theoretical predictions shows that the theory overestimates the tip deflection by a small but noticeable amount:

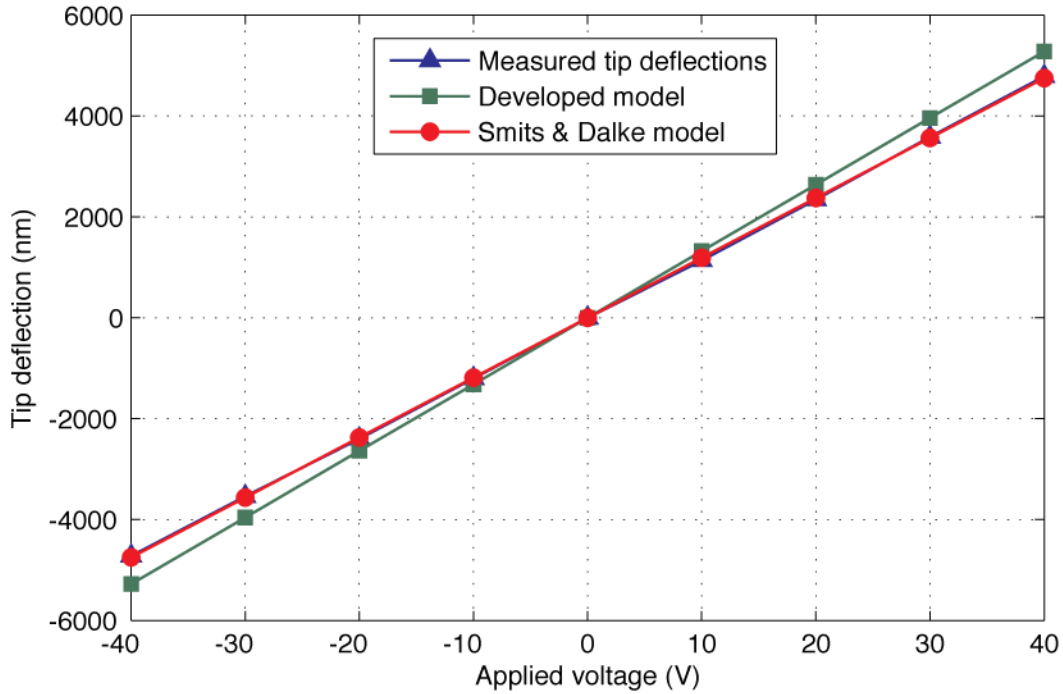


**Figure 4.5**

The relative error between the developed model and the experimental results is about 10% for each applied voltage. The model derived by Smits & Drake [20] is accurate to within 5% for all data points, and within 1% for most.

### 4.3 Excitation using Vibration Shaker

To test the beam's response to accelerations, the PCB with the wire-bonded die was fastened securely to the shaker mount. An Agilent function generator was used to drive the shaker, and the output signal from the piezoelectric device was buffered and amplified so it could be measured with an oscilloscope.

However, since the output current of the function generator is limited, sufficient acceleration levels could not be created. Using a Phidgets accelerometer, the applied acceleration was measured and was found to have a magnitude of only about 0.1 g.

In an attempt to resolve this issue, an Apex PA-98 amplifier was also used to drive the shaker. This did result in an improved acceleration output, but the shaker output was then limited by the low current capability of the amplifier (~40mA). To facilitate future testing, an amplifier configuration with a higher output current will be used, as the PA-98 can support up to 200mA of output.

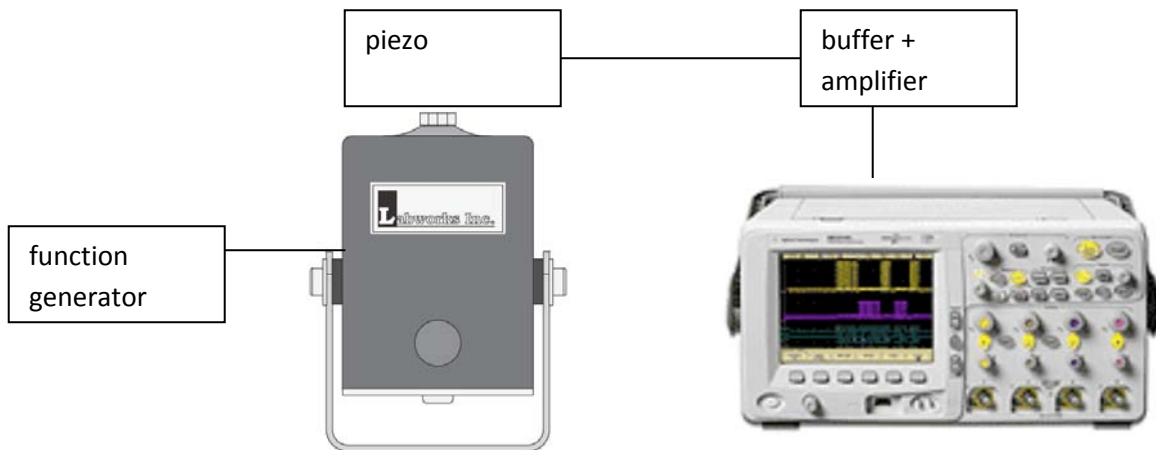


**Figure 4.6: Diagram of shaker setup**

## **5. CONCLUSIONS AND RECOMMENDATIONS**

It has been shown that the current device structure does not have scaling advantages in power per unit area or volume. It is difficult to produce sufficient displacement at small scales to generate a considerable voltage. At the microscale, resonance frequencies are too low to effectively convert ambient frequencies as found in nature.

As an illustration of the challenge of reaching lower frequencies with MEMS devices, consider a beam of equal width and thickness as the one tested, but a significantly larger length and an added proof mass. Using the frequency estimate in section 3.1.2, a 2000 $\mu\text{m}$  by 100 $\mu\text{m}$  by 2.6 $\mu\text{m}$  beam would need to have a 0.11mg proof mass to reach even 200 Hz. Using a relatively dense metal such as gold would still require a cubic proof mass of approximately 148 $\mu\text{m}$  on each side.

Due to the difficulty in reaching low frequencies with MEMS scale devices, these types of energy harvesters would be limited to applications with very high frequency vibrations. However, for compact systems with very low power requirements, MEMS microgenerators are a very attractive means of powering devices indefinitely.

Recommendations are to build devices of this form, with a proof mass added, while targeting lower resonant frequencies. Alternate geometries may help in lowering the resonant frequency, and gaining more power output. More effective solutions include designing a structure that is either not dependent on resonance, or has a means of tuning its resonant frequency. Examples of such devices have already been demonstrated by other researchers [24,25]. To take advantage of the large deflections and strains that go with a beam oscillating at resonance, the tuning approach is recommended as the most useful for power output. The challenge will be in adapting existing tuning approaches to the MEMS scale, or in devising a new means to tune the beams' resonant frequency.

## 6. REFERENCES:

1. A. Chandrakasan, R. Amirtharajah, J. Goodman, W. Rabiner, Trends in Low Power Digital Signal Processing, Proceedings of the 1998 IEEE International Symposium on Circuits and Systems (1998) 604 – 607.
2. S. Roundy, P.K. Wright, J. Rabaey, A study of low level vibrations as a power source for wireless sensor nodes, *Computer Communications*, 26 (2003) 1131–1144.
3. C.B. Williams, R.B. Yates, Analysis of a micro-electric generator for Microsystems, *Sensors and Actuators*, 52 (1996) 8-11.
4. D. Shen, J.H. Park, J. Ajitsara, S.Y. Choe, H.C. Wickle III, D.J. Kim, The design, fabrication and evaluation of a MEMS PZT cantilever with an integrated Si proof mass for vibration energy harvesting, *Journal of Micromechanics and Microengineering*, 18 (2008) 055017.
5. S. Roundy, P. K. Wright, A piezoelectric vibration based generator for wireless electronics, *Smart Materials and Structures*, 13 (2004) 1131-1142.

6. M. Marzencki, Y. Ammar, S. Basrour, Integrated power harvesting system including a MEMS generator and a power management circuit, *Sensors and Actuators A*, 145-146 (2008) 363-370.
7. Y.B. Jeon, R. Sood, J.H. Jeong, S.G. Kim, MEMS power generator with transverse mode thin film PZT, *Sensors and Actuators A* 122 (2005) 16–22.
8. A. Kasyap V.S., Development of MEMS-based Piezoelectric Cantilever Arrays for Energy Harvesting, Ph.D. dissertation, Department of Aerospace Engineering, University of Florida, 2007.
9. IEEE Standard on Piezoelectricity, *Standards Committee of the IEEE Ultrasonics, Ferroelectrics, and Frequency Control Society*, ANSI/IEEE Std 176-1987 (1988).
10. M. Marzencki, S. Basrour, B. Charlot, A. Grasso, M. Colin, L. Valbin, Design and fabrication of piezoelectric micro power generators for autonomous Microsystems, *Proc. Symp. on Design, Test, Integration and Packaging of MEMS/MOEMS DTIP05*, (2005) 299-302.
11. H. A. Sodano, J. Lloyd, D. J. Inman, An experimental comparison between several active composite actuators for power generation, *Smart Materials and Structures*, 15 (2006) 1211-1216.
12. J. Cho, M. Anderson, R. Richards, D. Bahr, C. Richards, Optimization of electromechanical coupling for a thin-film PZT membrane: I. Modeling, *Journal of Micromechanics and Microengineering*, 15 (2005) 1797-1803.
13. S. Roundy, E.S. Leland, J. Baker, E. Carleton, E. Reilly, E. Lai, B. Otis, J.M.Rabaey, P.K. Wright, V. Sundararajan, Improving Power Output for Vibration-Based Energy Scavengers, *IEEE Pervasive Computing*, 4 (2005) 28-36.
14. S.G. Braun, D.J. Ewins, S.S. Rao, *Encyclopedia of Vibration*, Volumes 1-3. Elsevier. Online version available at:  
[http://knovel.com/web/portal/browse/display?\\_EXT\\_KNOVEL\\_DISPLAY\\_bookid=1873&VerticalID=0](http://knovel.com/web/portal/browse/display?_EXT_KNOVEL_DISPLAY_bookid=1873&VerticalID=0)
15. A. Hajati, S.G. Kim, Rectifier-less piezoelectric micro power generator, *Proc. SPIE* 6928, 69281T (2008).
16. G.K. Ottman, H.F. Hofmann, A.C. Bhatt, G.A. Lesieutre, Adaptive Piezoelectric Energy Harvesting Circuit for Wireless Remote Power Supply, *IEEE Transactions on Power Electronics*, 17 (2002) 669-676.
17. P.J. Stephanou, Piezoelectric Aluminum Nitride MEMS Resonators for RF Signal Processing, Ph.D. dissertation, Department of Mechanical Engineering, University of California, Berkeley, 2006.
18. J.W. Yi, W.Y. Shih, and W.H. Shih, Effect of length, width, and mode on the mass detection sensitivity of piezoelectric unimorph cantilevers, *Journal of Applied Physics*, 91 (2002) 1680-1686.
19. D.L. DeVoe, A.P. Pisano, Modeling and Optimal Design of Piezoelectric Cantilever Microactuators, *Journal of Microelectromechanical Systems*, 6 (1997) 266-270.
20. J.G. Smits, S.I. Dalke, The constituent equations of piezoelectric bimorphs, *IEEE Ultrasonics Symposium 1989 Proceedings*, (1989) 781-784.
21. N.E. duToit, B.L. Wardle, S.G. Kim, Design Considerations for MEMS-Scale Piezoelectric Vibration Energy Harvesters, *Integrated Ferroelectrics*, 71 (2005) 121–160.

22. A. Erturk, D.J. Inman, A Distributed Parameter Model for Cantilevered Piezoelectric Energy Harvesters, *Journal of Vibrations and Acoustics*, 041002 (2008).
23. G. Piazza, Piezoelectric Aluminum Nitride Vibrating RF MEMS for Radio Front-End Technology, Ph.D. dissertation, Department of Electrical Engineering and Computer Science, University of California, Berkeley, 2005.
24. V.R. Challa, M.G. Prasad, Y. Shi, F. T. Fisher, A vibration energy harvesting device with bidirectional resonance frequency tenability, *Smart Materials and Structures*, 17 (2008) 1-10.
25. D. Spreeman, B. Folkmer, D. Mintenbeck, Y. Manoli, Novel non-resonant vibration transducer for energy harvesting, *PowerMEMS 2005 Proceedings*, (2005) 144-146.

# MIMOSA: MINE INTERIOR MODEL OF SMOKE AND ACTION

NSF Summer Undergraduate Fellowship in Sensor Technologies

Desirée E. Velázquez Rios (Mathematics) – University of Puerto Rico at Humacao

Advisors: Norman I. Badler and Jinsheng Kang

## ABSTRACT

The team goal for the summer is the simulation of underground coal mine fires, and the study of the physiological reactions occurring during evacuations. I undertook the task of searching for new ways to modify the map creation tools used by the original crowd simulation software using the *Crowds with Aleatoric, Reactive, Opportunistic, and Scheduled Action (CAROSA)* framework. I also modeled the mining equipment used to simulate a more realistic coal mine situation. First, a literature search on the web was done for software called Level Editors and Game Engines. Then, modeling the mining equipment, rigging the miner mesh model with a skeleton and animating both equipment and miner was done. These tasks used two pieces of Autodesk software; Maya and Motion Builder. Additionally, Maya was used to create the cell-portal mine map that the virtual miners use to move about in the space. Once the models and animations were created, they would be used for the simulation. With the simulation results we can validate a study made by U.S. Department of Health and compare the physiological models visualized in the simulation with the results of the study.

## 1. INTRODUCTION

An important element of our lives is fire and it could easily be said to be the most important discovery to man. Just as it has many positive uses, such as warming cold bodies or lighting the way, fire also has a negative side. House fires, along with forest fires, are of the most terrifying occurrences associated with fire. These fires can consume the home of many and leave families “on the street” in minutes. In these cases, the fire can easily escape or propagate due to the open space and abundance of wind but the same cannot be said for underground mine fires.

Underground coal mining is a dangerous occupation because coal is an easily combustible rock. With only one exit, both miners and fire must escape in the same direction. Although the saying goes “where there’s smoke, there’s fire”, we also know that it is also true in reverse. Fire produces smoke, so where there is fire, there will be smoke. When in large volumes, fire smoke can deplete the energy of the escapees until they eventually lose consciousness and die. To safely escape these fires, it is important to know what must be done during such an occasion. But

reproducing this situation is dangerous not just to people, but to the environment. Therefore, simulating a mine fire becomes highly important.

The team goal for the summer, until the end of August, is the simulation of underground coal mine fires and the study of the physiological reactions occurring during evacuations. Many other research projects have done case studies lasting more than 10 years of these fires and interviewed many survivors for their knowledge. During the 1970s, the United Kingdom was one of the first to conduct this type of study and United States Department of Human Health and Services followed with a complement of theirs [1]. The U.S Department of Human Health and Services' study shows statistics of different underground mine fires, taking into account the number of miners originally present and the surviving number, along with several other factors, such as age and years of experience. However, if we were to recreate these events, taking into account all the factors, there is no saying that the situation will go exactly the same every time. So part of the team goal is to validate the results of this study with the results of our simulation.

Visiting Professor Jinsheng Kang will be working on the smoke models that determine how the miners are affected and the scenario for the simulation. Graduate student Pengfei Huang will work on developing a new framework and the implementation of the smoke models for the simulation. The personal goal this summer will be searching for a new way to modify the map creation tool used by the framework for crowd simulations and the modeling and animations of various aspects of the underground coal mine. Also, modeling of the mine map and the mining equipment will be realized. After that the equipment and a miner model will be animated for the simulation. With these, a more realistic simulation of an underground coal mine can be implemented.

The following section will be background of the project. Section 3 will talk about the search for new alternative of map creation. Section 4 will be about the modeling that was done, while Section 5 complements the latter by explaining the animations done to some of the models. The following two sections, 6 and 7, will be the results and discussion, and the recommendations for the team. After that are the acknowledgements (Section 8), the references (Section 9), and two appendixes.

## **2. BACKGROUND**

### **2.1 Coal mining and underground fires**

Coal is a valuable organic rock used to provide electricity and for the production of steel and cement. This combustible fossil fuel can be found in many regions of the world in seams with lengths of hundreds of meters and is estimated to be extracted for another 130 years [2]. Because of its combustible nature and length of the seam, any spark that flames this rock will cause a fire the length of the seam. The fires are also very hard to extinguish and can keep burning for decades [3].

The methods used to extract coal from the ground depend on the landscape of the location where the coal is found. Surface (opencast) and underground (deep) mining are the two methods of coal

mining. Underground mining extracts 60% of the coal used in world productions, while surface mining extracts the remaining 40%. Of these two, underground mining contains two main methods called longwall and room-and-pillar mining. The method used for this research is room-and-pillar mining.

Room and pillar mining is done by cutting a series of “rooms” into the coal seam, supported by the remaining “pillars” of coal. This method leaves around 40% of the coal inside the pillars but can be later recovered. The mines can be as short as 700 meters in length where a minimum of eight mine workers (miners) per section extract the coal. As these mines run 24 hours a day, many miners work in the mine each day.

Coal can spontaneously combust, making it hard to fully train miners on how to act when in a mine fire situation. Therefore, by using computer simulations, it is possible to simulate these mine fire situations to use for training procedures. But, in order to simulate a realistic mine fire, data from past situations is needed. Using a study book conducted by the U.S. Department of Human Health and Services, we can know the physiological data needed to create the miner reactions to smoke and mine fire situations. Although the book is an accurate study full of data, we will use our results to compare with the study and can eventually validate the study.

## **2.2 CAROSA**

The *Crowds with Aleatoric, Reactive, Opportunistic and Scheduled Action* (CAROSA) [4] framework is a series of software and programming codes used in crowd simulations and created by the SIG Graphics Center. Through this framework, we can specify the characteristics of an agent, including their schedules and activities; allow the agent to have a certain degree of awareness and be able to interact with the environment accordingly; and allow the agents different action types resulting from certain events. CAROSA uses Maya for the creation of the agents and exports them to Cal3D in order to animate them. Cal3D is integrated into MACES+HiDAC, another creation by the SIG Graphics Library, for the crowd simulations.

Each agent has three levels of communication divided in high, middle and low, that determines their movements and involvements with the environment. CAROSA is the high level, where the agents’ characteristics are designed, along with the actions they can do. Following the high level is the middle level, MACES, where the agents determine how to interact with other agents and what routes to take in an evacuation simulation. With MACES, the agents learn of their surroundings and can make appropriate decisions. The last level is HiDAC and here the agents produce more human-like motions, such as detecting walls and objects in a room for avoiding collisions.

The maps where the agents interact are created with the Open Graphics Library (OpenGL) and CAROSA is highly dependent on rectangular maps. Because these maps are hardcoded in OpenGL, to create a new simulation with a new map would take unnecessary time. A solution to this is the use of level editors or game engines, explained in Section 3.

### 3. LEVEL EDITOR SEARCH

Although CAROSA is a working system, it relies heavily on a rectangular grid structure for the creation of the simulation maps. This, of course, means that diagonal paths are not easily constructed within the simulation. Because underground coal mines are designed to vary depending on geographical location, the paths within those mines become varied as well. To create these mine maps easily, we turn to new methods of modeling. A proposed idea is to use a type of software tool called a level editor.

Level editors essentially can create maps for various uses, the common one being level designing for games such as Quake or Half-life. Since level editors are usually used for a specific game or type of games, a more general level editor is required for designing mine maps. Wavefront object (.obj) files are one of the generic types of files commonly used by game designers. For this reason, a level editor that could export the map to such a file is needed. Another feature needed is the identification of what are and are not pathways to help the agents determine where they can or cannot go through. The last feature we needed was tagging of the world objects to identify which the agent could interact with. Tags will be placed on one of three entities: objects (e.g., cars and coal), cells (e.g. rooms and paths), and portals (e.g., doors). Automatic tagging is also a criterion for selecting a level editor.

To expand the limited search results of common search engines (e.g. Google), we also took into consideration game engines. These softwares are renderers for game developers or animators and can also contain level editors. The typical method when creating a homemade game is to develop your own level, render it for testing, then apply it to game. Both level editors and game engines were tested on a Dell Precision 670 running on Windows XP Professional (version 2002 Service Pack 3) with an NVIDIA GeForce 8800 GT video driver. Table 1 shows the results of the testing done on that workstation, including the names of the selected level editors and game engines, and the availability of the features needed.

Name	Features					
	Export to .obj	Identifiable pathways	Tagging abilities			
			Objects	Cells	Portals	Automatic
IrrEdit	3D mesh file.	No.	Nodes.	?*	?	?
Delta3D	No.	?	With labels to "actors".	?	?	?
OGRE	No.	Yes.	?	?	?	No.
Panda3D	No.	Yes.	?	?	?	No.
OpenSceneGraph	3D database plugin.	?	?	?	?	No.
jME	No.	?	As nodes.	As nodes.	?	No.
3D Rad	No.	Yes.	Object type.	?	?	?

Reality Factory	No.	No.	No.	No.	No.	No.
Anvil	?	?	?	?	?	?
Dim3**	No.	?	?	?	?	?
GenEdit	No.	No.	No.	No.	No.	No.
Blender	Yes.	No.	?	?	?	?
Maya	Yes.	?	Yes.	Yes.	Yes.	No.

\* The (?) symbol denotes that feature existence is unknown.

\*\* Runs only in MacOSX.

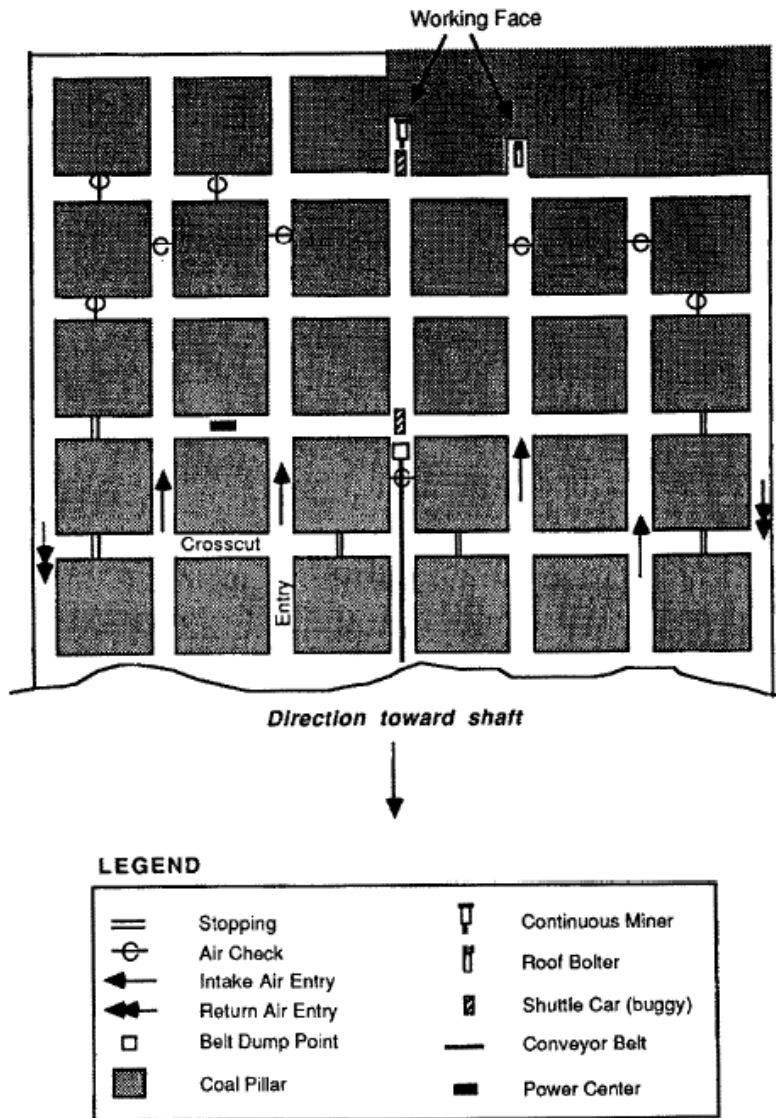
**Table 2. Matrix of the results of the level editor and game engine search.**

As Autodesk Maya contains most of the features needed for our simulation, it was chosen to model the maps and equipment used in underground mining. Maya is a very powerful modeling tool that is flexible enough to run scripts for just about any imaginable use. An example of this scripting is left for section 5 of animation.

A new framework combining the Qt C++ framework and the Object-oriented Graphics Rendering Engine (OGRE) was developed by graduate student Huang. Using this new framework, now called MIMOSA, all objects (e.g. maps, equipment and miners) are loaded using OGRE's mesh format. A Maya-OGRE exporter is used for exporting the models to such format.

#### **4. MODELING**

For this simulation to be possible, various aspects of the underground mine had to be modeled: the mine map, the mining equipment, and the miners. The structure of the map and the mining equipment used was researched beforehand by visiting Professor Kang. Using the names of the equipment, I searched for online pictures of those mining equipment to use as reference for the modeling. As time was an important factor for this project, we began with simple modeling to test with Huang's new framework.



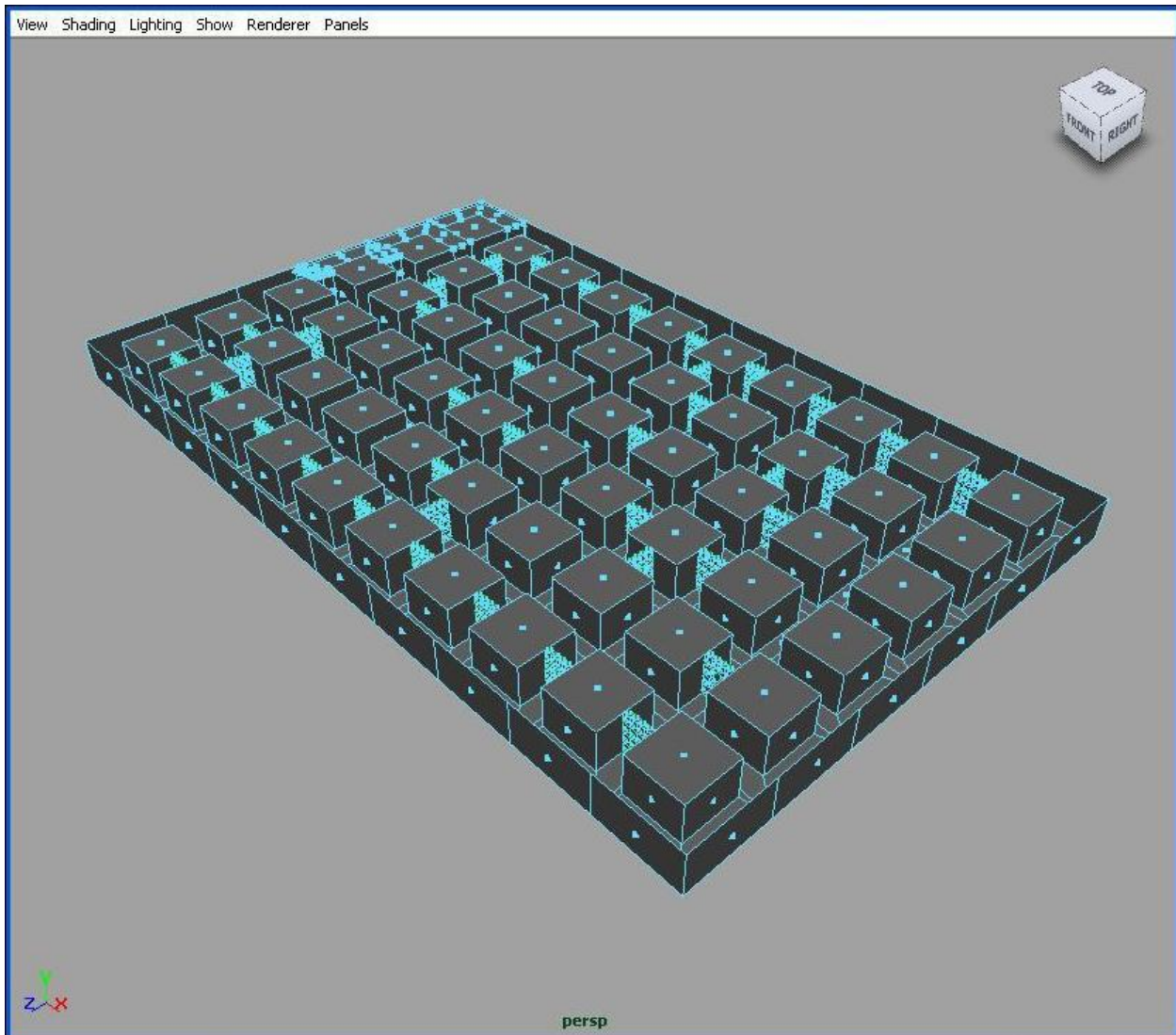
U. S. Bureau of Mines

Fig. 1.

**Figure 21. Room-and-pillar mine map from the U.S. Bureau of Mines.**

#### 4.1 Maps

To model the mine map of the room-and-pillar method of underground mining, we used an image from the U.S. Bureau of Mines (Figure 1). Using this image a first map was created (Figure 2) and was tested on the new framework. Later on, the change from obj to mesh files was quick with the exporter and testing continues to be good.



**Figure 22. The first mine map, shown inside Maya with the faces mode on. This map is not textured.**

Using the information Prof. Kang wrote on the mine scenario, a second map was created (Figure 3). This map contains more specific measurements for overall height, corridor and pillar width and length, and approximate height, width and length of the mining equipment. Since Maya can create models with different units (e.g., meters and centimeters), I chose to use the default setting of centimeters. Therefore, the new map, which should be 700 meters long, is only 700 centimeters long. Using free texture images, the map was also textured to look more like a coal mine.

## 4.2 Equipment

To simulate a more realistic underground coal mine, the mining equipment used by the miners is needed. But this equipment is varied and even one piece of equipment can contain different

models that will not necessarily look the same. While surface mining contains drilling and excavation equipment, underground mining has equipment that can claw through the seam and collect coal or bolt the roof of the mine for security. Various mining equipment catalogs from companies such as Joy Mining Machinery were looked over for reference. The equipment modeled was the following: a mantrip, a shuttle car, a roof bolter, a continuous miner and two different version of a conveyor belt.

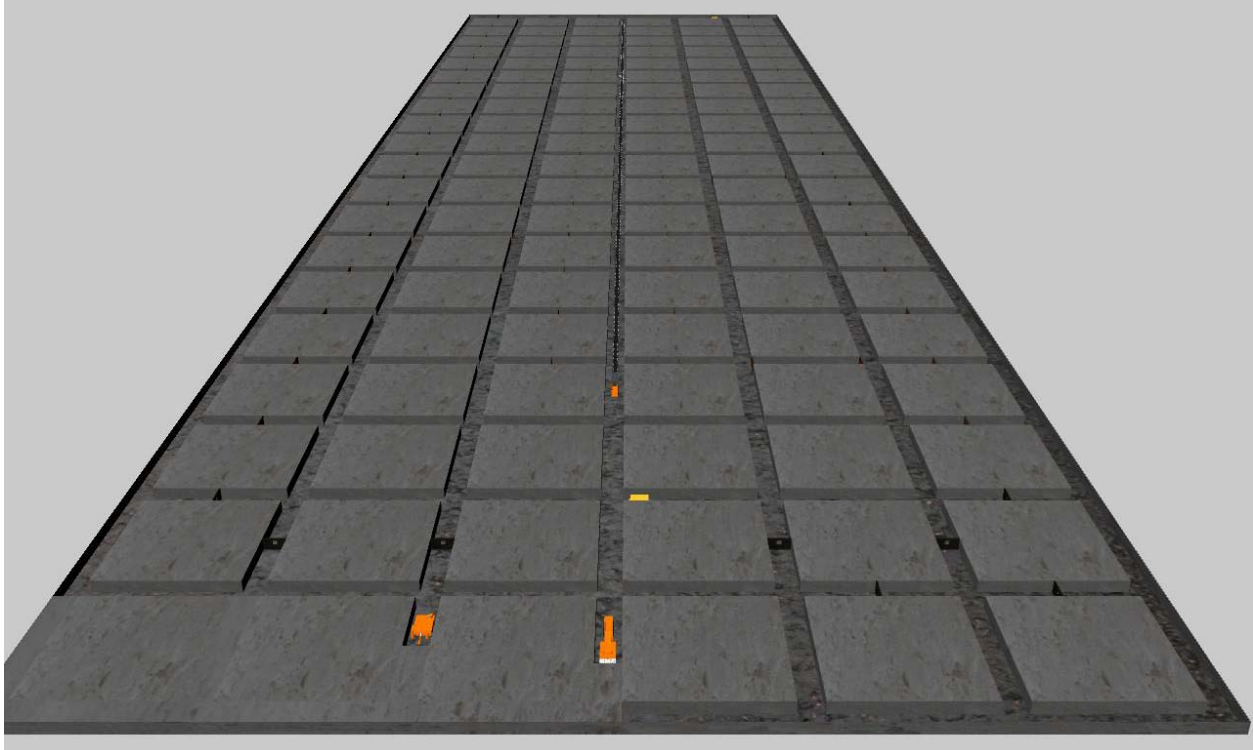


**Figure 23. Final mine map showing the mining equipment as well. This map is textured.**

The mantrip is the car that carries the miners from one end of the mine to the other. Shuttle cars carry the coal from the working face, where mine is currently being extracted from, to the conveyor belt dump point. The roof bolter is a machine to secure the roof of the mine from collapsing, while the continuous miner claws through the coal seam, extracting the coal and dumping it on the shuttle car. Finally, the conveyor belt travels along the mine to bring the extracted coal to the surface. Figure 4 shows all finished models of the aforementioned mining equipment.

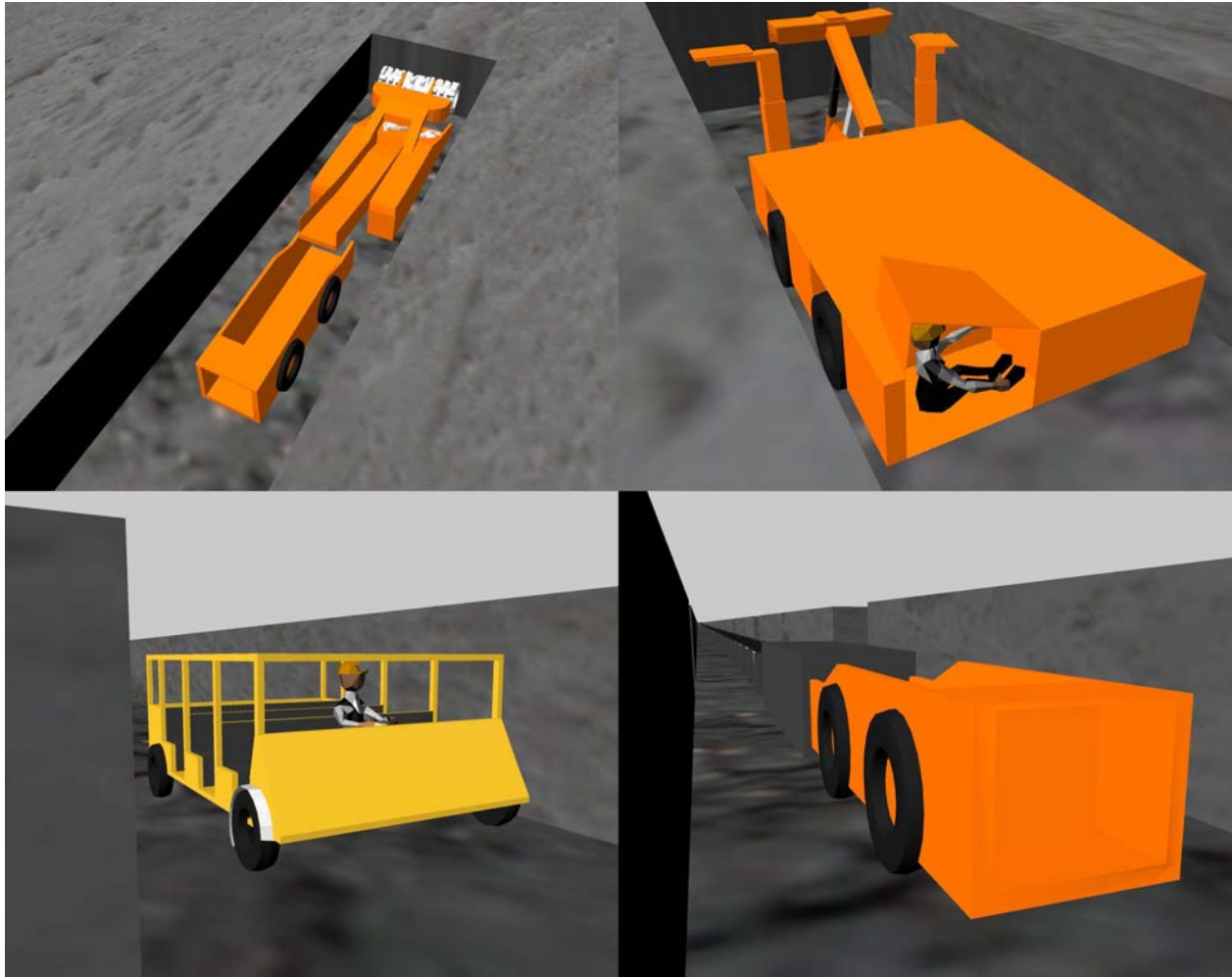


**Figure 24.** On the upper left are the continuous miner and a shuttle car while the upper right contains the roof bolter with a miner. Lower left is the mantrip with a miner and lower right is another shuttle car, the unfinished dump point and the end of the conveyor belt, extending to the start of the mine.

## 5. Animation

### 5.1 Miner

The miner model used in this project was obtained online from [5]. Though it was a pre-made model, this miner cannot move at all. Therefore, it is necessary to bind a skeleton to the model using Maya. To animate the miner, a collection of motion capture data was used to bind the skeleton to animation clips. For this method, Autodesk Motion Builder was used.

Although the miner may have animations now, those animations are bound to the skeleton and in order to export the miner and skeleton to OGRE format files, a repetition of import and export would need to be done. Since this is time consuming and would eventually create problems with

loading the miner to the simulation, a new method was developed with the help of consulting student Jon McCaffrey. Appendix A shows the python script for Maya to import every animation clip, save it in a Maya scene file and repeat the process until all the animation clips are contained in one miner skeleton where the skeleton is exported to an OGRE .skeleton file. This script can be used for various Autodesk FBX (.fbx) files and being a python script, takes around four hours to save 108 clips.

## 5.2 Equipment

The mining equipment was a much easier process to animate, albeit tediously long. With Maya it is possible to animate objects by key framing their movements. A process that helps this animation is walk cycles. Walk cycles are the repetition of a series of key frames that start and end in the same manner. This process is used often by animators when animating a human walking. Using this method for the mantrip, shuttle car and roof bolter, rotation and translation of the wheels makes it possible to pretend movement of the vehicles. The animation of the claws of the continuous miner and treads of the conveyor belts are done in the same fashion. The roof bolter contains additional animations for setting up the support of the roof bolter and bolting the roof.

Figure 5 shows the second conveyor belt since this model was created differently than the wheels of the vehicles. For the conveyor belt, a single tread was created and animated for each key frame to create the walk cycle. Afterwards, using the script in Appendix B, the tread was duplicated a number of times along with the animation and the animation was offset to create a natural motion. Finally all mining equipment and their vertex animations were exported using the Maya-OGRE exporter.

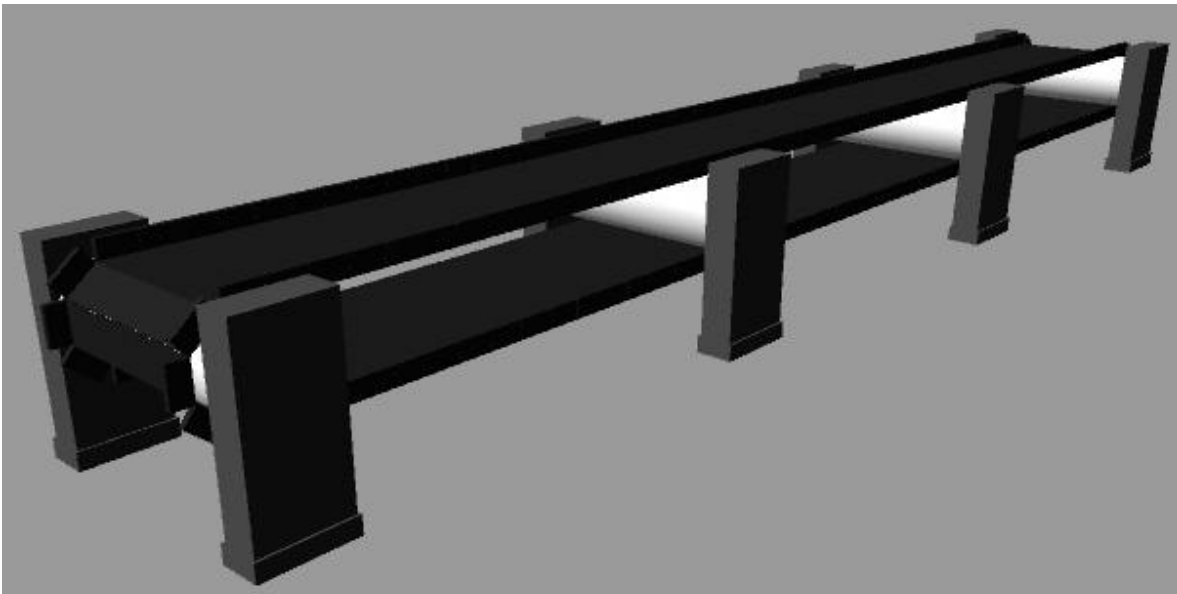


**Figure 25. The second version of the conveyor belt. Notice in the lower middle left side that the treads do not connect to a single object. They are different object with the same animation.**

## **6. DISCUSSION AND CONCLUSIONS**

As a side note, I was also in charge of updating the wiki page of the project with all the references given in our communication via e-mails.

It is important to note that all the goals set upon me have been fulfilled. The search for new methods of map creation concluded that Maya, a powerful modeling tool, fit the criterion of all except one of the features needed by the level editors or game engines. The mine map was successfully created using the measurements specifications given by Prof. Kang and can be loaded into the new framework by grad student Huang. The modeling and animation of all the important mining equipment was also finished. Only two pieces of the mine were never fully modeled: the conveyor belt dump point, where the coal was slowly thrown on the conveyor belt; and the generator that supplied power to the machines.

The animation of the miner was tediously finished and a decent walk cycle was made using the motion capture data. With all these elements, grad student Huang was able to make a small demo for the presentation.

## **7. RECOMMENDATIONS**

With the models and animations, it is possible to finish the simulation and obtain a realistic result that can be compared to the case study book. To validate our own results, it is important to talk with someone that has been through the experience of an underground mine fire or an expert on the subject. The recommendations I can give are to finish modeling the dump point and generator. It is also possible to change the texturing of the mine map to something less image dependent. With those recommendations and the results of a simulation, it is possible to write a good paper for publication and the project can be proposed to the the government for further development.

## **8. ACKNOWLEDGEMENTS**

I would like to thank Professor Jan Van der Spiegel and Professor Norman I. Badler, both of the University of Pennsylvania, the former for the opportunity and the latter for expressing interest in me and offering me this project. I would also like to thank visiting Professor Jinsheng Kang, of Brunel University, for proposing this project in the first place and Pengfei Huang, of the University of Pennsylvania, the constant reminders of our weekly meetings and pushing me forward in my work. My thanks go out to the graduate student advisors involved in the project, especially Jon McCaffrey for not getting angry with me every time I asked where the same Maya button was. I would also like to thank the other students in the SIG Graphics Center for their help whenever I had a doubt. Finally, I would like to thank the NSF for their continuous support of the SUNFEST program through grants.

## **9. REFERENCES**

1. C. Vaught, M. J. Brnich, L.G. Mallett, H. P. Cole, W. J. Wiehagen, R. S. Conti, K. M. Kowalski, and C. D. Litton, *Behavioral and Organizational Dimensions of Underground Mine Fires*. Pittsburgh, PA: U.S. Department of Health and Human Services, Public Health Service, Centers for Disease Control and Prevention, National Institute for Occupational Safety and Health, Pittsburgh Research Laboratory, 2000, pp. 27-45.
2. World Coal Institute. (no date). Coal. Available: <http://www.worldcoal.org/coal/>
3. National Geographic Channel. (no date). Underground Inferno is their story & the science to save them from coal mine fires. Available: <http://www.ngcasia.com/Programmes/underground-inferno>
4. N. Pelechano, J. M. Allbeck, and N. I. Badler, *Virtual Crowds: Methods, Simulation, and Control*. Morgan & Claypool, 2008, pp. 47-112.
5. Human Body Art. (no date). 3D Low Polygon Miner. Available: [http://www.linefour.com/acatalog/LOW\\_POLYGON\\_MINER.html](http://www.linefour.com/acatalog/LOW_POLYGON_MINER.html).

## Appendix A

```
#####
##### Script to save all the takes in the FBX file to one Maya scene.
# Purpose: Export all takes in one OGRE mesh and skeleton with the skeleton having all
#         the animations in the FBX file.
# Written by: Jon McCaffrey and Desiree Velazquez
#####
#####

# Import libraries to use
import maya.mel
import maya.cmds

#####
##### First Part: Create file where all takes will be saved to
#####

# Create new Maya file, read the number of counts to save and import first take
maya.mel.eval('file -f -new ;')
maya.mel.eval('FBXRead -f minerAnim ;')
last = maya.mel.eval('FBXGetTakeCount ;')
maya.mel.eval('FBXImportShowUI -v false ;')
maya.mel.eval('FBXImport -f minerAnim -t 0 ;')

# OGRE Export names
directory = r'D:\Documents and
Settings\HMS\Desktop\601_031172_lowpolymanminer\OGRE_skeletons2\minerExport'
mesh = directory + '.mesh'
material = directory + '.material'
```

```

skeleton = directory + '.skeleton'

# Save Maya scene
nm = r'D:\Documents and
Settings\HMS\Desktop\601_031172_lowpolymanminer\timeline.mb'
maya.mel.eval('file -rename "' + nm + '" ;')
maya.mel.eval('file -save -type "mayaBinary" ;')

framecount = {} # map of numbers
offset = 0.0
clips = ""
for take in range(last): # Go through all the takes and do:
#####
##### # Second Part: Add key frames of current take to maps
#####
#####

files = {} # "Create" a new one for memory saving purposes

# Create a new Maya file, read the FBX file, and import current take
maya.mel.eval('file -f -new ;')
maya.mel.eval('FBXRead -f minerAnim ;')
maya.mel.eval('FBXImportShowUI -v false ;')
maya.mel.eval('FBXImport -f minerAnim -t ' + str(take) + ' ;')

# Print to see which take we are currently saving
takeStr = 'Take ' + maya.mel.eval('FBXGetTakeName ' + str(take) + ' ;')
print take, ': ', takeStr

maxframe = 0

# Maps
files[takeStr] = {}

files[takeStr]['Hips'] = {}
files[takeStr]['Spine'] = {}
files[takeStr]['Neck'] = {}
files[takeStr]['Head'] = {}
files[takeStr]['HeadTop'] = {}
files[takeStr]['LeftShoulder'] = {}
files[takeStr]['LeftArm'] = {}
files[takeStr]['LeftElbow'] = {}
files[takeStr]['LeftWrist'] = {}
files[takeStr]['LeftHand'] = {}
files[takeStr]['RightShoulder'] = {}

```

```

files[takeStr]['RightArm'] = {}
files[takeStr]['RightElbow'] = {}
files[takeStr]['RightWrist'] = {}
files[takeStr]['RightHand'] = {}
files[takeStr]['LeftLeg'] = {}
files[takeStr]['LeftKnee'] = {}
files[takeStr]['LeftAnkle'] = {}
files[takeStr]['LeftFootEnd'] = {}
files[takeStr]['RightLeg'] = {}
files[takeStr]['RightKnee'] = {}
files[takeStr]['RightAnkle'] = {}
files[takeStr]['RightFootEnd'] = {}

files[takeStr]['Hips']['tx'] = {}
files[takeStr]['Hips']['ty'] = {}
files[takeStr]['Hips']['tz'] = {}

for object in files[takeStr]:
    files[takeStr][object]['rx'] = {}
    files[takeStr][object]['ry'] = {}
    files[takeStr][object]['rz'] = {}

    for field in files[takeStr][object]:
        num = maya.cmds.keyframe(object, q=True, kc=True, at=field)

        for i in range(num):
            pair = maya.cmds.keyframe(object, q=True, index=(i,i), at=field,
timeChange=True, valueChange=True)
            files[takeStr][object][field][pair[0]] = pair[1]
            if pair[0] > maxframe:
                maxframe = pair[0]
            #time, location = [0.80000000000000004, 3.6132581233978267]

framecount[takeStr] = maxframe

#####
##### # Third Part: Open the Maya scene and save the key frames from offset
#####
#####

maya.mel.eval('file -f -o "' + nm + "' ;')

for object in files[takeStr]:
    for field in files[takeStr][object]:
        for keyframe in files[takeStr][object][field]:

```

```

        tiempo = offset + keyframe
        maya.cmds.setKeyframe(object, at=field, time=tiempo,
value=files[takeStr][object][field][keyframe])

    t1 = offset
    offset += framecount[takeStr]
    t2 = offset
    offset += 1.00
    clipName = "CLIP" + takeStr
    clips += ' -skeletonClip ' + clipName + ' startEnd ' + str(t1 + 1.00) + ' ' + str(t2) + ' frames
sampleByFrames 1 '

    maya.mel.eval('file -save ;')

#####
##### Last Part: Clean the file and export to OGRE mesh
#####
#####

# Delete the unnecessary
maya.mel.eval('parent -world minrhlmt ;')
maya.mel.eval('parent -world Hips ;')
maya.mel.eval('select -r skelton_root BVH:Hips Character_Ctrl:Reference group1 transform2
Skeleton_root Light ;')
maya.mel.eval('doDelete ;')

# Detach / Attach skin
maya.mel.eval('select -r Hips ;')
maya.mel.eval('gotoBindPose ;')
maya.mel.eval('select -r minrhlmt ;')
maya.mel.eval('doDetachSkin "2" { "1", "1" } ;')
maya.mel.eval('select -r Hips minrhlmt ;')
maya.mel.eval('SmoothBindSkin ;')
maya.mel.eval('select -r Hips minrhlmt ;')

maya.mel.eval('file -save ;')

# Export to OGRE mesh
maya.mel.eval('ogreExport -all -world -lu pref -scale 1 -mesh "" + mesh + "" -shared -v -n -t -mat
"" + material + "" -skel "" \
+ skeleton + "" -skeletonAnims -np bindPose -skeletonClip "" +
clips + "" ;')
print offset

```

```
#####  
##### END  
#####  
#####
```

## Appendix B

```
#####  
##### Script to duplicate a tread with key frames.  
# Purpose: Duplicate a created tread with key frames to create a conveyor belt.  
# Written by: Jon McCaffrey and Desiree Velazquez  
#####  
#####  
  
# Import libraries to use  
import maya.mel  
  
for i in range(101):  
    # Select tread and duplicate with animation  
    maya.mel.eval('select -r conveyor_tread01;')  
    maya.mel.eval('duplicate -rr -un;')  
  
    # Rename the duplication to something else  
    nm = 'conveyor_dup_0' + str(i)  
    maya.mel.eval('rename "conveyor_tread02" "' + nm + "';')  
  
    # Rename the translations and rotations to coincide with tread name  
    maya.mel.eval('rename "conveyor_tread01_translateX1" "' + nm + '_translateX";')  
    maya.mel.eval('rename "conveyor_tread01_translateY1" "' + nm + '_translateY";')  
    maya.mel.eval('rename "conveyor_tread01_rotateZ1" "' + nm + '_rotateZ";')  
  
    # Offset the translations and rotations by i and note that i can be changed (necessary for  
speed)  
    maya.mel.eval('keyframe -e -iub true -r -o over -tc ' + str(i) + ' ' + nm + '_translateX ;')  
    maya.mel.eval('keyframe -e -iub true -r -o over -tc ' + str(i) + ' ' + nm + '_translateY ;')  
    maya.mel.eval('keyframe -e -iub true -r -o over -tc ' + str(i) + ' ' + nm + '_rotateZ ;')
```

---

[<sup>i</sup>] Z. Bliznakov, G. Mitalas and N. Pallikarakis, “Analysis and Classification of Medical Device Recalls,” in *IFMBE Proc.*, 2006, pp. 3782-3785.

[<sup>ii</sup>] W. H. Maisel, M. O. Sweeney and W. G. Stevenson, “Recalls and safety alerts involving pacemakers and implantable cardioverter-defibrillator generators,” *JAMA* vol. 286(7), pp. 793-799, 2001.

[<sup>iii</sup>] FDA. (2009, July 23). *Medical Devices: List of Device Recalls*. [Online]. <http://www.fda.gov/MedicalDevices/Safety/RecallsCorrectionsRemovals/ListofRecalls/default.htm>

- 
- [<sup>iv</sup>] A. J. Compton, H. Bolouri and A. W. Nathan, "Arrhythmia recognition strategies and hardware decisions for the implantable cardioverter-defibrillator- A review," *Med. Eng. Phys.*, vol. 17(2), pp. 96-103, Mar. 1995.
- [<sup>v</sup>] E. P. Gerstendfeld, private communication, June, 2009.
- [<sup>vi</sup>] J. Coromilas, "Physician credentials and ICD implantation: Certified "electricians" best deal with electrical problems," *JAMA* vol. 301(16), pp. 1713-1714, 2009.
- [<sup>vii</sup>] D. E. Arterburn, P. K. Crane and S. D. Sullivan, "The coming epidemic of obesity in elderly Americans," *J. Am. Geriatrics Society*, vol. 52(11), pp. 1907-1912, Nov. 2004.
- [<sup>viii</sup>] K. Bibbins-Domingo, P. Coxson, M. J. Pletcher, J. Lightwood and L. Goldman, "Adolescent overweight and future adult coronary heart disease," *New England J. of Med.*, vol. 357, pp. 2371-2379, Dec. 6, 2007.
- [<sup>ix</sup>] K. P. Anderson, "The changing epidemiology of ventricular arrhythmias," *Clin. Cardiol.*, vol. 26(3), pp. 321-333.
- [<sup>x</sup>] Food and Drug Administration. *FDA Enforcement Report*. Rockville, Md: National Press Office; February 12, 1997.
- [<sup>xi</sup>] MIT. (2009, Apr. 27). *PhysioBank Archive Index*. [Online]. <http://www.physionet.org/physiobank/database/>
- [<sup>xiii</sup>] (2006, Dec.). *MedSim300B Patient Simulator Operators Manual*. Fluke Biomedical. [Online]. [http://assets.fluke.com/manuals/medsim\\_omeng0000.pdf](http://assets.fluke.com/manuals/medsim_omeng0000.pdf)
- [<sup>xiii</sup>] M. Boulakia, M. A. Fernandez, J. F. Gerbeau and N. Zemezmi, "Towards the numerical simulation of electrocardiograms," *LNCS*, vol. 4466, pp. 240-249, 2007.
- [<sup>xiv</sup>] N. Trayanova, K. Skouibine and F. Aguel, "The role of cardiac tissue structure in defibrillation," *Chaos* vol. 8, pp. 221, 1998.
- [<sup>xv</sup>] "Electronic Health Records Overview," National Institutes of Health , National Center for Research Resources, McClean, VA, 2006.
- [<sup>xvi</sup>] G. B. Moody and R. G. Mark, "The impact of the MIT-BIH database," *IEEE Eng. In Med and Biol.*, May/June 2001.
- [<sup>xvii</sup>] B. Taccardi and B. B. Punske, "Body Surface Potential Mapping," in *Cardiac Electrophysiology: From Cell to Bedside*, D. P. Zipes and J. Jalife, Ed. Philadelphia: Saunders, 2004, pp. 803-811.
- [<sup>xviii</sup>] T. B. Garcia and N. E. Holtz, *12-Lead ECG: The Art of Interpretation*, Sudbury, MA: Jones & Bartlett Pub., 2001.
- [<sup>xix</sup>] B. Bojovic, L. Hadzievski and P. Belicev, "Device and procedure for visual three-dimensional presentation of ECG data," U.S. Patent 72266408, Sept. 4, 2007.
- [<sup>xx</sup>] (2008). *NI Single-Board RIO Embedded Control and Acquisition Devices*. National Instruments. Austin, TX. [Online]. [http://www.ni.com/pdf/products/us/cat\\_sbRIO\\_96xx.pdf](http://www.ni.com/pdf/products/us/cat_sbRIO_96xx.pdf)
- [<sup>xxi</sup>] J. P. DiMarco and J. T. Philbrick, "Use of Ambulatory Electrocardiographic (Holter) Monitoring," *Annals of Internal Medicine*, vol. 113, pp. 53-68, 1990.
- [<sup>xxii</sup>] P. J. Zimetbaum and M. E. Josephson, *Practical Clinical Electrophysiology*, Philadelphia: Lippincott Williams and Wilkins, 2009.
- [<sup>xxiii</sup>] A. S. Go, E. M. Hylek, K. A. Phillips, Y. Chang, L. E. Henault, J. V. Selby, D. E. Singer, "Prevalence of Diagnosed Atrial Fibrillation in Adults," *JAMA.*, vol. 285(18), pp. 2370-2375, May 9, 2001.